LEAD FREE CERAMIC/POLYMER BASED HYBRID PIEZOELECTRIC NANOCOMPOSITES AS MECHANICAL ENERGY HARVESTERS

THESIS
SUBMITTED FOR THE DEGREE OF
DOCTOR OF PHILOSOPHY (SCIENCE)
OF
JADAVPUR UNIVERSITY
2022

By

Shewli Pratihar

Index No.: 174/18/Phys./26
Registration No.: SOPHY1117418

Functional Materials and Devices Division
CSIR-Central Glass & Ceramic Research Institute
196 Raja S. C. Mullick Road, Jadavpur
Kolkata-700032
India

CERTIFICATE FROM THE SUPERVISOR

This is to certify that the thesis entitled "**LEAD FREE CERAMIC/POLYMER BASED HYBRID PIEZOELECTRIC NANOCOMPOSITES AS MECHANICAL ENERGY HARVESTERS"** submitted by **Smt. Shewli Pratihar** who got her name registered on **18th September, 2018 (Registration No: SOPHY1117418, Index no: 174/18/Phys./26)** for the award of Ph. D (Science) degree of Jadavpur University, is absolutely based upon her own work under the supervision of Dr. Shrabanee Sen, Principal Scientist, Functional Materials and Devices Division, CSIR-CGCRI, Kolkata, West Bengal-700032 and neither this thesis nor any part of it has been submitted for either any degree/ diploma or other any academic award anywhere before.

Shrabanee Sen 12/8/2022
………………………………………

Dr. Shrabanee Sen
Principal Scientist
Functional Materials and Devices Division
CSIR-CGCRI
Jadavpur, Kolkata-700032

Dr. Shrabanee Sen
Principal Scientist
Functional Materials and Devices Division
CSIR-Central Glass & Ceramic Research Institute
Kolkata - 700 032

Dedicated to
My Parents

Acknowledgement

This dissertation is an assembly of network support, encouragement and inspiration that I have received during the journey of my thesis work. First and foremost, I'd like to express my heartfelt gratitude to my honorable supervisor Dr. Shrabanee Sen, Principal Scientist, Functional Materials and Devices Division, CSIR-Central Glass & Ceramic Research Institute (CGCRI), Kolkata, for her inspiring guidance, insightfulness, creative ideas and constructive suggestions which directed me in realizing the goals of this research.

I am deeply thankful to Dr. Sunirmal Jana, Senior Principal Scientist (Specialty Glass Division, CSIR-CGCRI), subject expert of my RAC committee for giving various valuable suggestions regarding my research work.

I acknowledge Innovation in Science pursuit for Inspired Research (INSPIRE) program of Department of Science and Technology (DST), Government of India for providing me the financial support through research fellowship to complete my research work.

I really feel honored for having come across brilliant teachers/mentors throughout my whole career. I would like to convey my genuine appreciation and profound gratitude to all of them. I acknowledge the divisional head of FMDD for various supports and all the scientist faculties of FMDD for different scientific interactions. I am highly obliged Dr Suman Kumari Mishra (Director, CSIR-CGCRI), Dr. K Muraleedharan (Ex-Director) for their benevolent permission and approval to carry out this work in this institute.

I am also thankful to all the technical staffs of FMDD and MCID of CGCRI especially Md. Jalaluddin Mondal, Sk. Md. Mursalin, Mr. Raju Manna, Dr. Sagnik Das, Mrs. Mousumi Baral Narjinary and Mr. Nitai Dey for various helps received during this thesis work. Their active technical helps during different experimental works have caused my thesis work to be faster and smooth. I shall fail in my appreciation, if I do not recognize the cooperation and support received generously from scientists and staff of several divisions and laboratories along with those from the civil, electrical, canteen, store, library, reception, security section and the administrative office of CSIR-CGCRI.

I would like to give huge and warm thanks to my seniors, juniors and fellow research scholars Ipsitadi, Abhishekda, Avijitada, Aniketda, Anuragda, Arindamda, Epsitadi, Puja, Arindam, Sourav, Gaurav, Pounomi, Somya, Animesh, Deepak for their constant help, constructive criticism and astonishing support during the PhD period. I am also thankful to other seniors, juniors and friends of CSIR-CGCRI namely Subhankarda, Taniadi, Aditidi, Susmitadi, Payeldi, Sukanyadi, Partha, Preeti and others. The sweet memories of their association in CSIR-CGCRI will remain with me forever.

Words fell to express my deep-felt gratitude to my beloved parents (Maa-Baba), younger sister (Bon), and entire family members who have continuously encouraged and mentally supported me to overcome all the hurdles during my PhD journey, keeping me aside from any difficulties in the family. Without their heartfelt blessing, I believe I would not reach to my goal.

Last but not the least, I'm greatly privileged to thank "Almighty God" for giving me the strength and faith in successful completion of my thesis.

………………………..
Shewli Pratihar

ABSTRACT

Energy harvesting from easily available mechanical vibrations in our surroundings has gained attractive substantial attention for its application in the field of artificial skins (electronic skin), shoes, wearable electronics, foldable displays and environment monitoring. Polar Poly(vinylidene) fluoride (PVDF) and its copolymers are the most responsive piezoelectric polymers that can be used as self-powered flexible energy harvesters due to its strong piezoelectric response, chemical and mechanical durability. Consequently, different strategies have been developed to enhance electroactive polar phase fraction of PVDF such as development of specific processing technology, inclusion of specific fillers, mechanical stretching, electrospinning, electrical poling, etc. Therefore, different types of ceramic fillers such as PZT, $BaTiO_3$, $LiNbO_3$, $KNaNbO_3$, $ZnSnO_3$ etc. have been used to fabricate the PVDF composites. In this regard, Zinc Oxide (ZnO) incorporated PVDF composites are very promising materials in this field owing to the inherent piezoelectric property of ZnO as well as environment benign nature. The nucleation and stabilization of the polymer depends upon shape, size as well as concentration of filler. Therefore, in order to investigate the morphological influence of ZnO on the stabilization of β phase of PVDF as well as dielectric, ferroelectric and piezoelectric properties of PVDF based composites, two types of morphologically different ZnO i.e. wet chemically synthesized ZnO particles and hydrothermally synthesized ZnO nanorods were incorporated into PVDF to fabricate their respective composite films. One dimensional (1D) rod shape structure was found to be more effective in enhancing the dielectric, ferroelectric, energy storage and energy harvesting performance PVDF compared to particle like structure of ZnO. Furthermore, to study the effect of aspect ratio of ZnO nanorod on the electrical properties of PVDF, ZnO nanorods with different aspect ratio were synthesized and incorporated into PVDF matrix to fabricate the resulting composite film. ZnO filler with high aspect ratio increased the polar phase fraction of PVDF composite which triggered the enhancement of dielectric properties along with ferroelectric and piezoelectric properties. Thereby, the aspect ratio of ZnO nanorods was tuned to achieve the performance enhancement of the resulting PVDF based composites. For further enhancement of electrical performances, third phase conductive filler such as multi-

walled carbon nano tube (MWCNT) was impregnated in the flexible ZnO/PVDF composites. MWCNT has supported homogeneous dispersion of ZnO in PVDF matrix by reducing compatibility issues. This uniform dispersion of filler in the matrix improved the polarity of the matrix by enhancing the interfacial interaction between $–CH_2$ dipoles of PVDF and surface charges of fillers, which lead to the enhancement of dielectric, ferroelectric, energy storage density and mechanical energy harvesting performance of the composite. ZnO filler was further modified by incorporating Al^{3+} ions into the ZnO host lattice, which lead to the modification of the surface charge of the nano-filler and reduced oxygen point defects. Use of Al^{3+} ions incorporated ZnO as filler in PVDF matrix enhanced the dielectric constant of the composite with a considerably low dielectric loss and reduced the leakage current value. The enhanced surface charge of ZnO filler improved the polar phase, dielectric permittivity, energy storage density and mechanical energy harvesting performance of the resulting PVDF-HFP based composite films. 10 wt% Al@ZnO loaded poled PVDF-HFP (10PALZO-P) composite was considered as the most suitable candidate to design the energy harvester owing to its best performance in terms of dielectric, ferroelectric, piezoelectric properties as well as output performance i.e. output voltage, current and power density. In order to achieve the real life applicability of the fabricated energy harvester, it was used to harvest energy from different types of human body motions such walking, running, hand or wrist movement etc. This piezoelectric energy harvester (PZEH) has also been utilized as an efficient height-monitoring sensor. Thereby, the present thesis work established the feasibility of using ZnO-based composites towards low cost, flexible as well as wearable piezo-electric energy harvesting devices.

TABLE OF CONTENTS

Chapter 3: Results and discussions

Chapter 4: Summary and future scope

CHAPTER-1

Background, Literature Review and Objective

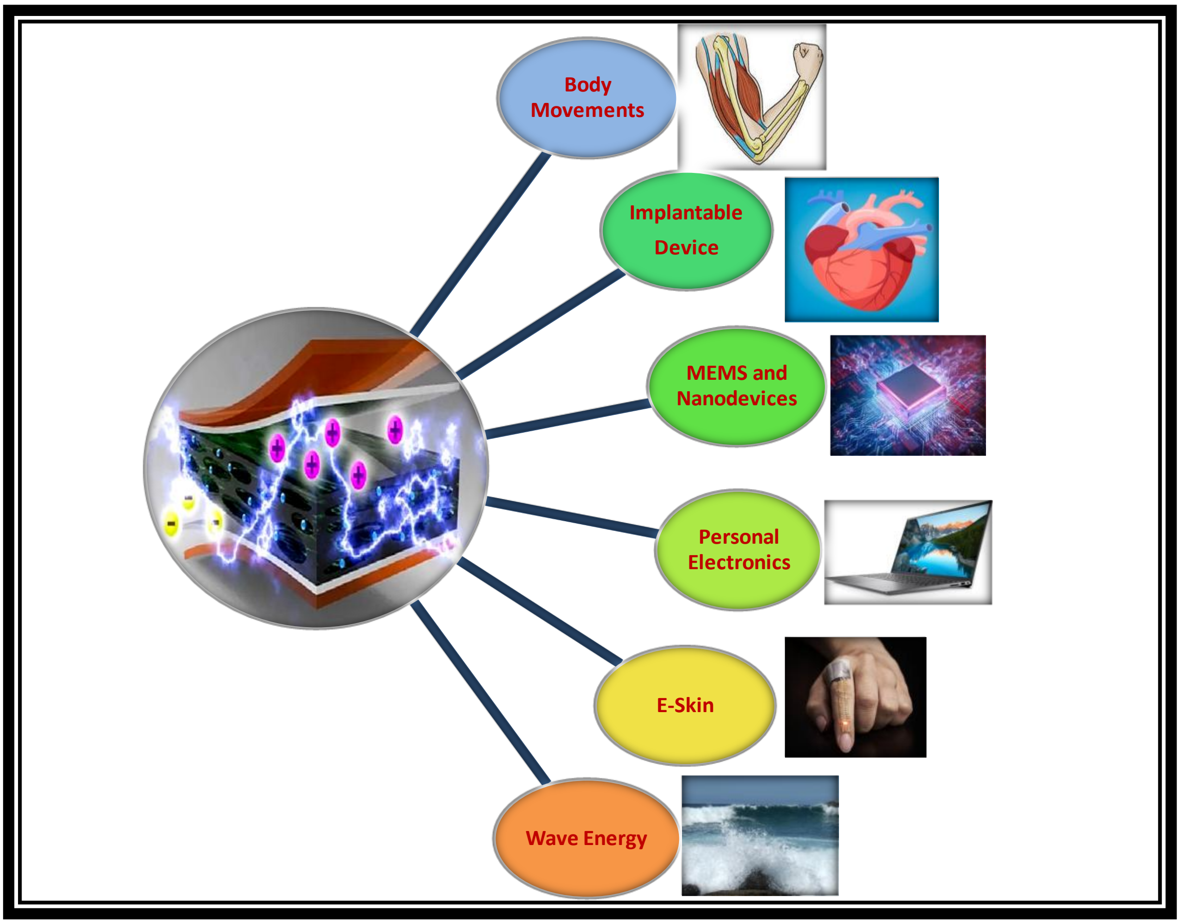

The main objective of this thesis work to develop lead free polymer-ceramic composite as mechanical energy harvester which can harvest electrical energy from ambient vibration and able to power up some small scale electronic gadgets. Therefore the perspective and implication of mechanical energy harvester along with background, motivation and objectives of the desertion work were described in Chapter 1. The origin, fundamental theory, classifications and their application in nanogenerator were described in detail. Based on the review, PVDF and its co-polymers were considered as a superior material for real life application due to their high toughness, low fatigue behavior which can generate voltage under long-term continuous vibration. Among the different techniques to attain β polymorph of PVDF and its co-polymers, incorporation of ZnO as a ceramic filler was chosen owing to its superior piezoelectric, pyroelectric properties, biocompatibility and easy synthesis method.

Chapter 1: Background, Literature Review and Objective

1.1 . Motivation

The rapid depletion of fossil fuels and global warming are two major serious issues for human civilizations [1-2]. In the last century, global energy consumption has been increased aggressively due to the rapidly growing industrialization and urbanization [1]. Conventional energy sources mostly rely on fossil energy sources causing serious issues such as global warming, shortage of resources, as well as environmental pollution [2]. But due to the rapid growth of human population, industrialization and the use of modern equipments, today's energy demand is also increasing day by day.

To address these issues, efficient energy harvesting has been developed as one of the most important technology in today's green and renewable energy science [3]. Large scale energy harvesting schemes from renewable resources are mainly focused on solar, wind, hydro, geothermal, biomass, nuclear etc. [4-9]. Though these energy sources can power up from mega to giga watt range power scale, they are not always accessible and dependent on environmental factors [10-12]. Moreover, most of these energy resources need high set-up cost and large installation area. On the other hand, the increasing demand for portable, flexible and wearable electronics in daily life is boosting the growth of new technologies like Internet of Thing (IOT), Internet of Action (IOA), Micro-electromechanical systems (MEMS) and wireless sensor networks which are used for health monitoring, infrastructure monitoring, military and security surveillance etc. All of these devices require a large amount of small scale energy in portable and wearable form [10]. The demands of these kinds of devices are rising day by day in recent times. These devices are mainly powered by conventional batteries which have several limitations such as, large size, limited lifetime, requirement of periodic maintenance and finally environmental pollution issues during their disposals after the end of their lifetime [10-12, 13]. Hence, development of small scale energy resources in echo friendly way is required urgently.

Thus, development of such echo friendly energy sources are needed which can harvest electrical energy from ambient vibration in an autonomous way which is easily available in our nature and the corresponding device may be operated in self powered mode. There are various energies available in our surrounding which are not being used properly. Among all available surrounding energy resources, the most ubiquitously waste energy is mechanical vibrations which residues in different forms like human motion, walking, blood circulation, breathing and heartbeat, vehicle vibration, water flow, air flow, etc [14-20]. Therefore, if small amount of these irregular waste energies could be converted into electricity, it can replace batteries to power up some small scale devices such as mobile phone, small sized computer, GPS, radio communication devices and wearable electronics, etc. Hence, the development of such innovative technology is highly desirable which can convert ambient mechanical energy into electrical energy [21].

1.2 . Mechanical Energy harvesting

In the last decades, mechanical energy harvesting has attracted much attention due to its wide availability and greater accessibility anytime and anywhere. Mechanical energy harvesting offers innovating ways to capture wasted environment mechanical energy such as human motions, vehicle motion, mechanical rotation, vibration of bridges, ocean wave, wind etc and thereby generating electrical energy. This green and sustainable energy sources effectively generates usable electric power for self-powered micro/nanodevices. Therefore, the most promising technologies have been developed to harvest electrical energy from mechanical energy by utilizing two major effects, namely piezoelectric effect and triboelectric effect. A brief outline of these mechanical energy harvesting systems are discussed in below.

Piezoelectric nanogenerators can directly convert mechanical stress into electrical power by the well known process called piezoelectric effect. In simplest terms, the piezoelectric effect is driven by the coupling phenomenon between mechanical and electrical states. When mechanical stress is applied to a piezoelectric material, the crystal structure deformed in such a way to cause the movement of electrical charges and hence an output voltage generated [22].

Triboelectric nanogenerators generate electrical output using triboelectric effect and electrostatic induction. By means of contact electrification effect, a material surface becomes electrically charged, when it comes into contact with a triboelectricity different material. In this manner, triboeletric nanogenerators create electrical energy through charge transfer between the two materials with proper insulation between each layer [23]. Triboelectric nanogenerator operates in four different modes: vertical contact-separation mode, lateral sliding mode, single electrode mode and freestanding mode.

Recently, piezoelectric [24-26] and triboelectric [27] and energy sources have been actively investigated to scavenge energy from ambient environmental and biomechanical energy, especially from human movement or touch. Such thin, low weight devices are suitable for portable and flexible electronics working at low frequency. Triboelectric and piezoelectric energy generators are also cost effective in comparison to other nonconventional energy sources. But the main limitations associated with the triboelectric devices are complex structure, low stability, low durability, industrial packaging problem in open environment due to humidity, high output voltage which can damage the electronic circuit, producing fire etc., especially where general electronic circuitry required low power [24-26]. Therefore, the piezoelectric energy harvester has gained considerable attention, owing to its key advantages such as large power density and ease of implementation of piezoelectric devices in both nano and microscale based on well-developed production technique.

1.3 . Piezoelectric energy harvesting

Since the present work deals with the development of polymeric piezoelectric composites for energy harvesting, a relevant description on piezoelectric energy harvester including the current status, application and market predictions is being involved in this section.

Recently, piezoelectric energy harvesting technology has attracted much attention as a renewable power source mainly due to its energy efficiency and environmental benefits. Some piezoelectric components can provide the highest efficiency and power output by size and cost when compared with other types of harvesting technologies, making it possible to replace batteries that brings environmental benefits and cost effectiveness.

Since 1990's, the output power of piezoelectric energy harvester has increased dramatically from µW to mW scales. This enables it to be utilized in a wide range of applications such as remote controls, switches, wireless sensor networks, condition monitoring sensors (e.g. tire pressure, rotor blades in helicopters), industrial asset tracking GPS/GPRS, etc. There are various ways to generate energy by using piezoelectric materials like energy harvesting from human movements in train stations or other public places, using dance floors to produce electricity, and harvesting vibrations from industrial machinery to charge batteries for backup supplies or to power microprocessors and wireless radios. Furthermore, piezoelectric micro/nano-generators would also be able to power muscle-driven elements and self-powered body implantable devices, etc [21].

The energy harvesting market has increased from £450 million in 2012 to more than £950 million by 2017, and that investments in piezoelectric energy harvesting has increased to $145 million in 2018 creating a $667 million market by 2022 [21]

1.3.1. Piezoelectricity

The piezoelectric energy harvesting technology is based on the piezoelectricity of the respective piezoelectric material. Thus a detail description of the piezoelectricity is essential in this context.

1.3.2. Origin and history of piezoelectricity

The word ‘Piezoelectricity’ is originated from the Greek word ‘piezein’, which means ‘squeeze’ or ‘press’ [21]. Thus piezoelectricity defines the generation of electricity coming from stress (strain). This process is based on the accumulation of electric charge under the application of external mechanical strain in certain materials such as crystals, ceramics, and biological substance such as bone, DNA and proteins [21].

Piezoelectric effect was first discovered by Curie brothers in 1880 [28]. They found that Quartz and Rochelle salt showed maximum piezoelectricity, but did not predict the reverse piezoelectric effect which was mathematically deduced from basic thermodynamic principles by Lippmann in 1881 [29]. This encouraged curie brothers to experimentally confirm the existence of the converse effect and continue the work to prove the complete reversibility of electro-elasto-mechanical deformations in piezoelectric crystals quantitatively. Later, in 1910, Woldemar Voigt published a textbook on ‘Crystal Physics’, which contains 20 classes of natural piezoelectric crystals with their respective piezoelectric constants using tensor analysis [30].

According to Gautschi, this Piezoelectric effect is the linear electromechanical interaction between mechanical and electrical state in crystalline materials without inversion symmetry [31], and it is a reversible process: the generation of electricity resulted from applied mechanical strain (in generators or transducers) and the generation of mechanical strain resulted from applied electric field (in actuators). Thus this property can be easily used in many applications from production of ultrasonic waves, detection of sound and electronic devices etc. for everyday uses.

During World War I, in France, Piezoelectric devices were first used as sonar (ultrasonic submarine detector) to calculate distances between objects. In the next few decades, new piezoelectric devices were created and developed such as ceramic phonograph cartridges, ultrasonic transducer for measurement of elasticity and viscosity and ultrasonic time-domain reflectometers [21].

During World War II, different research groups from the USA, Russia and Japan discovered ferroelectrics which had much higher piezoelectricity than natural materials. Research was focused on material like Barium Titanate (BT) and Lead Zirconium Titanate (PZT). Quartz crystals were the first commercially used piezoelectric material in the USA, but scientists kept searching for materials with better performances. In Japan, piezoelectric ceramic materials were developed for application like piezoelectric filters, buzzers, audio transducers, igniters, gas-grill lighters, and ultrasonic transducers which was first used in early television remote controls [21].

1.3.3. Mechanism

Piezoelectric effect mainly arises due to electromechanical interactions between electrical and mechanical states of certain materials which have no inversion symmetry in their crystal structure [31]. There are two types of piezoelectric effects, namely, direct piezoelectric effect and reverse piezoelectric effect. When a mechanical stress is applied to a piezoelectric material, electric charges are generated within the material which is proportional to the applied stress. This phenomenon is known as direct piezoelectric effect (**Fig. 1.1.a**) [32]. On the other hand, converse piezoelectric effect occurs when the material is subjected to external electric field, there is a mechanical strain proportional to the applied electric field produced within the material (**Fig. 1.1.b**) [32]. Each mode can be used for different application; mechanical sensor and energy harvesting device for the direct effect while actuator and ultrasound transducer for the reverse effect. Piezoelectricity in solid materials is closely related to their electric dipole which possibly be carried by molecular groups or be induced by ions on crystal lattice sites with asymmetric charge environments [21]. When these materials are subjected to mechanical stress, they are deformed in such a way that, a net separation of charged ions is created within the structure. Hence, positive and negative directions are formed in the respective unit cells. Thus, electric charges on the surface of the non-centrosymmetric crystalline unit cells are manifested by this phenomenon known as dielectric displacement. In this way the direct piezoelectric effect arises. For converse piezoelectric effect, all these phenomena occur in reverse direction [33].

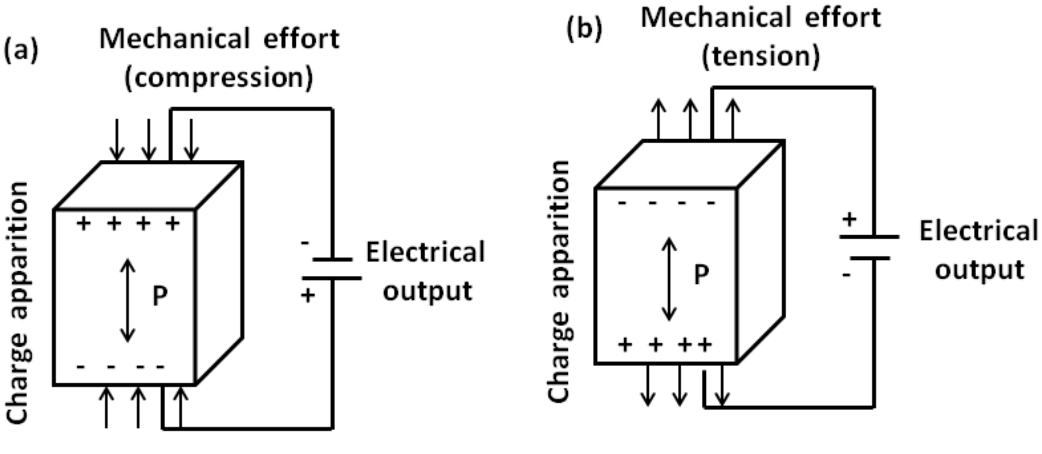

Fig. 1.1 (a) Direct and **(b)** reverse piezoelectric effect

1.3.4. Crystal classes and piezoelectricity

In order to have a better understand, the relation between piezoelectricity and crystal structure, the fundamentals of piezoelectricity and related materials are presented in this section. When a dielectric material is kept under electric field, it becomes polarized to separate positive and negative charges, thereby creating a dipole having dipole moment which is defined as the product of the charges developed and the distance between them. Hence polarization can be defined as the dipole moment per unit volume. In certain class of dielectric material lacking centre of inversion symmetry, a large piezoelectric strain can occur, in response to the electric field [34]. The relationship among dielectric , piezoelectric, pyroelectric and ferroelectric materials are shown in **Fig. 1.2.**

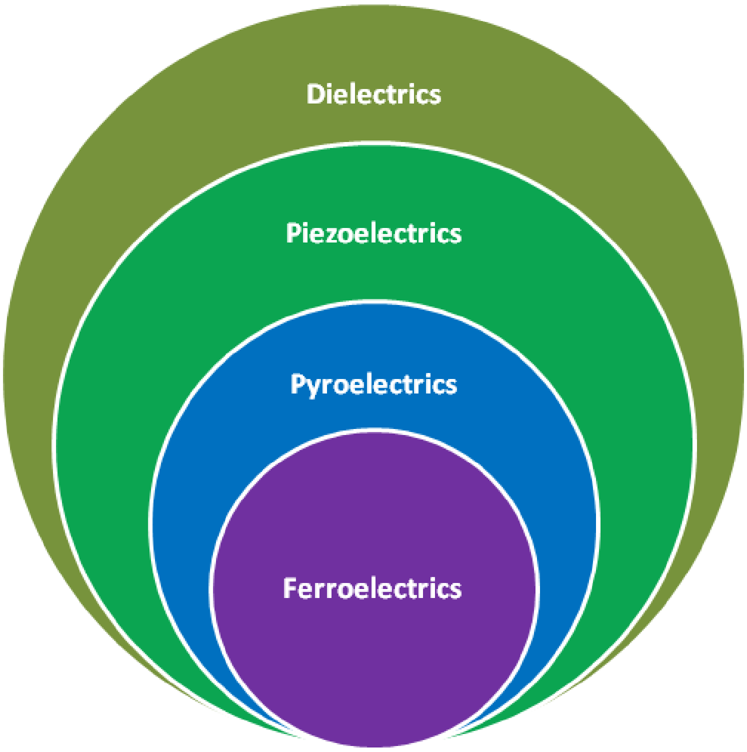

Fig. 1.2 Inter-relationship among piezoelectric, ferroelectric, pyroelectric and dielectric property of the materials

A material's crystal structure must be non-centrosymmetric for it to show piezoelectricity, and be both non-centrosymmetric and posses a unique axis of symmetry (making it polar structure) for it to be pyroelectric. Out of 32 crystal classes, 20 classes are piezoelectric with non-centrosymmetric structure. Among 20 piezoelectric crystal classes, 10 classes have pyroelectric properties. In this type of materials, permanent dipoles are generated within a given temperature range and thus develop spontaneous pyroelectric polarization. Ferroelectrics are subgroup of pyroelectric materials, in which spontaneous polarization within the structure can be switched by an application of an electric field of sufficient magnitude.

1.3.5. Piezoelectric materials:

There are different types of piezoelectric materials which exhibit piezoelectricity like natural, biological, synthetic, polymer and organic nanostructure etc. are listed below

(a) **Natural crystals**: Quartz, Rochelle salt, Sucrose, Cane sugar, Topaz, Berlinite (structurally identical to quartz), Tourmaline-group minerals, Lead titanate ($PbTiO_3$, it occurs in nature as mineral macedonite and is also synthesized in laboratory), etc. [35-37].

(b) **Synthetic crystalline materials:** Other than the naturally occurring crystalline piezoelectric materials, there are many materials, such as Barium Titanate ($BaTiO_3$), Lead Zirconate Titanate (PZT), Langasite ($La_3Ga_5SiO_{14}$), Gallium Orthophosphate ($GaPO_4$), Lithium Tantalate ($LiTaO_3$), Potassium Niobate ($KNbO_3$), Sodium Potassium Niobate ($(K, Na)NbO_3$), Lithium Niobate ($LiNbO_3$), Sodium Tungstate (Na_2WO_3), Barium Sodium Niobate ($Ba_2NaNb_5O_5$), Lead Potassium Niobate ($Pb_2KNb_5O_5$), Zinc Oxide (ZnO), Aluminium Nitride (AlN), Gallium Nitride (GaN), Indium Nitride (InN), Bismuth Ferrite ($BiFeO_3$), Bismuth Titanate ($Bi_4Ti_3O_{12}$), Sodium Bismuth Titanate ($NaBi(TiO_3)_2$), etc., which exhibit the phenomenon of piezoelectricity [38-39].

(c) **Biological piezoelectric materials**: Silk, Wood, Enamel, Cellulose, Dentin, DNA, Viral proteins, Dry bone, Collagen fibrils, Tendon, etc. [40-44].

Though the piezoelectric ceramics possesses better electromechanical properties than piezoelectric polymers [45], but they are brittle in nature. However, the requirement of the modern world includes good flexibility, lightweight and low toxicity of a material. Therefore polymer based composite systems have been chosen for study in the present dissertation work.

1.4. Piezoelectric polymers

Piezoelectric polymers mainly include poly(vinylidene fluoride) (PVDF) and its co-polymers along with other polymers such as epoxy, nylone and silicone. Kawai discovered that stretched and electrically poled poly(vinylidene fluoride) (PVDF) exhibited outstanding piezoelectricity [46]. Since then, PVDF and its copolymers such as P[VDF-TrFE], P[VDF-TFE] and P[VDF-HFP] and PVDF/PMMA blends have been studied extensively. Other polymers showing piezoelectricity include poly(vinylidene) cyanide and its copolymers, polyvinyl chloride, aromatic polyamides/odd nylons, polyvinyl fluoride, polyvinyl acetate and ferroelectric liquid crystal polymers [21].

There are two different classes of piezoelectric polymer. **Class-I**, material such as PVDF, mainly consists of the materials that are poled by high electric field which typically show a symmetry of $C_\infty v$ group. **Class-II,** materials are those composed of uniaxially oriented chiral molecules which are most commonly biopolymers macroscopically aligned by mechanical stretching or by magnetic field. The structure of class II material has the symmetry of $D_\infty h$. The representativematerial for class II is α-helical poly (amino acid) (e.g. PBLG) and polyesters with chiral repeat units [21].

Among the different piezoelectric polymers PVDF and P(VDF-TrFE) copolymers show greatest piezoelectricity in temperature range of -40°C to 100°C. Piezoelectricity in these polymers occurs due to the attraction and repulsion between the intertwined long chain molecules under an electric field. The perpetual dipole polarization of these polymers is enhanced by stretching and poling of extruded thin polymer sheet. These piezoelectric polymers are mostly used in ultrasonic hydrophones and directional microphones [21]. However, P(VDF-TrFE) copolymers, are expensive and extremely difficult to produce, and thus occupy quite a small percentage of commercial piezoelectric polymer. In comparison, PVDF is inexpensive and dominates all important commercial piezoelectric polymer applications which is an important reason to be chosen as the base materials for this work.

1.4.1. Poly(vinylidene fluoride)

Poly(vinylidene fluoride) (or polyvinylidene difluoride, PVDF) is a pure non- reactive thermoplastic fluoropolymer and is produced by the polymerization of vinylidene fluoride (or vinylidene difluoride). It is generally used in applications with requirement of high purity, strength, resistance to solvents, acids, bases and heat andlow smoke generation. PVDF has a relatively low melting point of approximately 145°C [47] a low density, and less expensive compared to other fluoropolymers. It is available as sheets, films, panels, tubing, piping products, crosslinked closed-cell foams and premium wire insulators. It can be extruded; injected moulded or welded and is commonly used in chemical, medical, defence, semiconductor industries and in lithium ion batteries [48].

1.4.2. Structure and phases of PVDF

PVDF is made-up of semi-crystalline long chain polymer, that forms as repeated unit - CF_2 -CH_2– (as shown in Fig.1.3) [49]. The inherent polar property of PVDF, is due to the different polarity of hydrogen (positive charge) and fluoride (negative charge) compared to carbon.

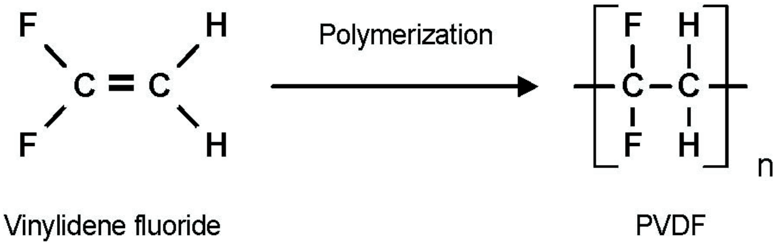

Fig. 1.3: Structure of Poly(vinylidene fluoride).

PVDF([-CH_2-CF_2-]) is a semi-crystalline polymer and posses five different crystalline phases α, β, γ, δ and ε. Out of these phases the α phase is kinetically favourable, thus it has the most thermodynamically stable state at ambient temperature and pressure. Therefore, normal crystallization from the melt and solution-casting from non-polar solvents typically result in the α phase. However, the β phase of PVDF is thermodynamically more stable. Therefore, the β phase can be obtained by high-pressure crystallization from the melt or mechanical stretchingand/or electric poling (exceeding 100 V/μm) of the original α phase. In addition, the γ phase can be obtained by either solution-casting from strongly polar solvents such as N, N-dimethyl formamide (DMF), N, N-dimethyl acetamide (DMAc), and dimethyl sulfoxide (DMSO), or crystallization at high temperatures [21]. The α phase possess the helical TGTG′(T- trans, G- gauche+, G′-gauche), β phase has all trans (TTTT) and the γ phase has T_3GT_3G' conformations [50-56]. The schematic structure of these three most important phases of PVDF is shown in Fig.1.4. When chains of PVDF are packed into crystalline lattices, a net dipole will be created in β, γ and δ phases making them polar crystalline phases, and there is no net dipole in α phase thus making it non-polar. Among three polar phases, β phase has the greatest spontaneous polarization per unit cell, thus shows the best piezoelectric and ferroelectric properties [47].

1.4.3. Properties:

This section includes a detail description of the different properties of semi crystalline PVDF. Some of the unique features of PVDF are as follows:

Strong piezoelectricity*:*

The piezoelectricity of PVDF was observed in 1969, and poled PVDF thin films were found to have much stronger piezoelectric coefficient (6–7 pC/N) than any other polymeric counterparts [46]. It has a negative piezoelectric constant (d_{33} value), which means that it will contract instead of expand (or vice versa), unlike other piezoelectric materials under the same electric field.

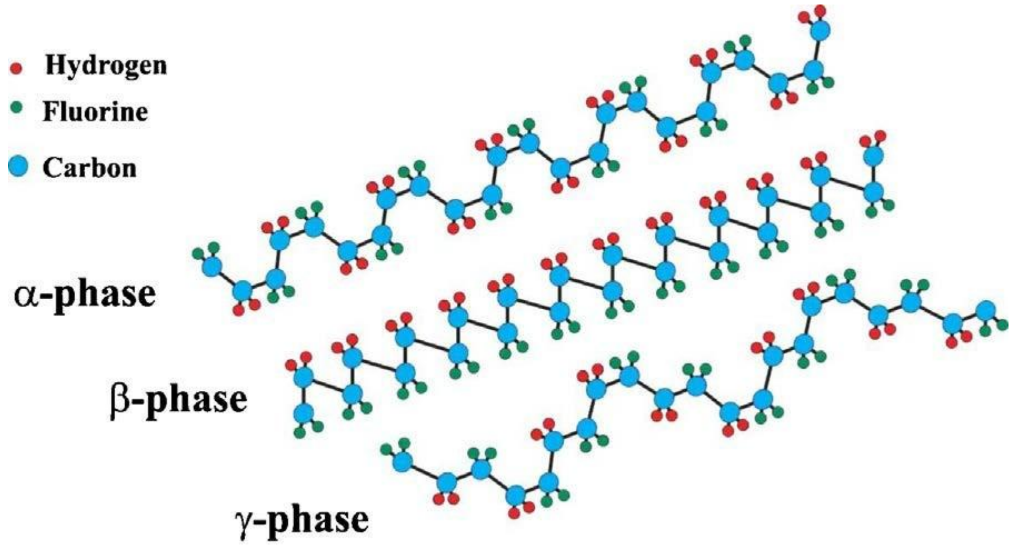

Fig.1.4: Schematic representation of the chain conformation for the α, β and γ phase of PVDF.

Glass transition temperature:

The glass transition temperature (Tg) of PVDF is approximately −40°C and the crystallinity is about 50 to 60% [47].

Thermal stability:

The thermal stability of PVDF is quite high. it has a decomposition temperature above 400°C. During this decomposition procedure hydrogen fluoride gas evolves from PVDF [47]. In addition to that it possess a high chemical corrosion resistance, low permeability to most gases and liquids, good mechanical strength, low thermal conductivity [47] etc.

1.4.4. Applications

The piezoelectric property of PVDF has been explored in sensors [57-58], actuator [59] and transducers [60]. For conventional applications, PVDF is commonly used as insulation for electrical cables and printed circuit board due to its flexibility, light weight, low thermal conductivity, heat resistance and high chemical corrosion resistance. In electronic industry, PVDF is used to produce low-cost strain gauges, tactile sensor arrays, light weight audio transducers and as a standard binder material in the manufacture of composite electrodes for lithium ion batteries. In addition, PVDF is used for monofilament fishing lines with lower optical density, harder surface and higher density comparing to nylon ones [48]. However, it has its wide applications in filtration technology by using PVDF as membrane [61-62].

1.5. Earlier work:

In this section, fundamental aspects of Poly(vinylidene fluoride) (PVDF) based composite is reviewed. This review starts with the enhancement of electroactive β phase and dielectric properties of PVDF by incorporating different micro/nano fillers. Then the applications of different PVDF based composites in the energy harvesting technology, is discussed in details.

1.5.1. PVDF based piezoelectric nanogenerator:

It has already been discussed in the previous section that out of the several possible phases of PVDF, electroactive β phase assumes paramount importance over the other phases due to its better piezo-electric, ferro-electric, pyro-electric and dielectric properties. Thus a PVDF composite with enhanced β phase fraction is suitable for energy harvesting technology. In addition to that, composite with low dielectric tangent loss is also required to obtain superior nanogenerators. But obtaining electroactive are difficult since PVDF normally exhibits nonpolar α phase which is kinetically very stable. So it is a great challenge to induce this electroactive phase in PVDF. Therefore, for improving electroactive phases in PVDF, several techniques have been attempted such as mechanical stretching [63], electrospinning [64], applied high pressure [65], electrical poling [66], solvent casting [67], incorporation of nanofiller [68-69] into PVDF matrix, etc. Among them, incorporation of ceramic filler in PVDF matrix is a cost effective approach to enhance electroactive phase. The interfacial interaction between the surface of ceramic filler and the PVDF matrix helps to orient the molecular dipole of PVDF resulting in the development of permanent dipole moment [70-71]. The alteration of chain conformation due to this interaction leads to the formation of polar phases of PVDF. Based on the above discussion, filler inclusion in PVDF matrix is chosen to improve its electroactive performance. Furthermore, development of PVDF-filler based composites is one of the main objectives of the present dissertation work. In this regard, it is to be mentioned that the filler loading in PVDF commonly reduces the flexibility of the composite system. Therefore, filler loading will be kept limited to some lower extent (lower amount of filler loading) for every composite system studied in the present thesis work**.** Since, this work is focused on PVDF based composite, therefore a detail review regarding the effect on crystalline phase and piezoelectricity of PVDF, due to the incorporation of several filler is being included in this section as illustrated in **Table 1.1**.

Table 1.1 Summary of some research works on PVDF-metal oxide based filler composites.

Sl. No.	**Name of the material**	**Filler wt%**	**Output**	**Ref. no**
1.	ZnO	40 vol%	Open circuit output voltage (V_{OC}) ≈ 7 V, Short circuit current (I_{SC})≈ 1000 nA, Used for self powered pH sensor	72
2	$BaTiO_3$	30 vol%	Dielectric constant ε ≈ 28 at 1 kHz, Energy storage density (U_{stored}) ≈ 2 J/cm^3	73
3.	$Pb(ZrTi)O_3$	40 vol%	Dielectric constant (ε) ≈ 35 at 1 kHz	74
4.	PZT	70 vol%	Piezoelectric coefficient (d33) ≈ 40 pC/N	75
5.	$BaTiO_3$	40 vol%	ε ≈ 70 at 1 kHz	74
6.	$Ba(Ti,Zr)O_3$	25 wt%	Output piezoelectric voltage (V_{OC}) ≈ 22 V, Generated short circuit current (I_{SC}) ≈ 2 µA, Power density (P) ≈ 0.15 µW/cm^2 , Used as fluid velocity sensor	77
7.	$BiFeO_3$	50 vol%	ε ≈ 100 at 1 kHz	78
8.	CuO	5 wt%	F(EA) ≈ 90%	79
9.	ZrO_2	5 wt%	F(EA) ≈ 70%	80
10.	Fe_2O_3	5 wt%	F(EA) ≈ 80%, ε ≈ 12.5	81
11.	Fe_3O_4	0.14 wt%	F(EA) ≈ 85%	82
12.	$SmFeO_3$	20 vol%	ε ≈ 5.6	83
13.	$MgTiO_3$	40 vol%	F(EA) ≈ 65%, ε ≈ 10	84
14.	$BaFe_{12}O_{19}$	30 wt%	ε ≈ 12.8	85
15.	BNT-ST	-	Voc~ 1.3 V	86

16.	Bi_2O_3	16 wt%	Voc ~ 4V	87
17.	$BiVO_4$	8 wt%	F(EA) ≈ 98%, ε ≈ 45	88
18.	$KNaNbO_3$	10 wt%	F(EA) ≈ 75%, ε ≈ 30	89

1.5.2. Origin of the work

In 2006, Wang and Sung first introduced the idea of piezoelectric nanogenerator which could successfully convert irregular vibration into a useful electrical output based on the energy conversion by ZnO nanostructured material [90]. Development of this nanogenerator based on the coupling of the semiconductor and piezoelectric properties of ZnO NW array was established. Following the basic mechanism of this work, researchers have started developing new technologies and protocols to improve the output performance of the fabricated nanogenerator.

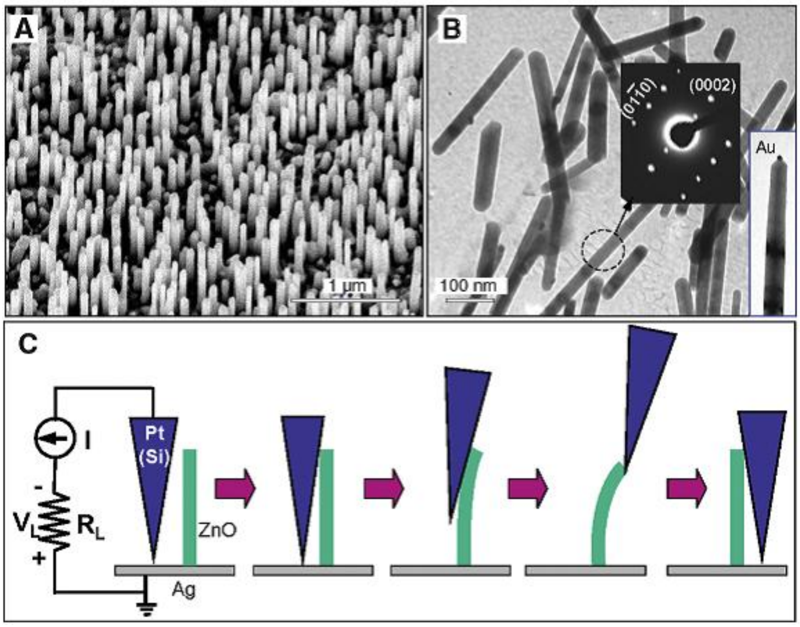

Fig. 1.5 *Wang & Song's experiment for converting mechanical energy into electrical energy using a vertical piezoelectric ZnO nanowire array* ***a.*** *SEM micrograph of ZnO pillars as fabricated on* Al_2O_3 *substrate,* ***b.*** *TEM image showing gold particles which are attached to*

the top of some of nanowires, inset with diffraction pattern, ***c.*** *Pt coated AFM tip rasters the sample surface in contact mode and generates electrical energy by compressing ZnO nanowires and creating Schottky barrier with gold particles at the tip of nanowires [90].*

Further vertically aligned ZnO NWs array also developed by Wang's group based on direct current nanogenerator. Qin and co-workers fabricate a novel type of nanogenerator based on ZnO NWs grown around textile fibers [91] which can harvest energy from light, wind and body movement. In 2009, a single ZnO NW on a flexible kapton substrate fully packaged with PDMS was developed by Yang. et al [92] and they exhibited excellent robustness and stability of the material with alternating current. Since 2010, the integration of ZnO NW with different alignment and embedded in different flexible substrate paid more attention to develop high output nanogenerator to obtain a standalone device for energy harvesting. There are many literatures reported on the ZnO-based piezoelectric nanogenertor. **Table 1.2** show the different forms of ZnO explored for generating output voltage and current and power density.

Table 1.2.Comparison of the piezoelectric output of ZnO-based Piezoelectric nanogenerator using different techniques.

Name of the ZnO nanostructure	Size of ZnO	Substrate	Working mode	Area of (NG) (cm^2)	Piezo voltage (V)	Power density	Ref.
Li doped ZnO nanowires	Diameter ~100-150	PET	Bending	4	9	-	93
V doped ZnO nanosheet	Thickness-15~20 nm	PET	Bending	16	32	-	94
S doped ZnO nanospires	Diameter ~20-200 nm	PET	Environmental vibration		0.646	27.9 nW	95
Cl-doped ZnO nanowires	Diameter ~100 nm	PET	Mechanical strain	1	2.45	-	96

Ga-doped ZnO nanowires	Diameter ~300 nm	Ti foil	Hammer compressing	1	1.1	-	97
Fe-doped ZnO nanowires	Diameter ~200 nm	Ti foil	Hammer compressing	-	1.5	-	98
Ag-doped ZnO nanowires	-	Polyster	Sound waves of 80 dB	10	4	0.5 µW	99
Y doped ZnO nanosheets/PDMS	Thickness ~30-40 nm	PET	Finger tapping	6	20 V	-	100
Co doped ZnO Nanowire	-	Grown on Ti substrate	Stepper motor Force (34 N, 1 Hz)	-	~ 1.8 V	-	101
Sb doped ZnO nanowire	-	Ti-substrate	Stepper motor force (34 N, 1.6 Hz)	6.25	1.35 V	-	102
La doped ZnO nanorods	Average diameter ~ 15 nm	Incorporated in PDMS	Linear motor of force 2N	1	13 V	~2.5 mW/m^2	103
Aligned ZnO nanorods	~40 nm	α-Al_2O_3	Contact force 5 nN	-	9 mV	-	104
Aligned ZnO nanorods	~90 nm	Graphene/Al_2O_3	Pushing 0.5 kgf	3.1	20 mV	-	105
ZnO nanorods	~150 nm	GaN/Al_2O_3	Sound 100 dB		53 mV	-	106
Random ZnO NRs	~ 57 nm	SiO2	Press 20N	4.5	70 mV	-	107
ZnO NRs (spin coating)	~ 60 nm	PET	Compress 14 N	2	0.1 V		108
ZnO NRs (Seed less)	~ 200 nm	PET	Bending 10 Hz	0.25	0.56 V		109
ZnO NRs (Spin coating)	~50 nm	Textile	Bending 3 µN	-	0.15 V	-	110
ZnO NRs (hydrothermal)	~ 800 nm	Paper	Handwriting	0.16	4.8 V		111
ZnO NRs (Spin coating)	~250 nm	Graphene/PET	Bending 3 µN	-	0.1 V	-	112
ZnO NRs (Spin coating)	~ 300 nm	PEDOT:PSS	Bending	-	2 V	-	113
ZnO NRs (Seedless)	~115 nm	PEN	Deflection 4 mm	3	0.22 V		114

ZnO NRs (Hydrothermal)	< 100 nm	PC	Bending 75 Hz	0.8	1.15 V	-	115
ZnO NRs (Spin coating)	~60-100 nm	Graphene :PET	Press 49 N	4	0.17 V	-	116
ZnO NRs (Evaporation)	~855 nm	PU/Graphene	Stress 0.2 Hz	9	0.5 V	-	117
ZnO NRs (hydrothermal)	~70 nm	Carbon fibre	Strain 2 Hz	16	6.8 V	-	118
ZnO NRs (Evaporation)	300 nm	Kapton	Bending 13 Hz	-	1.6 V	-	119
ZnO NRs	~ 184 nm	Polycarbonate (PC)	Tapping 5Hz	5	150 mV		120
ZnO NRs	-	Aluminum foil	Pressing 80N	4	625 mV	-	121
Cr/Au-ZnO/PMMA/Cr-Au	~150 nm	Cr/Au	-	1	20V	-	122
PDMS/ZnO NFs/Au-PET	Thickness ~ 10 nm	Au-PET	Stress 7N	1	470 V		123
ITO-PET/ZnO-graphene/ZnO/ITO-PET	~ 60 nm	ITO/PET	Stress 49 N	-	1 V	-	124
Cu-Cu_2O/ZnO-Ag/paper	~ 100 nm	Cu	Strain		42 mV	-	125
Ni-NiO/ZnO-Al	-	Ni foils	Vertical pushing	1	430 mV	-	126
Cu-PET-CuO/ZnO-Au	Thickness~ 60 nm	Cu/PET	Stress	-	7.5 V	-	127
FTO-Ag/ZnO-Au/Cr	~200 nm	FTO	Finger tapping	-	2 V	-	128
ITO/P_3HT/ZnO/Au		ITO	-	4	1.45 V	-	129
ITO-Li:ZnO/PDMS		ITO coated PET	-	100	180 V	-	130
ITO/PET-Y:ZnO NSs/PDMS-Al/PES	Thickness ~ 34 nm	ITO coated PET	Tapping 0.01 kgf	6	6 V	-	131

ITO/PET-Nd:ZnO/PDMS-Al	110 nm	ITO coated PET	Tapping 0.3 N	4	31 V	-	132
Cu/PET-Br:ZnO/CuO-Cu	150 nm	Cu/PET	Stress 1 MPa	-	8.1 V	-	133
Cu-ZnO/CuO/PDMS-Cu	-	Cu	Press 2 N	-	9 V	-	134
SUS/ZnO//PDMS-Ti/Au	80 nm	Stainless steel substrate (SUS)	Stress 0.5 kgf	1	3.2 V	-	135
Si-SiMPs/ZnO/PDMS-Ti/Au	-	Si substrate micropillar (SiMP)	Stress 0.5 kgf	-	4 V	-	136
ZnO NW	ZnO diameter ~ 30 nm PVDF diameter ~ 180 nm	PVDF	Bending tester	-	~ 6.9 V	-	137
Co-doped ZnO nanorods/PVDF-HFP fiber	-	Al foil	Vibrating shaker	-	~2.8 V	-	138
ZnO/PVDF fiber	-	PDMS substrate	Applied strain at 10 Hz	-	~ 40 mV	-	139
ZnO NP/PVDF fiber	Particle Size ~ 50-100 nm	Al substrate	Force 1.5 N		~ 70 mV	32nW/cm^2	140

As listed in **Table 1.2**, the various techniques were utilized to enhance the piezoelectric output performance of ZnO-based PNGs such as surface treatment and interfacial modification techniques, doping techniques, electrospinning, surface treatment technique etc.

Though a lot of experimental research has been done including different methods and structures for enhancement of performance of ZnO based nanogenerator, But the limitations of these nanogenerator devices are associated with the facts like low output power density, low economic performance, less durability etc. Therefore, there are lot of scopes which are not explored till date. In order to explore newer perspective in the field of energy storage and harvesting, main focus has been given in ZnO filler for incorporation into PVDF matrix. The greatest advantages of this material arise from the facile and cost effective fabrication technique and simple synthesis process. In addition these materials can be grown in different orientation and can also be integrated in various substrates without altering any physical characteristics.

As per the earlier discussion, different parameter of fillers influences the electroactive phase of PVDF. Among them, morphology of filler is one of the most important parameter as piezoelectric properties are structure-dependent. Fillers with tuned morphology such as 1D nanostructure are more efficient to induce polar phase compared to spherical and other geometry. Maximum amount of electroactive phase may be obtained by incorporation of high aspect ratio 1D nanostructure such as nanorods and nanowires etc. Superior piezoelectric properties are expected only in the case of 1D nanostructures with an extremely high aspect ratio since the piezoelectric coefficient increases with increment of the aspect ratio of 1D nanostructure. Therefore to study the effect of filler morphology, on the dielectric, ferroelectric and piezoelectric properties of PVDF, two different nanostructures, including 0D nanoparticle, 1D nanorod of ZnO were chosen.

On the other hand, two different morphology of ZnO structures were used as fillers in PVDF among which rod shaped structure exhibit the best performance in improving the electrical properties of the composite system. Therefore we choose 1D rod shaped structure as a filler material in PVDF for further investigation. Aspect ratio of filler plays a crucial role to study the electrical properties of polymer based composite system. Here, we investigated the effect of filler aspect ratio on the electrical properties of ZnO incorporated poly(vinylidene fluoride)

(PVDF) matrix.

The aspect ratio of ZnO nanorods was tuned to achieve the performance enhancement of the resulting PVDF based composites. Here in the present work, we have tried to improve the electrical performances of the flexible PVDF-ZnO composites by using a third phase addition.

Addition of third phase conducting fillers like reduced graphene oxide (rGO), carbon black, graphite, single/multi-walled carbon nanotubes, etc. in polymer based composites have been previously studied by several researchers in order to improve their electrical and energy harvesting performances. Introduction of third phase conductive filler within polymer matrix reduce the dissimilarity of the difference of local electric field between ceramic filler and polymer matrix within the nanocomposite. Besides, third phase conductive filler improves the homogeneity of dispersion of fillers within polymer matrix and prevents the agglomeration within the nanocomposites. On the other hand, the electronic conductivity of PVDF is very low and hence, the uniformly distributed fillers in PVDF become isolated by PVDF insulation layers between them. But, for achieving enriched output piezoelectric performance, good connectivity between each piezoelectric ZnO nanorods is a must needed parameter. So, the addition of optimized amount of conducting third phase in PVDF-ZnO composites creates good electrical connections between each ceramics particle and hence, enhancement of conductivity in the nanocomposites is achieved which in turn improves its peizo-response. Owing to their good electronic conductivity, the third conducting phase not only creates electrical bridge between each ZnO nanorods, but also creates good connectivity with top and bottom electrodes of the composite film which in turn improves the output piezoelectric performance through good charge transmission between the composite films and electrodes. Further, the improved homogeneous distribution of nanomaterials in the PVDF matrix induced by the third conducting phase reduces the internal resistance of the nanocomposites and as a result, output electrical performances are improved.

Modifications of ceramic fillers such as aspect ratio variation, shape variation, addition of conductive filler etc. have already been investigated to improve the energy storage and harvesting applications of the respective PVDF based composite systems. In this section of work, ZnO filler was further modified by adding different dopants. There are several reports regarding doping of different ions in ZnO to increase its electrical property. On the other hand, the doping technique also changes the leakage current of ZnO and modify surface charge of the nanorods. Surface charge of filler plays an important role in determining the strength of interfacial interaction with polymer. Considering all these facts, ZnO was doped with Al^{3+} ion and the effect was studied throughout the present investigation. Herein flexible piezocomposite was developed using Al@ZnO nanorods with PVDF-HFP polymer which is a co-polymer of PVDF. Compared to PVDF and other co-polymer, PVDF-HFP exhibits significantly higher piezoelectric-coefficient (d_{31}) and electromechanical coupling factor (k_p). On the other hands, its exhibit good mechanical property with chemical stability compared to other co-polymer.

1.6 Current scenario, challenges in this field and scope of thesis

Energy harvesting from easily available mechanical vibration in our surroundings have gained attractive substantial attention for application in field of artificial skin, shoes, wearable electronics, environmental monitor and foldable displays. Polar PVDF is the most responsive piezoelectric polymer used as self-powered flexible NG application due to its strong piezoelectric response, chemical and mechanical durability, marks it as a valuable material for this application. Different strategies have been developed to obtain electroactive β phase of PVDF, mainly focusing on development of specific processing technology and the inclusion of specific fillers. PVDF-ZnO based piezoelectric composites are very promising materials in this field. But shape, size and concentration of filler material are major three factors for the nucleation and stabilization of electroactive β-PVDF. Understanding all these parameters and optimizing them to obtain a bio-safe, flexible and wearable polymer composite based NG for self-powered sensor application are still very inspiring and challenging field of research.

1.7 Objectives

The objectives of the present dissertation work have been discussed through broad literature survey as depicted earlier. For the sake of simplicity the key objectives of the thesis are summarized below

(i) Development of PVDF based composite films with lower amount of filler loading was a major objective of the present work as the flexibility of the device was very much required.

(ii) Development of lead free flexible piezoelectric energy harvester is one of the main objectives of the present dissertation work. For this purpose ZnO has been chosen as a filler material in PVDF matrix due to its superior piezoelectric property, bio-compatibility and easy synthesis method.

(iii) Morphology of filler is one of the most important parameter as piezoelectric properties are structure-dependent. The effect of filler morphology, on the dielectric, ferroelectric and piezoelectric properties of PVDF, two different nanostructures i.e. 0D nanoparticle, 1D nanorods were chosen and the performance of their respective composite film will be investigated.

(iv) Considering the superiority of 1D rod shape structure compared to other morphology based fillers studied here, this filler is then considered for modification purpose, in order to achieve performance enhancement in terms of desired applications.

(v) Aspect ratio of filler plays a crucial role to study the electrical properties of polymer based composite system. Here, we investigated the effect of filler aspect ratio on the electrical properties of ZnO incorporated poly(vinylidene fluoride) (PVDF) matrix.

(vi) For further improvement of electrical properties of PVDF, third phase MWCNT was added into PVDF-ZnO matrix and detail study was carryout.

(vii) In order to achieve performance enhancement in terms of applications, modification technique such as the modification of leakage current density of ZnO filler through doping of different elements is targeted here and the performance of the corresponding PVDF based composite films will be investigated.

With the above objectives, experiments have been performed in the present dissertation work. The detail experimental techniques and fabrication procedure are described in Chapter 2. All experimental results and their scientific analysis are depicted in Chapter 3. Chapter 4 summaries all the experimental results and discussion and future scope of the thesis work.

References:

1. G. J. Aubrecht, Energy: Physical, Environmental, and Social Impact, Pearson Education, London 2006.
2. C. Beggs, Energy: Management, Supply and Conservation, *Elsevier*., Oxford 2002.
3. E. Kar, N. Bose, B. Dutta, N. Mukherjee, S. Mukherjee, *ACS Appl. Nano Mater*., 2013, **7**, 10424.
4. X. Li, Z. Lv, H. Zhu, *Adv. Mater*., 2015, **27**, 6549 – 6574.

5. G. Lijuan, B. Fengxian, D. Weijie, *Eng. Mater*., 2014, **613,** 185 – 192.
6. A. F. D. O. Falcao, Renew. *Sustainable Energy Rev*., 2010, **14**, 899 – 918.
7. P. A. Qstergaard, H. Lund, *Appl. Energy*., 2011, **88**, 479 – 487.
8. P. McKendry, Energy production from biomass (Part 1): overview of biomass, *Bioresour. Technol*., 2002, **83**, 37 – 46.
9. B. W. Brook, A. Alonso, D. A. Meneley, J. Misak, T. Blees, J. B. Vanerp, *Mate. Tech*., 2014, 1–2 , 8 – 16.
10. Z. L. Wang, J. Chen, L. Lin, *Energy Environ. Sci*., 2015, **8,** 2250 – 2282.
11. J. Yan, Y. G. Jeong, *ACS Appl. Mater. Interfaces*., 2016, **8**, 15700 – 15709.
12. Z. Lin, J. Chen, J. Yang, *J. Nanomater.,* 2016, 1 – 24.
13. S. Panero, C. Romoli, M. Achilli, E. Cardarelli, B. Scrosati, *J. Power Sources.*,1995, **57,** 9 – 12.
14. J. Song, J. Zhou, Z. L. Wang, *Nano Lett*., 2006, **6**, 1656 – 1662.
15. A. Nanda, M. A. Karami, *J. Appl. Phys., 2017,* **121**, 124506 – 124515.
16. S. Jung, J. Lee, T. Hyeon, M. Lee, D. H. Kim, *Adv. Mater*., 2014, **26,** 6329 – 6334.
17. Z. L. Wang, *Adv. Funct. Mater*., 2008, **18** ,3553 – 3567.
18. A. Dakhole, A. Boke, *J. Electri. Electron. Eng*., 2017, **12**, 46 – 49.
19. D. Hoffmann, A. Willmann, R. Göpfert, P. Becker, B. Folkmer, Y. Manoli, *J. Phys. Conf. Ser.*, 2013, **476** , 012104 – 012109.
20. H. Sun, D. Zhu, N. M. White, S. P. Beeby, *J. Phys. Conf. Ser.*, 2013,**476**, 012057 – 012061.
21. H. Song, Fabrication and characterisation of electrospunpolyvinylidene fluoride (PVDF) nanocomposites for energy harvesting applications, Wolfson Centre of M aterial Processing Brunel University, London 2016 .
22. S. Priya, D. J. Inman, Energy harvesting technologies, *Springer.,* 2009; Vol. 21.

23. L. Dhakar, Triboelectric devices for power generation and self-powered sensing application. *Springer.*, 2017.
24. R. Ding, He. Liu, X. Zhang, *Funct. Mater.*, 2016.
25. V. Bhavanasi, V. Kumar, K. Parida, J. Wang, P. S. Lee, *ACS Appl. Mater. Interfaces.*, 2016, **8**, 521.
26. M. L. Seol, J. H. Woo, D. I. Lee, H. Im, J. Hur, Y. K. Choi; *Small.*, 2014, **10**, 3887.
27. Z. L. Wang, Faraday Discuss, 2014, **176**, 447
28. J. Curie, P. Curie, *Bull. Soc. Minéral. France.*, 1880, **3**, 90–93.
29. G. Lippmann, *Philos. Mag.*, 1881, **5**, 11, 474-475.
30. W. Voigt, Lehrbuch der Kristallphysik, Ed: B.G. Teubner, Publisher: Leipzig, Berlin, 1910.
31. G. Gautschi; Piezoelectric Sensors. In: Piezoelectric Sensorics. Springer, Berlin, Heidelberg, 2002.
32. J. Krautkrämer, H. Krautkrämer, Ultrasonic Testing of Materials. *Springer., 1990,* **119**, 149.
33. M. Birkholz, *Z. Phys. B.*, 1995, **96**, 325
34. J. F. Nye, Oxford university press:1985.
35. D. Radusinović, C. Markov, Macedonite – Lead Titanate: a new mineral, Am. Mineral., 1971, **56**, 387 – 394.
36. E. A. J. Burke, C. Kieft, Second occurrence of makedonite, $PbTiO_3$, Långban, Sweden, Lithos., 1971, **4,** 101 – 104.
37. M. Akizuki, M. S. Hampar, J. Zussman, An explanation of anomalous optical propertiesof topaz, *Mineral. Mag.,*1979*,* **43**, 237 – 241.
38. S. Roberts, *Phys. Rev.*, 1947, **71,** 890 – 895.
39. Piezoelectricity – Wikipedia. https://en.wikipedia.org/wiki/Piezoelectricity.

40. M. Jolandan, M. F. Yu, *Nanotechnology.,2009,* **20**, 085706 – 085711.

41. R. S. Lakes, IEEE Trans. *Biomed. Eng.* BME-27 (5), 1980, 282 – 283.

42. O. R. Becker, A. A. Marino, Electrical properties of biological tissue (piezoelectricity), electromagnetism & life, Albany, NY S. T. of NY Press, 1982.

43. S. R. Pollack, E. Korostoff, W. Starkebaum, W. Lannicone, , In Brighton, NY: Grune & Stratton, 1979.

44. D. I. Fotiadis, G. Foutsitzi, C. V. Massalas, *Acta Mechanica*., 1999, **137**, 65 – 81.

45. K. H. Prasad; Characterization of composite piezoelectric materials for smart joint applications, LSU Master's Thesis., 2010, 3661.

46. H. Kawai*, Jpn. J. Appl. Phys*., 1969, **8**, 7.

47. P. Martins, A.C. Lopes, S. Lanceros-Mendez, *Prog. Polym. Sci*., 2014, **39**, 683.

48. P. Ueberschlag, *Sensor Review*., 2001, **21**, 118

49. N. Karawasa; W. A. Goddard; *Macromolecules.*, 1992, **25**, 7268

50. A. J. Lovinger., *Macromolecules.*, 1981, 1**4**, 322.

51. X. Zhou, B. Chu, B. Neese, M. Lin, Q. M. Zhang, *IEEE Trans. D electr. Electr. Insul*., 2007, 14, 1133.

52. Y. Lu, J. Claude, B. Neese, Q. M. Zhang, Q. Wang, *J. Am. Chem. Soc*., 2006, **128**, 8120.

53. N. Karawasa; W. A. Goddard; *Macromolecules.*, 1992, **25**, 7268.

54. A. B. Silva, M. Arjmand, U. Sundararaj, R. E. S. Bretas, *Polymer.*, 2014, **55**, 226.

55. V. Tomer; E. Manias; C. A. Randall*; J. Appl. Phys*., 2011, 110, 044107.

56. P. Thakur; A. Kool; B. Bagchi; S. Das; P. Nandy; *Appl. Clay Sci.,* 2014, **99**, 149.

57. F.C. Bauer, IEEE transactions on ultrasonics, 2000, **47**, 6.

58. Y. H Huh; J. I. Kim; J. H. Lee; S.G. Hong; J. H. Park, *Procedia Engineering*., 2011, **10**, 3304.

59. Z. Chen, K. Y. Kwon, X. Tan, *Sensors and Actuators A*, 2008, **144**, 231.
60. L. F. Brown, *IEEE transactions on ultrasonics, ferroelectrics, and frequency control.*, 1996, **43**, 4.
61. X. Tan, S.P. Tan, W. K. Teo, K. Lia, *Journal of Membrane Science.*, 2006, **271**, 59.
62. S. Simone, A. Figoli, A. Criscuoli, M. C. Carnevale, A. Rosselli, E. Drioli, *Journal of Membrane Science.*, 2010, **364**, 219.
63. S.P. Bao, G. D. Liang, S. C. Tjong, *Carbon.,* 2011, **49**, 1758.
64. S.W. Choi, J. R. Kim, Y. R. Ahn, S. M. Jo, E. J. Cairns, *Chem. Mater.,* 2007, **19**, 104.
65. K. Matsushige, *Phase Trans.,* 1989, **18**, 247.
66. K. S. Ramadam, D. Sameoto, S. Evovy, *Smart Mater. Struct.,* 2014, ***23***, 033001.
67. S. Satapathy, S. Pawar, P. K. Gupta, K. B. R. Varma, *Bull. Mater.Sci.*, 2011, **34**, 727.
68. B. Adak, I. Chinya, S.Sen, *RSC Adv.,* 2016, **6**, 105137.
69. P. Martins, C. M. Kosta, G. Botelho, S.L. Mendez, *Mater. Chem. Phys.,* 2012, ***131***, 698.
70. Rovisco, A. D. Santos, T. Cramer, J. Martins, R. Branquinho, H. Aguas, B. Fraboni, E. Fortunato, R. Martins, R. Igreja, P. Barquinha, *ACS Appl. Mater. Interfaces.*, 2020, **12**. 18421 – 18430.
71. A. R. Chowdhury, A. M. Abdullah, I. Hussain, J. Lopez, D. Cantu, S. K. Gupta, Y. Mao, S. Danti, M. J. Uddin, *Nano Energy.*, 2019, **61**, 327 – 336.
72. B. Saravanakumar, S. Soyoon, S.-J. Kim, *ACS Appl. Mater. Interfaces.,2014,* **6**, 13716 – 13723.
73. M. Bi, Y. Hao, J. Zhang, M. Lei, K. Bi, *Nanoscale.,*2017, **9**, 16386 – 16395.
74. R. Gregorio Jr., M. Cestari, F. E. Bernardino, *J. Mater. Sci.,* 1996, **31** , 2925 – 2930.
75. Z. De-Qing, W. Da.-Wei, Y. Jie, Z. Quan-Liang, W. Zhi-Ying, C. Mao-Sheng, , Chin. *Phys. Lett.*, 2008, **25**, 4410 – 4413.

76. R. Gregorio Jr., M. Cestari, F. E. Bernardino, *J. Mater. Sci.*, 1996, **31**, 2925 – 2930.
77. M. Sahu, S. Hajra, K. Lee, P L Deepti, K. Mistewicz, H. J. Kim, *Crystals.*, 2021, **11,** 85.
78. S. Dash, R. N. P. Choudhary, M. N. Goswami, *J. Alloys Compd*., 2017, **715**, 29 – 36.
79. B. Dutta, E. Kar, N. Bose, S. Mukherjee, *RSC Adv*., 2015, 5 , 105422 – 105434.
80. R. Naik, T. S. Rao, *Mater. Res. Express*., 2019, **6**,115330.
81. R. Gonçalves, P. M. Martins, C. Caparrós, P. Martins, M. Benelmekki, G. Botelho, S. Lanceros-Mendez, A. Lasheras, J. Gutiérrez, J. M. Barandiarán, *J. Non-Crystal. Solids*., 2013, **361**, 93 – 99.
82. T. Prabhakaran, J. Hemalatha, *Mater. Chem. Phys*., 2013, **137,** 781 – 787.
83. A. Ahlawat, S. Satapathy, R. J. Choudhary, M. M. Shirolkar, M. K. Singh, P. K. Gupta, *RSC Adv*., 2016, **6**, 44843 – 44850.
84. R. S. Bharath, T. Chakraborty, N. Hariharan, B. Masin, K. Ashok, H. Sreemoolanadhan, C. Oommen, S. Elizabeth, *J. Mater. Chem. C*., 2019, **7** , 4484 – 4496.
85. X. Jing, X. Shen, H. Song, F. Song, *J. Polym. Res*., 2011, **18** , 2017 – 2021.
86. S. H. Ji, J. H. Cho, Y. H. Jeong, J.-H. Paik, J. D. Yun, J. S. Yun, *Sens. Actuator A Phys.,*2016, **247**, 316 – 322.
87. A. Biswas, S. Garain, K. Maity, K. Henkel, D. Schmeißer, Dipankar Mandal, *Polym. Compos.,*2019*,* 40, 265 – 274.
88. S. Sarkar, S. Garain, D. Mandal, K. K. Chattopadhyay, *RSC Adv*., 2014, **4**, 48220 – 48227.
89. S. Bairagi, S. W. Ali, *J. Mater. Sci.*, 2019, **54**, 11462 – 11484.
90. Z. L. Wang, *Science.*, 2006, **312**, 242-246.
91. Y. Qin, X. Wang, Z.L. Wang, *Nature.*, 2008, **451**, 809-813.

92. R. Yang, Y. Qin, L. Dai, Z.L. Wang, *Nat. Nanotechnol*., 2009, **4**, 34-39.

93. S.-H. Shin, Y.-H. Kim, M. H. Lee, J.-Y. Jung, J. H. Seol, and J. Nah**,** *Nanoscale.***,** 2016, **8**, 1314-1321.

94. C.-L. Hsu, I.-L. Su, T.-J. Hsueh, *RSC Adv*., 2015, **5**, 34019–34026.

95. C. Liu, A. Yu, M. Peng, M. Song, W. Liu, Y. Zhang, J. Zhai, *J. Phys. Chem. C.,* 2016, **120**, 6971−6977.

96. T. Zhao, Y. Fu, Y. Zhao, L. Xing, X. Xue, *Journal of Alloys and Compounds.*,2015, **648** , 571-576.

97. D. Zhu, T.Hu, Y. Zhao, W. Zang, L. Xing, X. Xue, *Sensors and Actuators B.*, 2015, **213** ,382–389.

98. S.H. Lee, J.S. Lee, W.B. Ko, S.N. Cha, J. Sohn, J.M. Kim, J.G. Park, Y. Park, J.P. Hong, *Nanoscale.*, 2013,**5**, 9609-9614.

99. N. Sinha, S. Goel, A. J. Joseph, H. Yadav, K. Batra, M. K. Gupta, B. Kumar, *Ceramics International.*, 2018,**44**, 8582-8590.

100. W. Zang, P. Li, Y. Fu, L. Xing , X. Xue, *RSC Adv***.**, 2015, **5**, 84343-84349

101. Y. Zhu, Q. Li, P. Wang, W. Zang, L. Xing, X. Xue, *Materials Letters.,* 2015, **154**, 77–80.

102. P. Rajagopalan, P. Jakhar, I. A. Palani, V. Singh, S. J. Kim, *International Journal of Precision Engineering and Manufacturing-Green Technology*., 2020, **7**,77–87.

103. Z. L. Wang and J. Song, *Science*., 2006, 312, 242-246.

104. B. Kumar, K. Y. Lee, H.-K. Park, S. J. Chae, Y. H. Lee, and S.-W. Kim, *Acs Nano.,* 2011, 5, 4197-4204.

105. S. N. Cha, J. S. Seo, S. M. Kim, H. J. Kim, Y. J. Park, S. W. Kim, and J. M. Kim, *Adv. Mater*., 2010, **22** , 4726-4730.

106. M. S. Al-Ruqeishi, T. Mohiuddin, B. Al-Habsi, F. Al-Ruqeishi, A. Al-Fahdi, and A. AlKhusaibi, *Arab. J. Chem*., 2019, **12**, 5173-5179.

107. D.-M. Shin, E. L. Tsege, S. H. Kang, W. Seung, S.-W. Kim, H. K. Kim, S. W. Hong, and Y.- H. Hwang, *Nano Energy.,* 2015, **12** , 268-277.

108. G. Poulin-Vittrant, C. Oshman, C. Opoku, A. Dahiya, N. Camara, D. Alquier, L.-P. T. H. Hue, and M. Lethiecq, *Phys. Proc*., 2015, **70,** 909- 913.

109. A. Khan, M. Hussain, O. Nur, and M. Willander, *J. Phys. D Appl. Phys*., 2014, **47**, 345102.

110. E. Nour, M. Sandberg, M. Willander, and O. Nur, *Nano energy.,* 2014, **9** , 221-228.

111. M. Hussain, M. A. Abbasi, Z. H. Ibupoto, O. Nur, and M. Willander, *Phys. Status Solidi-A*., 2014, **211**, 455- 459.

112. E. Nour, C. O. Chey, M. Willander, and O. Nur, *Nanotechnology*., 2015, **26** , 095502.

113. C. Opoku, A. S. Dahiya, C. Oshman, F. Cayrel, G. Poulin-Vittrant, D. Alquier, and N. Camara, *Phys. Proc*., 2015, **70**, 858-862.

114. S. Stassi, V. Cauda, C. Ottone, A. Chiodoni, C. F. Pirri, and G. Canavese, *Nano Energy.,* 2015, **13**, 474-481.

115. D.-M. Shin, E. L. Tsege, S. H. Kang, W. Seung, S.-W. Kim, H. K. Kim, S. W. Hong, and Y.- H. Hwang, *Nano Energy*., 2015, **12**, 268-277.

116. X. Li, Y. Chen, A. Kumar, A. Mahmoud, J. A. Nychka, and H.-J. Chung, *ACS Appl. Mater. Inter., 2015,* **7,** 20753-20760.

117. G. H. U. Banna and I.-K. Park, *Nanotechnology*., 2017, **28**, 445402.

118. G. Poulin-Vittrant, A. S. Dahiya, S. Boubenia, K. Nadaud, F. Morini, C. Justeau, and D. Alquier, *Mater. Sci. Semicond. Process*., 2019, **91** , 404-408.

119. F. L. Boughey, T. Davies, A. Datta, R. A. Whiter, S.-L. Sahonta, and S. Kar-Narayan, *Nanotechnology.,* 2016, **27**, 28LT02.

120. A. A. Narasimulu, P. Zhao, N. Soin, K. Prashanthi, P. Ding, J. Chen, S. Dong, L. Chen, E. Zhou, and C. D. Montemagno, *Nano Energy*., 2017, **40**, 471-480.

121. Y. Hu, L. Lin, Y. Zhang, and Z. L. Wang, *Adv. Mater*., 2012, **24** , 110-114.

122. W. He, Y. Qian, B. S. Lee, F. Zhang, A. Rasheed, J.-E. Jung, and D. J. Kang, *ACS Appl. Mater. Inter.,*2018, **10**, 44415- 44420.

123. D.-M. Shin, E. L. Tsege, S. H. Kang, W. Seung, S.-W. Kim, H. K. Kim, S. W. Hong, and Y.- H. Hwang, *Nano Energy.,* 2015, **12** , 268-277.

124. J. Lei, B. Yin, Y. Qiu, H. Zhang, Y. Chang, Y. Luo, Y. Zhao, J. Ji, and L. Hu, *RSC Adv*., 2015, **5**, 59458-59462.

125. B. Yin, Y. Qiu, H. Zhang, J. Lei, Y. Chang, J. Ji, Y. Luo, Y. Zhao, and L. Hu, *Nano Energy*., 2015, **14**, 95-101.

126. S.-H. Shin, M. H. Lee, J.-Y. Jung, J. H. Seol, and J. Nah, *J. Mater. Chem. C.* , 2013, **1,** 8103-8107.

127. S. Lu, Q. Liao, J. Qi, S. Liu, Y. Liu, Q. Liang, G. Zhang, and Y. Zhang, *Nano Res*., 2016, **9**, 372-379.

128. K. Y. Lee, B. Kumar, J.-S. Seo, K.-H. Kim, J. I. Sohn, S. N. Cha, D. Choi, Z. L. Wang, and S.-W. Kim, *Nano Lett*., 2012, 12, 1959-1964.

129. S.-H. Shin, Y.-H. Kim, M. H. Lee, J.-Y. Jung, J. H. Seol, and J. Nah, *ACS nano.,* 2014, **8**, 10844-10850.

130. N. Sinha, S. Goel, A. J. Joseph, H. Yadav, K. Batra, M. K. Gupta, and B. Kumar, *Ceram. Int*.,2018, **44**, 8582-8590.

131. K. Batra, N. Sinha, S. Goel, H. Yadav, A. J. Joseph, and B. Kumar, *J. Alloys Compd*., 2018, **767**, 1003-1011.

132.. Y. Zhang, C. Liu, J. Liu, J. Xiong, J. Liu, K. Zhang, Y. Liu, M. Peng, A. Yu, and A. Zhang, ACS Appl. Mater. Inter. 8 (2016) 1381-1387.

133. R. Pandey, N. P. Maria Joseph Raj, V. Singh, P. Iyamperumal Anand, and S.-J. Kim, *ACS Appl. Mater. Inter*., 2019, **11**, 6078-6088.

134. D.-Y. Jung, S.-H. Baek, M. R. Hasan, and I.-K. Park, *J. Alloy. Compd*., 2015, **641**, 163-169.

135. M. R. Hasan, S.-H. Baek, K. S. Seong, J. H. Kim, and I.-K. Park, *ACS Appl. Mater. Inter.,* 2015, **7,** 5768-5774.

136. M. S. Al-Ruqeishi, T. Mohiuddin, B. Al-Habsi, F. Al-Ruqeishi, A. Al-Fahdi, and A. AlKhusaibi, *Arab. J. Chem*., 2019, **12**, 5173-5179.

137. D.-M. Shin, E. L. Tsege, S. H. Kang, W. Seung, S.-W. Kim, H. K. Kim, S. W. Hong, and Y.- H. Hwang, *Nano Energy.,* 2015, **12** , 268-277.

138. G. Poulin-Vittrant, C. Oshman, C. Opoku, A. Dahiya, N. Camara, D. Alquier, L.-P. T. H. Hue, and M. Lethiecq, *Phys. Proc*., 2015, **70,** 909- 913.

139. A. Khan, M. Hussain, O. Nur, and M. Willander, *J. Phys. D Appl. Phys*., 2014, **47**, 345102.

140. E. Nour, M. Sandberg, M. Willander, and O. Nur, *Nano energy.,* 2014, **9** , 221-228.

CHAPTER-2

Synthesis and Characterization Techniques

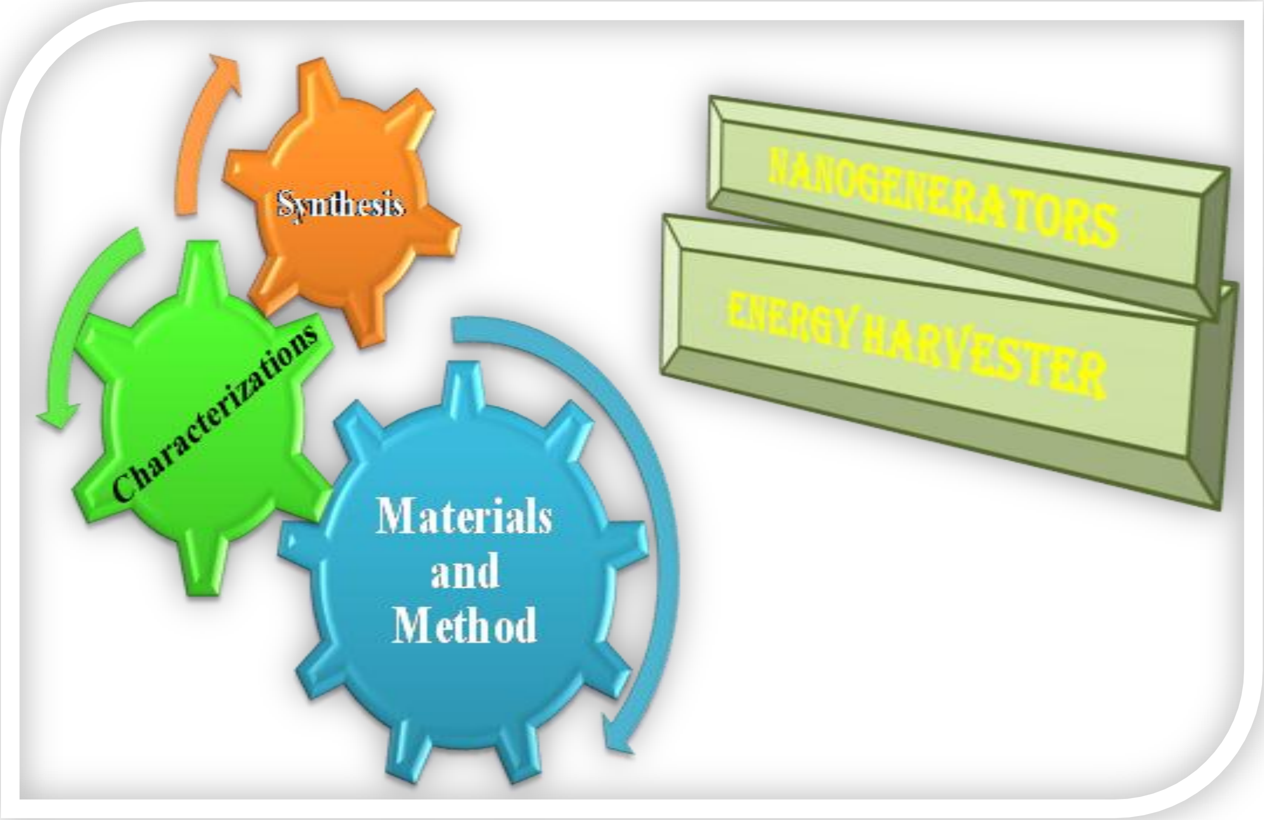

A brief overview of the different synthesis procedure of ZnO and their different nano structures such as rod, particles are discussed in this chapter. Various characterization techniques such as XRD, morphological analyses such as, SEM, FESEM, TEM in addition to different spectroscopic analysis such as, UV-Vis emission, FTIR, Raman, XPS, etc. have been highlighted. Detailed fabrication procedure of the PVDF and its co polymer based composite films using ZnO as a filler material have been illustrated here. The methods for measurement of different electrical parameters of the fabricated composites using instruments like Impedance analyzer, P-E loop tracer have been discussed in detail to optimize the best performance of the filler. The detailed measurement procedures of output piezo performance of the composites have also been mentioned in this chapter.

This chapter aims to describe the detail experimental procedures for the synthesis of different morphology of ZnO nanostructure and their respective PVDF based composites. The fabrication techniques of several PVDF composite based devices have also been included in this chapter. In addition to that, this chapter also describes about the different types of characterization methods/tools adopted for the fulfillment of the entire work.

2.1 Synthesis of filler particle

2.1.1 Brief description of synthesis process

There are different techniques like, co-precipitation, hydrothermal synthesis, sputtering, microemulsion, microwave, sol-gel, ultrasound, spark discharge, template synthesis, solid-state reaction, biological synthesis, etc. to synthesize nanomaterials [1]. Among these techniques, the following methods were utilized to synthesize the filler particles.

2.1.1.1 Hydrothermal synthesis

For synthesis of nanomaterials, hydrothermal synthesis is very useful technique for synthesizing desired particles where control in morphology is required. The word „hydrothermal‟ consists of two significant terminologies; „hydro‟ means water and „thermal‟ means heat. Hydrothermal synthesis of nanomaterials is performed from its aqueous solution in a sealed container at high temperature and vapor pressure. This synthesis is generally performed inside an exclusive Teflon lined stainless steel vessel known as „Autoclave‟. The autoclave material has been lined with Teflon having a higher thermal expansion coefficient. The schematic presentation of hydrothermal autoclave is shown in **Fig. 2.1.** This synthesis can be performed in a wide temperature range starting from room temperature to high temperature. Morphology of nanoparticles is controlled by varying the vapor pressure inside the Teflon lined autoclave cavity.

The process is cost effective and consumes lower amount of energy which are advantages of this method. [2].

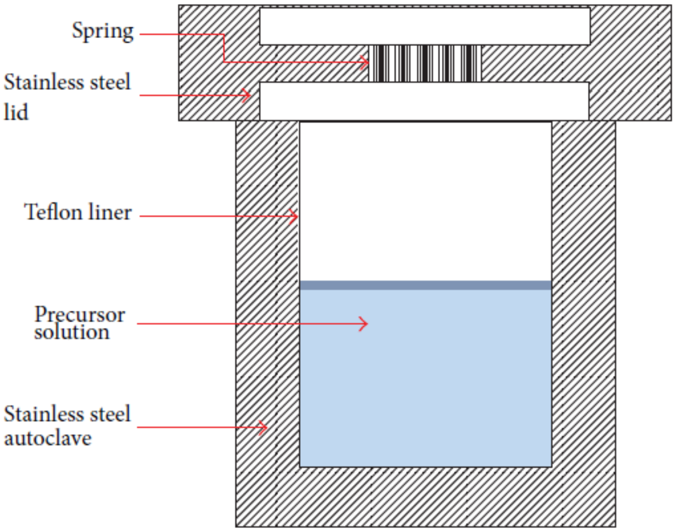

Fig. 2.1 *Schematic presentation of hydrothermal autoclave [reproduced from ref. 3].*

Hydrothermal method has several advantages over other synthesis techniques. Nanomaterials which are unstable at elevated temperature can be produced from hydrothermal synthesis. The synthesized grains or particles exhibit good crystallinity, controlled morphology and size. Low energy consumption during synthesis has made this technique very advantageous.

2.1.1.2 Co-precipitation

To synthesize oxide materials, co-precipitation is perhaps the simplest technique. Economically and industrially it is one of the most viable techniques. Different steps involved in co-precipitation synthesis technique are shown the flow chart given in **Fig. 2.2**. In this process, the product powder is obtained without any additional agglomeration steps.

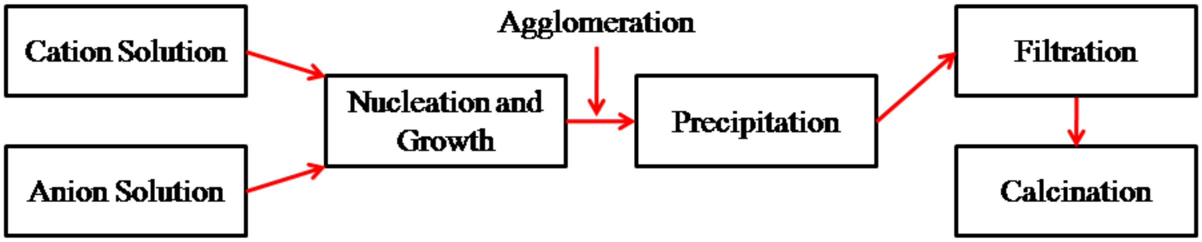

Fig. 2.2 *Flowchart containing different steps involved in co-precipitation technique.*

By adjusting the pH of solution, the synthesis temperature, solvent used for synthesis and precipitating agent, the size of the particles can be controlled [4].

2.1.2 Synthesis of fillers

The exact procedure of synthesis of filler materials is described in this section. Different synthesis mechanisms as described earlier in section 2.1.1 were utilized to synthesize filler particles. The procedures are described below.

2.1.2.1 Synthesis of different aspect ratio ZnO nanorods by hydrothermal

Raw Materials: Chemicals were purchased from the following sources. Analytical-grade Zinc Nitrate Hexahydrate [$Zn(NO_3)_2.6H_2O$] (Sigma Aldrich), Sodium Hydroxide pellets [NaOH] (Merck), Ethanol (C_2H_5OH) (Merck), Ethylenediamine [$C_2H_4(NH_2)_2$, EDA] (Merck) and distilled water were used as starting precursor materials to synthesize different aspect ratio ZnO nanorods. Poly(vinylidene fluoride) (PVDF) pellets [Molecular weight ≈275,000 by GPC Sigma-Aldrich] and N,N-Dimethylacetamide (DMAc) [$CH_3CON(CH_3)_2$] (Merck) were used to fabricate PVDF/ZnO composite films.

Synthesis: ZnO nanorods were synthesized by hydrothermal technique. In a typical reaction, the required amount of zinc nitrate hexahydrate and sodium hydroxide pellets were first dissolved in distilled water separately at a molar ratio ($Zn^{2+:}$ OH^{-}=1:20). The two solutions were mixed to prepare a stock solution. Then 3 ml of the stock solution, 5 ml distilled water and 25 ml ethanol were mixed and kept under continuous stirring for 1 h. Ethylenediamine was then added to the above solution and stirred for 1 h. Then the well mixed solution was sonicated under an ultrasonic water bath for 1 h. Finally the mixed solution was transferred to a Teflon-line autoclave. To obtain different aspect ratio ZnO nanorods, the hydrothermal reaction time was varied from 4 h to 20 hat a fixed temperature 180° C. After the reaction, white precipitate was collected and washed several times with water and ethanol and then dried in an oven at 70° C. As-synthesized ZnO nanorods are designated as ZnO-4 (for reaction time 4h), ZnO-8 (for reaction time 8 h) and ZnO-20 (for reaction time 20 h) respectively [5].

2.1.2.2 Synthesis of ZnO nanorods by co-precipitation method

Raw materials: Zinc Nitrate Hexahydrate [$Zn(NO_3)_2.6H_2O$] (99%, Sigma Aldrich), Sodium Hydroxide pellets [NaOH] (≥ 97%, Merck), Ethanol (C_2H_5OH) (99%, Merck), Ethylenediamine ($C_2H_4(NH_2)_2$) (EDA) (Merck) and distilled water were used as precursor materials to synthesize ZnO rods by wet chemical synthesis.

Synthesis of ZnO nanorods: ZnO nanorods were synthesized by following a room temperature wet chemical synthesis route. Briefly, 20 ml of zinc nitrate hexahydrate aqueous solution and 20 ml of sodium hydroxide aqueous solution were first mixed together inside a 500 ml capped Teflon bottle (the molarity of these two solutions was so chosen that the ratio Zn^{2+}:OH^{-} becomes equal to 1: 20). After 1 h of mixing through continuous stirring, 200 ml of absolute ethanol was added to the mixed solution and kept for stirring (350 rpm) at room temperature for 3 h. Then 10 ml of EDA was added to the above mixed solution and the whole mixture inside the capped

Teflon bottle was stirred for 3 days at room temperature. After the synthesis, a white precipitate was found which was collected and centrifuged several times with water and ethanol. The obtained white product was dried in an oven at 60^0 C for 12 h to get the desired powder sample of ZnO nanorods [6].

2.1.2.3 Synthesis of ZnO nanoparticle by co-precipitation method:

Materials: Zinc acetate dihydrate ($Zn(O_2CCH_3)_2(H_2O)_2$) and sodium hydroxide (NaOH) were used as precursor materials. Absolute ethanol was then added to the mixed solution. All reagents were analytically pure and used as received without any further purification.

Synthesis: ZnO nanoparticles were synthesized by mixing two different solutions: solution A and solution B; solution A contained 3 mmol of zinc acetate dihydrate dissolved in 40 ml of ethanol; solution B contained 7 mmol of NaOH dissolved in 40 ml of distilled water and then in 25 mL of ethanol. Solution B was added dropwise to solution A under vigorous and constant stirring for 2 h at 65 °C, after which solution was allowed to cool down to room temperature. As-synthesized ZnO samples were collected by centrifugation and washed thoroughly with pure ethanol and water for several times and then dried at 60 °C for 2 h.

2.1.2.4 Synthesis of Al doped ZnO nanorods by co-precipitation method

Materials: The analytical-grade Zinc Nitrate Hexahydrate [$Zn(NO_3)_2.6H_2O$] (Sigma Aldrich), Aluminium Nitrate Nonahydrate [$Al(NO_3)_2.\ 9H_2O$], Sodium Hydroxide pellets [NaOH] (Merck), Ethanol (C_2H_5OH) (Merck), and distilled water were used as precursor materials to synthesize ZnO nanorods.

Synthesis of Al doped ZnO nanorods: Pure ZnO nanorods as well as 5 wt % Al doped ZnO ($Zn_{0.95}Al_{0.05}O$) nanorods were prepared by wet chemical synthesis procedure at ambient temperature. During this procedure, first of all, 2.974 gm zinc nitrate hexahydrate was dissolved in distilled water and then 8 gm sodium hydroxide wasadded to the mixed solution. For Al doped ZnO synthesis, 0. 235 gm aluminium nitrate nonahydrate was added to the above specified solution. After that,mixed solution was continuously stirred for 1 h at room temperature (30ºC). There after pure ethanol was added to the resultant solution which and kept for continuous stirring for 24 h. Finally, a precipitate was being collected and centrifuged for several times by using distilled water and ethanol to eliminate any kind of impurities. The obtained product was white in color and it was dried (60ºC) for further evaporation of any kind of solvent present.

2.2 Fabrication of PVDF based composite films

2.2.1 Detail Fabrication procedure

Materials: The PVDF based composite films were fabricated by using poly(vinylidene fluoride) (PVDF) powder (Sigma Aldrich, average M_W~534000 by GPC) (or PVDF pellets, Sigma Aldrich, average M_W~275000 by GPC) and N,N-dimethyl formamide (DMF) [$HCON(CH_3)_2$] (Merck, ≥99%) along with synthesized filler particles.

Fabrication: The simple drop casting method was being utilized to synthesize bare PVDF and other composite films. A series of composite films with different wt% was fabricated by dissolving PVDF pellets in N,N-Dimethylformamide (DMF) under constant stirring at 40ºC. After complete dissolution of PVDF in DMF, different weight percentage of wet chemically synthesized ZnO powder (5wt%, 10wt%, 15 wt% powder with respect to PVDF) were added, individually. Thereafter, to obtain a homogeneous mixture, the solutions were continuously stirred for 24h and sonicated for 1 h. After that, the polymer-composite films were fabricated by casting the resultant solution on a glass substrate and evaporated at 85ºC for 4 h. Finally, at room temperature (30ºC), the dried films were pulled off from the glass substrates to obtain self-standing composite films

2.2.2. Detail composition of the fabricated composite films

Total 4 sets of experiments were conducted in the present work. All the sets did not exhibit same nature during film fabrication. In each set of experiments, fillers were added to the PVDF matrix up to the maximum extent (with respect to the particular set) which was possible in the available experimental conditions. Detail compositions and nomenclatures of the fabricated composite films of each set are summarized below.

(i) 5, 10 and 15 wt% ZnO particles and ZnO nanorods filler with respect to PVDF were added to PVDF-DMF solution separately. In 0.49 g PVDF powder dissolved in 6 ml DMF solution, the required amounts of each filler were 0.0258 g, 0.054 and 0.086 g for 5, 10 and 15 wt% filler loaded composites, respectively. Thickness of all the composite films was ~ 0.04 mm.

Table 2.1 Compositions and nomenclatures of the fabricated composite films.

Name of the Sample	Type of the synthesized ZnO filler	wt% of filler
PVDF		0
ZP-5	ZnO nanoparticles (ZP)	5
ZP-10		10
ZP-15		15
ZR-5	ZnO nanorods (ZR)	5
ZR-10		10
ZR-15		15

(ii) 5, 10 and 15 wt% ZnO-4, ZnO-8 and ZnO-20 fillers with respect to PVDF were added to PVDF-DMAc solution separately. In 0.49 g PVDF powder dissolved in 6 ml DMAc solution, the required amounts of fillers were 0.025 g, 0.054 g and 0.85 g for 5, 10 and 15 wt% filler loaded composites, respectively. Thickness of all the composite films was ~ 0.04 mm.

Table 2.2 Compositions and nomenclatures of the fabricated composite films.

Name of the Sample	Type of the synthesized ZnO nanorods	Wt% of filler
PVDF		0
5wt% PVDF/ZnO-4	ZnO-4	5
10wt% PVDF/ZnO-4		10
15Wt% PVDF/ZnO-4		15
5wt% PVDF/ZnO-8	ZnO-8	5
10wt% PVDF/ZnO-8		10
15Wt% PVDF/ZnO-8		15
5wt% PVDF/ZnO-8	ZnO-20	5
10wt% PVDF/ZnO-8		10
15Wt% PVDF/ZnO-8		15

(iii)5wt%, 10wt%, 15wt% ZnO powder with respect to PVDF were added to the DMF-PVDF solution in three different batches. Further, optimized amount of MWCNT (0.1 wt %) was added to each PVDF-ZnO mixed solution for fabrication of three phase composite.

Table 2.3 Compositions and nomenclatures of the fabricated composite films.

wt% of PVDF pellets w. r. to DMF	wt% of ZnO filler loading w. r. to PVDF	wt% of third phase MWCNT loading w. r. to PVDF	Name of the composite films
8	0	0	PVDF
8	5	0	5PZO
8	10	0	10PZO
8	15	0	15PZO
8	5	0.1	5PZNT
8	10	0.1	10PZNT
8	15	0.1	15PZNT

(iv) 5 and 10 wt% Al@ZnO filler with respect to PVDF-HFP was added to PVDF-DMF solution separately. In 0.49 g PVDF-HFP powder dissolved in 6 ml DMF solution, the required amounts of filler were 0.0258 g, 0.054 g for 5 wt%, 10 wt% filler loaded composites, respectively. Thickness of all the composite films was ~ 0.05 mm.

Table 2.4 Compositions and nomenclatures of the fabricated composite films

Name of the Sample	Type of the synthesized filler	Wt% of filler
PVDF-HFP		0
5PALZO	Al@ZnO	5
10PALZO		10
10PALZO-P (Poled)		10

2.3 Fabrication of devices:

For dielectric measurement and fabrication of energy storage device, both sides of all the composite films (cut in small square shape) were electroded with high quality silver paste. For the measurement of nanogenerator output, the two electrodes of each film (3 cm × 2 cm) were connected with copper wires (copper wires were connected by using single side adhesive tape). Different amount of force were applied on the nanogenerator device and the output electrical signal was studied by oscilloscope.

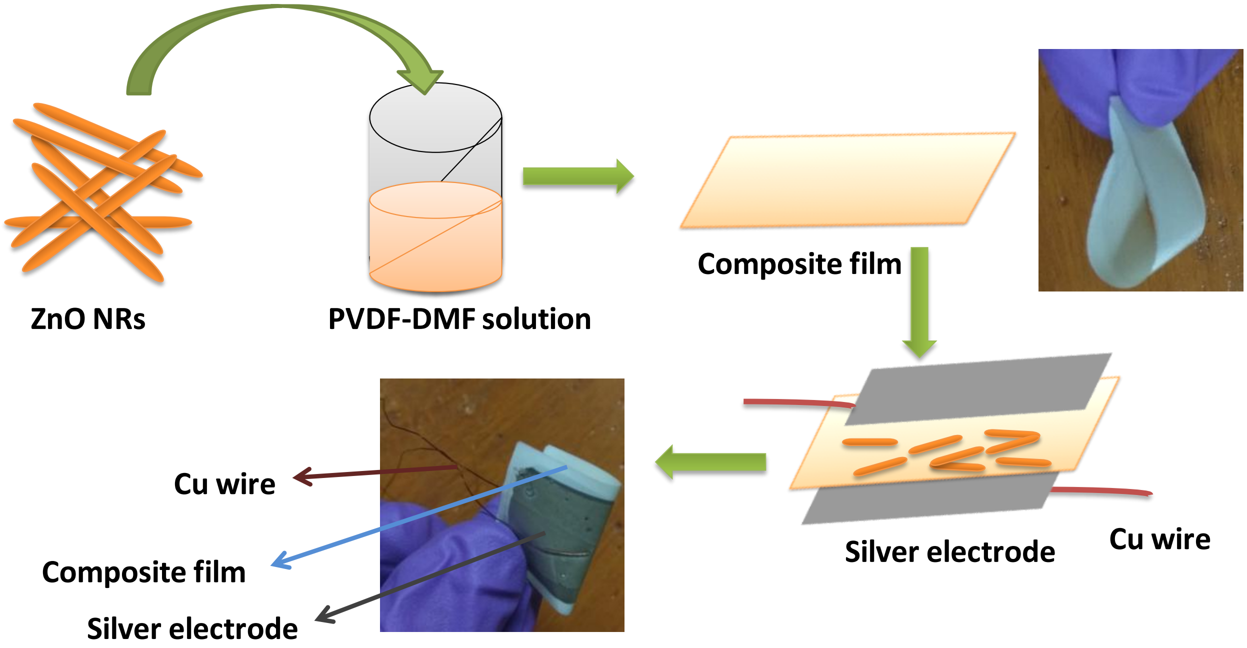

Fig. 2.3: Schematic of fabrication procedure of nanogenerator device

2.4 Characterizations

2.4.1 Brief description of various characterization techniques:

A variety of characterization techniques were used for a various purposes. The basic concept and operating principles of various instruments and characterization techniques are covered briefly below.

2.4.1.1. X-ray diffraction (XRD)

X-ray diffraction is a versatile, non-destructive analytical method for identification and quantitative determination of various crystalline forms, known as "phases" of compound present in powder and solid samples. These X-rays are the electromagnetic radiations which can penetrate deep into the materials to provide crystallographic information about the samples [7-10]. X-rays are generated when a focused electron beam accelerated across a high voltage field and bombards a stationary or rotating solid target. Cu-Kα and Mo-Kα radiations are commonly used as targets in X-ray tubes, which emit 8 KeV and 14 KeV X-rays corresponding to the wavelengths of 1.54 Å and 0.8 Å, respectively. X-rays primarily interact with electrons in atoms and during the course of interaction some photons from the incident beam deflected away to cause diffraction. The scattered X-rays carry information about the electron distribution in materials. Diffracted waves from different atoms can interfere with each other and the resultant intensity distribution is strongly modulated by this interaction. If the atoms are arranged in a periodic fashion, as in crystals, the diffracted waves will consist of sharp interference maxima (peaks) with the same symmetry according to the atomic distribution. Schematic diagram of X-ray diffraction is shown in **Fig. 2.4**. Measuring the diffraction pattern therefore allows one to deduce the distribution of atoms in a material. Interaction of X-rays with sample creates secondary "diffracted" beams of X-rays related to interplanar spacings in the crystalline powder according to a mathematical relation called "Bragg"s Law" as follows

$2d \sin\theta = n\lambda$………….. (2.1)

where n is an integer, λ is the wavelength of the X-rays, d is the interplanar spacing generating the diffraction and θ is the diffraction angle. λ and d are measured in the same units, usually in angstroms [7-10].

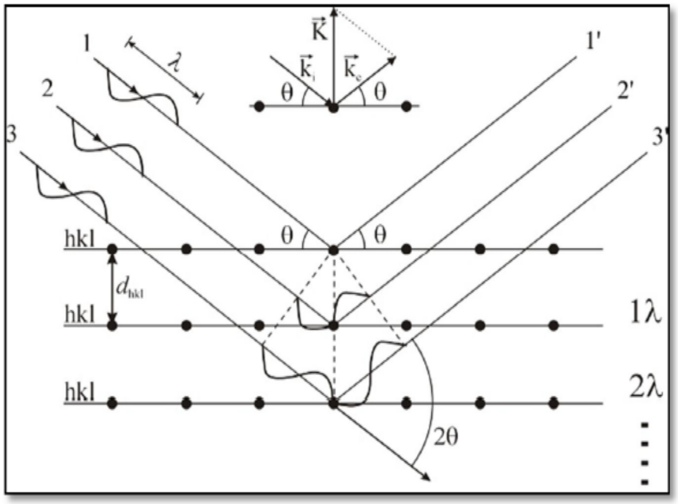

Fig. 2.4 *Schematic diagram of X-ray diffraction* [https://fys.kuleuven.be/iks/nvsf/experimental-facilities/x-ray-diffraction-2013-bruker-d8-discover]

X‟pert Pro MPD (PAN analytical), Rigaku Powder XRD system and Rigaku GIXRD system are the different X-ray diffractometers used for different purpose in the present work.

2.4.1.2 Raman spectroscopy

Raman spectroscopy is mainly used to discover vibrational, rotational, and other low-frequency modes present in a chemical system, which offer the molecule's unique structural fingerprint [11]. The inelastic scattering (or Raman scattering) of monochromatic light (typically a laser beam) by the molecule under study is the main phenomena employed in this spectroscopic technique. A shift in the energy of the laser phonon happens when it interacts with molecular vibrations, phonons, or other excitations in the system. The information regarding molecular vibrations comes from the shift in energy level of laser phonons. **Fig. 2.5** represents the energy levels of several Raman spectroscopy states.

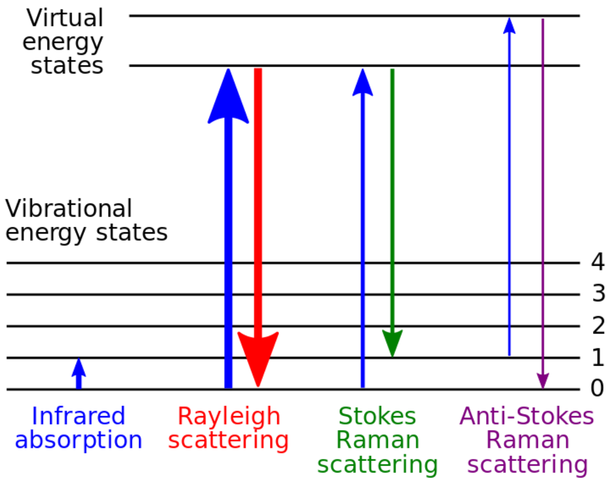

Fig. 2.5 *Energy level diagram showing the states involved in Raman spectra* [12].

The structural properties of various filler particles were studied using a Micro Raman spectrometer (RENISHAW) in the current study.

2.4.1.3 Fourier-transform infrared (FTIR) spectroscopy

In this technique vibration spectroscopy is used as the measurement technique to find the local bonds in a composite. Under infrared (IR) radiation, some of the molecules with permanent dipole moment, response with characteristic frequency of the vibration mode. Even the molecules which have no permanent dipole moment can also vibrate with characteristics frequency. As shown in Fig. 2.6, the reflected beams are produced into the interface of fixed and movable mirror due to the optical path difference. After going through the sample, the light beam with frequency dependent phase vibration is received by the detector. After that, the frequency vibration is converted to intensity vibration with the help of fourier transform technique (called inter ferogram). Again, this interofergram converts wavenumber dependent spectrum by software called Cooley-Tukey algorithm. As compared to conventional IR spectrometer, FTIR has higher resolution, faster speed, and better signal to noise ratio.

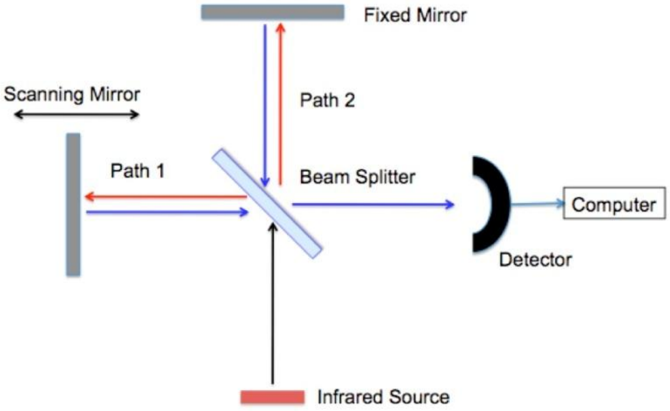

Fig. 2.6 *Schematic of working mechanism of FTIR instrument [14]*

In the present work, FTIR spectra of zinc oxide nanorods and its polymer based composites have been measured between 4000 and 400 cm^{-1} Perkin Elmer FTIR instrument.

2.4.1.4 UV-Visible spectroscopy (UV-Vis)

The basic principle of Ultraviolet-visible spectroscopy (UV-Vis) is the excitation of bonding and anti-bonding electrons to higher energy molecular orbitals by absorbing energy in the form of ultraviolet or visible light [15]. In this technique, absorption or reflectance spectroscopy in the ultraviolet and visible region is achieved. UV-Vis spectroscopy is widely used in various practical applications like, determination of rate constant of chemical reactions and quantitative determination of different analytes in analytical chemistry. But in the present work, this technique was mainly used to determine the optical band gap of some filler materials.

In this dissertation work, UV-Vis spectra of the samples have been characterized by UV-Vis-NIR spectrophotometer (Shimadzu UV-2450,; photometric accuracy: transmission ±0.3%, wavelength resolution, 0.10 nm).

2.4.1.5. X-ray photoelectron spectroscopy (XPS)

In XPS, irradiating by a beam of X-ray on the material and simultaneously measuring the kinetic energy (KE), the spectra are obtained. The number of electrons that escape from the top 1 to 10 nm of the materials being analysed. It is a quantitative spectroscopic technique. It provides the information about the elemental composition, empirical formula, chemical state and electronic state of the elements present in the materials. When a soft X-ray irradiates the surface, the core-level electrons are emitted from the surface (**Fig. 2.7**). The binding energy (EB) of each of the emitted electron can be determined by using the equation,

$$\text{EB} = \text{EPhoton} - (\text{EK} + \Phi) \; \ldots \ldots \ldots \; (2.2)$$

where, $E_{\text{Photon}}=h\nu$ is the X-ray energy, which is being used. EK is the kinetic energy of the electron as measured by the instrument and Φ is the work function of the spectrometer [16].

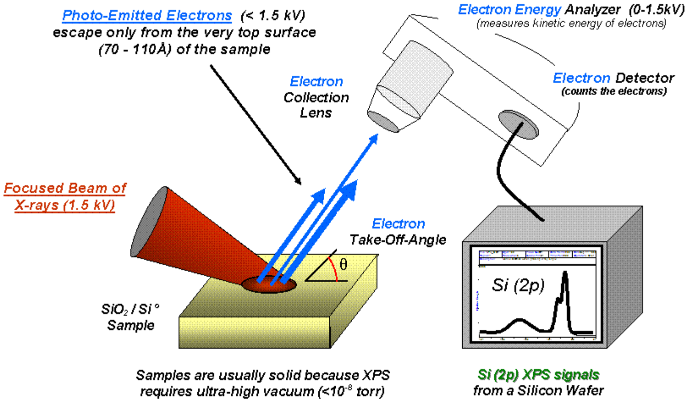

Fig. 2.7 *Basic components of monochromatic XPS [16]*

Then the EB can be calculated which is the main goal of the spectrometer. All the binding energies (EB) are referred to the C_{1s} peak (set at 284.6 eV) arising from surface hydrocarbons (or adventitious hydrocarbon). The X-ray photoemission spectroscopy analysis was carried out with the help of PHI 5000 Versa probe II scanning XPS microprobe (ULVAC-PHI, U.S.) for investigating the change in binding energy of the carbon atom in composite as compared to neat PVDF. This investigation was done to predict about the bonding mechanism between the surface of ZnO and PVDF dipole. The measurements were performed at room temperature and at a base pressure lower than 6×10^{-10} mbar. All spectra were recorded with monochromatic Al Kα (hν= 1486.6 eV) radiations with a total resolution of about 0.7 eV and a beam size of 100 µm.

2.4.1.6. Transmission electron microscopy (TEM)

TEM is a well-known microscopic technique where a beam of electrons interact with a thin specimen of sample and produces a magnified image of the sample. It has normally higher resolution than optical microscope since electrons have smaller De Broglie wavelength. In TEM high energy electrons (upto 300 kV accelerating voltage) are emitted by an electron gun forming electron beam is transmitted through the specimen, in which some electrons get through and scatters others out of the beam. After emerging from the specimen, both scattered and non-scattered electrons carry the information about the structure of the specimen, which is magnified by the objective lens of the microscope and can be viewed in some different ways, for instant by projecting magnified image onto a phosphor–coated viewing screen or recording the image in a CCD (charge couple device) camera and displaying image on a computer monitor. This is the most common technique used when working with TEM microscopes (**Fig. 2.8**) [17-18]. When electron beam is transmitted through the specimen without being scattered, it interacts with the CCD camera producing a signal of certain intensity resulting generation of contrast image by the „spatial distribution of the elastically scattered electrons‟. In other words, thick region of the specimen or regions containing atoms with high atomic number will appear dark, while thin regions or region containing no atoms or low atomic number will appear bright, forming two dimensional projection of the sample down the optic axis. In this thesis bright field TEM images

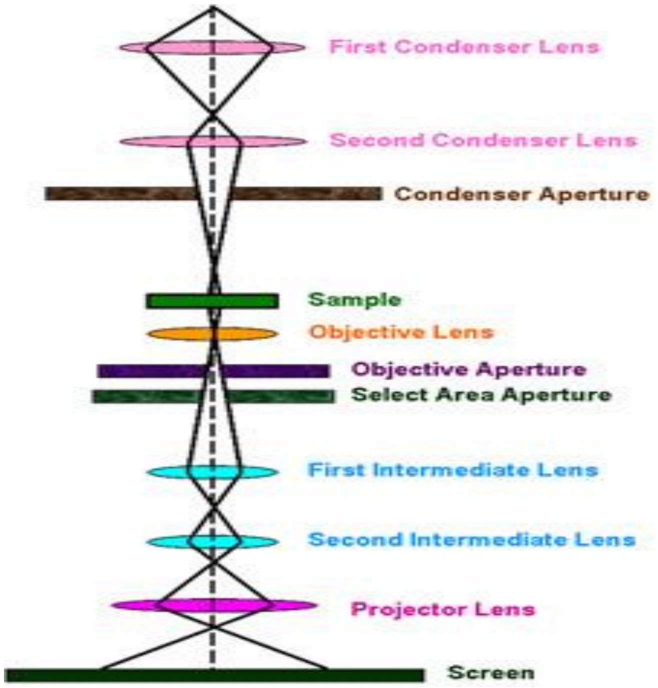

Fig. 2.8 *The instrumentation of HRTEM*

have been taken from all synthesized sample in order to observe the size and shape distribution of the rods. In dark field imaging technique, diffracted electron beam coming from the sample is imaged rather than transmitted beam. In this method, image contrast is better than bright field though image details are not obtained. In selected area electron diffraction (SAED), the contrast is formed by the angular distribution of small angle elastically scattered electrons that hit the viewing screen or the CCD camera. Electron diffraction is of a great utility for study the structure of different crystalline materials since it determines the spacing of planes and gives a good amount of crystallographic information about those materials. Energy dispersive X-ray spectrometry (EDS) utilizes X-ray spectrum to obtain a localized chemical analysis of sample. Both qualitative and quantitative analysis can be performed by the identification and intensity measurement of the lines in the spectrum. Elemental mapping shows the spatial distribution of the elements in a sample. The image is produced by progressively restoring the electron beam point by point over an area of interest. Transmission Electron Microscopic analysis of all the samples has been done by FEI Tecnai G^2 TEM.

2.4.1.7. Field emission scanning electron microscopy (FESEM)

Scanning electron microscope (SEM) is an important tool for microscopic feature measurement and surface topography study. The electron gun of an electron microscope produces electron beam in an evacuated column (less than 1x10-7 Pa). The vacuum allows electron movement along the column without scattering and helps prevent discharges inside the instrument. The vacuum design is a function of the electron source due to its influence on the cathode emitter lifetime. The function of the electron gun is to provide a large and stable current in a small beam. There are two classes of emission source: thermionic emitter and field emitter. Emitter type is the main difference between the SEM and FESEM. Thermionic Emitters use electrical current to heat up a filament; the two most common materials used for filaments are tungsten (W) and lanthanun hexaboride (LaB_6). When the heat is enough to overcome the work function of the filament material, the electrons can escape from the material. Thermionic sources have relative low brightness, evaporation of cathode material and thermal drift during operation. As a result, getting high magnification images (~×100000) often becomes difficult. Field Emission is one way of generating electrons that avoids these problems. A Field Emission Source (FES); also called a cold cathode field emitter, does not heat the filament. The emission is reached by placing the filament in a huge electrical potential gradient. The FES is usually a wire of tungsten (W) fashioned into a sharp point. The significance of the small tip radius (~ 100 nm) is that an electric field can be concentrated to an extreme level, becoming so big that the work function of the material is lowered and electrons can leave the cathode. FESEM uses Field Emission Source producing a cleaner image, less electrostatic distortions and spatial resolution < 2 nm. Imaging by capturing and analysing secondary electrons, which are ejected from the material under investigation, is the most common technique used for electron microscopy. An electron-collecting device collects these secondary electrons to produce an electronic signal. The electronic signal is amplified and the image of the sample surface is finally displayed on the screen of a PC. **Fig. 2.9** schematically illustrates the basic parts of operation of SEM [19].

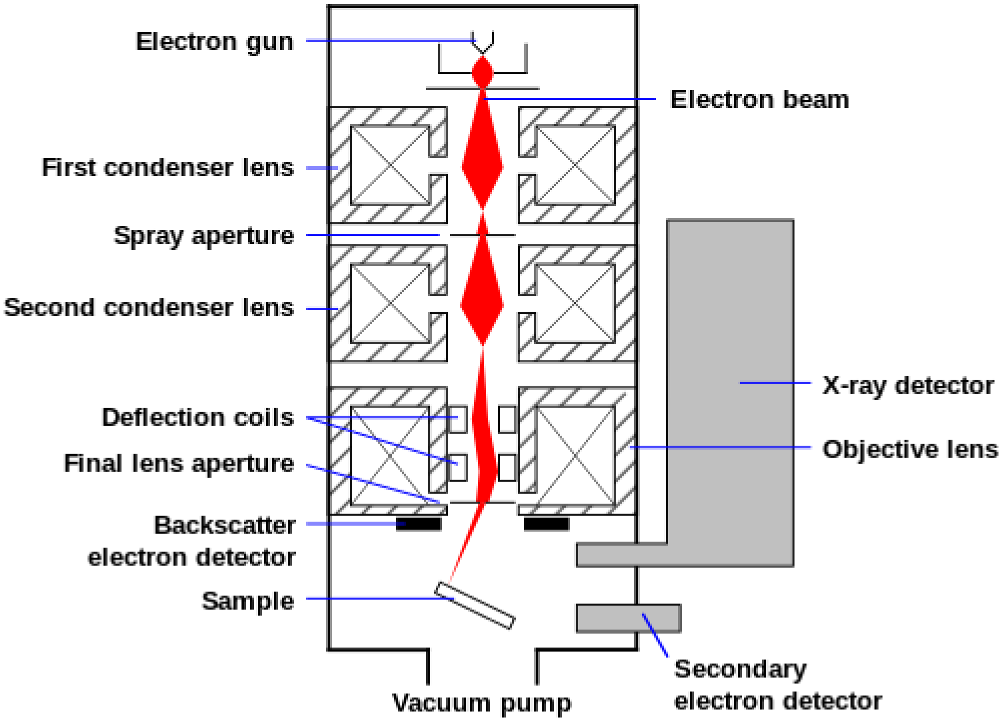

Fig. 2.9 *Schematic of the basic parts of FESEM [19]*

In the present work, FESEM (Supra 35 VP) and FESEM (Carl Zeiss) instruments were used to study the surface morphology of fillers, some bulk ceramic samples and somecomposite films. The elemental details of the filler materials were also studied by the EDS apparatus equipped with these FESEM instruments.

2.4.1.8 Piezo force microscopy (PFM)

Piezoresponse force microscopy (PFM) is a variant of atomic force microscopy (AFM) that allows imaging and manipulation of piezoelectric/ferroelectric materials domains. This is achieved by bringing a sharp conductive probe into contact with a ferroelectric surface (or piezoelectric material) and applying an alternating current (AC) bias to the probe tip in order to excite deformation of the sample through the converse piezoelectric effect . The resulting deflection of the probe cantilever is detected through standard split photodiode detector methods and then demodulated by use of a lock-in amplifier (LiA). In this way topography and ferroelectric domains can be imaged simultaneously with high resolution that is used to scan the specimen surface (**Fig. 2.10**) [20-21].

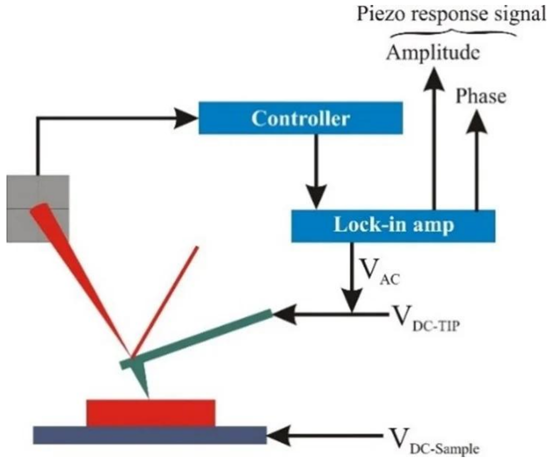

Fig. 2.10 *Components of piezo force microscope*

2.4.1.9 Zeta potential measurement

Zeta potential (ξ) is scientifically known as electro kinetic potential in colloidal dispersions. Theoretically zeta potential is the electric potential developed in the interfacial double layer (DL) at the location of the slipping plane relative to a point in the bulk fluid away from the interface or potential difference between the dispersion medium and stationary layer of dispersion medium. This is instigated by net electrical charge contained within the region restricted by the slipping plane as well as its location. Thus, it is widely used for quantification of the magnitude of the charge. The zeta potential mainly justifies the stability of colloidal dispersions [22]. Here we have interestingly utilized this particular phenomenon of Zinc nanorods to understand the variation of its surface charge with variation in synthesis technique and with modification by different filler using water as the dispersion medium. The zeta potential measurements were carried out with Horiba Nanoparticle Analyzer SZ100.

2.4.1.10 Dielectric study using Impedance analyzer

As the present work deal with the electrical properties of filler loaded PVDF film, the measurement of dielectric properties of the composite films is very essential. On the other hand, the stored energy density of any material is proportional to the effective dielectric permittivity of the material. Therefore, to study the energy storage performance of the composites, dielectric study is also required [23]. In this context an Impedance Analyzer (Wayne Kerr, 6500B) was utilized to study the dielectric properties of all the composite films and some bulk samples comprising of filler materials. This instrument measures the complex electrical impedance as a function of test frequency. In the present work, a broad frequency range of 100 Hz to 1 MHz was utilized. The attached furnace with the instrument can alter the temperature of the sample which helps to study the temperature dependent complex impedance. Impedance Analyzer basically works on the principle of LCR meter [24] which is used to measure the inductance (L), capacitance (C), and resistance (R) of an electronic component. Usually the device under characterization is subjected to an AC voltage and the current through the device and voltage across it is measured by the meter. The meter then calculates the required parameters by using the ratio of this current and voltage [24]. Advanced LCR meters can determine the phase angle too.

2.4.1.11 Ferroelectric study

P-E hysteresis loop tracer basically measures the variation of polarization as a function of applied electric field. A high voltage is applied across the sample by an attached amplifier and the polarization is measured accordingly. The most common and basic circuit to investigate the P-E loops was developed by Sawyer and Tower [33] as shown in Fig. 2.11. The circuit was then modified suitably by different researchers. Furthermore, the introduction of microprocessor, development of new and modern software, emergence of cheap PC hardware and availability of different wave form have made the P-E loop measurement technique more reliable and appropriate. P-E loops have been measured by using various methodology and circuitry arrangement by different researchers.

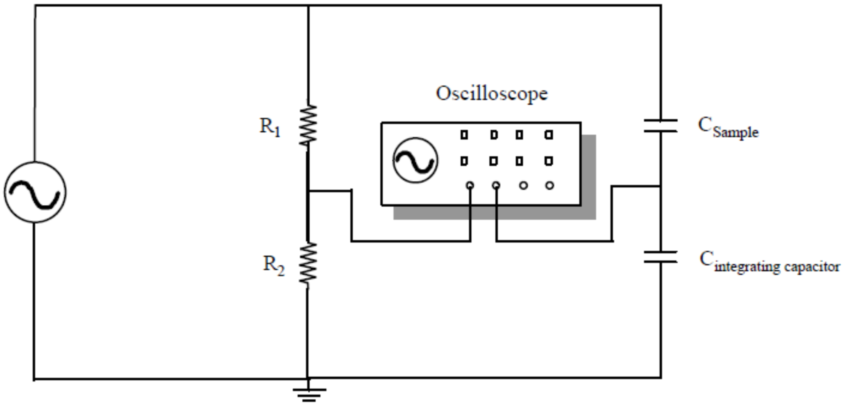

Fig. 2.11 *Schematic of configuration setup the modified Sawyer-Tower circuit [33]*

In the present work, P-E loops of different composite systems and some bulk samples (comprising of fillers only) were measured by using a Ceramic Multilayer Actuator Test Bench (aixACCT System GmbH, Germany) and a RADIANT ferroelectric test systems (Radiant Technologies Inc.) using Vision software (Version 3.1.0). Leakage current of some samples were also measured by the RADIANT instrument.

2.4.1.12 Corona poling

For the study of external electrical poling dependent dielectric, ferroelectric, energy storage, energy harvesting properties, and for investigation of electric breakdown strengths of some composite films, a corona poling unit (Milman) was utilized. The basic operation of corona poling is the corona discharge (partial breakdown of air) which is commonly initiated by higher electric field at ambient pressure.

2.4.1.13 Piezo-response measurement

As the present work deals with the generation of electrical power from mechanical energy, it is essential to utilize an electrical signal measuring setup. In this purpose a Digital Storage Oscilloscope (DSO) was used. DSO is the conventional form of digital oscilloscope. Digital storage oscilloscope operates on the basis of simple circuit arrangement. The stages of operation of a digital storage oscilloscope are shown in Fig. 2.12.

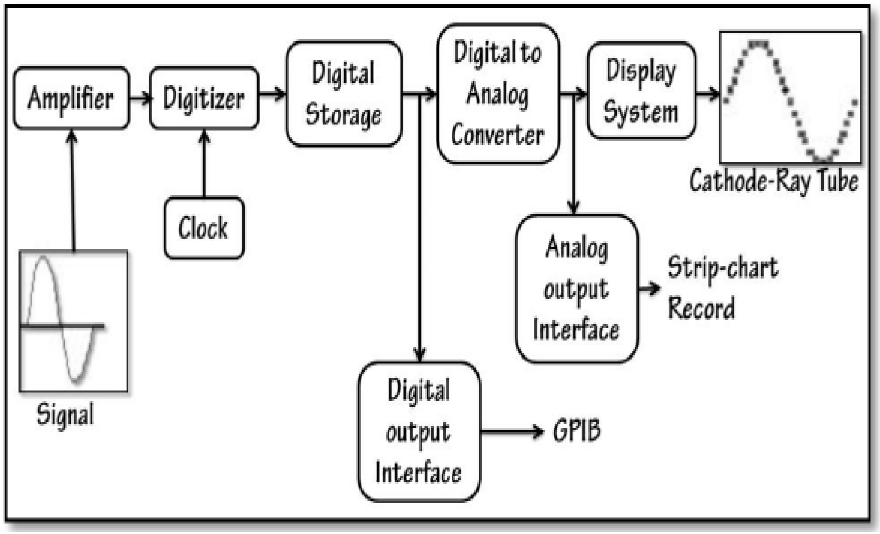

Fig. 2.12 *Subsystems of a digital oscilloscope*

To study various electrical parameters, a multimeter was utilized. A multimeter is a multifunctional electronic instrument which can measure various electronic parameters like resistance, voltage, capacitance, etc. by using special type of circuit arrangement. Multimeter was also used to study the DC output voltage from the fabricated nanogenerator devices after rectification.

2.4.1.14 Others

Along with the above major instruments, various other instruments were also used. During sample fabrication, magnetic stirrer, sonicator, high temperature furnace, vacuum oven, hot pressing setup, etc. was used. Piezometer was employed to determine the piezoelectric coefficients of the composite films. Different electrical components like, bridge rectifier ICs, resistors, capacitors, etc. were also used during the measurements of energy harvesting performance.

References

1. A. V. Rane, K. Kanny, V. K. Abitha, S. Thomas, Methods for synthesis of nanoparticles and fabrication of nanocomposites, in: S. M. Bhagyaraj, O. S. Oluwafemi, N. Kalarikkal, S. Thomas, Synthesis of Inorganic Nanomaterials: Advances and Key Technologies, *Elsevie*r., 2018, 121-139.
2. 3. Y. X. Gan, A. H. Jayatissa, Z. Yu, X. Chen, M. Li, Hydrothermal Synthesis of Nanomaterials, *J. nanometer*., 2020, 8917013.
3. N. Asim, S. Ahmadi, M. A. Alghoul, F. Y. Hammadi, K. Saeedfar, K. Sopian, *International Journal of Photoenergy.*, 2014, 518156.
4. Co-precipitation – CSIR – NAL. https://www.nal.res.in/en/techniques/co-precipitation,
5. S. Pratihar, S.K.Medda, S.Sen, P.S.Devi, *Polymer Composites*., 2020, **41**, 3351-3363.
6. S.Pratihar, A.Patra, A.sasmal, S. K. Medda, S.Sen, *Soft matter*., 2021, **17**, 8483.
7. W. H. Bragg, W. L. Bragg, The Structure of the Diamond, *Nature*., 1913, **91**, 557.
8. R. W. G. Wyckoff, E. Posnjak, The crystal structure of Ammonium Chloroplatinate, 1921, 43 2292-2309.
9. K. Lonsdale, The Structure of the Benzene Ring, *Nature*., 1928, **122**, 810.

10. B.D. Culity, S.R.Stock, *Prentice Hall Pub*.,N.J., 3rd Ed.,2001, 622-648

11. 22. D.J. Gardiner, Practical Raman spectroscopy. *Springer-Verlag*, 1989, ISBN 978-0-387-50254-0.

12. Raman spectroscopy – Wikipedia. https://en.wikipedia.org/wiki/Raman_spectroscopy

13. Fourier Transform Infrared Spectroscopy (FTIR) – CHEM 174 Physical Chemistry Laboratory II – Howard University. https://chem.libretexts.org/Courses/Howard

14. O. Faix, Ch-4: Methods in lignin chemistry, *Springer Berlin Heidelberg*, 1992, 83-109

15. Ultraviolet-visible spectroscopy – Wikipedia

16. X-ray photoelectron spectroscopy – Wikipedia. https://en.wikipedia.org/wiki/Xray_photoelectron_spect

17. Transmission electron microscopy – Wikipedia. https://en.wikipedia.org/wiki/Transmission_electron_microscopy

18. Transmission electron microscopy – ncmn, https://ncmn.unl.edu/enif/microscopy/TEM.shtml

19. Scanning electron microscope – Wikipedia. https://en.wikipedia.org/wiki/Scanning_electron_microscope

20. Piezo force microscopy –wikipedia https://en.wikipedia.org/wiki/Piezoresponse_force_microscopy

21. https://www.nanosurf.com/en/application/piezo-response-force-microscopy-pfm

22. A.D. McNaught, A. Wilkinson, 2nd Ed, *Blackwell Scientific Pub*., Oxford, 1977, 72-98

23. L. Wu, K. Wu, D. Liu, R. Huang, J. Huo, F. Chen, Q. Fu, *J. Mater. Chem. A*., 2018, **6** 7573-7584.

24. LCR meter – Wikipedia. https://en.wikipedia.org/wiki/LCR_meter.

CHAPTER-3

Results and Discussions

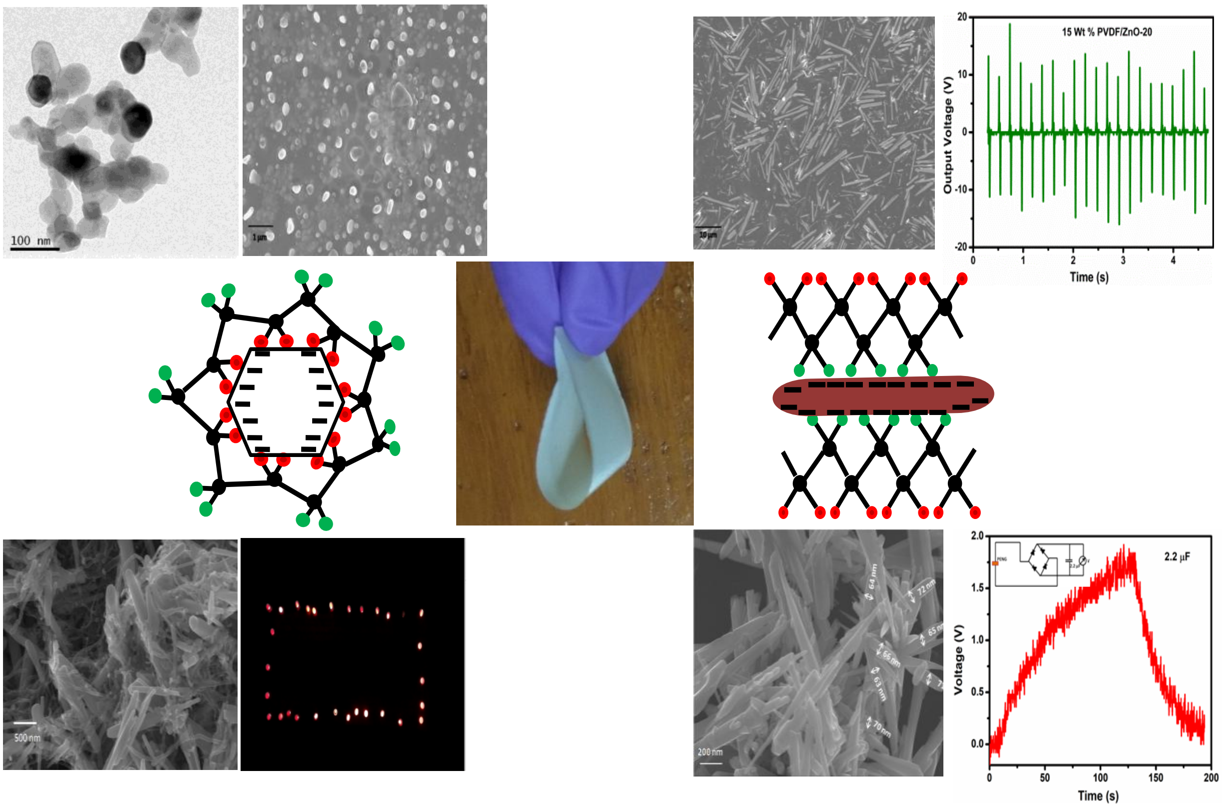

In this chapter, different parameters of fillers were explored which influences the electroactive phase fraction, energy storage and energy harvesting property of PVDF nanocomposites. This chapter is divided into four subsections. In the first section, morphological influence on the nucleation and stabilization of electroactive phase in PVDF was carried out with hydrothermally synthesized ZnO nanorods and wet chemically synthesized ZnO nanoparticles. One dimension filler having rod shape structure was found to be more effective in enhancing the dielectric, ferroelectric, energy storage and energy harvesting performance of their PVDF based composite films compared to particle like structure. In the next section, the effect of filler aspect ratio on the electrical properties of ZnO incorporated poly(vinylidene fluoride) (PVDF) matrix was investigated. High aspect ratio ZnO filler loading in PVDF matrix increased the polar phase fraction in the nanocomposite system which triggered the enhancement of dielectric properties along with ferroelectric and piezoelectric properties. In the third section, further improvement in the electrical performances of the flexible PVDF-ZnO composites by using MWCNT as a third phase addition was attempted. Conductive MWCNT improved the connectivity between ZnO nanorods dispersed in insulating PVDF matrix and the composite films and electrodes which improved the output mechanical energy harvesting performance. In the fourth section, ZnO was doped with Al $^{3+}$ ion and the effect on the electrical properties of PVDF-HFP was studied

Chapter 3: Results and Discussion

3.1: Effect of morphology of ZnO filler on the electroactive phase and electrical performance of their PVDF based nanocomposites:

3.1.1. Introduction:

As per the earlier discussion in chapter 1, different parameter of fillers influences the electroactive phase of PVDF. Among them, morphology of filler is one of the most important parameter as piezoelectric properties are structure-dependent. Fillers with tuned morphology such as 1D nanostructure are more efficient to induce polar phase compared to other geometry [1-2]. Maximum amount of electroactive phase may be obtained by incorporation of high aspect ratio 1D nanostructure such as nanorods and nanowires etc [3]. Superior piezoelectric properties are expected only in the case of 1D nanostructures with an extremely high aspect ratio since the piezoelectric coefficient increases with increment of the aspect ratio of 1D nanostructure [3-4].

It is noteworthy to mention that ZnO can be obtained in different architecture and their morphology can be tuned easily. Here in this chapter, the morphological effect of ZnO on the stabilization of β phase as well as dielectric, ferroelectric and piezoelectric properties of polymer based composites was studied experimentally with two different morphology i.e. ZnO particle and rod. Therefore, ZnO filler was used as a nucleating agent in PVDF and systematically study the morphological influence of ZnO on the stabilization of β phase in PVDF nanocomposites.

In this regard, ZnO with two different morphology such as nanoparticles (ZP) and nanorods (ZR) were synthesized by wet chemical and hydrothermal methods, respectively and their respective PVDF based composite films were fabricated by loading 5, 10 and 15 wt% of each filler in PVDF matrix (5wt%, 10wt%, 15wt% ZP loaded PVDF films were named as ZP-5, ZP-10 and ZP-15; ZR loaded PVDF films were named as ZR-5, ZR-10 and ZR-15, respectively). A net PVDF film was also fabricated to make the comparison with respect to the piezopolymer. The maximum output performance of each set of nanocomposites was optimized by systematically studying the microstructural, dielectric, ferroelectric and piezoelectric properties of the composites.

3.1.1.1. Characterization of two different shape of ZnO fillers:

In order to investigate the phase purity and crystalline nature of the synthesized ZnO particles and nanorods, XRD characterization was carried out. **Fig. 3.1.1** presents the XRD pattern of ZnO with different morphology; wet chemically synthesized particles (ZP) and hydrothermally synthesized nanorods (ZR). In each case, XRD pattern shows the crystalline nature of synthesized ZnO samples. All the diffraction peaks were well matched with standard Joint Committee on Powder Diffraction Standards file (JCPDS-card number # 79-2205). Therefore the peaks were indexed in the figure on the basis of this JCPDS file which confirmed the hexagonal wurtzite structure (with $P6_3mc$ space group and lattice constant a=0.32498 nm, c= 0.52066 nm) of the synthesized ZnO filler. The absence of any additional peak confirmed the phase purity of the synthesized ZnO products.

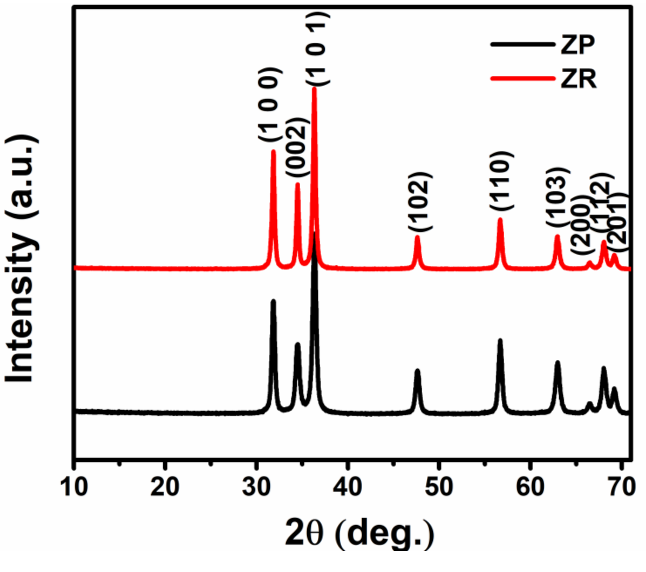

Fig. 3.1.1 *XRD patterns of ZP and ZR samples*

To have a morphological idea about the synthesized fillers, FESEM characterization was carried out. **Fig. 3.1.2(a)** represents the FESEM image of the synthesized ZnO nanoparticles. The figure reveals that the ZnO particles are agglomerated in nature. The FESEM micrograph of the synthesized nanorods under low magnification is shown in **Fig. 3.1.2(b)** which clearly indicated that uniform microstructure of the synthesized nanorods.

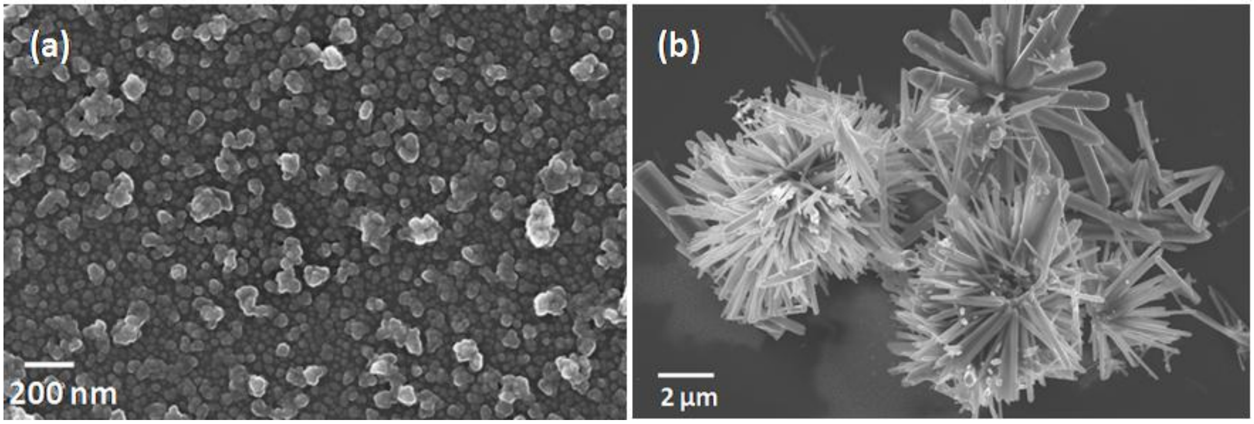

Fig. 3.1.2 *FESEM images* ***(a)*** *ZnO nanoparticle and* ***(b)*** *ZnO nanorods*

In order to understand the crystalline nature and size of the fillers, TEM characterization was carried out. **Fig. 3.1.3(a)** represents the typical TEM images of ZnO nanoparticles and inset shows the diameter distribution of the particles as obtained from the TEM image. TEM images confirmed the most of the ZnO nanoparticles are hexagonal with the diameter ~ in the range of 45 nm. Selected Area Electron Diffraction (SAED) pattern (**Fig. 3.1.3(b)**) revealed that diffraction pattern of ZnO nanoparticles ascribed to (010), (002), (011), (012), (110) and (103) planes are well matched with XRD database. High Resolution Transmission Electron Microscopy (HRTEM) study reveals that good crystallinity of ZnO nanoparticles **(Fig. 3.1.3(c))**. On the other hand, TEM images of ZnO nanorods are shown in **Fig. 3.1.3(d)** along with diameter distribution (inset) which infers the well aligned uniform microstructure of the nanorod with average diameter~180 nm. Further SAED pattern of ZnO nanorods (**Fig. 3.1.3(e)**) confirmed the presence of crystalline plane which also supported the XRD result. HRTEM study (**Fig. 3.1.3(f)**) clearly indicates the high crystallinity of the synthesized nanorods.

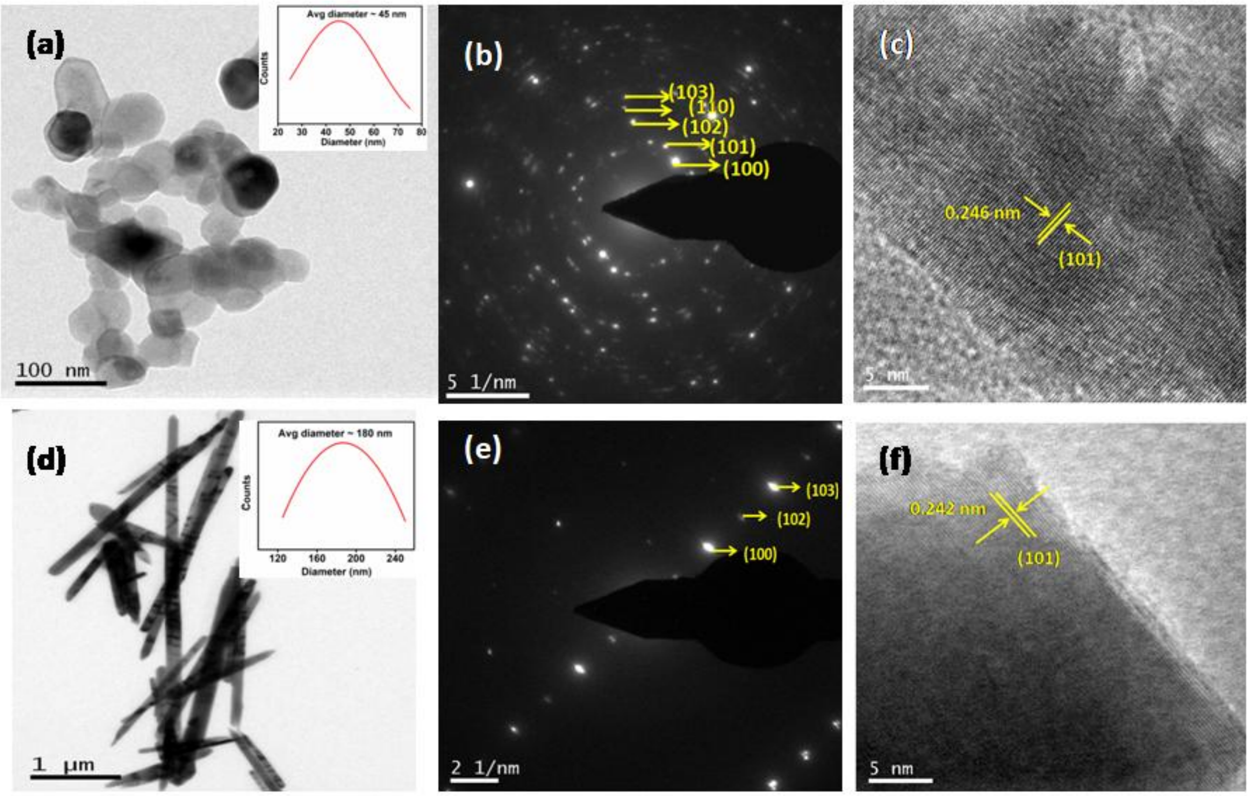

Fig. 3.1.3 ***(a)*** *TEM image of ZnO nanoparticles, inset shows the average diameter ~ 45 nm ,* ***(b)*** *SAED pattern,* ***(c)****HRTEM image of ZnO nanoparticles;* ***(d)****TEM image of ZnO nanorods, inset shows the average diameter of the rods ~ 180 nm* ***(e)*** *SAED pattern,* ***(f)****HRTEM image of ZnO nanorods*

In order to identify the vibrational bond of the synthesized ZnO nanostructure, FTIR characterization was carried out within the wavenumber region 4000-400 cm^{-1} (shown in **Fig. 3.1.4(a)**). The peak observed at 500 cm^{-1} corresponds to the stretching vibration of Zn-O bond. Another broad peak observed at 3500 cm^{-1} for both sample is ascribed due to the hydroxyl (-OH) group which indicates the hygroscopic nature of ZnO. The stretching vibration band of hydroxyl group (C-OH) and C-O stretching vibration of COOH group were observed at 1400 cm^{-1} and 1620 cm^{-1}, respectively. There is no other metal bond present within the synthesized ZnO nanostructures which confirmed the purity of the synthesized sample [4].

Raman spectra of both ZnO nanoparticles and nanorods are illustrated in **Fig. 3.1.4(b)**. All the spectroscopic peaks for both the samples indexed in **Fig. 3.1.4(b)** can be attributed to the wurtzite structure of ZnO. Among them, the most strong intensity peak located at 437 cm^{-1} confirmed the hexagonal wurtzite structure of ZnO fillers [5].

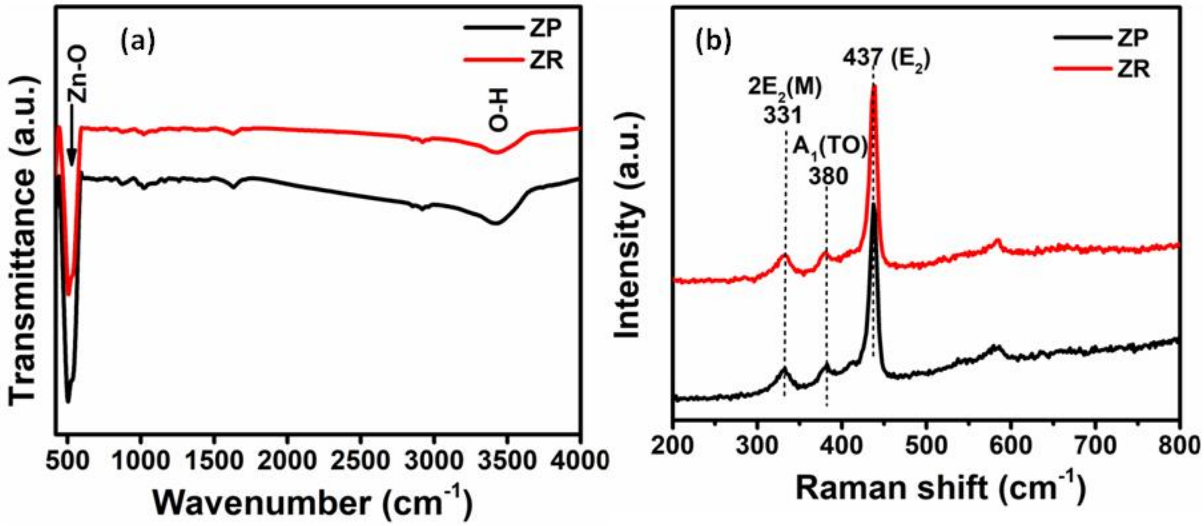

***Fig. 3.1.4 (a)** FTIR spectra, **(b)** Raman spectra of ZnO particle and ZnO nanorods*

Zeta potential study is an important parameter to evaluate the surface electrostatic interaction between ZnO filler and PVDF matrix which is mainly responsible for the formation of β phase nucleation. The surface electrostatic charge of the synthesized nanoparticles and rods as obtained from the zeta potential study is represented in **Fig.3.1.5** which clearly indicated that both the nanofiller i.e. particles and nanorods have negative surface charge on their surface which can interact with the positive –CH_2 dipole of PVDF via local ion-dipole electrostatic interaction. As a consequence, this electrostatic interaction leads to the β phase nucleation within PVDF composites. Thus each nanofiller's surface acts as a nucleation centre for the formation of polar phase [6].

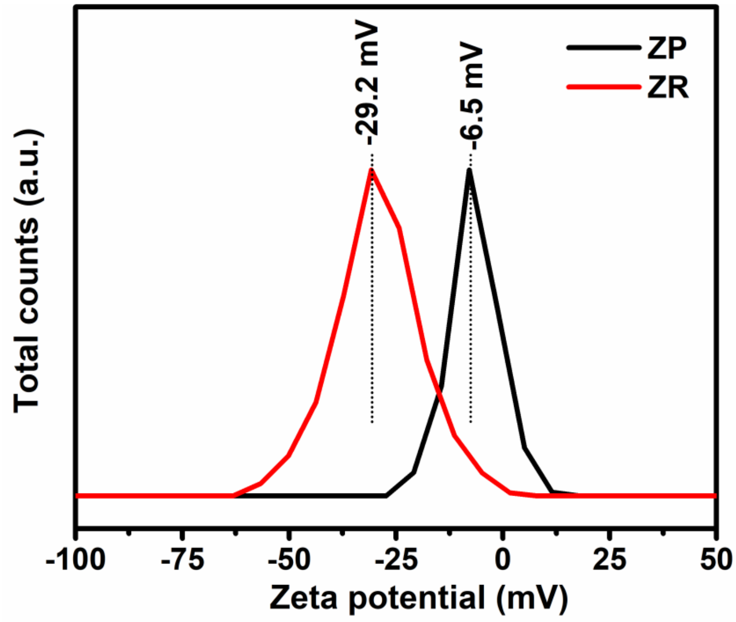

Fig. 3.1.5 *Zeta potential study of ZnO particles and nanorods*

3.1.1.2. Phase analysis of different shaped ZnO nanostructures based PVDF composite films

The presence of electroactive polar phase within PVDF is the prerequisite for the enhancement of dielectric permittivity, ferroelectric and piezoelectric properties of the composites due to the large dipole moment of polar β phase of PVDF. The incorporation of ceramic filler in PVDF matrix leads to the higher amount of β phase formation by modifying the nonpolar α phase [7]. In order to investigate the presence of electroactive polar phase in the neat PVDF and after addition of different morphology of ZnO filler, XRD characterization was carried out. **Fig. 3.1.6(a)** represents the XRD pattern of neat PVDF, ZnO nanoparticles and nanorods impregnated

PVDF nanocomposite films (from each series, the composition which exhibit maximum polar phase is presented here). A closer observation to the **Fig. 3.1.6(a)** reveals the semi crystalline nature of PVDF as well as PVDF/ZnO nanocomposite film. Pure PVDF exhibits peak at 2θ values 18.5° (020), 19.8° (021) and 26.6° [(201), (310)] which are mainly attributed to the non-electroactive α phase of PVDF [8].

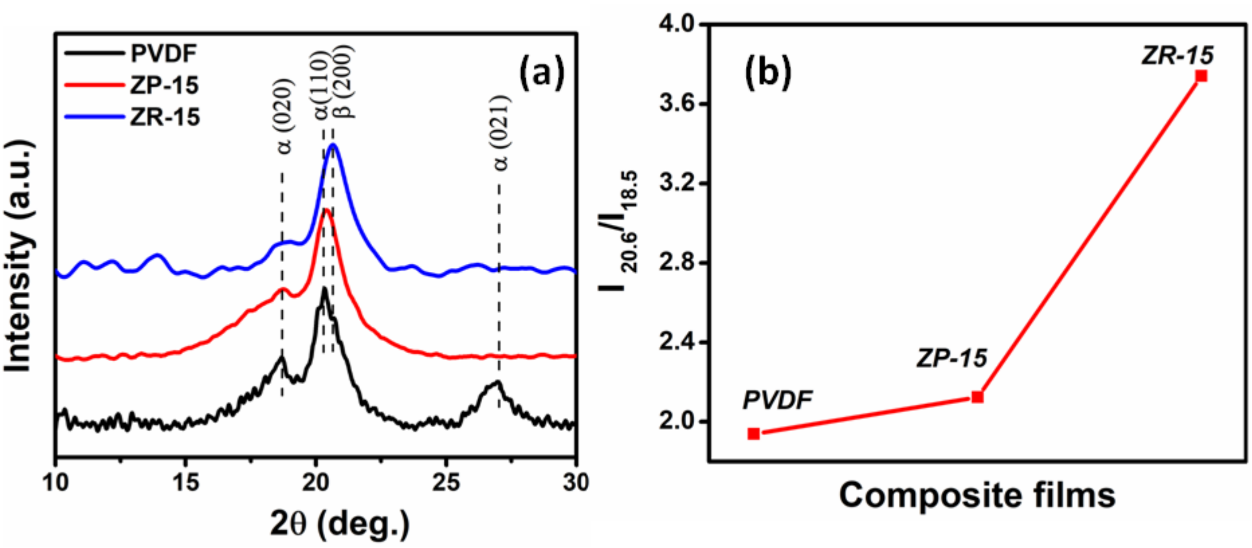

Fig. 3.1.6(a) *XRD pattern of pure PVDF, ZP-15 and ZR-15 composites,* ***(b)*** *Ratio of* $I_{20.6}/I_{18.5}$ *of the PVDF and composites calculated from XRD pattern*

After the incorporation of ZnO nanoparticles in PVDF, the relative intensity of the α phase peak $2\theta=18.5^{\circ}$ is decreased and the peak at $2\theta=26.6^{\circ}$ completely disappeared for ZP-15 composite which may be due to the addition of crystallize ZnO nanoparticles changed the crystallinity of PVDF matrix. On the other hand, for ZnO nanorods incorporated PVDF composite, the main characteristics peak of electroactive polar β phase appeared at $2\theta=20.6^{\circ}$ prominently by diminishing all the nonpolar α phase peak. To have a quantitative idea about β and α phase fraction present within the sample, the filler dependence intensity ratio parameter $I_{20.6^{\circ}}/I_{18.5^{\circ}}$ was calculated from the XRD results (shown in **Fig. 3.1.6(b)**) by taking the intensity ratio of the two peaks at 20.6º (characteristics peak of β phase) and 18.5º (characteristics peak of α phase). The intensity ratio $I_{20.6^\circ}/I_{18.5^\circ}$ was found to be increased to 3.71 for ZnO nanorods incorporated composite (ZR-15) from 1.93 for pure PVDF which indicates the maximum interaction took place between the ZnO nanorods and PVDF matrix. Therefore, XRD result infers that one dimensional rod shaped structure of ZnO can more efficiently nucleate the polar phase in PVDF matrix compared to particle like morphology. This result also indicates that one dimensional ceramic filler can significantly increase the dielectric, ferroelectric and piezoelectric properties of the composites due to the large amount of polar phase formation [8].

A detailed quantitative study of the crystalline phases in terms of local phonon bands of PVDF has been carried out by FTIR spectroscopy. Among the five crystalline phases of PVDF, β phase has polar structure due to all TTTT chain conformation where γ phase has semi polar structure for $T_3G^+T_3G^-$ chain conformation of PVDF [8-10]. As β phase of PVDF is more polar and stable in nature, it is expected to have better piezoelectric properties. In order to investigate more detail study about phase analysis FTIR characterization was carried out. FTIR absorption spectra of pure PVDF, ZnO nanoparticles and nanorods incorporated PVDF composite films are shown in **Fig. 3.1.7(a)** and **Fig. 3.1.7(e)** within the wavenumber region 1000-400 cm^{-1}. In this spectra, pure PVDF exhibits strong absorption peak at 409 cm^{-1}, 488 cm^{-1} (CF_2 wagging), 532 cm^{-1} (CF_2 bending), 615 cm^{-1} and 764 cm^{-1} (CF_2 bending and skeletal bending), 796 cm^{-1}, 856 cm^{-1} and 976 cm^{-1} (CH_2 rocking) which corresponds to nonpolar α phase and weak absorption band 431 cm^{-1} (correspond to polar γ phase), 510 cm^{-1} (CF_2 stretching corresponds to polar β phase) and 840 cm^{-1} (CF_2 stretching, CH_2 stretching and skeletal C-C stretching corresponds to polar β and γ phase [9-10].

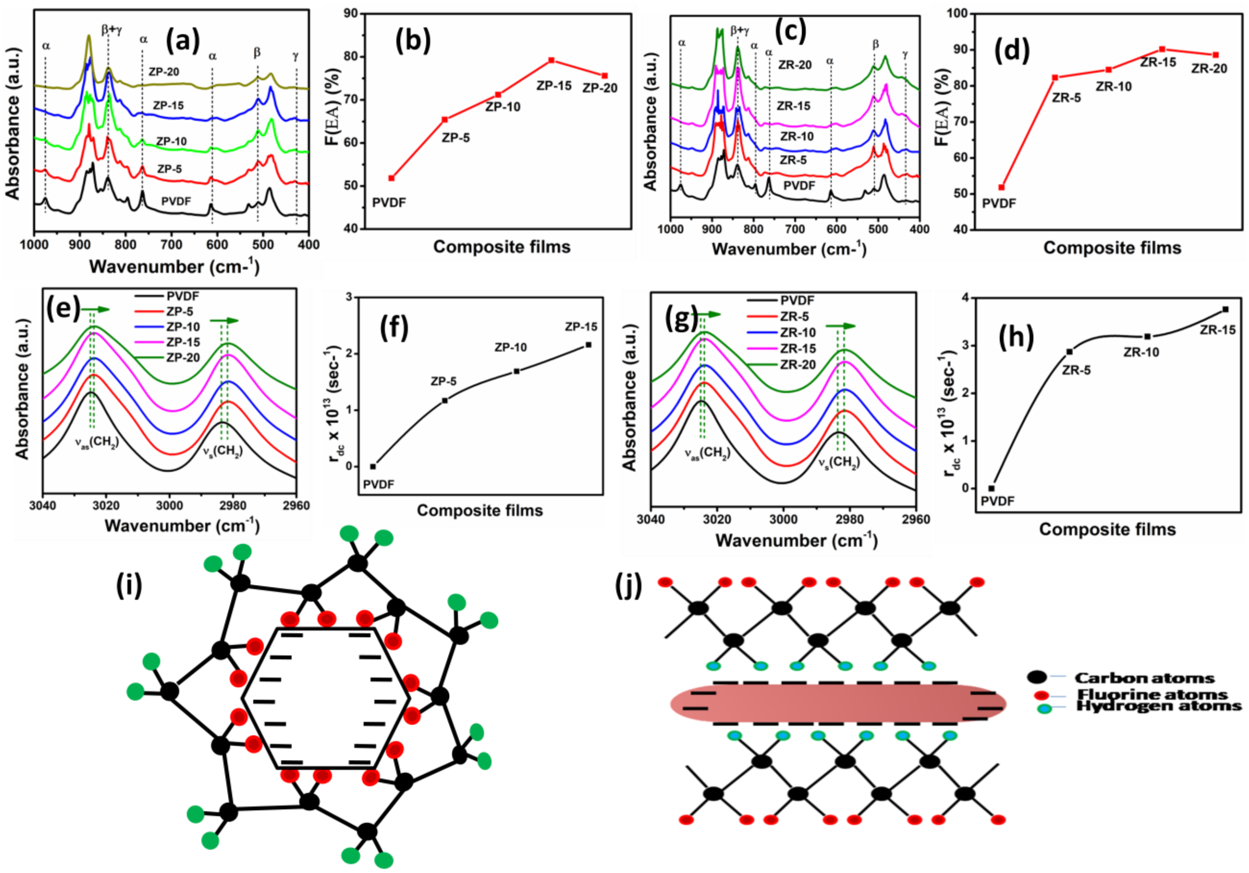

Fig. 3.1.7(a) *FTIR spectra,* ***(b)*** *Polar phase fraction of composite films calculated from FTIR spectra,* ***(c)*** *FTIR stretching vibration band shift and* ***(d)*** *damping co-efficient of pure PVDF, ZP-5, ZP-10 and ZP-15 and ZP-20 composites;* ***(e)*** *FTIR spectra,* ***(f)*** *Polar phase of composite films calculated from FTIR spectra,* ***(g)*** *FTIR stretching vibration band shift and* ***(h)*** *damping co-efficient of pure PVDF, ZR-5, ZR-10 and ZR-15 and ZR-20 composites,* ***(i)*** *schematic of polar phase formation between ZnO particle and PVDF,* ***(j)*** *schematic of polar phase formation between ZnO nanorods and PVDF*

It can be seen from both the figures, the relative intensity of the peaks corresponding to nonpolar α phase decreased with the filler loading and some of the peaks disappeared completely for the both ZnO particle and nanorods incorporated PVDF composites. The intensity of the peaks at

510 cm^{-1} and 840 cm^{-1} increased after incorporation of both type of ZnO filler. Therefore polar β and γ phase of composite films increased compared to pure PVDF which clearly indicates the phase transformation of PVDF from nonpolar phase to polar phase which also supports the XRD study. The quantitative amount of polar phase within each composite films was calculated from Beer-Lambert law as given by **Equation 3.1.1**

$$F(EA)=\frac{A_{EA}}{\left(\frac{K_{840}}{K_{764}}\right)A_{NEA}+A_{EA}} \times 100\ \% \qquad \text{-- ----------------} \ (3.1.1)$$

Where, F(EA), A_{NEA} and A_{EA} represents the amount of electroactive phase fraction, the intensity of the absorbance bands at 764 cm^{-1} and 840 cm^{-1} respectively. K_{840} (=7.7 × 10^4 cm^2 mol^{-1}) and K_{764} (= 6.1× 10^4 cm^2 mol^{-1}) represents the absorption coefficient at 840 cm^{-1} and 764 cm^{-1} respectively [10].

The calculated amount of electroactive polar phase as a function of filler loading for both ZnO nanpoarticles and nanorods incorporated composite films were represented in **Fig. 3.1.7(b)** and **(f),** respectively. The amount of electroactive polar phase was found to be increased with filler loading and reached a maximum value (~79.2%) for ZP-15 composites and beyond this concentration polar phase fraction decreased due to agglomeration of ZnO particle in PVDF composite. In case of ZnO nanorods incorporated PVDF composites, ZR-15 composite containing 15 wt% nanorods exhibited maximum polar phase (~90.9%) and after that it becomes almost saturated. The electroactive polar phase increased to 90.9% for ZR-15 from 63.8% for pure PVDF which indicates rod shape structure was more efficient as nucleating agent for polar phase nucleation compared to particle like morphology which may be due to 'inplane' orientation of one dimensional nanorods in PVDF matrix during the fabrication of composites [11]. The dipoles of PVDF also reorient themselves by interaction between nanofillers and –CH_2

dipole of PVDF. For better interpretation of the interfacial interaction, FTIR spectra of all samples within the wavenumber region 3100 cm^{-1} to 2900 cm^{-1} were studied because this region mainly attributed for symmetric (ν_s) and asymmetric (ν_{as}) stretching vibration band of $–CH_2$ dipole which are not coupled with any other vibrational modes. Therefore the absorption spectra within this region provide detailed information about the interfacial interaction between $–CH_2$ dipole of PVDF and nanofiller surface [10, 12]. The FTIR absorption spectra of PVDF and ZnO nanoparicles and nanorods impregnated composite films were shown in **Fig 3.1.7(c)** and **(g)**, respectively within the wave number region 3100-2900 cm^{-1}. A closer observation to both the figures reveals that, after incorporation of ceramic filler in PVDF matrix, symmetric and asymmetric stretching vibrational band of $–CH_2$ dipole shifts towards lower wavenumber region compared to pure PVDF. This gradual shift of vibrational bands towards lower energy can be explained by damped harmonic oscillator model. At first, it was assumed that these two vibration bands have no damping when no filler was included in PVDF matrix. With filler loading in PVDF matrix damping will arise due to electrostatic interaction between $–CH_2$ dipole of PVDF and filler surface. Now when ZnO fillers were incorporated into PVDF matrix interfacial interaction occurs which resulted in the peak shifting towards lower energy region. In order to get the quantitative amount of electrostatic interaction, damping coefficient of the composite films was calculated from the peak shifting of the asymmetric $–CH_2$ stretching vibrational band using following **Equation 3.1.2**

$$r_{dc} = 4\pi C(\bar{\upsilon}_{PVDF}^2 - \bar{\upsilon}_{COMP}^2)^{1/2} \text{ ------------------------(3.1.2)}$$

where r_{dc} represents damping coefficient, C indicates the velocity of light in free space, $\bar{\upsilon}_{PVDF}$ and $\bar{\upsilon}_{COMP}$ represent the peak position of asymmetric $–CH_2$ stretching vibrational band of pure PVDF and composites, respectively [13]. Damping coefficient of PVDF, both ZnO particles and nanorods incorporated composite films were shown in **Fig. 3.1.7 (d)** and **(f),** respectively**.** It was observed that the damping coefficient increases with filler loading for both type of fillers. Damping coefficient value was maximum for ZR-15 composites due to the maximum interfacial interaction between ZnO nanorods and PVDF matrix. Therefore, XRD and FTIR study confirmed the existence of maximum polar phase in ZR-15 composite film.

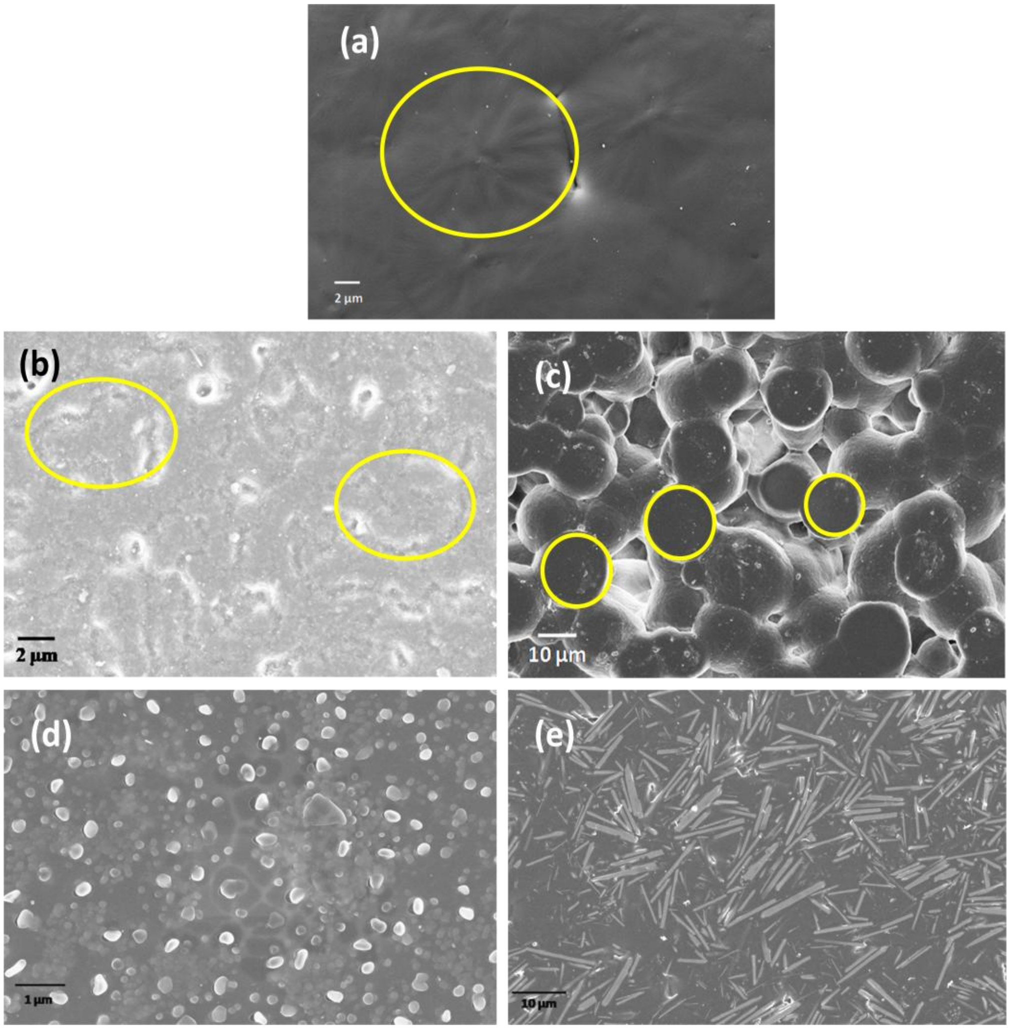

Fig. 3.1.8 *FESEM image of* ***(a)*** *pure PVDF,* ***(b)*** *ZP-15 (upper surface) and* ***(c)*** *ZR-15 (upper surface),* ***(d)*** *ZnO particle embedded in PVDF matrix (lower surface),* ***(e)*** *ZnO nanorods embedded in PVDF (lower surface)*

FESEM image of pure PVDF (**Fig. 3.1.8(a)**) shows the highly compact uniform microstructure without formation any crack. The fibril like morphology as observed in FESEM micrograph of PVDF is absent for the composite, which indicates the predominant presence of α spherulite structure of PVDF [12, 14]. The presence of large spherulite having an average diameter ~ 14 μm is observed in FESEM micrograph of PVDF. On the other hand, the spherulite size decreases for the ZP-15 and ZR-15 composite as observed in **Fig. 3.1.8(b)** and **(c),** respectively (as ZP-15 and ZR-15 composite films exhibited maximum polar phase in the series, FESEM study only these two composite film were carried out)**.** The absence of fibril like structure in nanocomposite indicates the formation of β phase within the composite. The reduction of spherulite size for both the composite films compared to pure PVDF indicates the faster nucleation process which may be due to the additional no of nucleation centre present within the composites [12]. In addition, for the ZR-15 composite (**Fig. 3.1.8(c)**), spherulites are uniformly distributed within the composites which indicate that uniform dispersion of filler within PVDF matrix. Also, the presence of commom boundary between the spherulites reveals the faster nucleation process within the ZR-15 composite. **Fig. 3.1.8(d)** represents the lower surface of ZP-15 composites which infers the successful incorporation of nanoparticles within PVDF matrix. ZnO nanorods are uniformly dispersed and well embedded in PVDF matrix which is also confirmed by the FESEM micrograph (shown in **Fig. 3.1.8(e)**).

3.1.1.3 Dielectric properties

Frequency dependent dielectric permittivity and dielectric loss of both type composites were investigated as a function of ZnO nanoparticles and nanorods filler loading within the PVDF matrix at room temperature and ambient pressure over the frequency range 100 Hz to 1 MHz. **Fig. 3.1.9(a)** and (**c)** represent the frequency dependent dielectric constant and dielectric loss of

ZnO nanoparticles impregnated PVDF composites, respectively. A similar type of frequency dependent dielectric constant and loss of ZnO nanorods incorporated PVDF composites are shown in **Fig. 3.1.9(b)** and **(d),** respectively.

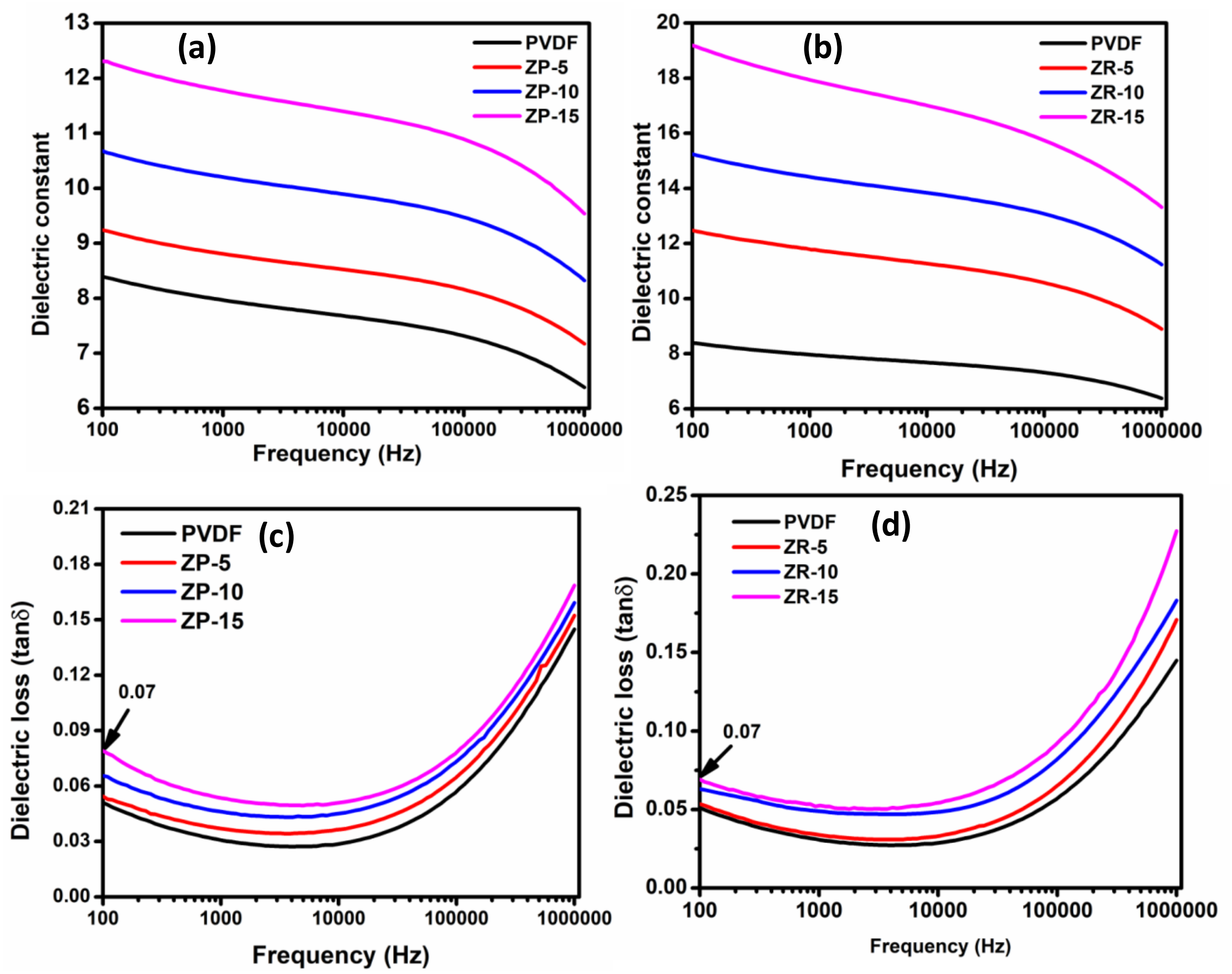

Fig. 3.1.9 (a-b) *frequency dependent dielectric permittivity and* ***(c-d)*** *dielectric loss of pure PVDF and all composite films*

All the sample shows similar type of response. Both the figures reveal that, dielectric permittivity decreases at high frequency which can be attributed due to the reduction of no of aligned dipole per unit volume with increasing frequency [15-16]. When the frequency of electric field is low,

($\omega\eta$≪1 where η is the relaxation time), the dipoles can follow the field, but with the increase of frequency of electric field, the dipoles begin to lag behind the field. As a result, dielectric constant value decreased gradually upto the characteristics value ($\omega\eta$=1). At high frequency (when $\omega\eta$>>1), the dipoles find themselves unable to follow the field and dielectric constant decreases significantly [15]. Dielectric constant value was found to be increased with filler loading and it reaches a maximum value ~ 18 for ZR-15 containing 15 wt% ZnO from a value ~ 8 for neat PVDF which can be attributed due to Maxwell-Wager-Siller interfacial polarization effect [15-16]. With the application of electric field, space charge accumulation and short range dipole-dipole interaction occur at the interface between the filler and PVDF matrix which leads to the higher value of dielectric constant at low frequency region. On the other hand, the enhancement of dielectric permittivity in the high frequency region may be due to the enhanced dipolar polarization. This enhancement of dipolar polarization can be explained by the interfacial interaction between filler and PVDF matrix. For ZnO nanorods incorporated PVDF system, dielectric value increased significantly compared to particle morpholgy due to the easily formation of conductive pathway in composite which reduces the internal resistance of the PVDF matrix. Therefore, for fabrication of high dielectric composites, incorporation of rod shape structure in PVDF matrix is the best choice compared to particle morphology. Dielectric loss of pure PVDF and all the composite system was shown in **Fig. 3.1.9(c-d)**. It was observed (**Fig. 3.1.9(c-d)**) that dielectric loss of PVDF also increased with increasing both type of filler concentration. This increased dielectric loss in the low frequency region was due to enhanced conductive network formation of PVDF after filler loading and the dielectric loss in the high frequency was due to the effect of enhanced interfacial interaction –CH_2 dipole of PVDF with the filler surface. The movement of PVDF dipole may enhance the dielectric loss. When no fillers were included in PVDF matrix, there was no restriction in the movement of polymer chains. But with increasing filler loading in PVDF matrix, interfacial interaction gradually increases which hindered the polymer chain movement, thus resulting reduction of dielectric loss. In the low frequency region, dielectric loss of composite films gradually increased mainly due to the space charge polarization. But in the high frequency region, space charge polarization disappeared. Therefore loss value increased due to the enhanced interfacial interaction of PVDF dipoles with filler surface, which was unable to follow up high frequency. The dielectric loss value of all the composites were found to be very low (<0.1 up to 100 kHz and < 0.25 up to 1 MHz) in the entire frequency region which can be considered as a good material for application purpose [17].

3.1.1.4 Ferroelectric Properties of composite film:

Ferroelectric property completely depends on the electroactive polar phases presence within the PVDF which are mainly responsible for the piezoelectric behaviour of the material. Among the five crystalline α, β, γ, δ and ε phases of PVDF, β and γ phases exhibit ferroelectric behaviour due to their non-zero dipole moment in their respective TTTT and $T_3G^+T_3G^-$ chain orientation. Ferroelectric domains composed of molecular dipoles are randomly oriented within the polymer matrix. In PVDF nanocomposites, remnant polarization occurred due to the molecular dipole orientation. With filler loading, the molecular dipoles are oriented in a preferred orientation which is due to the interaction between the filler materials and PVDF dipoles. As a result, material exhibit ferroelectric as well as piezoelectric properties. Hysteresis loop measures the change in polarization with the application of electric field which is generated by the acceleration of the internal charge within the PVDF nancomposite [9]. As a consequence, phase separation is observed between the voltage and charge due to energy dissipation of the PVDF nanocomposites. As a result, a loop with definite area is formed indicating the charge storage capacity of the material. The variation of electric field dependent electric displacement (D-E) or polarization (P-E) loops as a function of different ZnO filler loading in PVDF for both the system was shown in Fig. **3.1.10(a-b).**

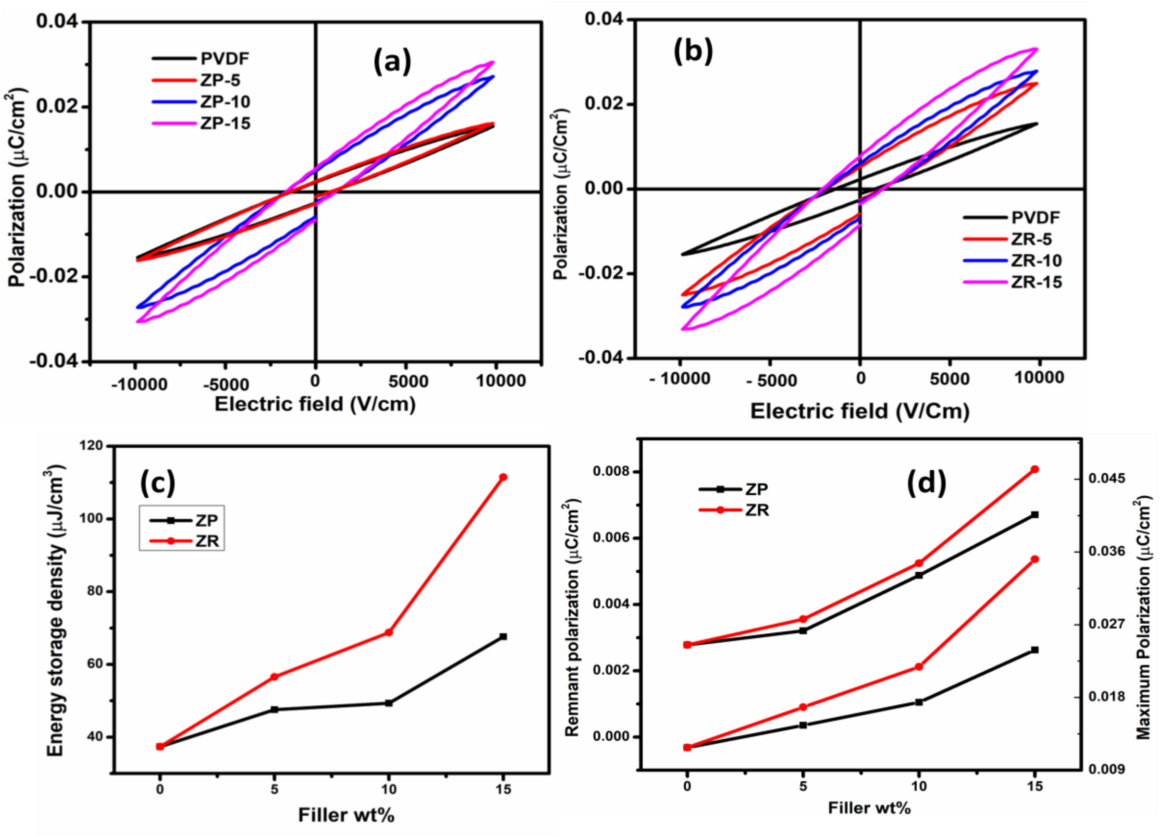

__Fig. 3.1.10 (a)__Electric displacement vs applied electric field (D-E) loop of (a)ZP-PVDF composites, __(b)__ ZR-PVDF composites; __(c)__Variation of energy storage density of nanocomposites with different wt % of ZnO filler,__(d)__ comparison of D_{max} of the nanocomposites with different wt% of ZnO filler,

The polarization increases gradually with the applied electric field which indicates that the orientation of the molecular dipoles have taken place along the field direction. A maximum polarization value of 0.018 μC/cm^2 was obtained from ZR-15 at an applied electric field

100kV/cm. To have a detailed study about the ferroelectric loops, the filler concentration dependent maximum electric displacement (D_m) of the pure PVDF and all composite films were presented in **Fig. 3.1.10(d)**) under same applied electric field. From this figure, it is clearly evident the Dm values were comparatively higher for ZnO rod shaped PVDF composites compared to other structure which was due to easier formation of conduction pathway in the composites. This result confirmed the enhancement of ferroelectric properties of the composites .This enhancement of ferroelectric properties was due to the strong interfacial interaction between PVDF matrix and ZnO filler. The enhanced interfacial interaction leads to an enhancement of polar phase within the composites which increases the ferroelectric property. On the other hand, the leakage current of the composites also increases due to the formation of more conducting network with increased filler loading [13]. This increased leakage current after being added with real displacement current leads to an enhancement of remnant and maximum electric displacement. Thus the ferroelectric property of the samples gets enhanced due to the above factor.

The energy storage density (U_{stored}) of the fabricated composites were calculated from D-E loops using an integral formula given in **Equation 3.1.3.**

$$U_{stored}=\int_{D_r}^{D_m} EdD \text{-----------------------} \quad (3.1.3)$$

Fig. 3.1.10(c) presents the filler concentration dependent energy storage density of pure PVDF and ZnO particle and nanorods incorporated composite films. For both the system, the stored energy density increased with increasing filler concentration and stored energy density value increased to161.32 $\mu J/cm^3$ for ZR-15 from a value 40.1 $\mu J/cm^3$ for pure PVDF and hence there was an increment of energy storage density by 17% which may be due to maximum dielectric constant and D_m of the ZR-15 composite. Therefore, ZR-15 sample may be used for energy storage application purpose.

3.1.1.5. Energy harvesting performance of PVDF and composites

To investigate the efficiency of the composite films as an efficient mechanical energy harvesting device , the voltage generation capacity of the fabricated composite films, under compressing and releasing process of finger imparting on them were observed (Pressure~4 kPa, Frequency ~5 Hz). As ZnO nanorods incorporated composite films exhibited maximum polar phase as well as dielectric and ferroelectric properties compared to particle incorporated PVDF system, energy harvesting properties only of this system were carried out.

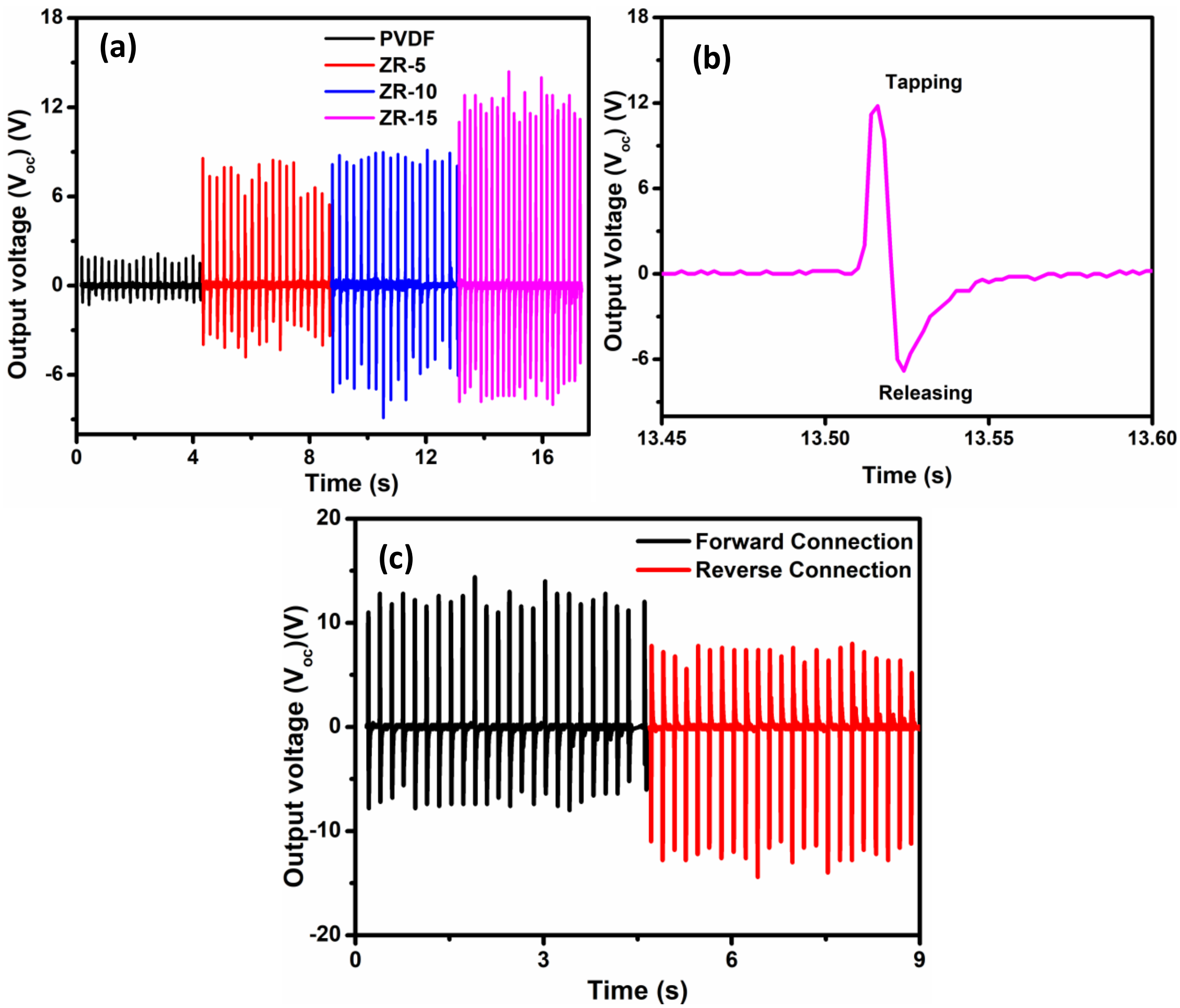

Fig. 3.1.11 *Comparison of open circuit output a.c. voltage of* ***(a)*** *PVDF, ZR-5, ZR-10 and ZR-15, nanocomposites,****(b)****Magnified image of one output pulse,* ***(c)*** *switching polarity test of ZR-15 composite*

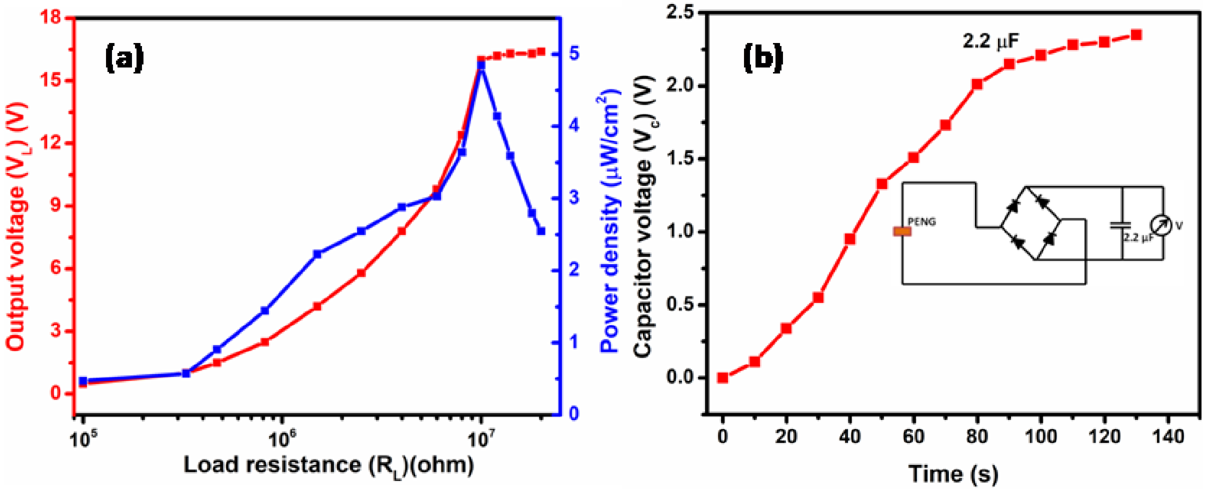

***Fig. 3.1.12 (a)** Variation of output voltage and power density as a function of load resistance, ZR-15 composites, **(b)** Charging of 2.2 µF capacitor*

Fig. 3.1.11(a) represents the open-circuit a.c. output voltage of PVDF and ZR-5, ZR-10 and ZR-15 composite film. The maximum open circuit a.c. output voltage of ZR-15 film was ~18 V which was due to its maximum polar phase formation in the system. It is evident from the XRD and FTIR results that the addition of high aspect ratio filler enhances the β-phase of PVDF and maximum β- crystalline phase present in the ZR-15 nanocomposites which can be attributed due to the strong interaction between the oppositely charged ZnO surface and the -CH_2-dipoles of PVDF. This enhances the nucleation of polar β-phase by surface charge induced polarization. In addition, by an application of mechanical force, the crystal structures of the PVDF composites were deformed and the external pressure creates a potential difference within composite, which aligns the dipoles in the PVDF matrix. Magnified image of an output pulse is presented in **Fig. 3.1.11(b)** where the peak related to the tapping and releasing motion of finger imparting was indexed. In order to check that the output voltage arises from piezoelectricity or not, switching polarity test of ZR-15 (as it exhibits maximum voltage in the series) composite was done by reversing the electrodes connection. Almost same voltage was obtained after reversing the electrode connection (shown in **Fig. 3.1.11(c)**) which confirmed that the output voltage was obtained from the piezoelectric effect and not from any other source. The output voltages are almost same both in forward and reverse connection with opposite polarity. Thus the origin of electrical signals are solely from the piezoelectric effect [18].

The generated a.c. output voltage of ZR-15 composite was converted to d.c. output voltage using a bridge rectifier IC (DB 107). This rectified d.c. voltage was able to charge a 2.2 μF capacitor up to ~ 2.3 V was represented in **Fig. 3.1.12(a)**. The output voltage vs. load resistance graph of ZR-15 composite film is shown in **Fig. 3.1.12(b)**. The output voltage was gradually increased with load resistance and reached a saturation value at 10 MΩ. The power density (P) was calculated from the output voltage (V_L) through different load resistance (R_L) by using the **Equation 3.1.4** given below [19].

$$P = \frac{1}{A}\frac{V_L^2}{R_L} \text{----------------------} \qquad (3.1.4)$$

where A is the area of the composite film. The maximum power density of ZR-15 composite film was found to be ~4.6 μW cm^{-2} at 10 MΩ load resistance (shown in **Fig. 3.1.12(b)**).

For real life applications, the fabricated ZR-15 film was integrated to a health data glove (as shown in **Fig.3.1.13**) for right hand to monitor the minute finger movements. The recorded signal was presented in **Fig. 3.1.13(a)** and **(b)** which were generated by the stretching and bending motion of index and middle finger, respectively. It can be seen from the figures that the e-skin can distinctly sense and precisely detect the fine motion of index and middle finger. These well recognizable single patterns, arise due to the movement of individual finger may be used for tracking the movement of body parts of bedridden patients and controlling the hand of surgical robot [20-22].

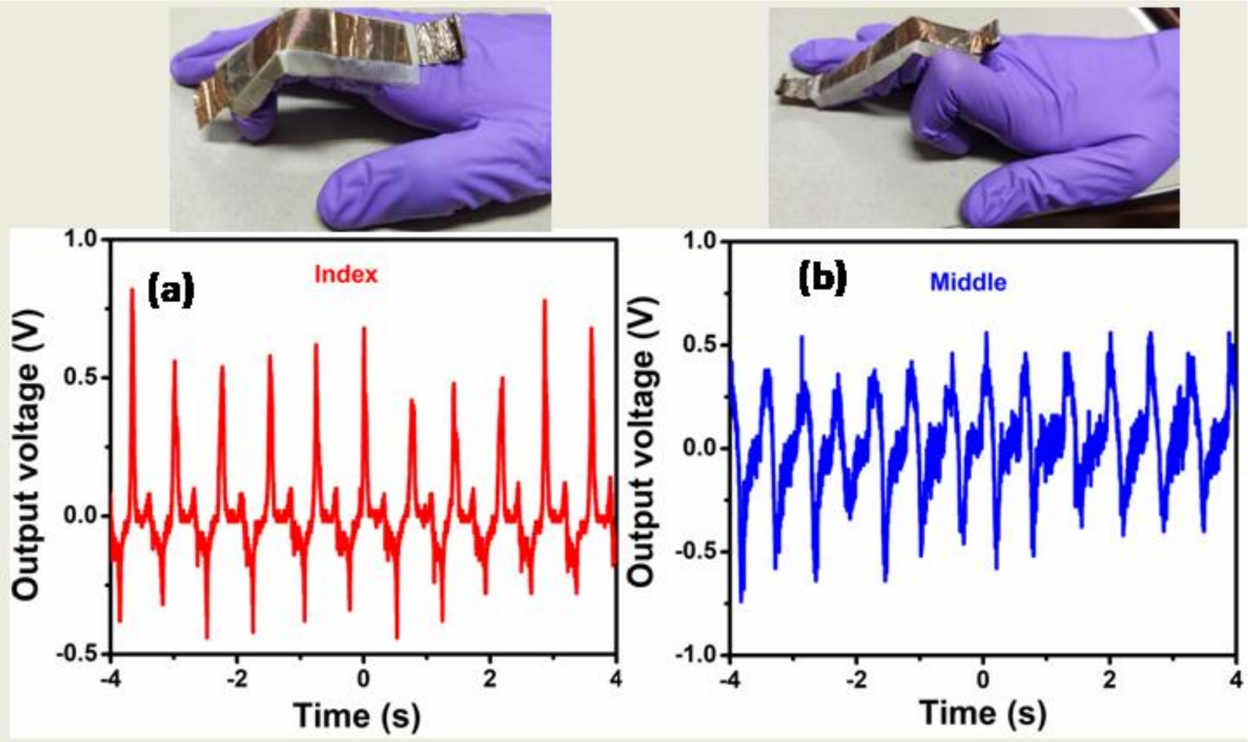

Fig. 3.1.13 *Voltage generation by the stretching and bending motion of the* ***(a)*** *index,* ***(b)*** *middle finger*

On the other hand, ZR-15 composite film can be used as a mechanosensor to demonstrate the precise detection of different static mechanical pressures. As a consequence, this mechanosensor was used in passive mode to detect the static pressure stimuli. In the passive mode, with the application of external mechanical stimuli (0.12-1.032 kPa) on the mechanosensor (area ~2.5 cm × 2.1 cm) leads to a change in capacitance and impedance values depending on the static mechanical pressures. A closer observation to the **Fig. 3.1.14 (a-b)** reveals that with increasing static pressure the capacitance of the mechanosensor increases (**Fig. 3.1.14(a)**), and simultaneously, the impedance of the sensor decreases (**Fig.3.1.14(b)**). **Fig. 3.1.14(c)** exhibits the almost linear variation in capacitance and impedance with the applied static mechanical pressure indicating the ability of the device as a linear sensor for detection of low to medium range mechanical pressure. Depending on the change in capacitance with the application of the static mechanical pressure, The static pressure sensitivity (S) of the device can be calculated using the relation $S = (\Delta C/C_0)/\Delta P$, where ΔC is the change of capacitance, C_0 is the initial capacitance, and ΔP are the change in capacitance, change in applied pressure values, respectively. The obtained static pressure sensitivity value of the device is 19.28 MPa^{-1}. The mechanosensor can reliably detect a ultra small weight which caused a noticable change in capacitance. Even a small increase in applied pressure can significantly changes the capacitance value of the mechanosensor can be assigned due to the reduction of distance between two electrodes leads to a polymer composite film of adequate flexibility and high dielectric constant. Additionally, the reduction of intraparticle distance (ZR-15) in the PVDF matrix easily creates a conductive pathway in the medium which leads to an increase of dielectric constant of the nanocomposite and thus leading to a significant increase in the capacitance value with a small change in the applied pressure. The current−voltage (I−V) curves of the mechanosensor was shown in **Fig. 3.1.14(d)**. A closer observation to this figure reveals that electrical current increases with an applied static mechanical pressure in the range of 0−0.62 kPa, which indicates that the mechanosensor can successfully detect the static mechanical pressure through the I−V characteristics [8, 16].

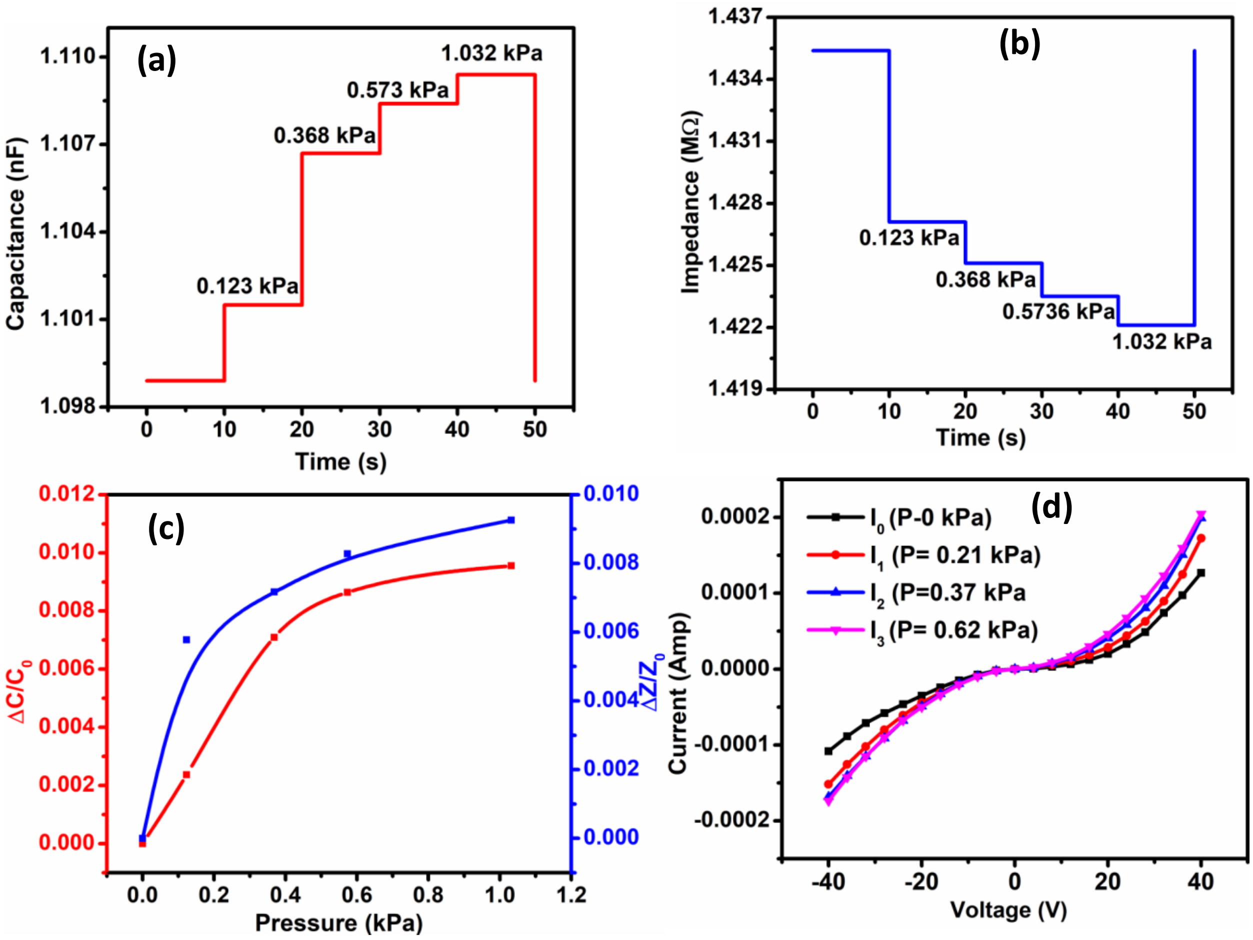

***Fig. 3.1.14** Real time monitoring of variable static pressure stimuli, **(a)** measurement of capacitance and **(b)** impedance of ZR-10 mechanosensor; **(c)** Linear variation of capacitance and impedance values of the mechanosensor with the change of static pressure, **(d)** Current-Voltage plot (I-V) of the mechanosensor under different static pressure in the range of 0-0.62kPa.*

3.1.1.6. Conclusion

The effect of morphology of ZnO nanofillers on the polar phase nucleation and electrical properties of PVDF was investigated. As a consequenc, two forms of ZnO nanostructures i.e. particles and rods were synthesized via wet chemical and hydrothermal method and incorporated in the PVDF matrix, respectively with varying filler concentration. ZnO filler having rod shape structure was found to be more effective in enhancing the dielectric, ferroelectric, energy storage and energy harvesting performance of their PVDF based composite films compared to particle like structure. This result may be due to the stronger electrostatic interaction for ZnO rods compared to particle which was due to the 'in plane' orientation of ZnO rods during solvent casting. Therefore, it may be concluded that the tailored electrical properties and output piezo-response of composites can be tuned by controlling the morphology of the nanofiller, which provides a new approach of fabricating polymer nanocomposites for application in both energy storage and harvesting devices.

References:

1. G. Chen, W.L. Yang, J. Lin, X. Wang, D.P. Li, Y. Wang, M.F. Liang, W.M. Ding, H. D. Li, Q. Q. Lei, *J. Mater. Chem. C.*, **5**, 2017, 8135-8143.
2. F. Deng, Q. S. Zheng, L.F. Wang, C.W. Nan, *Appl. Phys. Lett.*,**90**, 2007, 021914-021916.
3. S. H. Yao, Z. M. Dang, M. J. Jiang, H. P. Xu, *Appl. Phys. Lett.*,**91**, 2007, 212901-212903.
4. J. Kaur , H. Singh, *Ceramics International* ., 2020, **46**, 19401–19407.
5. A. K. Bhunia, P. K. Jha, D. Rout and S. Saha, *Journal of Physical Sciences*., 2016, **21**, 111-118.
6. H. Parangusan, D. Ponnamma, M. A. A. Al-Maadeed, *ACS Omega*., 2019, **4**,4, 6312–6323.
7. S. K. Karan , D. Mandal , B. B. Khatua , *Nanoscale*., 2015 ,7 , 10655 .
8. E. Kar , N. Bose, B. Dutta , S. Banerjee, N. Mukherjee, S. Mukherjee, *Energy Conversion and Management*., 2019,**184,** 600–608.
9. S. Ojha, S. Paria, S. K. Karan, S. K. Si, A. Maitra, A. K. Das, L. Halder, A. Bera, A. De and B. B. Khatua, *Nanoscale*., 2019, **11**, 22989.

10. A. Sasmal, S. Sen, P.S. Devi. *Phys. Chem. Chem. Phys*., 2019, **21**, 5974.

11. I. Chinya, A. Sasmal, A. Pal and S. Sen, *Cryst. Eng. Comm.*, 2019, **21**, 3478.

12. E. Kar, N. Bose, B. Dutta, N. Mukherjee, S. Mukherjee. *ACS Appl. Nano Mater*., 2013,**7,** 10424.

13. A. Sasmal, P.S. Devi, S. Sen, *Soft Matter.***,** 2020,**16**,8492-8505.

14. D. Mandal, K. J. Kim, J. S. Lee, *Langmuir*., 2012, **28**, 10310.

15. E. Kar, N. Bose, S. Das, N. Mukherjee, S. Mukherjee, *Phys.Chem.Chem.Phys*., 2015, **17**, 22784

16. B. Dutta, E. Kar, N. Bose , and S. Mukherjee, *ACS Sustainable Chem. Eng.,* 2018, 6, **8**, 10505–10516.

17. A. Sasmal, S. K. Medda. P. S. Devi and S. Sen, *Nanoscale*., 2020, **12**, 20908-20921.

18. T. K. Sinha, S. K. Ghosh, R. Maiti, S. Jana, B. Adhikari, D. Mandal, S. K. Ray, *ACS Appl. Mater. Interfaces*., 2016, **8**, 14986.

19. E. Kar, N. Bose, B. Dutta, N. Mukherjee, and S. Mukherjee, *ACS Appl. Mater. Interfaces .,* 2019, **11**, 17501−17512.

20. S. K. Ghosh et al. Nano Energy., 2017, **36**, 166.

21. T. Q. Trung, N. E. Lee, *Adv. Mater*., 2016, **28**, 4338.

22. L. Wanga et al. *Nano Energy*., 2017, **36**, 38.

3.2: Study the effect of different aspect ratio ZnO filler in PVDF matrix and electrical performance of their PVDF based nanocomposites:

3.2.1. Introduction

In our previous study, two different morphology of ZnO structures were used as fillers in PVDF among which rod shaped structure exhibit the best performance in improving the electrical properties of the composite system. Therefore we choose 1D rod shaped structure as a filler material in PVDF for further investigation. Aspect ratio of filler also plays a crucial role to study the electrical properties of polymer based composite system [1]. Several research works already demonstrated that the piezoelectric output performance can be enhanced by appropriate tuning of aspect ratio [2-4].

Here, we investigated the effect of filler aspect ratio on the electrical properties of ZnO incorporated poly(vinylidene fluoride) (PVDF) matrix. ZnO nanorods having different aspect ratio were synthesized by hydrothermal technique with varying reaction time 4h to 20h at a fixed temperature and PVDF based nanocomposites of the respective ZnO nanorods with different wt% filler loading were fabricated. As-synthesized ZnO nanorods were designated as ZnO-4(for reaction time 4h), ZnO-8 (for reaction time 8 h) and ZnO-20 (for reaction time 20 h) respectively. Then, to obtain different series (PVDF/ZnO-4, PVDF/ZnO-8 and PVDF/ZnO-20) composite films 5wt%, 10wt%, 15wt% powder of each sample with respect to PVDF were then added to the PVDF solution. A pure PVDF film was also fabricated for comparison purpose. The effect of different aspect ratio of filler on the dielectric, ferroelectric, energy storage and mechanical energy harvesting performance of its PVDF based composites is studied throughout the present work.

3.2.1.1. Characterization of filler particle

X-Ray Diffraction study was performed to investigate the phase of synthesized ZnO nanorods grown at different reaction times (4h, 8h and 20h). XRD patterns of as-synthesized samples are shown in **Fig. 3.2.1a.** All the diffraction peaks matched well with standard powder diffraction data of ZnO (JCPDS card number #79-0205).There is no additional peak present in the XRD patterns which indicates thatpure hexagonal structure phase of ZnO is formed. Average crystallite sizes (L) of the sample were calculated using Debye-Scherrer formula [5]. Average crystallize size of samples were 41, 43 and 47 nm for reaction time respectively which indicates that crystallite size increases with increasing reaction time.

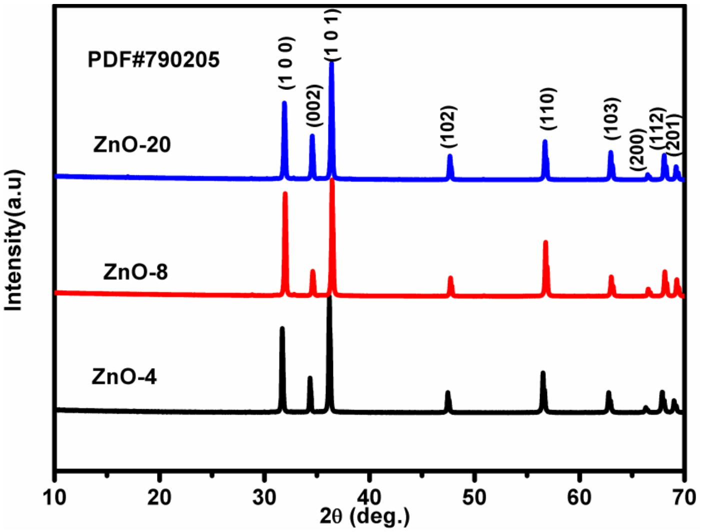

Fig.3.2.1 *XRD patterns of ZnO-4, ZnO-8 and ZnO-20 nanorods*

To have morphological idea about synthesized nanorods, FESEM characterization was carried out. Qiu et al. demonstrates that growth time is an important parameter which determines both morphology and aspect ratio of ZnO nanorods [1]. **Fig. 3.2.2(a-c)** represents the FESEM images of the synthesized ZnO-4, ZnO-8 and ZnO-20 nanorods, respectively. From FESEM images we observed that the length of synthesized ZnO nanorods increased with increasing hydrothermal reaction time. To calculate average length and diameter of synthesized nanorodswe used ImageJ software.

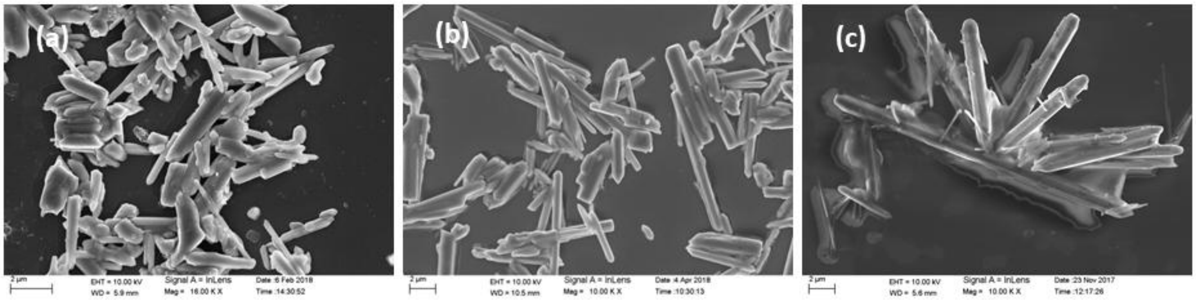

Fig. 3.2.2 *FESEM images of* ***(a)*** *ZnO-4 nanorods,* ***(b)*** *ZnO-8 nanorods,* ***(c)*** *ZnO-20 nanorods*

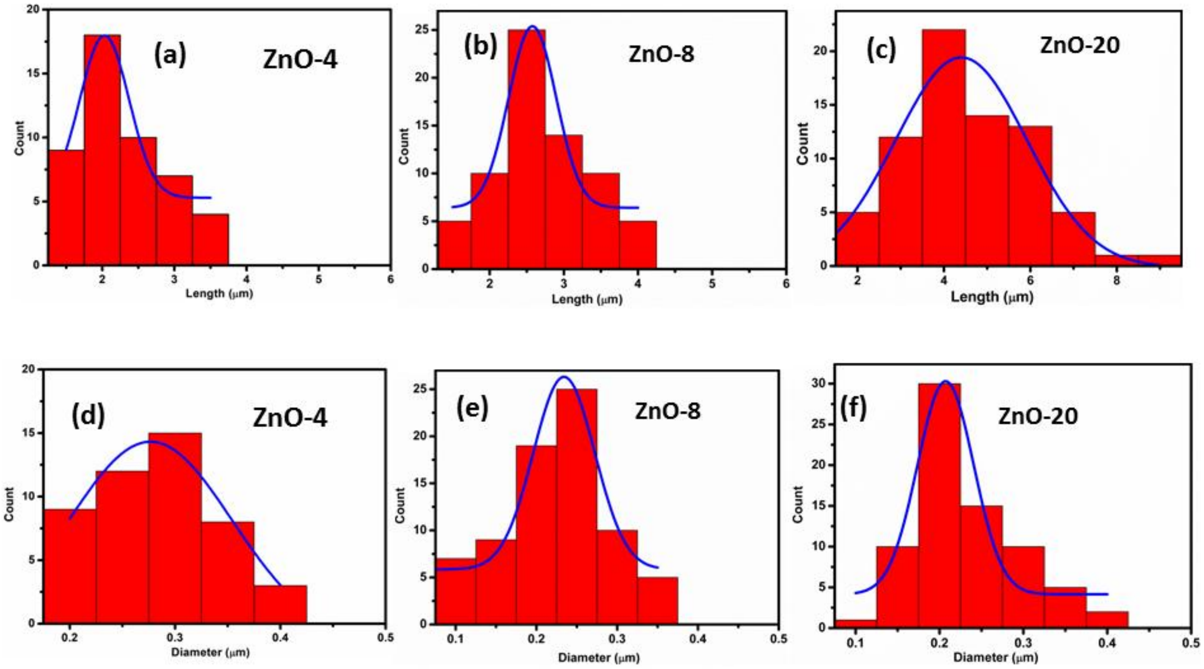

Fig. 3.2.3 *ZnO nanorods size distribution: length distribution of* ***(a)*** *ZnO-4 nanorods,* ***(b)*** *ZnO-8 nanorods,* ***(c)*** *ZnO-20 nanorods; diameter distribution of* ***(d)*** *ZnO-4 nanorods,* ***(e)*** *ZnO-8 nanorods,* ***(f)*** *ZnO-20 nanorods*

The length and diameter distribution of ZnO-4, ZnO-8 and ZnO-20 samples are shown in **Fig. 3.2.3(a-f)**. It is found that the calculated average diameter and length of ZnO-4, ZnO-8 and ZnO-

20 nanorods are 275 nm, 220 nm, 175 nm and 2µm, 2.3 µm, 4.7 µm respectively. The calculated aspect ratios of ZnO-4, ZnO-8 and ZnO-20 nanorods are found to be 7.2, 10.4 and 26.8 respectively which indicated a direct correlation between the reaction time and aspect ratio of fabricated rods. Well-aligned uniform microstructure was observed for high aspect ratio ZnO-20 nanorods [1].

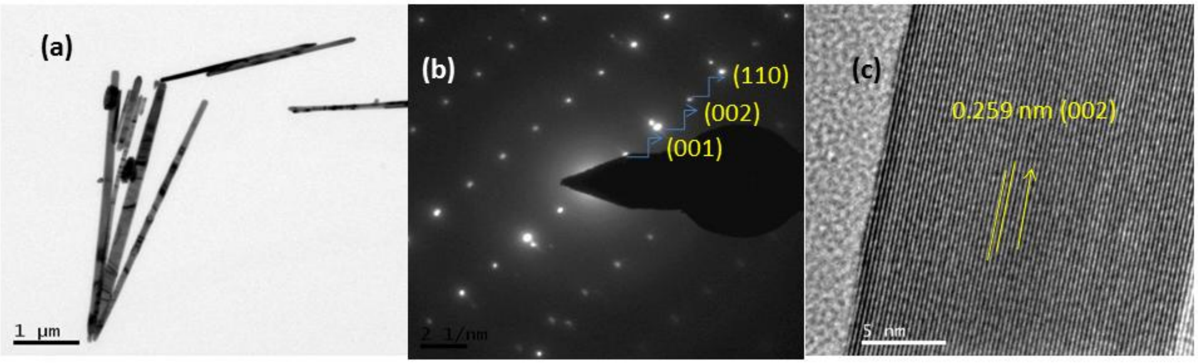

Fig. 3.2.4 ***(a)*** *TEM images,* ***(b)*** *SAED pattern,* ***(c)*** *HRTEM images of ZnO-20 nanorods.*

Fig. 3.2.4(a) represents bright field TEM image of ZnO-20 nanorods which further indicated the uniform microstructure of synthesized rods. The selected area electron diffraction (SAED) pattern of ZnO-20 samples is shown in **Fig. 3.2.4(b)**.The planes indexed in SAED pattern matched well with XRD database and confirmed the crystallinity of nanorods. HRTEM study of ZnO-20 (shown in **Fig. 3.2. 4(c)**) further confirmed the good crystallinity of the nanorods.

Zeta potential study was carried out to understand the surface electrostatic interaction between ZnO filler and PVDF matrix [5]. **Fig. 3.2.5** represents the zeta potential study of ZnO-4, ZnO-8 and ZnO-20 nanorods which confirmed that ZnO filler has negative surface charge on its surface. This negative surface charge interacts with the $-CH_2$ dipole of PVDF. It was also observed that ZnO-20 nanorods have more negative surface charge located on its surface.

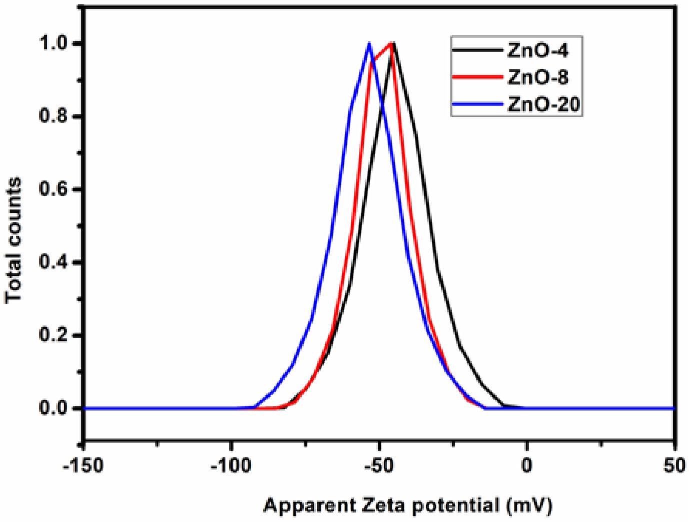

Fig. 3.2.5 *Zeta potential study of ZnO-4, ZnO-8 and ZnO-20 nanorods.*

3.2.1.2. Phase analysis of PVDF nanocomposites

The XRD study is carried out to investigate the polar phase formation in the PVDF based composite system. **Fig. 3.2.6(a)** represents the XRD pattern of pure PVDF, PVDF/ZnO-4, PVDF/ZnO-8 and PVDF/ZnO-20 composite films. In pure PVDF, XRD pattern peaks observed at 2θ=17.7º, 18.4º, 19.6ºand 26.6º corresponding to (100), (020), (110) and (021) planes respectively which is basically due to the the non-polar α phase [6-7] as already discussed in previous chapter. But after the incorporation of ZnO nanorods in PVDF matrix the peaks at 2θ=17.9º and 26.5º both disappear which indicates that the crystalline ZnO nanorods have changed the PVDF crystallinity. It is found that the peak at 2θ=19.9º shifted towards higher value angle in the PVDF/ZnO-20 composite system which indicates that after addition of high aspect ratio ZnO nanorod in PVDF matrix, polar phase of PVDF is enhanced. The maximum polar phase is observed in PVDF/ZnO-20 composite system.

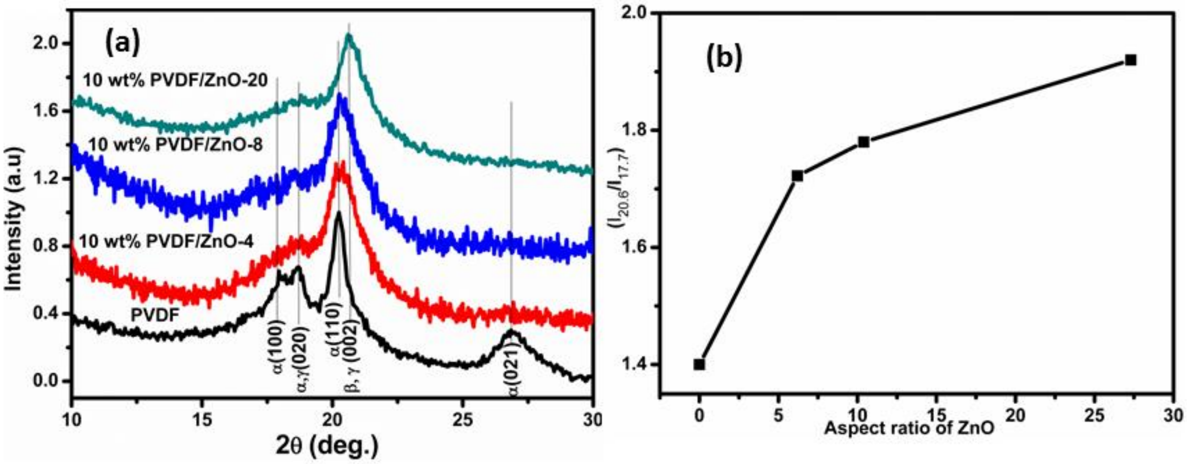

Fig. 3.2.6.*(a) XRD patterns of pure PVDF, PVDF/ZnO-4, PVDF/ZnO-8 and PVDF/ZnO-20 composite films, (b) Ratio of* $I_{20.6}$*and* $I_{17.7}$ *of the samples with aspect ratio of ZnO calculated from XRD pattern.*

The quantitative phase fraction (α and β) present in the samples are calculated from the intensity ratio of the peaks at 20.6° and 17.7° ($I_{20.6}/I_{17.7}$) and the obtained values are plotted with respect to aspect ratio of ZnO (represented in **Fig. 3.2.6 (b)).** The value of $I_{20.6}/I_{17.7}$ is enhanced with increasing aspect ratio of ZnO nanorods and reaches maximum value for PVDF/ZnO-20 composite system. This result indicated that highest polar phase nucleation occured in PVDF/ZnO-20 composite system.

The effective nucleation of polar phase in ZnO incorporated composites film is further confirmed from FTIR spectroscopy. **Fig. 3.2.7(a)** represents the FTIR spectra (in the region 400 cm^{-1} to 1500 cm^{-1}) of pure PVDF, PVDF/ZnO-4, PVDF /ZnO-8 and PVDF/ZnO-20 composites system. The IR spectra of pure PVDF exhibits peak at 409 cm^{-1}, 488 cm^{-1} (CF_2 wagging), 532 cm^{-1} (CF_2 bonds bending), 614 cm^{-1} and 764 cm^{-1} (CF_2 bending and skeletal bending), 796 cm^{-1}, 856 cm^{-1}

and 976 cm^{-1} (CH_2 rocking) which is due to the nonpolar α phase [7] as discussed in previous section 3.1.

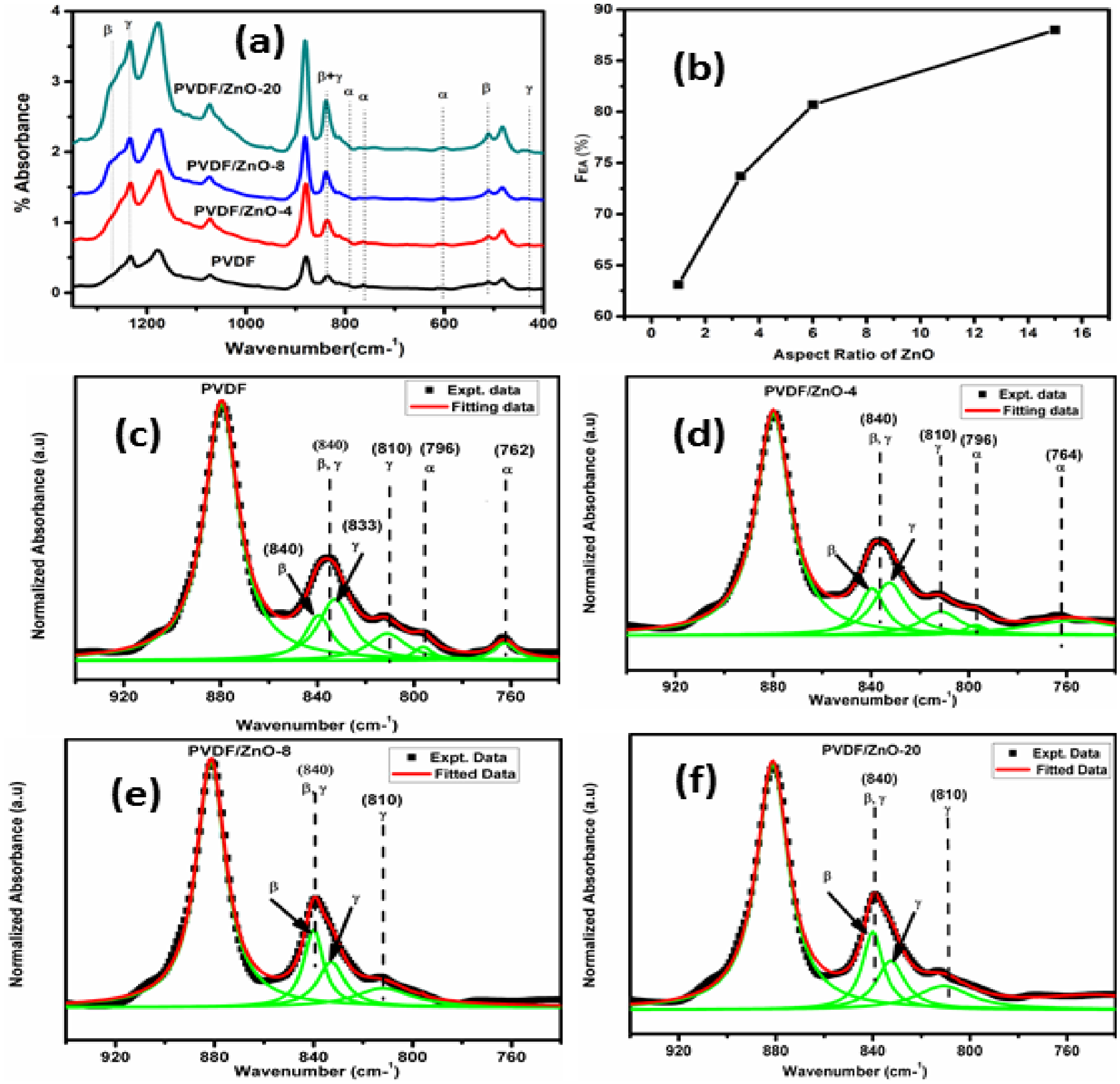

Fig. 3.2.7(a) *FTIR spectra of pure PVDF, PVDF/ZnO-4, PVDF/ZnO-8 and PVDF/ZnO-20 composite films,* ***(b)*** *Variation of polar-phase with aspect ratio of ZnO evaluated from IR spectra, The deconvolution curve of FTIR spectra in the region 940-740* cm^{-1} *of* ***(c)*** *pure PVDF film,* ***(d)*** *PVDF/ZnO-4,* ***(e)*** *PVDF/ZnO-8,* ***(f)*** *PVDF/ZnO-20 nanocomposites film.*

Some α characteristics peaks are suppressed after addition of ZnO nanorods in PVDF matrix. Small characteristics peaks are observed at 431 cm^{-1} (polar γ phase), 510 cm^{-1} (CF_2 stretching corresponding to polar β phase) and 840 cm^{-1} (CH_2 rocking, CF_2 stretching and skeletal C-C stretching), 1233 cm^{-1} (γ phase) and 1273 cm^{-1} (polar β phase) in the composite films which represents the polar phase formation. The amount of electroactive polar phase (F(β)) present is calculated from Beer-Lambert law described in **Equation 3.1.1**. The calculated percentage of electroactive phase fraction are 63.1 %, 73.7 %, 80.7 % and 88% for pure PVDF, PVDF/ZnO-4, PVDF/ZnO-8 and PVDF/ZnO-20 composite films respectively. The amount of phase fraction with respect to aspect ratio of ZnO is represented in **Fig. 3.2.7(b)**. Maximum 88% polar phase was obtained in PVDF/ZnO-20 composite system which was also supported by the XRD study. In order to investigate the individual β and γ phases in PVDF composites, the peak of 840 $cm-^{1}$ of FTIR curves was deconvoluted [8]. The deconvoluted figure was shown in **Fig. 3.2.7(c-f)** where the broadening peak was considered for the γ peak and the sharp peak was considered for the β peak. The following equations were used to quantify the β and γ phases individually.

$$F(\beta)= F_{EA}\times \frac{A_\beta}{A_\beta+A_\gamma}\times 100\% \text{ ---------------------------------- } (3.2.1)$$

$$F(\gamma)= F_{EA}\times \frac{A_\gamma}{A_\beta+A_\gamma}\times 100\% \text{------------------------ } (3.2.2)$$

where A_β and A_γ are the integrated area of β peak and γ peak of the deconvoluted curve, respectively. The individual quantification of F(β) and F(γ) from FTIR study for each sample was calculated and shown in **Table 3.2.1**. Relative amount of β phase (w.r.t γ phase) ($F_{\beta\gamma}$) and γ phase (w.r.t to β phase) ($F_{\gamma\beta}$) were also calculated using following Equation.

$$F_{\beta\gamma} = \frac{F(\beta)}{F(\beta)+F(\gamma)}\times 100\% \text{ ----------------------- } (3.2.3)$$

$F_{\gamma\beta} = \frac{F(\gamma)}{F(\beta)+F(\gamma)} \times 100\%$ ---------------------- (3.2.4)

The percentage of β and γ phase was calculated from FTIR data given in **Table 3.3.1**.

Table 3.2.1 *Individual quantification of polar phase present within the composites*

Sample Name	Polar phase Fraction (F_{EA} %)	β phase Fraction (F_{β} %)	γ phase Fraction (F_{γ} %)	Relative amount of β phase w.r.t to γ phase ($F_{\beta\gamma}$)	Relative amount of γ phase w.r.t toβ phase ($F_{\gamma\beta}$)
PVDF	63.1	27.9 %	35.18 %	44.2 %	55.71 %
PVDF/ZnO-4	73.7	34.5 %	39.1 %	46.87 %	53.12 %
PVDF/ZnO-8	80.7	41.66 %	39.03 %	51.61 %	48.38 %
PVDF/ZnO-20	88	46.59%	41.4 %	52.9 %	47.09 %

Fig. 3.2.7(d-f) clearly indicated that the deconvoluted β peak is more prominent for high aspect ratio ZnO nanorod where the γ peak gets gradually weakened with increase aspect ratio of ZnO nanorods. From **Table 3.2.1**, it was observed that the relative amount of β phase (with respect to γ phase) increased gradually with aspect ratio of ZnO nanorods and relative amount of γ phase (with respect to β) decreases with increase aspect ratio of ZnO nanorods. High aspect ratio PVDF/ZnO-20 nanocomposite exhibited maximum β phase. Thus the polar phase fraction is enhanced after high aspect ratio ZnO-20 filler loading in PVDF matrix. This is caused mainly due to the interaction of the interfaces between PVDF matrix and ZnO filler. Above result confirmed that the introduction of high aspect ratio ceramic filler enhanced the formation of polar phase which indicates that the high aspect ratio ceramic filler may be more effective for increasing electrical properties [9]. After inclusion of ZnO filler in PVDF matrix, an interaction

occurs between positive –CH_2 dipole of PVDF and negative surface charge of ZnO fillers which leads to TTTT and ($T3G^{+}T3G^{-}$) configuration in PVDF. It is also observed that the zeta potential value is increased with increasing aspect ratio of ceramic filler which suggested that the negative surface charge increases on ZnO-20 filler surface. As a result, more polar electroactive (β and γ) phases were obtained in PVDF/ZnO-20 composite system than the other composite. According to Luo et al., the effective nucleation of polar phase in ferroelectric polymers like PVDF is very helpful to enhance the permittivity and piezoelectric/ferroelectric properties of the composite due to large dipole moment of this phase [9]. Incorporation of ceramic filler into PVDF matrix led to the transformation of nonpolar phase to polar phase of PVDF [10-13].

The interfacial interaction between ceramic filler ZnO and PVDF matrix was further confirmed by XPS study. The C1s core level XPS spectrum of neat PVDF and PVDF /ZnO composite is shown in **Fig. 3.2.8(a).**

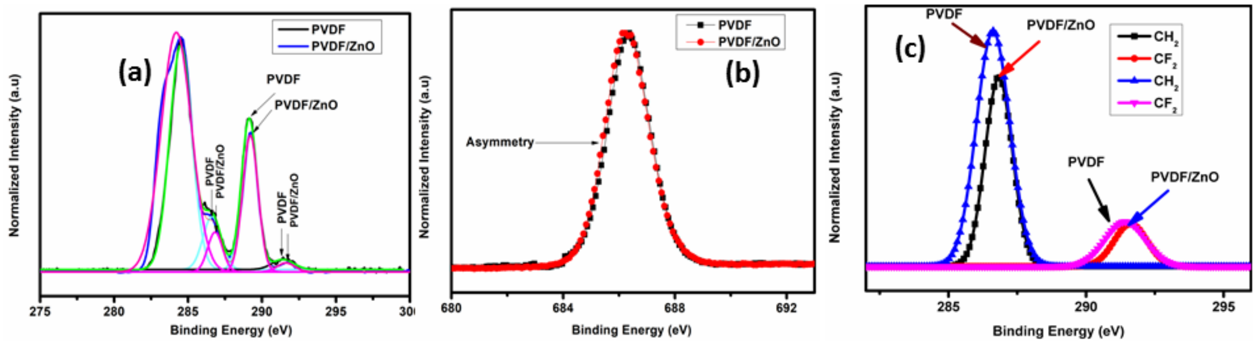

Fig. 3.2.8 *Core level XPS spectrum of (a) C1s, (b) F1s of pure PVDF and 15 Wt% PVDF/ZnO-20 nanocomposite system, (c) Comparison of –CH_2 peak and –CF_2 peak of C1s spectra of pure PVDF and 15 Wt % PVDF/ZnO-20 composite system.*

The C1s spectrum of neat PVDF exhibited peaks at 286.5 eV and 291.4 eV indicated the presence of –CH_2 dipole and –CF_2 dipole of PVDF respectively (shown in **Fig. 3.2.8(c)**). The intensity of the peaks were decreased and shifted towards higher binding energy in the composite system which may be due to interfacial interaction between PVDF and ZnO nanorods. The peak area of –CH_2 (A_{CH2}) dipole is reduced by 43% for composite system with respect to neat PVDF which clearly indicates the presence of interfacial interaction between PVDF matrix and ZnO [6]. The F1s spectrum of neat PVDF and PVDF/ZnO composite system is shown in Fig. **3.2.8(b).** F1s spectrum shows that the line broadening of peak is asymmetrical and the peak shifted towards lower binding energy which further indicates the existence of interfacial interaction [14-15]. The XPS study supported the FTIR result described earlier.

The SEM micrographs of PVDF/ZnO-4, PVDF/ZnO-8 and PVDF/ZnO-20 nanocomposite films are shown in **Fig. 3.2.9(a-c)**. FESEM images indicated the good dispersion of ZnO nanorods in PVDF matrix. It was observed that high aspect ratio ZnO-20 nanorods exhibited better homogeneous dispersibility in PVDF matrix which may be due to the strong interaction between –CH_2 dipole of PVDF and more negative surface charge of ZnO-20 filler.Finally, nanocomposites with higher aspect ratio nanorods showed excellent dispersion and compatibility in PVDF matrix.

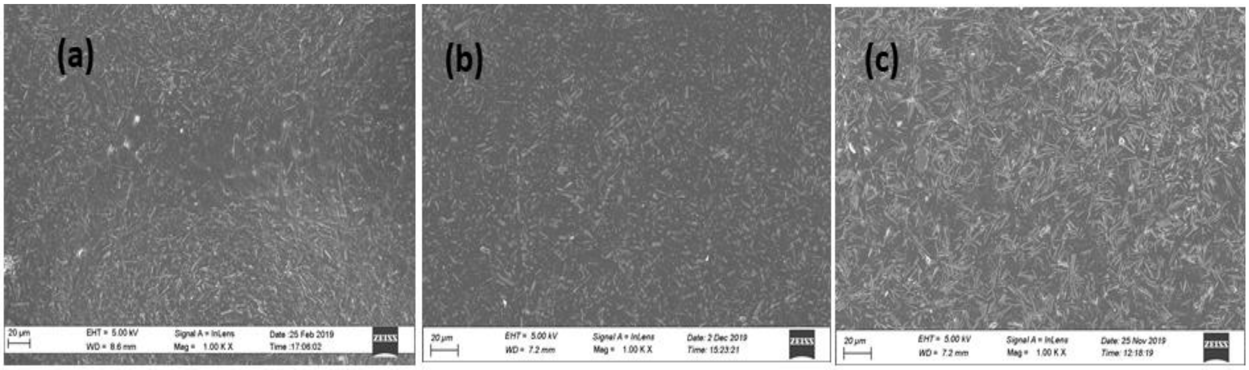

Fig. 3.2.9 *SEM micrograph of (a) PVDF/ZnO-4, (b) PVDF/ZnO-8, (c) PVDF/ZnO-20 nanocomposites*

3.2.1.3. Dielectric properties of PVDF composite film

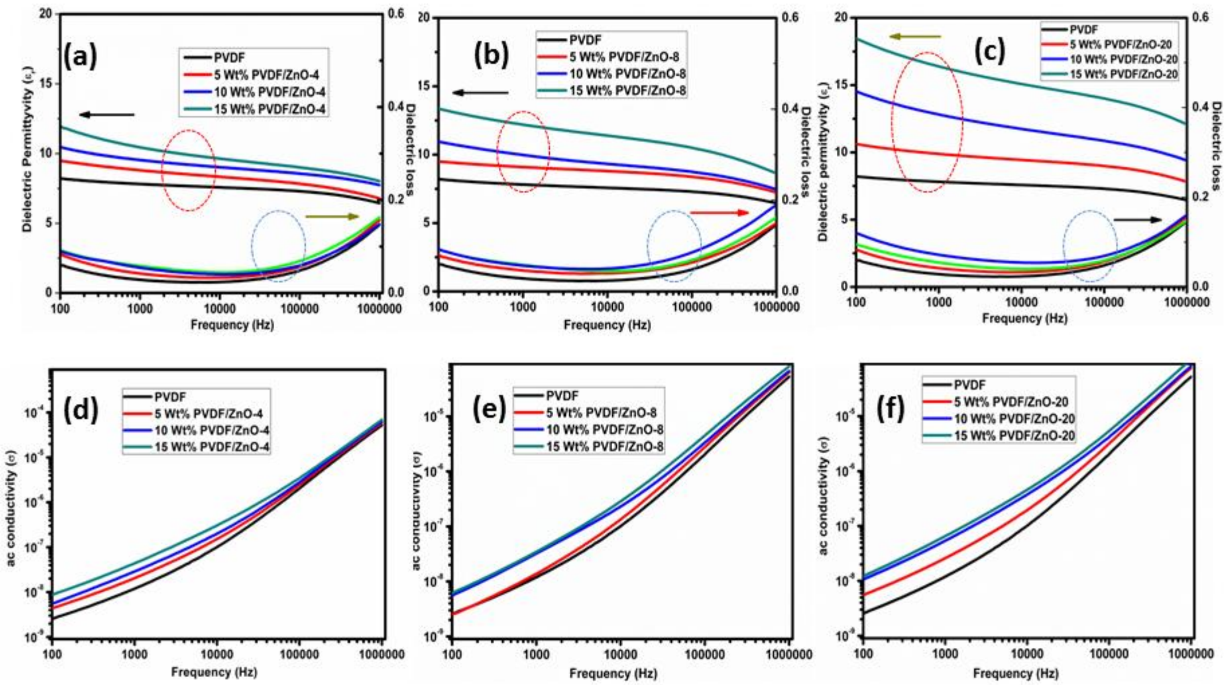

***Fig. 3.2.10** frequency dependent dielectric permittivity and dielectric loss of **(a)**PVDFZnO-4, **(b)** PVDF/ZnO-8, **(c)**PVDF/ZnO-20 nanocomposites ; a.c. conductivity of **(d)** PVDF/ZnO-4, **(e)** PVDF/ZnO-8, **(f)**PVDF/ZnO-20 nanocomposites*

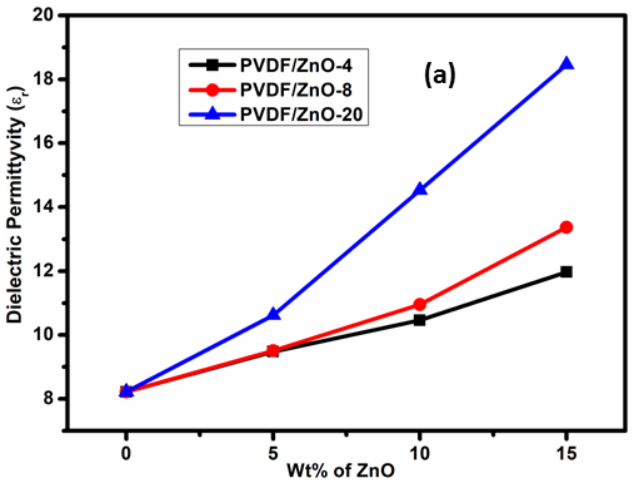

***Fig. 3.2.11**Comparison of dielectric permittivity of nanocomposites as a function of different wt% of ZnO (Measured at same frequency)*

This dielectric study clearly indicates that the aspect ratio plays an important role for enhancement of dielectric constant of the nanocomposites. H. Tang et al. already demonstrated that there is a relationship between aspect ratio of fillers and dielectric constant of the composites [4]. Many previous reports and theoretical models such as Maxwell Garnet Model have shown that the dielectric properties of the nanocomposites can be enhanced significantly with increasing filler aspect ratio [4, 16]. Moreover, high aspect ratio ceramic filler has many advantages compared to low aspect ratio filler. High aspect ratio filler reach the percolation threshold easily which leads to the formation of a continuous path way in the system resulting an improvement of dielectric constant of the composite system [4]. Besides, the high aspect ratio ceramic filler possesses large dipole moment which may be very effective to improve dielectric constant of the nanocomposites and high aspect ratio ceramic filler have low surface energy which is favourable for good dispersion and can enhance the dielectric constant of the nanocomposites [9]. Additionally, high aspect ratio ceramic filler promotes the formation of polar phase which play a very important role on the increment of dielectric constant of the nanocomposites [9]. PVDF/ZnO-20 nanorods exhibited maximum permittivity value due to the above said reason.

The variation of dielectric loss tangent value of the samples PVDF/ZnO-4, PVDF/ZnO-8 and PVDF/ZnO-20 with ZnO filler loading are shown also in **Fig.3.2.10 (a-c).** It is observed that the dielectric loss increased with increasing ZnO filler concentration. Both dielectric constant and dielectric loss of PVDF nanocomposites increases with ZnO filler concentration due to the interfacial space charge polarization. Higher amount of filler loading creates more interfacial area which increases conductive network between PVDF and ZnO filler. High aspect ratio ZnO nanorods showed higher dielectric loss than low aspect ratio ZnO rods. As high aspect ratio ZnO nanorods exhibit better dispersion in PVDF matrix, interafacial area between filler and PVDF matrix also increased and as a result polymer chains were separated into smaller domains [6, 17]. Thus more PVDF dipoles get rotated which enhances the dielectric loss.

This is further confirmed from a.c. conductivity plot of the composites where a.c. conductivity increased with increasing ZnO filler loading for all composite system (**Fig. 3.2.10(d-f)**). a.c. conductivity of dielectric material can be expressed as

$\zeta = 2\pi f.\ \varepsilon_0.\ \varepsilon_r''$--------------------- (3.2.5)

This result shows that a.c. conductivity of the composite films is greater than PVDF polymer which is due to the more conducting network causing more leakage current (shown in **Fig. 3.2.12 (f)**) in the composite system. **Fig. 3.2.11** represents the variation of dielectric permittivity of PVDF/ZnO-4, PVDF/ZnO-8 and PVDF/ZnO-20 samples with different filler loading (at same frequency). The permittivity value increased with ZnO filler loading for all the samples. It also showed that PVDF/ZnO-20 composite films exhibited higher dielectric permittivity than other composite films for same ZnO filler loading.

3.2.1.4. Ferroelectric properties of composite film

Fig. 3.2.12(a-c) represent the typical electrical displacement-electric field (D-E) loops of the PVDF/ZnO-4, PVDF/ZnO-8 and PVDF/ZnO-20 composite films with different percentage of ZnO filler loading. It was observed from **Fig. 3.2.12 (a)**, maximum electric displacement (D_m) and remnant electric displacement (D_r) increased after ZnO addition in PVDF matrix. **Fig. 3.2.12 (b) and 3.2.12 (c)** also followed similar trend. It was also observed that D_m can be improved with increasing aspect ratio of ZnO nanorods. 15 wt % PVDF/ZnO-20 nanocomposite exhibited maximum polarization value under an same applied electric field 100 V/cm. This result suggested that ferroelectric properties of the composites increased with increasing aspect ratio and filler loading. This may be due to the interaction of ceramic ZnO filler and PVDF matrix.

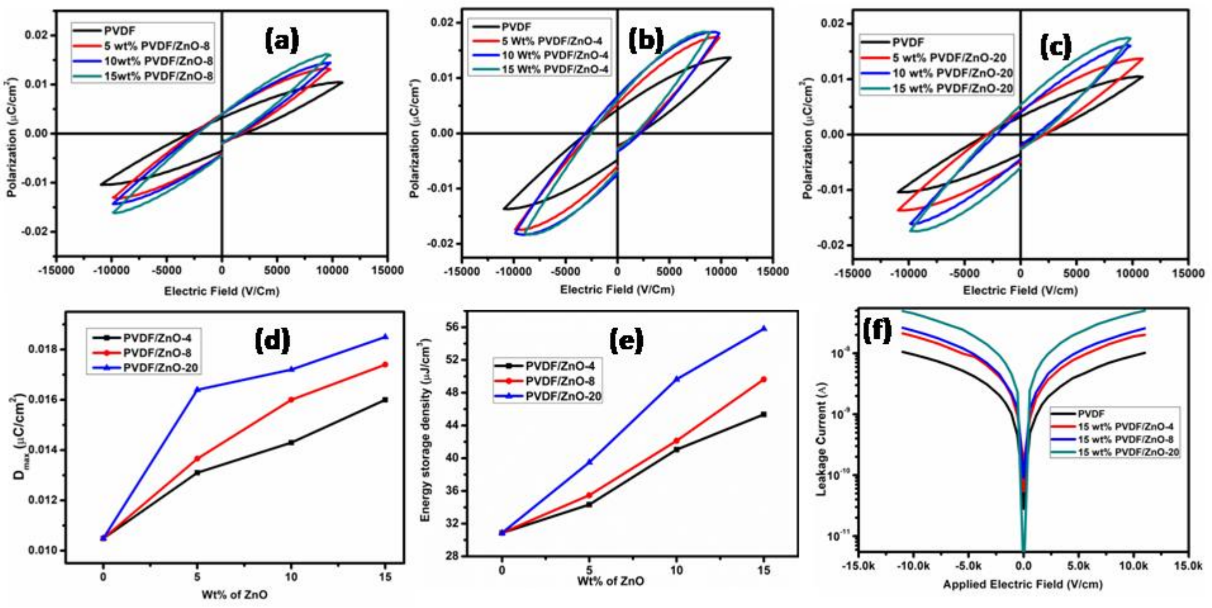

Fig. 3.2.12 *Electric displacement vs applied electric field (D-E) loop of* ***(a)****PVDF/ZnO-4,* ***(b)*** *PVDF/ZnO-8,* ***(c)*** *PVDF/ZnO-20 composites;* ***(d)*** *comparison of D_{max} of the nanocomposites with different wt% of ZnO,* ***(e)****Variation of energy storage density of nanocomposites with different wt % of ZnO,* ***(f)*** *Electric Field dependent leakage current of PVDF, PVDF/ZnO-4, PVDF/ZnO-8 and PVDF/ZnO-20 nanocomposites (measured at 1 Hz).*

Electric displacement equation can be expressed as $D=\varepsilon_0\varepsilon_r E$, where ε_0 and ε_r are free space permittivity and relative permittivity of the nanocomposites respectively [16]. Therefore, D_{max} of composite system increased with increasing dielectric value of the composite. The variation of D_{max} of the nanocomposites with increasing filler loading or aspect ratio of ZnO under the same electric field (E) is shown in **Fig. 3.2.12(d).** Therefore it is assumed that ferroelectricity is increased due to the above mentioned factors.

The dielectric and ferroelectric property of the composite film increased with addition of ZnO filler or increasing aspect ratio, and hence it can be assumed that energy storage density will also increase. The values of energy storage capability of the fabricated composites were evaluated from D-E loops using an integral formula described in **Equation 3.1.3**. **Fig. 3.2.12(e)** represents the stored electrical energy density of PVDF/ZnO-4, PVDF/ZnO-8 and PVDF/ZnO-20 composite systems as a function of filler loading of the nanocomposites. Energy density of the nanocomposites increases as the polarization increased with the concentration of ZnO filler. Aspect Ratio (AR) also plays a crucial role for determining the storage energy density of the composites. It is observed that the PVDF/ZnO-20 nanocomposites exhibited a higher energy storage density than the other composites at same applied electric field. Energy storage density increased due to the enhancement of dielectric permittivity and electrical displacement (D_m) of the PVDF/ZnO nanocomposites with increased filler concentration and aspect ratio of ZnO nanorods. Leakage current of pure PVDF and composite system as a function of applied electric field is shown in **Fig. 3.2.12(f).** Leakage current increases with increasing aspect ratio of ZnO rods in PVDF matrix which was due to increasing conducting network within composites. In addition high aspect ratio ZnO filler in PVDF matrix creates larger leakage current which enhances the conductive network in PVDF matrix.

3.2.1.5. Energy harvesting properties of composite film

ZnO is extensively studied as ceramic filler in PVDF matrix because of its superior piezoelectric performance. Therefore, it is expected that PVDF/ZnO nanocomposite will exhibit good piezoelectric performance. Hence the piezoelectric properties of PVDF, PVDF/ZnO-4, PVDF/ZnO-8 and PVDF/ZnO-20 nanocomposite systems were studied by applying repeated human finger tapping using a digital oscilloscope.

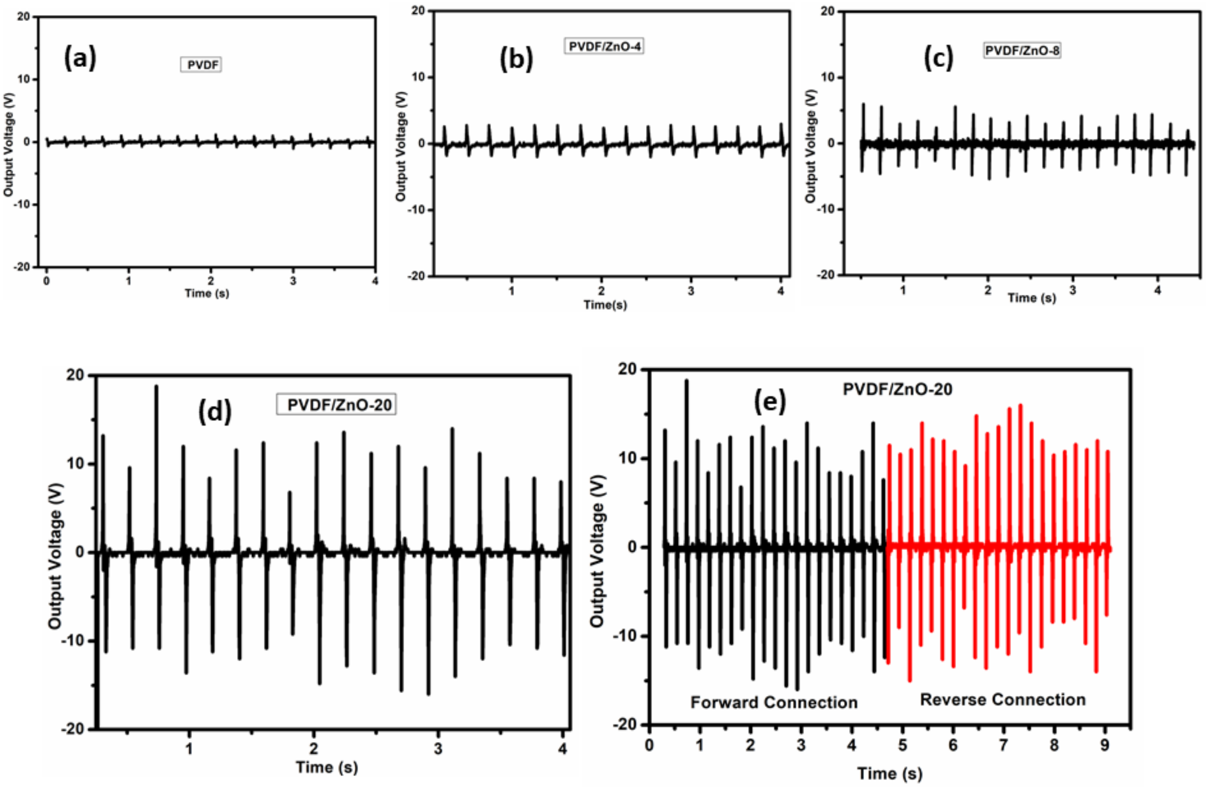

*Fig. 3.2.13 Comparison of open circuit output a.c. voltage of **(a)** PVDF, **(b)** PVDF/ZnO-4, **(c)** PVDF/ZnO-8, **(d)** PVDF/ZnO-20 nanocomposites, **(e)** Switching polarity test of PVDF/ZnO-20 sample*

Fig. 3.2.13(a-d) represents the open-circuit a.c. output voltage of PVDF, PVDF/ZnO-4, PVDF/ZnO-8 and PVDF/ZnO-20 composite films. It is observed that there is an enhancement of open circuit output voltage with increasing aspect ratio of ZnO nanorods. The 15 wt % PVDF/ZnO-20 composite film showed maximum value compared to pure PVDF and other composite films. The maximum open circuit a.c. output voltage of this film was 20 V which was originated due to its maximum polar phase formation in high aspect ratio composite system. In addition, the enhancement of this output voltage may be due to more interfacial interaction which leads to an enhancement of conductive network between the composite films. In order to investigate that the output voltage was obtained from pure piezoelectric effect or not, switching polarity test was carried out simply by changing electrode connections in reverse direction (shown in **Fig. 3.2.13(e)**). In reverse connection, almost same level of output voltage with opposite polarity was observed for every sample which confirmed that the output voltage was obtained from the piezoelectric effect and not from any other source [17]. The output voltages are almost same in forward and reverse connection with opposite polarity. Thus the electric signals are purely piezoelectric.

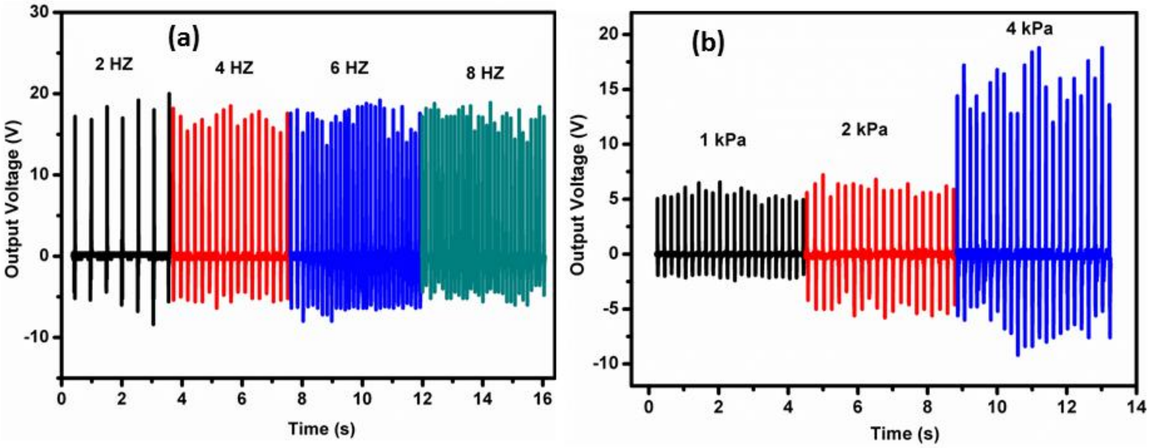

***Fig. 3.2.14 (a)** Comparison of output a.c. voltage of PVDF/ZnO-20 sample at different frequencies., **(b)** Comparison of output a.c. voltage of PVDF/ZnO-20 sample at different pressure*

Frequency dependent piezoelectric test performance was done in the frequency region 2Hz to 8 Hz for the sample PVDF/ZnO-20 (shown in **Fig. 3.2.14(a)**). Output voltage was almost same in the frequency region 2 Hz to 8 Hz. Output voltage did not depend on the applied frequency which may be due to the mismatch between the resonating frequency of the film and the applied frequency [15]. The piezoelectric output voltage of PVDF/ZnO-20 nanocomposite with different tapping pressure is presented in **Fig. 3.2.14(b)**. Open circuit output voltage increased with increasing applying pressure ~1 KPa to 4 KPa at applied frequency of 5 Hz. This result indicates that PVDF/ZnO nanocomposite can be explored as self-powered sensors.

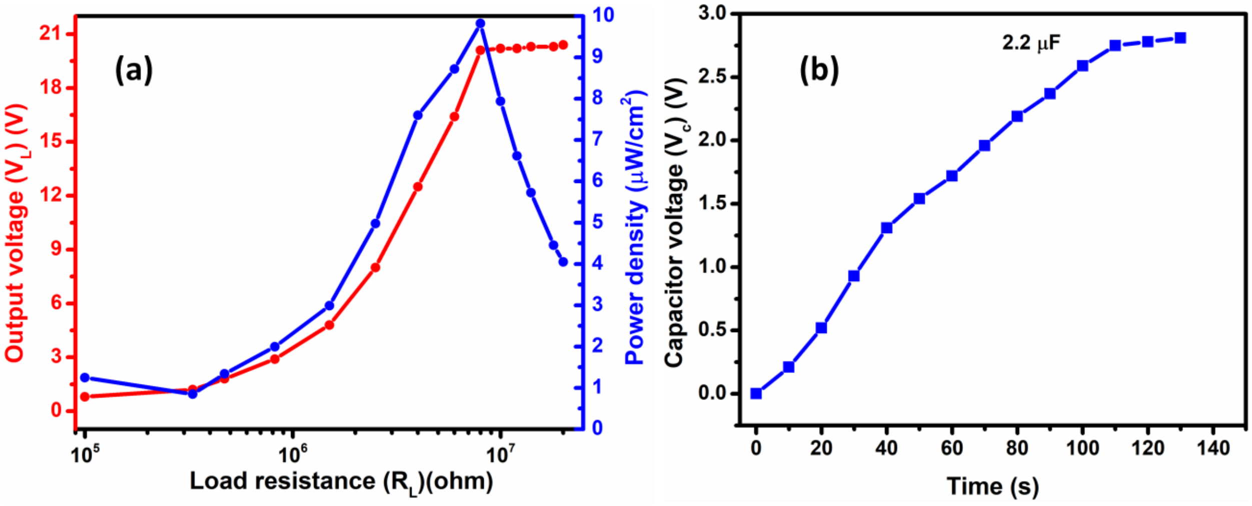

Fig. 3.1.15 (a) *Variation of output voltage and power density as a function of load resistance of PVDF/ZnO-20 composite,* ***(b)*** *Charging of 2.2 μF capacitor*

The output voltage vs. load resistance graph of PVDF/ZnO-20 composite film is shown in **Fig. 3.1.15(a)**. The output voltage was gradually increased with load resistance and reached a saturation value at 8 MΩ. The power density (P) was calculated from the output voltage (V_L) through different load resistance (R_L) by using the **Equation 3.1.4** (described in 3.1 section). The maximum power density of PVDF/ZnO-20 composite film was found to be ~ 9.6 μW cm^{-2} at 8 MΩ load resistance (shown in **Fig. 3.1.15(a)**). The generated a.c. output voltage of PVDF/ZnO-20 composite was converted to d.c. output voltage using a bridge rectifier IC (DB 107). This rectified d.c. voltage was able to charge a 2.2 μF capacitor up to ~ 2.7 V was represented in **Fig. 3.1.15(b)**.

3.2.1.6. Piezo force microscopy (PFM)

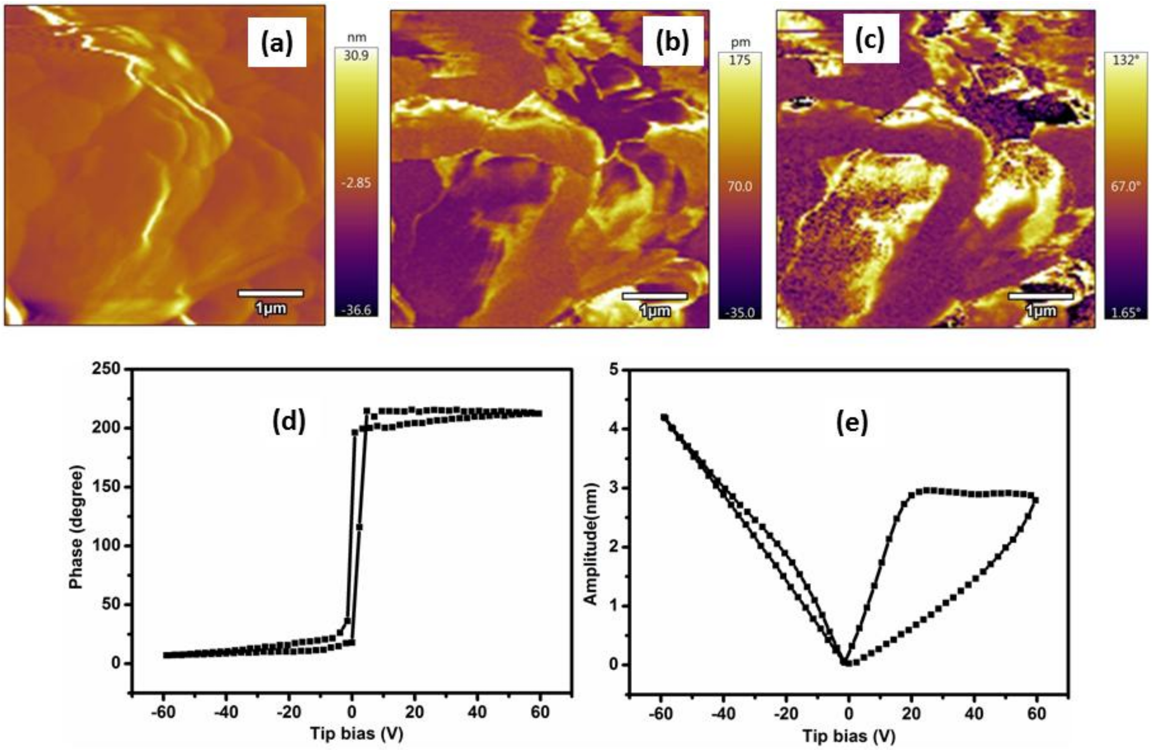

Fig. 3.2.16 (a-c) *Topography image, PFM amplitude and phase images of PVDF/ZnO-20 sample, (d) PFM amplitude-voltage loop of PVDF/ZnO-20 sample, (e) PFM phase-voltage hysteresis loop for PVDF/ZnO-20 sample.*

Piezoresponse Force Microscopy (PFM) measurement was carried out to check the local ferroelectric and piezoresponse properties existing within PVDF/ZnO-20 composite film. PFM amplitude represents the local piezoelectric displacement of the sample under an applied electric field and PFM phase represents the direction of polarization of sample domains [18]. **Fig. 3.2.16** (a), (b) and (c) represent the topography image, out of plane amplitude and phase images, respectively. The polarization of domains (**Fig. 3.2.16(c)**) is in opposite direction can be distinguished by image contrasts [18]. Different contrasts were observed in both amplitude and phase images which indicated the presence of piezoelectricity and ferroelectricity within the composite film [19]. Phase voltage hysteresis loop was shown in **Fig. 3.2.16(d)**. Phase-voltage hysteresis loop shows 180◦ difference at a tip voltage V_{dc} = ± 60 V. Under an applied electric field, dipoles are easily switched which indicated that an in-situ poling process was generated in the composite film [18]. Amplitude Voltage butterfly loop was shown in **Fig. 3.2.16(e)**. Under an applied electric field mechanical strain was generated within the composite film i.e converse piezoelectric phenomena occured. The asymmetry of the amplitude loop may be due to the internal bias field inside the composite film [18, 20]. The phase voltage hysteresis loop and butterfly loop confirmed the local ferroelectric and piezo response properties existing within the composite film.

3.2.1.7. Conclusion:

Different aspect ratio ZnO nanorods were prepared by hydrothermal technique with varying reaction time and PVDF based nanocomposites of the respective ZnO nanorods with different wt% filler loading were fabricated. In this study we have highlighted the dependence of aspect ratio of ZnO nanorods on the electrical performance of PVDF when embedded in its matrix. It has been demonstrated that piezoelectric properties can be improved significantly with using high aspect ratio filler addition in PVDF matrix. A small amount of high aspect ratio ZnO filler loading in PVDF matrix increased the polar phase fraction in the nanocomposite system which triggered the enhancement of dielectric properties. Maximum dielectric permittivity was observed in 15wt% PVDF/ZnO-20 nanocomoposite than that of other two composites comprising of comparatively lower aspect ratio ZnO and PVDF (15 wt% PVDF/ZnO-4 and 15 wt% PVDF/ZnO-8).Further 15 wt% PVDF/ZnO-20 composite system exhibited maximum energy density and maximum open circuit a.c. voltage (20 V). This work provides a new approach for using high aspect ratio ceramic filler to enhance the dielectric, ferroelectric and piezoelectric properties of the composites of the same filler and polymer PVDF.

References:

1. Y. Qiu, D. Yang, J. Lei, H. Zhang, J. Ji, B. Yin, J. Bian, Y. Zhao, L. Hu, *J. Mater Sci: Mater Electron.,* 2014, **25**, 2649.
2. Q. Wang, D. Yang, Y. Qiu, X. Zhang, W. Song, L. Hu, *Appl. Phys. Lett.,* 2018, **112**, 063906.
3. J. Li, S. Chen, W. Liu, R. Fu, S. Tu, Y. Zhao, L. Dong, B. Yan, Y. Gu, *J. Phys. Chem. C*., 2019, **123**, 11378.
4. H. Tang, Z. Zhou, H. A. Sodano, *ACS Appl. Mater. Interfaces.,* 2014, **6,** 5450.
5. H. Parangusan, D. Ponnamma, M A A. Al-Maadeed, *ACS Omega*., 2019, 4, **4**, 6312–6323.
6. I. Chinya, A. Pal, S. Sen, *J. Alloy. Compd*., 2017, **722**, 829.
7. A. Sasmal, S. Sen, P. S. Devi, *Phys. Chem. Chem. Phys.,* 2019, **21**, 5974.
8. C. Zhang, Y. Fan, H. Li, Y.Li, L. Zhang, S. Cao, S. Kuang, Y. Zhao, A. Chen, G. Zhu, Z. L. Wang, *ACS Nano.,* 2018*,* **12***,* 4803.
9. H. Luo, J. Roscow, X. Zhou, S. Chen, X. Han, K. Zhou, D. Zhang, C. R. Bowen, *J. Mater. Chem. A.,* 2017, **5**, 7091.
10. S. Liu, J. Zhai, J. Wang, S. Xue and W. Zhang, *ACS Appl. Mater. Interfaces.,* 2014, **6**, 1533.
11. Y. Niu, Y. Bai, K. Yu, Y. Wang, F. Xiang, H. Wang, *ACS Appl. Mater. Interfaces*., 2015, **7**, 24168.
12. L. Xie, X. Huang, C. Wu, P. Jiang, *J. Mater. Chem.,* 2011, **21**, 5897.

13. X. Lin, P. H. Hu, Z. Y. Jia, S. M. Gao, *J. Mater. Chem. A.*, 2016, **4**, 2314.
14. L.Ying, P. Wang, E.T. Kang, K. G. Neoh, *Macromolecules.,* 2002, **35**, 673.
15. I. Chinya, A Sasmal, A Pal, S Sen*, CrystEngComm.,* 2019, **21**, 3478.
16. D. Zhang, X. Zhou, J. Roscow, K. Zhou, L. Wang, H. Luo, C. R. Bowen, *Sci. Rep*., 2017, **7**, 45179.
17. B. Adak, I. Chinya, S. Sen, *RSC Adv.,* 2016, **6**, 105137.
18. C. Zhang, Y. Fan, H. Li, Y.Li, L. Zhang, S. Cao, S. Kuang, Y. Zhao, A. Chen, G. Zhu, Z. L. Wang, *ACS Nano.,* 2018*,* **12**, 4803.
19. A. Ferri, S. Barrau, R. Bourez, A. D. Costa, M.-H. Chambrier, A. Marin, J. Defebvin, J. M. Lefebvre, R. Desfeux, *Composites Science and Technology.,* 2020*,* **186***,* 107914.
20. S. K. Ghosh, P. Adhikary, S. Jana, A. Biswas, V. Sencadas, S. D. Gupta, B.Tudu, D. Mandal, *Nano Energy*. 2017*,* **36***,* 166.

3.3: The effect of MWCNT addition as a third phase conductive filler in PVDF-ZnO system

3.3.1. Introduction

In our previous work, the aspect ratio of ZnO nanorods was tuned to achieve the performance enhancement of the resulting PVDF based composites. Here in the present work, we have tried to improve the electrical performances of the flexible PVDF-ZnO composites by using a third phase addition.

Addition of third phase conducting fillers like reduced graphene oxide (rGO), carbon black, graphite, single/multi-walled carbon nanotubes, etc. in polymer based composites have been previously studied by several researchers in order to improve their electrical and energy harvesting performances [1-4]. Introduction of third phase conductive filler within polymer matrix reduce the dissimilarity of the difference of local electric field between ceramic filler and polymer matrix within the nanocomposite. Besides, third phase conductive filler improves the homogeneity of dispersion of fillers within polymer matrix and prevents their agglomeration within the nanocomposites [2]. On the other hand, the electronic conductivity of PVDF is very low and hence, the uniformly distributed fillers in PVDF become isolated by PVDF insulation layers between them. But, for achieving enriched output piezoelectric performance, good connection between each piezoelectric ZnO nanorods is a must needed parameter. So, the addition of optimized amount of conducting filler in PVDF-ZnO composites creates good electrical connections between each ceramics particle and hence, enhancement of conductivity in the nanocomposites is achieved which in turn improves its peizo-response. Owing to their good electronic conductivity, the third conducting phase not only creates electrical bridge between each ZnO nanorods, but also creates good connectivity with top and bottom electrodes of the composite film which in turn improves the output piezoelectric performance through good charge transmission between the composite films and electrodes. Further, the improved homogeneous distribution of nanomaterials in the PVDF matrix induced by the third conducting phase reduces the internal resistance of the nanocomposites and as a result, output electrical performances are improved [5-9].

In this work, initially an attempt has been made to synthesize ZnO nanorods by wet chemical route. Then the as-synthesized ZnO nanorods have been added to PVDF matrix for fabrication of composite film (5wt%, 10wt%, 15wt% ZnO powder to get three different series (5PZO, 10PZO and 15PZO). Further enhancement in the output performance of the PVDF-ZnO composite film has been tried by using multi-walled carbon nanotubes (MWCNT) as an additive third conducting phase into it.CNT loaded PVDF composite films were named as 5PZNT, 10PZNT and 15 PZNT respectively. Neat PVDF film was also fabricated without adding any filler loading in PVDF-DMF solution. Among the different conducting materials, MWCNT was chosen here in order to match the morphology of third conducting phase with ceramic ZnO filler which may facilitates the filler distribution and alignment. As described above, the MWCNT addition can also improve the piezoelectric output of the PVDF-ZnO composites. The structural, morphological, vibrational, dielectric, ferroelectric, energy storage and energy harvesting performance of PVDF-ZnO composites before and after MWCNT addition have been studied in detail here in the present work. Theoretical simulation for ferroelectric polarization and piezoelectric potential has also been performed using COMSOL.

3.3.1.1. Characterization of filler material

The confirmation of phase formation and morphology of the filler material were evaluated by XRD and TEM characterizations, respectively. The XRD pattern of the synthesized ZnO powder is illustrated in **Fig. 3.3.1(a)**. All the diffraction peaks matched well with standard JCPDS data for ZnO (JCPDS card no.: 79-0208) with lattice constants a = b = 3.264Å and c = 5.219Å. Therefore the peaks were indexed in the figure on the basis of this JCPDS file which confirmed the hexagonal wurtzite structure (with $P6_3mc$ space group) of the synthesized ZnO filler. The absence of any additional peak confirmed the phase purity of the synthesized ZnO sample. The peak broadening of XRD pattern was found to be very low suggesting the large crystalline size of the synthesized ZnO sample which is very common for ZnO rods having length in the micrometer range. As the XRD characterization suggested large crystallite size of the synthesized ZnO, its morphological characterization is inevitable. The morphology and crystalline characteristics were investigated by TEM characterization. **Fig.3.3.1(b)** presents the bright field TEM image of the synthesized ZnO filler which confirmed its rod like morphology. The calculated average length and diameter of the synthesized ZnO nanorods were found to be ~ 60 nm and ~ 300 nm, respectively.The diameter distribution of the nanorods is shown in **Fig. 3.3.1(c)**. The HRTEM image of ZnO nanorods as presented in **Fig. 3.3.1(d)** confirmed the presence of the (1 0 1) plane which matched with the maximum intense peak of XRD pattern. **Fig. 3.3.1(e)** presents the EDX spectra of the synthesized nanorod, which confirmed the existence of the desired elements with almost desired proportion. The absence of signal from any other elements except copper (Cu) (signal from Cu appeared due to the usage of Cu grid during TEM characterization) proved the purity of the synthesized ZnO nanorods.Zeta potential study of ZnO nanorods was represented in **Fig. 3.3.1(f)**. The negative value of zeta potential (-20.7 mV) suggested the negative surface charge of the synthesized ZnO nanorods.

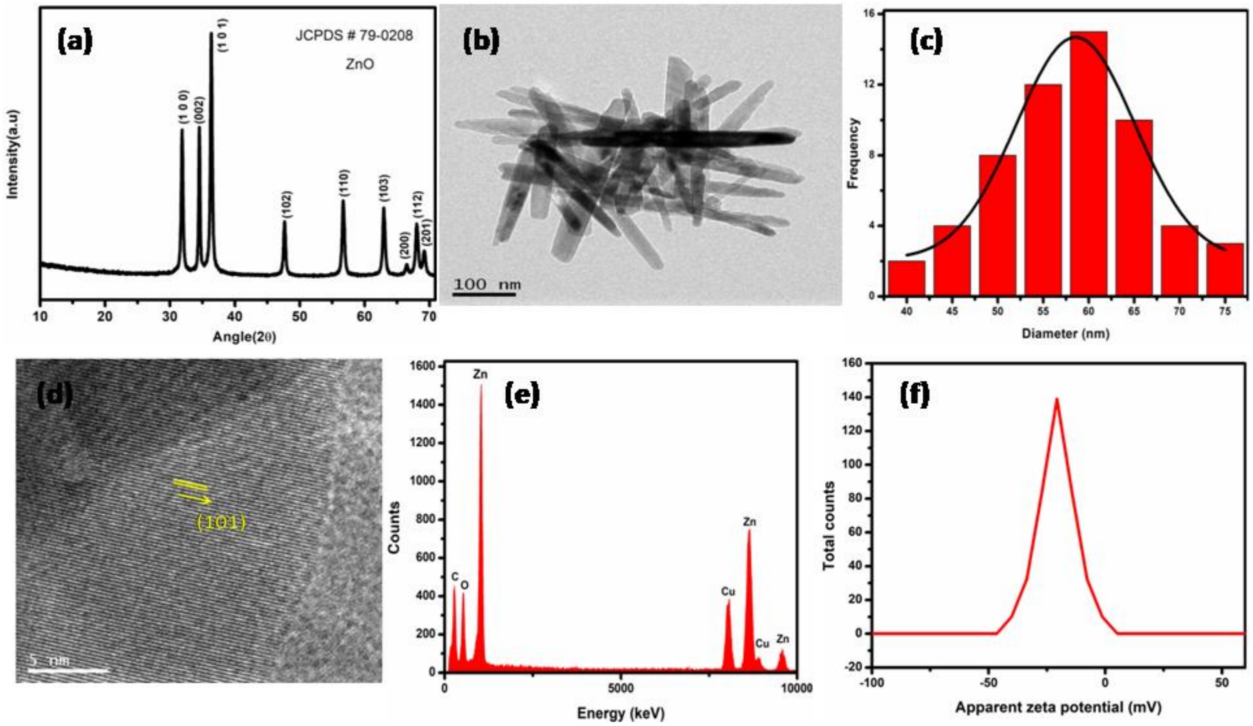

***Fig. 3.3.1(a)**XRD pattern, **(b)** TEM image, **(c)**Diameter distribution, **(d)** HRTEM image**(e)** EDX spectrum and (f) Zeta potential study of ZnO nanorods.*

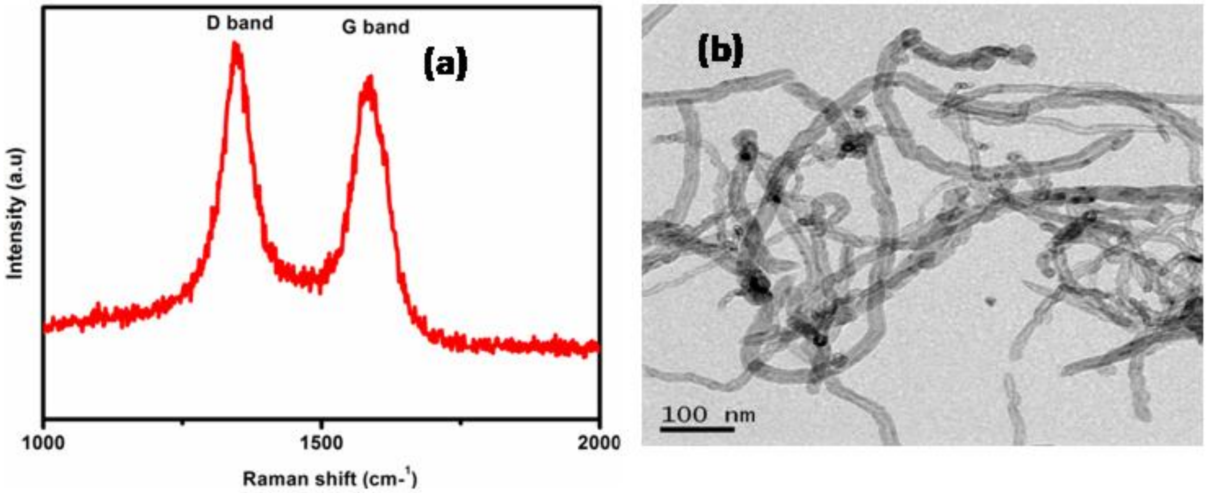

***Fig. 3.3.2 (a)** Raman spectra and **(b)** TEM image of MWCNT.*

Fig. 3.3.2(a) shows the Raman spectrum of CNT. Two strong bands appeared at 1358 cm^{-1} (Dband) and 1582 cm^{-1} (Gband) in raman spectrum. The 'D band' at 1358 cm^{-1} mainly appeared due to the structural defect in the CNT structure. The ‘G band’ appeared due to the raman active E_{2g} mode. **Fig. 3.3.2(b)** presents the TEM images of CNT which indicates that the average diameter of CNT is ~15 nm.

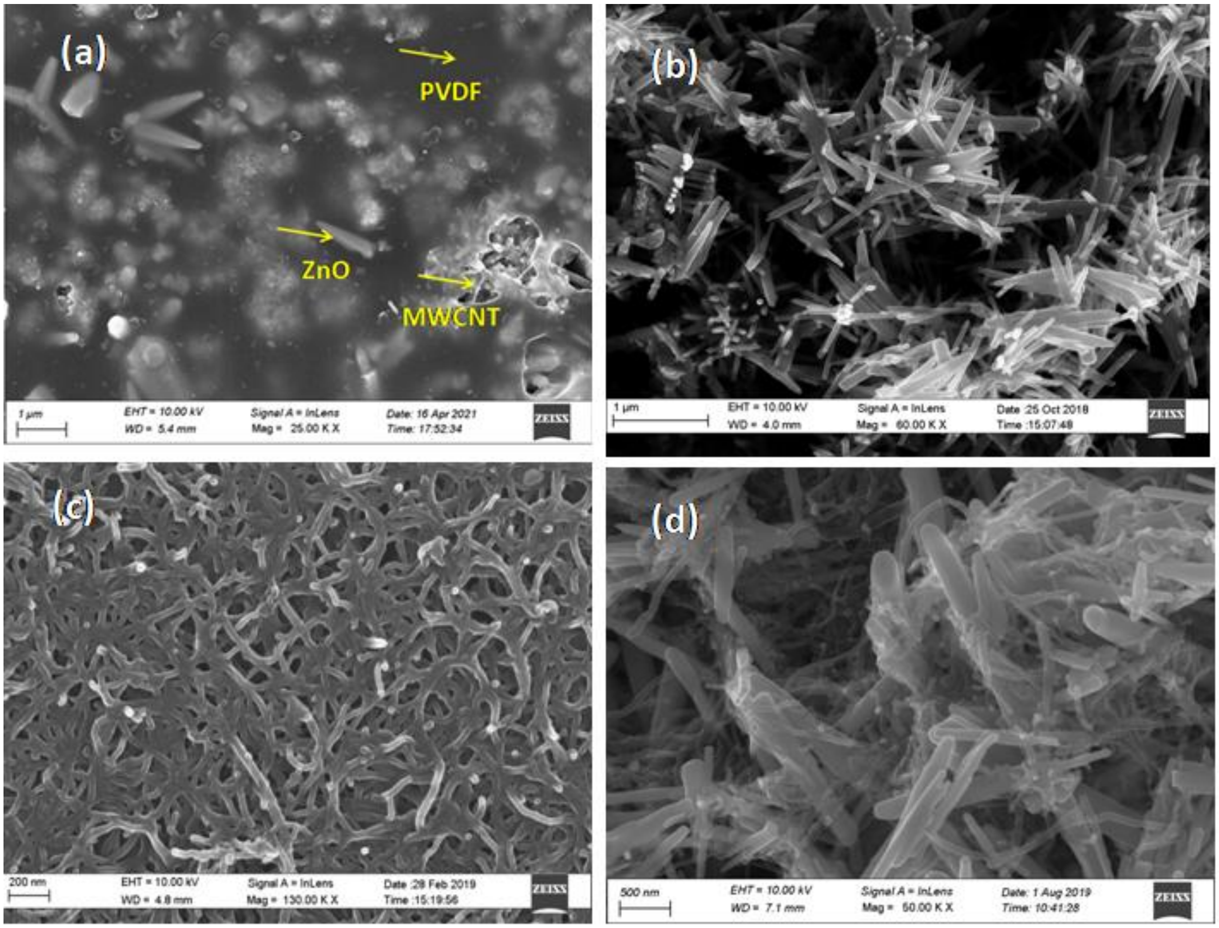

***Fig. 3.3.3(a)** FESEM image of 15PZNT film, FESEM image of **(b)** ZnO nanorod, **(c)** MWCNT and **(d)** ZnO-MWCNT powder after extensive sonication.*

As the composite films were fabricated by mixing of the constituents, the study of morphology is very much required.The morphology of the 15PZNT film was studied by using FESEM characterization and presented in **Fig. 3.3.3(a)** which confirmed the presence of ZnO nanorods and MWCNTs embedded within the PVDF matrix. Thus, the mixing of all the constituents was visualized from this characterization. In this regard, it is to be mentioned that, during the preparation of PVDF based composite films a total of 3 h ultrasonication was applied and in this condition there is always a chance of structural damage of MWCNT due to extensive ultrasonication. Therefore, to study this fact, ZnO, MWCNT and ZnO-MWCNT mixture were ultrasonicated in ethanol medium for 3 h and their morphology were studied by FESEM and presented in **Fig. 3.3.3(b-d)**, respectively. No structural damage of the fillers was seen from these figures. On the basis of this characterization, proper mixing of the constituents of the composite film without any structural damage was confirmed.

For optimization the MWCNT concentration in PVDF-ZnO matrix, composite films were fabricated by adding 15 wt% ZnO and different amount MWCNT (0, 0.05 wt%, 0.1 wt% and 0.15 wt%, respectively, for 15PZO-0 wt% CNT, 15PZO-0.05 wt% CNT, 15PZO-0.1 wt% CNT and 15PZO-0.2 wt% CNT) in PVDF matrix. Electrical performance of the composite films enhanced with increasing MWCNT concentration up to 0.1 wt% which was considered to be due to the formation of conductive network; but, further addition of MWCNT beyond 0.1 wt% caused the reduction in electrical performance which might be due to the increased agglomeration of MWCNT in the composite system.

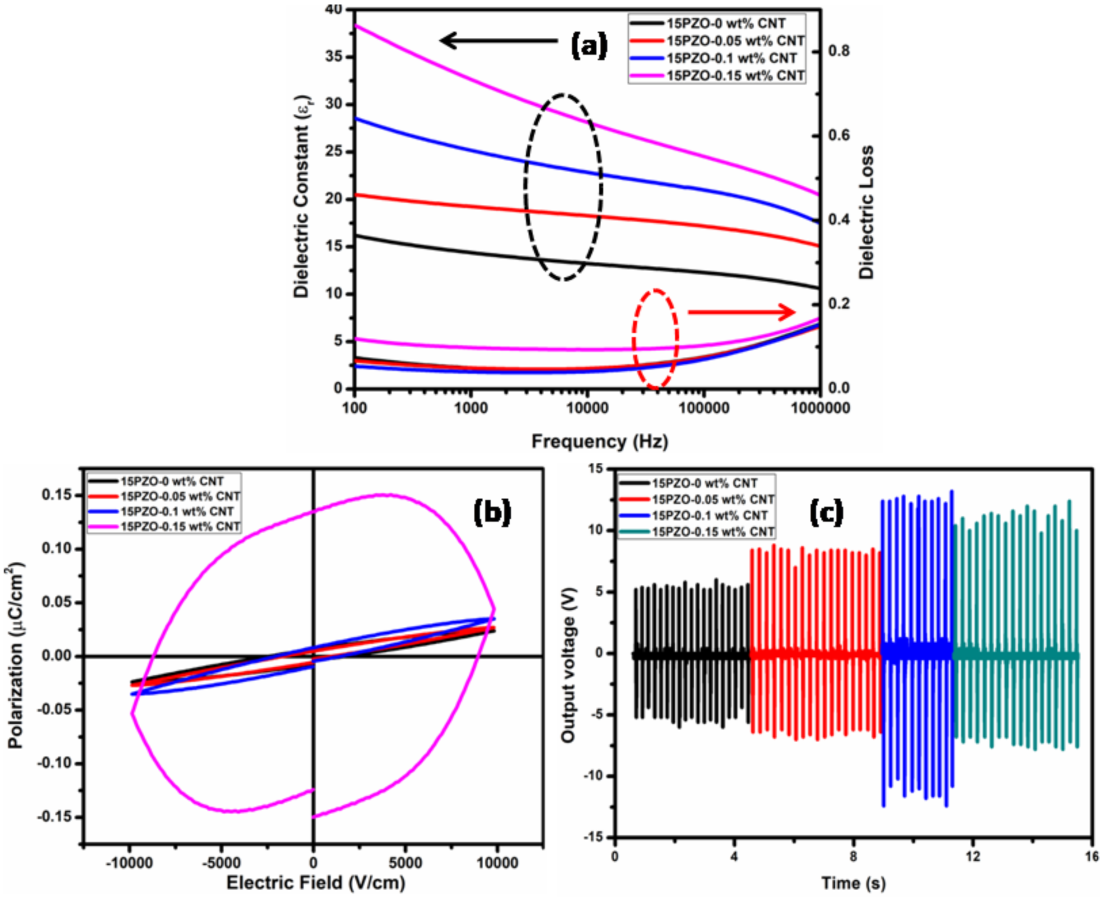

Fig. 3.3.4(a) *Frequency dependent dielectric permittivity and dielectric loss,* ***(b)*** *Polarization vs applied electric field (D-E) loop,* ***(c)*** *Comparison of open circuit output a.c. voltage of 15PZO-0 wt% CNT, 15PZO-0.05 wt%, 15PZO-0.1 wt% CNT and 15PZO-0.15 wt% CNT composite films.*

Though the dielectric permittivity increased gradually with 0.05, 0.1 and 0.15 wt% MWCNT addition in 15PZO film, the dielectric loss also increased significantly beyond 0.1 wt% which was due to the formation of more MWCNT agglomeration (**Fig. 3.3.4(a)**). The 15PZO-0.15 wt% CNT composites exhibited maximum value of dielectric permittivity but its dielectric loss tangent was very high. Therefore, this system was excluded. Hence, the 15PZO-0.1 wt% CNT film, exhibiting low dielectric loss along with significantly high dielectric permittivity, was chosen as the optimized one. The highly lossy nature of 15PZO-0.15 wt% CNT film was also confirmed from the study of P-E hysteresis loops of all the films (**Fig. 3.3.4(b)**). This lossy nature will result into the reduction of energy storage performance. Output voltage was also found to be maximum for 15PZO-0.1 wt% CNT composite film in comparison to those of other composite films (**Fig. 3.3.4(c)**). Considering all these facts, 15PZO-0.1wt% CNTs was considered as an optimized material to achieve high electrical performance. Therefore, 0.1 wt% MWCNT loading in the ZnO-PVDF composite films was selected in the present work.

3.3.1.2 Phase formation in the composite films

The presence of polar phase in the composite film is an important parameter for exhibiting good piezoelectric performance. The piezoelectricity arises due to the preferential orientation of CH_2/CF_2 dipoles which are positioned perpendicular to the polymer backbone [10]. The inclusion of filler particles in PVDF matrix generally improves the polarity of the resulting composite films [2, 11]. Actually, the filler material takes part in different types of interfacial interaction with -CH_2/-CF_2 dipoles of non-polar α-PVDF exhibiting TG^+TG^- chain conformation. As a result of this interfacial interaction, preferential re-orientation of the dipoles of PVDF occurs. Due to this re-orientation of dipoles, the TG^+TG^- structure (α-PVDF) of PVDF changes to TTTT (β-PVDF) and/or $T_3G^+T_3G^-$ (γ-PVDF) chain conformation resulting in non-polar to polar phase transformation. XRD and FTIR are two well known techniques which are widely used by researchers all over the world to determine this phase transformation.

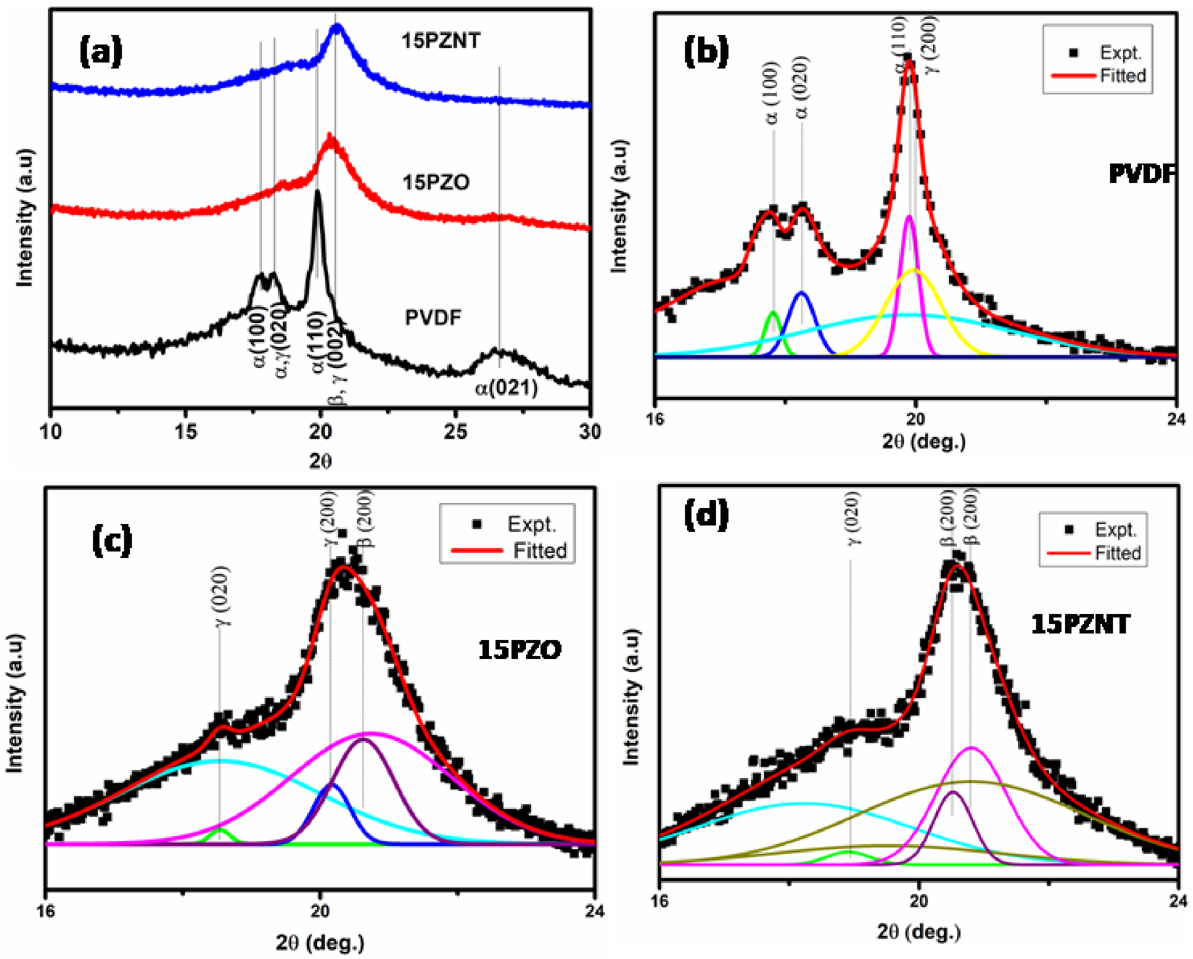

Fig. 3.3.5(a) *XRD pattern of pure PVDF, 15PZO and 15PZNT composites with 2θ ranging from 10º to 30º,* ***(b-d)*** *Deconvoluted XRD patterns of pure PVDF, 15PZO and 15PZNT composite films.*

To investigate the polar phase formation in the composite films, XRD characterization was first utilized. **Fig. 3.3.5(a)** presents the XRD patterns of pure PVDF, 15PZO and 15PZNT composite films. Pure PVDF exhibits characteristic peaks at diffraction angle 17.7°, 18.3°, 19.9° and 26.6° corresponding to planes (100), (020), (110) and (021), respectively, which confirmed the predominant presence of α-phase for this film [12-14]. On the other hand, for 15PZO and 15PZNT films, the peaks at 17.7° and 18.3° disappeared completely and the 26.6° peak gradually decreased its intensity. A new peak at 18.6° corresponding to γ-PVDF also appeared for these two films. Furthermore, the main characteristic peak at 19.9° for pure PVDF gradually shifted to higher diffraction angle for 15PZO and 15PZNT films, respectively. For 15PZNT composite, the intensities of the γ and β peaks enhanced significantly, which indicates the momentous enhancement of polar phase for this film. All these observations suggested that the polar phase of PVDF successively increased after ZnO and ZnO-MWCNT addition.

For better understanding of this non-polar to polar phase transformation, total degree of crystallinity and individual amount of beta crystallinity and gamma crystallinity of pure PVDF, 15PZO and 15PZNT films were calculated from deconvoluted XRD patterns (shown in **Fig. 3.3.5(b-d)).**The total degree of crystallinity of the nanocomposites was calculated from **Equation 3.3.1.**

$$\chi_{c_t} = \frac{\Sigma_{A_{cr}}}{\Sigma_{A_{cr}} + \Sigma_{A_{amr}}} \times 100\ \% \text{ ------------------ } (3.3.1)$$

Where $\sum A_{cr}$ and $\sum A_{amr}$ are the integral area of crystalline and amorphous region, respectively.Individual amount of beta and gama crystallinity were calculated from deconvoluted XRD graph from **Equation 3.3.2 and 3.3.3**, respectively.

$$\chi_{c_\beta} = \chi_{c_t} \times \frac{\Sigma_{A_\beta}}{\Sigma_{A_\beta} + \Sigma_{A_\gamma}}\ \%\text{-------------------- } (3.3.2)$$

$$\chi_{c_\gamma} = \chi_{c_t} \times \frac{\Sigma_{A_\beta}}{\Sigma_{A_\beta} + \Sigma_{A_\gamma}}\ \%\text{---------------------}(3.3.3)$$

Where $\sum A_\beta$and $\sum A_\gamma$ are the total integral area of β peak and γ peak, respectively.

The individual quantification of total crystallinity, beta phase crystallinity and gama phase crystallinity of PVDF, 15PZO and 15PZNT were represented in **Table 3.3.1.**

Table 3.3.1 *Amount of*χ_{c_t},χ_{c_β} *and* χ_{c_γ} *for PVDF, 15PZO and 15PZNT composite films.*

Sample Name	Total degree of crystallinity (χ_{c_t}) (%)	Beta phase crystallinity (χ_{c_β}) (%)	Gama phase crystallinity (χ_{c_γ}) (%)
PVDF	67.2		
15PZO	56.1	26.6	29.5
15PZNT	32.4	30.6	1.78

Total degree of crystallinity is reduced to 56.1% and 32.4% for 15PZO and 15PZNT films from a value of 67.2% for pure PVDF. This reduction in crystallinity of PVDF may be explained on the basis of the induced polymorphism after filler addition in its matrix [15]. When no fillers were included into PVDF matrix, homogeneous growth of its α-crystallites occurred and as a result, the total degree of crystallinity became comparatively high. But when fillers were included into its matrix, they acted as nucleation centres and interactsstrongly with PVDF dipoles. Therefore, the homogeneous growth of crystallites of PVDF was restrained and heterogeneous nucleation of crystallites occurred. The fillers also prevented the formation of extended chain conformation due to their existence in the region of inter-chain spacing. On the other hand, the large number of fillers, which did not interact with PVDF dipoles and was dormant in the PVDF matrix, also inhibited the growth of crystallites. All these facts together caused the reduction in total degree of crystallinity of PVDF after filler addition. The cross linking of polymers induced by fillers may also be another possible cause of the hindrance in crystallinity. The heterogeneous nucleation of crystallites is mainly governed by the interaction of PVDF dipoles with fillers. On the other hand, the interaction of PVDF dipoles with fillers commonly helps in the re-orientation of chain conformation of PVDF which cause the non-polar to polar phase transformation (discussed earlier). Therefore, the induced polymorphism may also be considered as a possible cause of enhancement of polarity of the composite films after filler addition. Beta crystallinity is significantly enhanced after CNT addition within ZnO-PVDF composite which indicated that the PVDF-ZnO-CNT composite may exhibit better piezoelectric response.

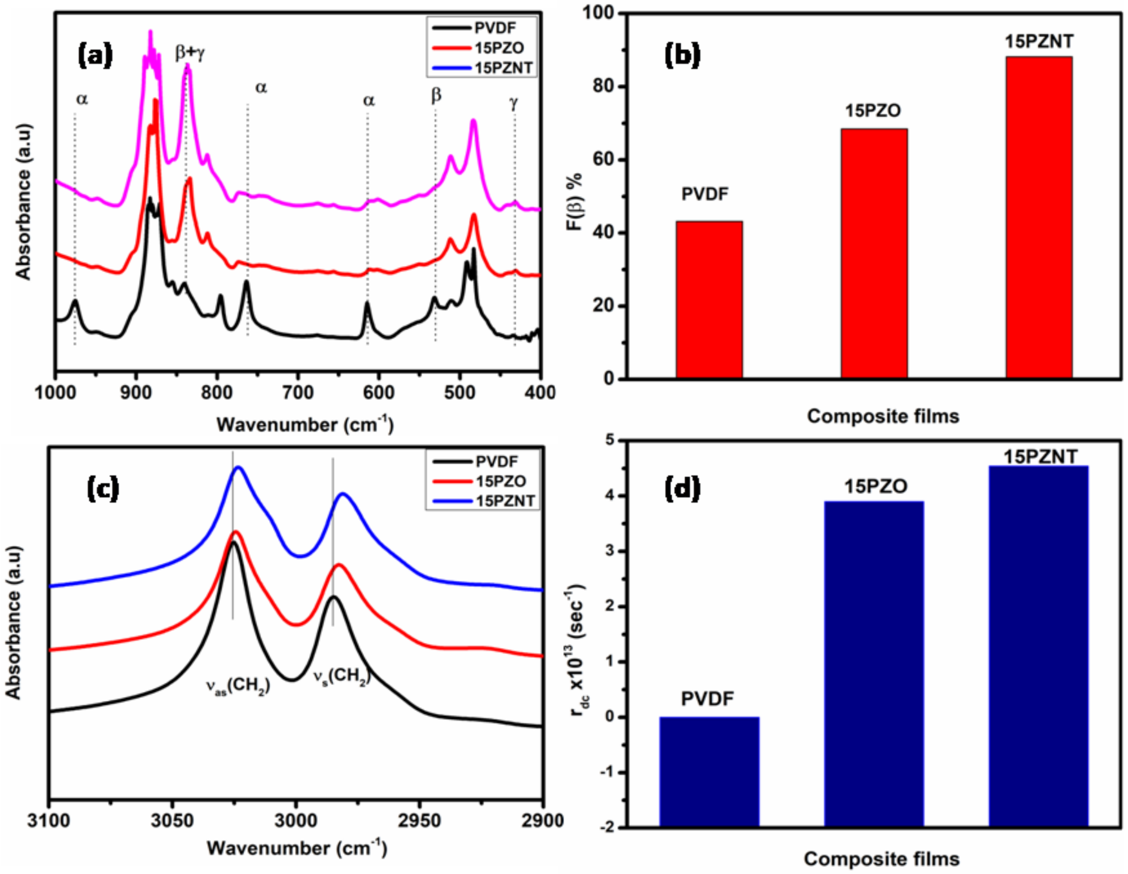

Fig. 3.3.6(a) *FTIR spectra,* ***(b)*** *Polar phase of composite films calculated from FTIR spectra,* ***(c)*** *FTIR stretching vibration band shift and* ***(d)*** *Damping co-efficient of pure PVDF, 15PZO and 15PZNT films, respectively.*

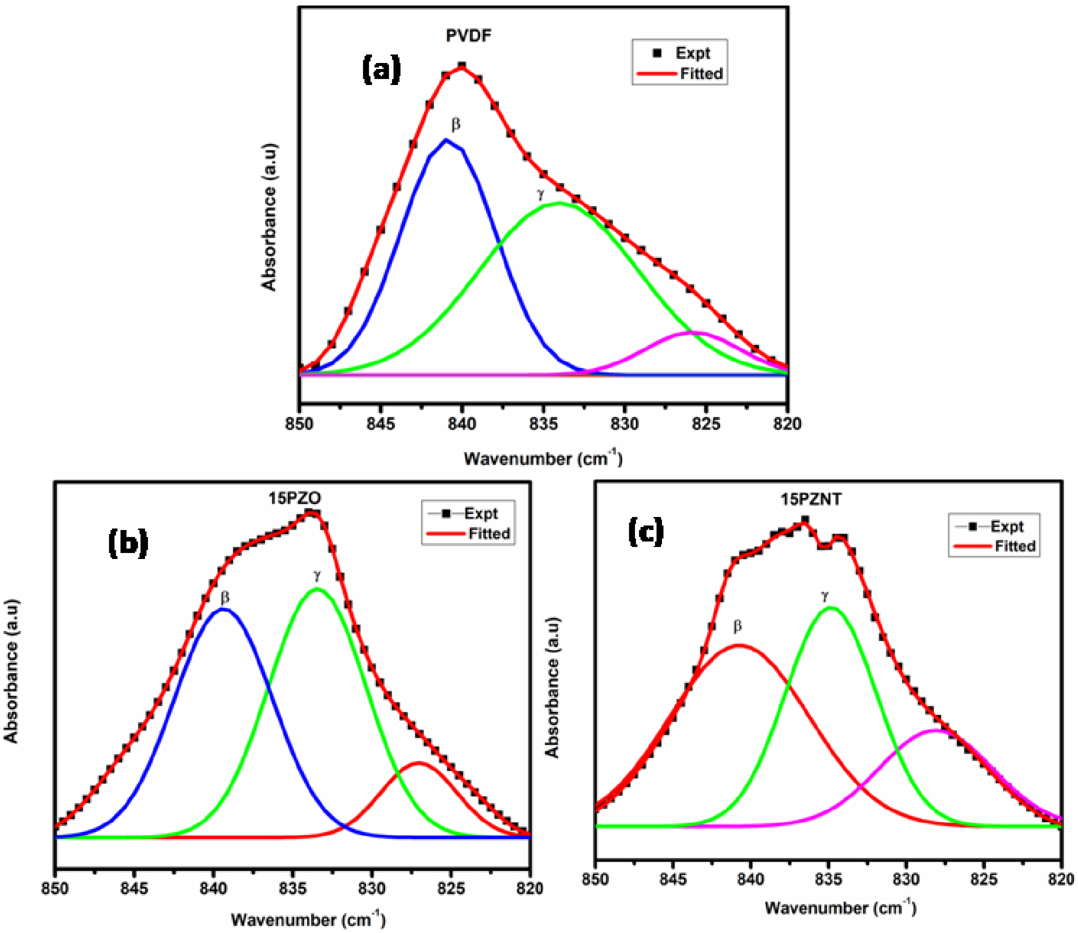

***Fig. 3.3.7** The deconvoluted FTIR spectra (range within 850-820 cm^{-1}) of**(a)**PVDF, **(b)**15PZO and **(c)**15PZNT composites*

For detail study of polar phase formation in the fabricated composite films, extensive FTIR study was also performed. **Fig. 3.3.6(a)** presents the FTIR absorption spectra of pure PVDF, 15PZO and 15PZNT composite films within the wavenumber region of 1000-400 cm^{-1}. Pure PVDF exhibited vibrational bands at 612 cm^{-1}, 764 cm^{-1}, 796 cm^{-1}, 976 cm^{-1} corresponding to nonpolar α phase, 510 cm^{-1} for β phase and 840 cm^{-1} for both β and γ phases [12, 14]. But after incorporation of ZnO rods in PVDF matrix, intensity of these α peaks reduced and bands were almost diminished. The intensity of the peak at 840 cm^{-1} increased gradually for 15PZO and 15PZNT films, respectively, which inferred the gradual enhancement of their polar phase. The amount of electroactive polar phase (F(EA)) present is calculated from Beer-Lambert law given by **Equation 3.1.1** [14].The calculated electroactive phase fraction (F(EA)) for all the composite samples is presented in Fig. **3.3.6(b)** and was found to be ~ 43.2, 68.5 and 88.9 % for pure PVDF, 15PZO and 15PZNT composite, respectively. The 840 cm^{-1} absorption bands of neat PVDF, 15PZO and 15PZNT films were deconvoluted **(Fig. 3.3.7.(a-c))** to evaluate the quantitative amounts of individual β and γ phases within them and the results are presented in **Table 3.3.2**.

Table 3.3.2 *Individual amount of polar phase calculation for PVDF, 15PZO and 15PZNT composites*

Sample Name	Polar phase Fraction (F_{EA})(%)	Β phase Fraction (F_{β}) (%)	γ phase Fraction (F_{γ}) (%)	Relative amount of β phase w.r.t to γ phase ($F_{\beta\gamma}$) (%)	Relative amount of γ phase w.r.t toβ phase ($F_{\gamma\beta}$) (%)
PVDF	43.2	19	24.1	44.1	55.8
PVDF/ZnO	68.5	34.2	34.4	49.7	50.3
PVDF/ZnO/CNT	88.9	45.3	43.6	50. 9	49

The concurrent incorporation of both ZnO nanorods and MWCNT produced an upsurge in the polar phase, which was one of the main motive of the present work. The cause of gradual enhancement of polar phase after ZnO and ZnO-MWCNT addition in PVDF matrix, respectively, may be explained in the following way. At first, when only ZnO was added to PVDF matrix, the polar phase increased due to interfacial electrostatic interaction between positively charged $–CH_2$ dipole of PVDF and negatively charged ZnO surface [11, 16]. In the next step, when three phase composites were fabricated by the addition of both ZnO and MWCNT into PVDF matrix, some extra effects arising from the third MWCNT phase played very important role along with the previously existed electrostatic interaction between –CH_2 dipoles of PVDF and ZnO surface. Firstly, the third MWCNT phase improved the homogeneity of filler distribution in PVDF matrix by reducing the compatibility issue between them. Secondly, the π-electrons of carbon atom of MWCNT interacted very strongly with the –CH_2 dipoles of PVDF. This type of results was also previously established by several researchers all over the world through various experimental and theoretical studies [2, 17-18]. Thus the obtained result of gradual improvement of polar phase of PVDF after ZnO and ZnO-MWCNT addition, respectively, is justified. The maximum polar phase was exhibited by 15PZNT film. For better interpretation of the interfacial interaction, FTIR spectra of PVDF, 15PZO and 15PZNT samples within the wavenumber region 3100 cm^{-1} to 2900 cm^{-1} were studied (Shown in **Fig.3.3.6(c)**) ; because, this region is mainly attributed to symmetric (ν_s) and asymmetric (ν_{as}) stretching vibration band of –CH_2 dipole which are not coupled with any other vibrational modes. Therefore the absorption spectra within this region provide detailed information about the interfacial interaction between –CH_2 dipole of PVDF and nanofiller surface. After incorporation of ZnO filler in PVDF matrix, symmetric and asymmetric stretching vibrational band of –CH_2 dipole shifted towards lower wavenumber region compared to pure PVDF. The gradual shift of vibrational bands towards lower energy can be explained by damped harmonic oscillator model. At first, it was assumed that, these two vibration bands had no damping effect when no filler was included in PVDF matrix. With filler loading in PVDF matrix damping appeared due to electrostatic interaction between –CH_2 dipole of PVDF and filler surface. The shifting of these absorption bands towards lower wavenumber region for 15PZNT compared to that of 15PZO film confirmed our earlier assumption of more interfacial electrostatic interaction of –CH_2 dipoles of PVDF with third MWCNT phase. In order to get the quantitative amount of electrostatic interaction, damping coefficient of the composite films was calculated (**Fig. 3.3.6 (d)**) from the peak shifting of the asymmetric –CH_2 stretching vibrational band using **Equation 3.1.2**. The damping coefficients were found to be 0, 3.90×10^{13} and 4.53×10^{13} sec^{-1}, respectively, for neat PVDF, 15PZO and 15PZNT films. The gradual increase in damping coefficient justified our consideration of gradual improvement of interfacial interaction for the respective films. The gradual enhancement of interfacial interaction between –CH_2 dipoles of PVDF and filler surface for 15PZO and 15PZNT films was further confirmed by the study of their FTIR absorption spectra within the wavenumber region of 3100 cm^{-1} to 2900 cm^{-1} where the stretching vibrations of –CH_2 dipoles are only responsible for the occurrence of the resulting bands. The gradual shift of –CH_2 stretching vibration band towards lower energy region and the increase in damping coefficient (r_{dc}) confirmed the gradual enhancement of interfacial interaction for pure PVDF, 15PZO and 15PZNT films, respectively [11, 19-21]. Thus the XRD and FTIR characterizations of the composite films confirmed the enhancement of polarity of PVDF after ZnO and MWCNT addition. Therefore, the electroactive properties like dielectric permittivity, ferroelectric polarization and piezoelectric performance are expected to be enhanced. In this regard, it is to be mentioned that the interfacial interaction between –CH_2 dipoles of PVDF and fillers helped to reorient the TG^+TG^- chain conformation of non-polar α-PVDF in a new fashion such that it achieves polar phase chain conformation. As this reorientation of dipoles could not be controlled in a desirable manner, the TG^+TG^- chain conformation took both the TTTT and $T_3G^+T_3G^-$ chain conformations corresponding to polar β-PVDF and γ-PVDF, respectively. Therefore, though the achievement of improved β phase in the composite films was one of the main target of the present work, enhancement of both the β and γ phase was obtained. It is worth mentioning that for both of these cases; the total amount of polarity increased which is very beneficial for the desired purpose of the present work.

3.3.1.3 Dielectric properties of the composite films

The dielectric properties are very important parameters for exploring the application of these films as energy storage and harvesting device. Dielectric constant measures the charge holding capacity of the material [11].

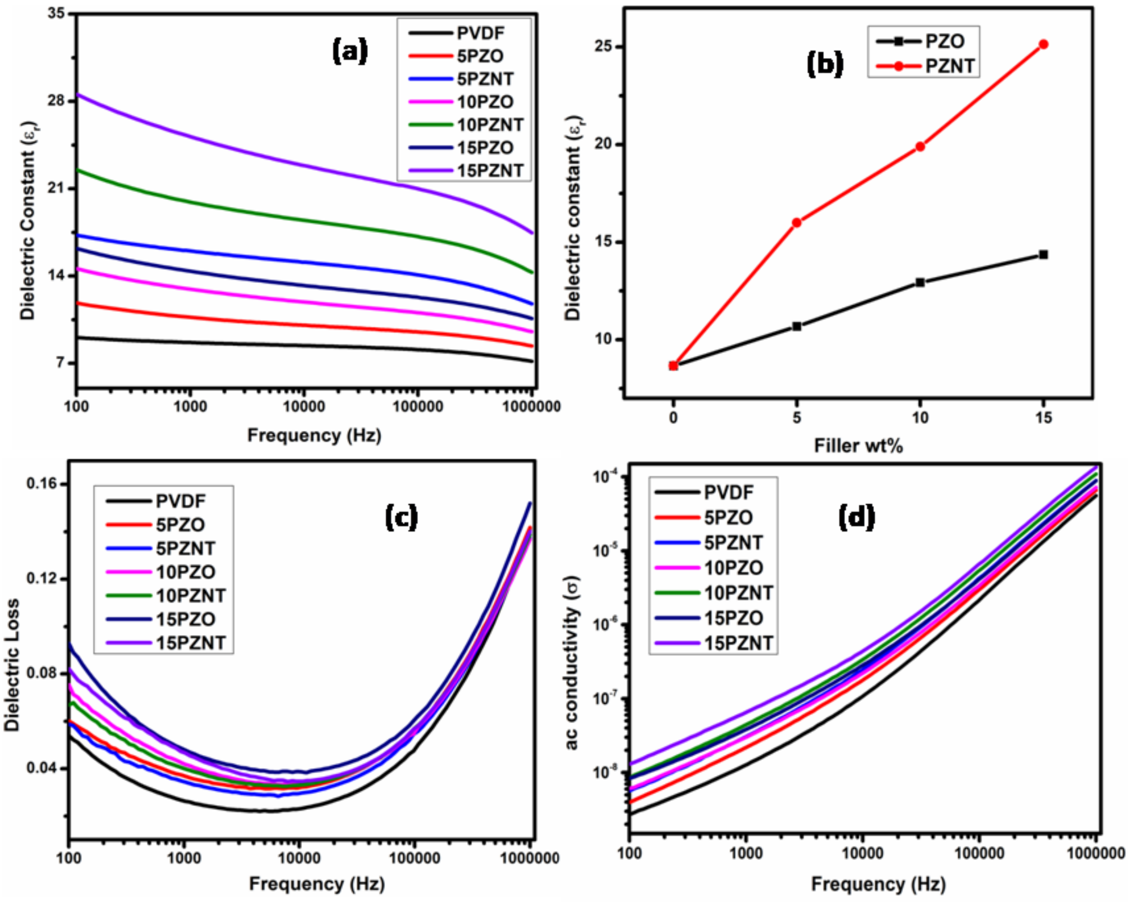

Fig. 3.3.8 *(a) Frequency dependent and (b) filler concentration dependent dielectric permittivity and Frequency dependent (c) dielectric loss, (d) a.c. conductivity of PVDF and all the composite films.*

Frequency dependent dielectric permittivity of pure PVDF and all composite film are shown in **Fig. 3.3.8(a)**. Dielectric permittivity decreased with increasing frequency for all composites. Generally, dielectric behaviour of composites comprises of four types of polarizations namely, electronic polarization, ionic polarization, orientation polarization and interfacial polarization. At low frequencies, the contributions of all these four types of polarizations are present but at higher frequency, ionic polarization and interfacial polarization almost disappear [22-23]. Maxwell-Wagner interfacial polarization occurs due to the charge carrier accumulation at the interface between polymer matrix and filler particles. Dielectric constant of PVDF composites increased with increasing ZnO concentration in PVDF matrix. After incorporation of MWCNT in ZnO-PVDF composites, dielectric value increased further (**Fig. 3.3.8(b)**) and the 15PZNT composite system exhibited maximum dielectric value. When ZnO filler was added in PVDF matrix, a capacitor like arrangement was created in PVDF matrix. As a result, more charges were stored in the composite system and the dielectric value got enhanced. After the addition of MWCNT as conductive third phase filler, the interfacial polarization increased between fillers and PVDF matrix leading to further enhancement in the dielectric value of the composite. MWCNT reduced the internal resistance of the composite system and also created a conduction pathway between ZnO nanorods and PVDF matrix. For MWCNT based composite system, interfacial interaction increased due to more compatibility of MWCNT in PVDF matrix [24]. On the other hand, the increase in dielectric permittivity may also be associated with the reduction in total degree of crystallinity as described earlier. The reduced crystallinity of the composite films helped in better movement of dipoles (along the applied field direction) in the amorphous region and as a result, the permittivity increased [11].

The frequency dependent dielectric loss of all the composite films was also studied (**Fig. 3.3.8(c)**). Dielectric loss increased successively after addition of ZnO rods in PVDF matrix and further addition of MWCNT into it. The increase in dielectric loss was associated with the formation of conducting network by addition of ZnO fillers into PVDF matrix which further increased due to conductive MWCNT addition into the composite system. The a.c. conductivity of dielectric materials can be expressed by **Equation 3.2.5**. Frequency dependent a.c. conductivity for pure PVDF and all the composite film are shown in **Fig 3.3.8(d)**, increased with increasing filler loading in PVDF which further increased after MWCNT addition into the system. This result can again be explained on the basis of formation of conducting network after filler addition and further MWCNT addition as described earlier.

3.3.1.4 Ferroelectric properties and energy storage performance

The ferroelectric attribution of the nanocomposites play very important role in determining its application as piezoelectric energy harvester. **Fig. 3.3.9(a)** depicts the room electric field (E) dependent electric displacement (D) or polarization (P) (P-E hysteresis loop or D-E hysteresis loop) of pure PVDF and all the composite films measured at room temperature. Ferroelectric properties of PVDF based composites are dependent on its electroactive phase. The ferroelectric domains consisting of molecular dipoles were randomly oriented in the polymer matrix. With the application of external electric field, the alignment of the dipoles changed and a preferred orientation of them along the field direction appeared which contributed to the enhancement of net polarization.

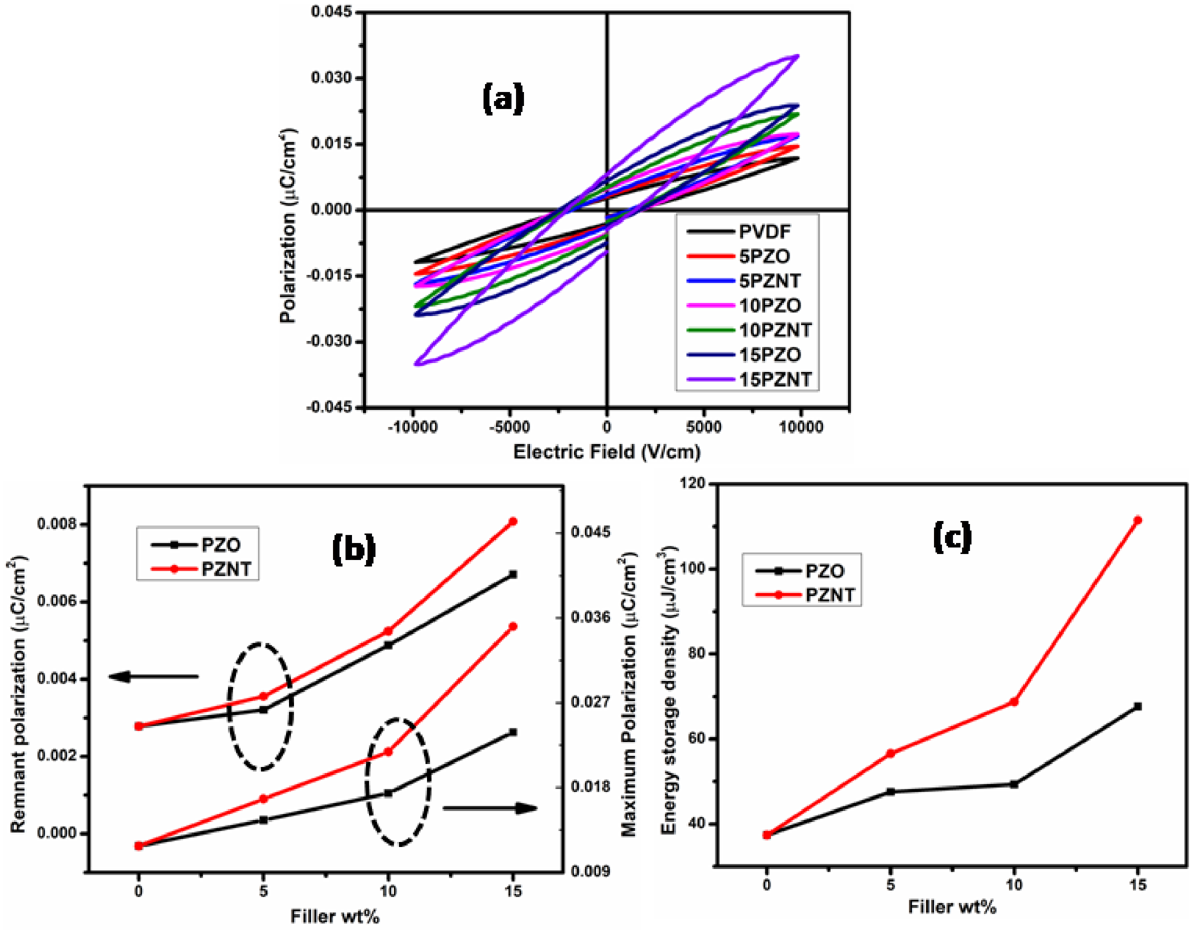

***Fig. 3.3.9 (a)** Electric displacement vs applied electric field (D-E) loop, filler concentration dependent **(b)** remnant and maximum electric polarization and **(c)** energy storage density of PVDF and all composite films.*

The variation of remnant polarization and maximum polarization with filler concentration are shown in **Fig. 3.3.9(b)**. After incorporation of ZnO nanorods in PVDF matrix, both remnant polarization and maximum polarization value increased compared to PVDF. The addition of MWCNT as conducting filler further increased the remnant polarization and maximum polarization value. 15PZNT composite film exhibited maximum polarization value 0.035μC/cm^2. This may be due to the more conducting nature of the added MWCNT than that of the polymer, which resulted in a change in mobilization within the particles and hence, increased the hetero polarization of the composite [3]. The ferroelectric properties of the composite films are also strongly dependent on the electroactive phase of PVDF [3, 25]. The addition of ZnO-MWCNT into the PVDF matrix played an important role in accelerating the internal change of the nanocomposite, which has changed the polarization within the sample.

The energy storage performance of any ferroelectric material strongly depends on its ferroelectric properties. Therefore, the energy storage density (U_{stored}) of all the composite films were calculated from their D-E loops using the **Equation 3.1.4**. The stored electrical energy storage density as a function of filler loading for all the composite films fabricated in the present work are presented in **Fig. 3.3.9(c)**. Energy storage density of the nanocomposites increased as the polarization increased with the increment in concentration of filler loading for both PVDF-ZnO (PZO) and PVDF-ZnO-MWCNT (PZNT) system. It is observed that the 15PZNT nanocomposite exhibited the highest energy storage density than the other composites studied here at the same value applied electric field. The energy storage density of PZNT system increased than that of PZO system due to the enhancement of dielectric permittivity of MWCNT added composites.

3.3.1.5 Energy harvesting performance of composite films

In order to investigate the piezoelectric properties of composite systems, the output electrical properties of the fabricated composites were studied by a digital oscilloscope using human finger tapping. After applying time varying applied force on the films, dipoles of the PVDF oscillated and an electrical potential generated across the film.

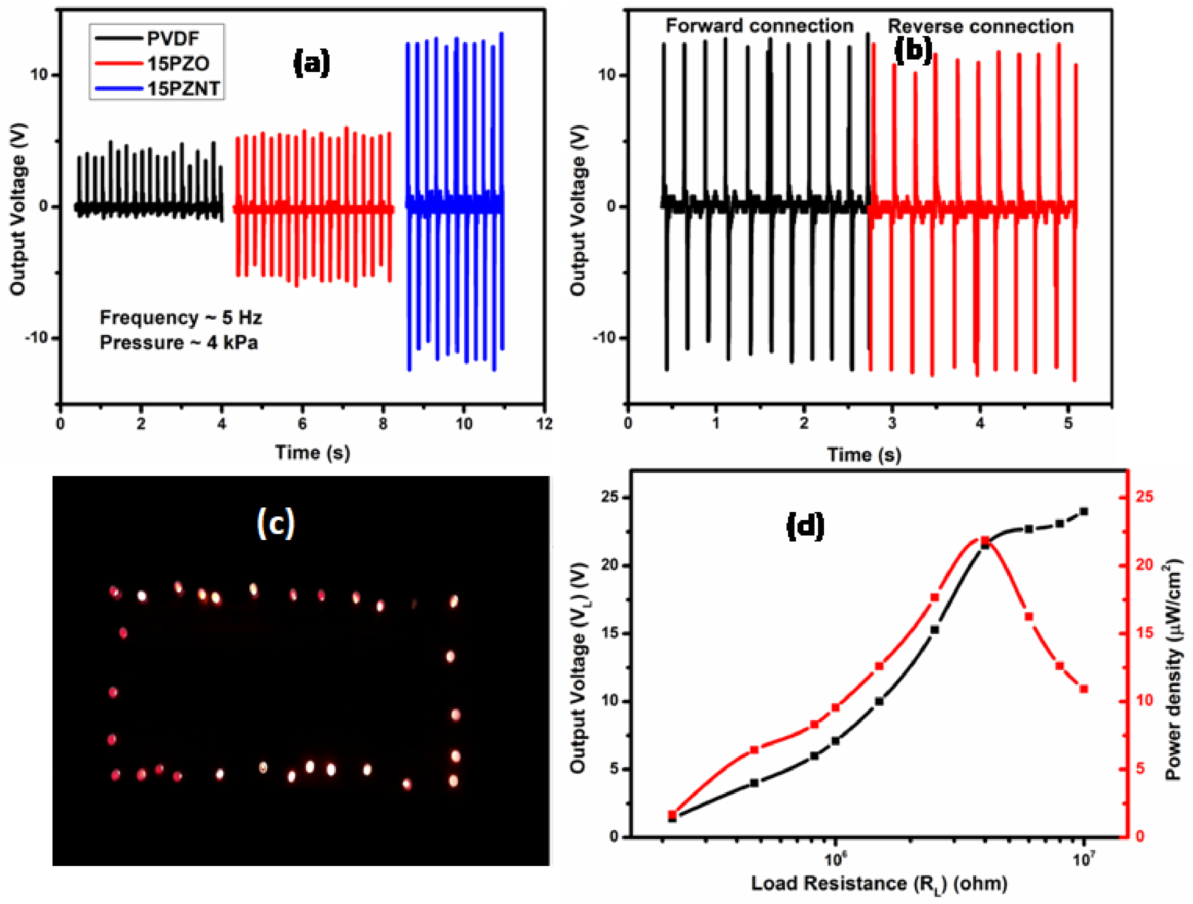

***Fig. 3.3.10 (a)** Comparison of open circuit output a.c. voltage of PVDF, 15PZO and 15PZNT composites film, **(b)** Switching polarity test of 15PZNTsample, **(c)** Led glowing performance at switch on condition of 15PZNT film and **(d)** Variation of output voltage and power density as a function of load resistance of 15PZNT film.*

Fig. 3.3.10(a) presents the output voltage (open circuit peak to peak a.c. voltage) of pure PVDF, 15PZO and 15PZNT composite films upon application of repeated human finger tapping and releasing force (Pressure ~ 4 kPa and Frequency ~ 5 Hz) on them. The maximum output voltage ~ 22 V was obtained in 15PZNT film. This happened due to the better dispersion of polymer ceramic composites after addition of MWCNT [3, 24]. Besides, MWCNT created a conduction pathway within the polymer composites that reduced the internal resistance of the composite system [3]. The film exhibited the same amplitude of output voltage in forward and reverse conditions by reversing the electrode connections (**Fig. 3.3.10(b)**) under the application of same stress. This result confirmed that the output voltage appeared due to piezoelectric effect only. The generated a.c. output voltage was converted to d.c. output voltage using a bridge rectifier IC (DB 107). This rectified d.c. voltage was able to charge a 10 μF capacitor up to ~ 3 V which was used to glow 30 commercial LEDs (**Fig. 3.3.10 (c)**). Output voltage vs. load resistance graph of 15PZNT composite film is shown in **Fig. 3.3.10 (d)**. The output voltage was gradually increased with load resistance and reached a saturation value at 4 MΩ. The power density (P) was calculated from the output voltage (V_L) through different load resistance (R_L) by using the Equation 3.1.4. The maximum power density of 15PZNT composite film was found to be 21.41 μW cm^{-2} at 4 MΩ load resistance (shown in **Fig. 3.3.10(d)**).

3.3.1.6 Verification of experimental results by theoretical simulation

To verify the experimental results, simulation was performed using COMSOL Multiphysics software. Electric field and polarization were simulated as a function of applied external voltage. Piezoelectric potential was simulated under similar amount of pressure applied on each of the devices for the same dimensions as our fabricated devices. It is well reported that, when rodshaped fillers are included into PVDF based films, the rods are generally oriented in the inplane direction; i.e., maximum number of rods orient themselves along the plane of the composite film and the occurrence of rod-shaped fillers along the film's thickness is very rare. But, during simulation, we need to consider the cross section of the composite films. For the sake of simplicity, both the ZnO nanorods and CNTs are considered to be oriented along the length of the film so that the film's cross section contains the cross sections of ZnO nanorods/ CNTs /PVDF matrix. The cross section of ZnO rods were considered as circular as the top surfaces of ZnO nanorods were almost round. Therefore, during simulation, ZnO rods and CNT are represented by big and small circle respectively. The remaining region is filled by PVDF matrix. In our work, a small portion of the film's cross section was considered for simulation for better view. Here, simulation was performed for PVDF/ZnO and PVDF/ZnO/CNT composites to understand the effect of MWCNT addition as a third phase conductive filler in PVDF matrix.

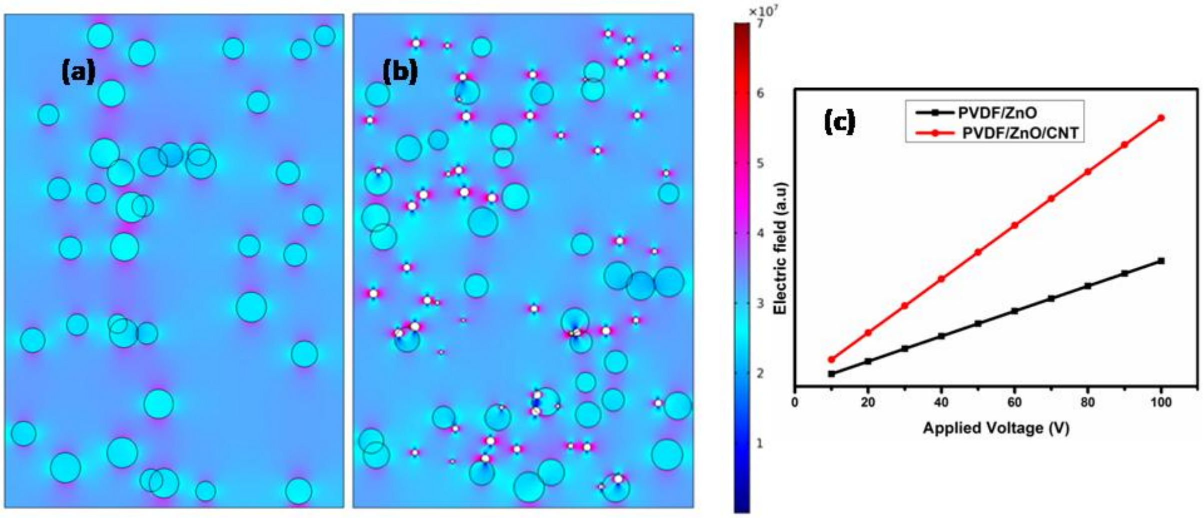

__Fig. 3.3.11__ Simulated electric field distribution under the applied voltage of 100 V for __(a)__ ZnO-PVDF and __(b)__ ZnO-MWCNT-PVDF composites, __(c)__ Simulated electric field intensity as a function of applied voltage of PVDF/ZnO and PVDF/ZnO/MWCNT composites.

Fig. 3.3.11(a) and Fig. **3.3.11(b)** presents the simulated electric field distribution of PZO and PZNT composites, respectively, under an external applied voltage of 100 V. The comparison of electric field enhancement of PZO and PZNT composites as a function of increasing applied voltage is shown in **Fig. 3.3.11(c)**. PZO and PZNT composites show similar trend of electric field enhancement. For both the composite films, electric field increased linearly with increasing applied voltage. **Fig. 3.3.11(a) and Fig. 3.3.11(b)** also suggested that the partial electric field on MWCNT (for PZNT composite) is much larger than that on ZnO. This was believed to be due to the increase in local electric field with the increased applied external voltage on the composites by the addition of MWCNT as conductive fillers within polymer-ceramic composites. This type of result was previously reported by several researchers [26-28]. Enhancement of electric field is a key factor to improve the polarization of the ferroelectric system [26].

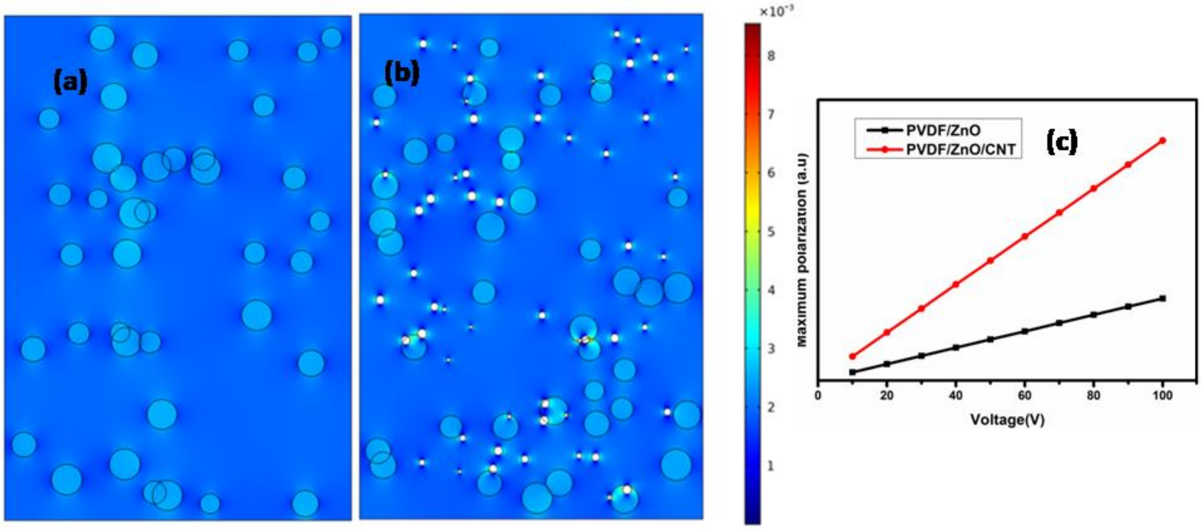

Fig. 3.3.12 *Simulated polarization distribution under the applied voltage of 100 V for* ***(a)*** *ZnO-PVDF and* ***(b)*** *ZnO-MWCNT-PVDF composites,* ***(c)*** *Simulated polarization distribution as a function of applied voltage of PVDF/ZnO and PVDF/ZnO/MWCNT composites.*

Polarization distribution of PZO and PZNT composites at an applied voltage 100 V are shown in **Fig. 3.3.12(a) and Fig. 3.3.12(b),** respectively, depicted by colour code with same scale across the composites. The comparison of simulated polarization of PZO and PZNT composites as a function of applied external voltage is shown in **Fig. 3.3.12(c)**. From this simulation it was observed that the polarization is much higher in PZNT composite system compared to that of PZO composite. As the fabricated PVDF based films are ferroelectric in nature, the improved polarization may be considered to be the main consequence of electric field enhancement as described earlier [29]. This result clearly indicates that the addition of MWCNT conductive filler has significantly enhanced the polarization of ZnO rods. Thus the increment of polarization in the experimental P-E loops after CNT addition is also justified.

In order to check the effect of MWCNT on the piezoelectric output voltage of PVDF composites, piezoelectric potentials of PZO and PZNT composites are also simulated using finite element method under the application of similar pressure on each device. During simulation, the main source of piezoelectric potentials of any composite system is the value of the piezoelectric coefficient (d_{33}) of its individual components. Though PVDF and ZnO are well known piezoelectric material, MWCNT shows no d_{33} value [30-31]. Therefore, it is evident that the simulation may not show any increment in piezoelectric potential after MWCNT addition in PZO composite system. On the other hand, it is reported that, after ZnO addition the electroactive β phase of PVDF increases significantly and after CNT addition the β phase of PVDF also increases [32-33]. From previous experiments in the present work, the electroactive β phase of PVDF, 15PZO and 15PZNT films was also found to be enhanced gradually. On the other hand, a linear relationship exists between the polar phase of PVDF and its d_{33} value [31]. Therefore, the d_{33} value of PVDF was gradually enhanced during simulation by certain amounts for PZO and PZNT films compared to that of bare PVDF [26, 34].

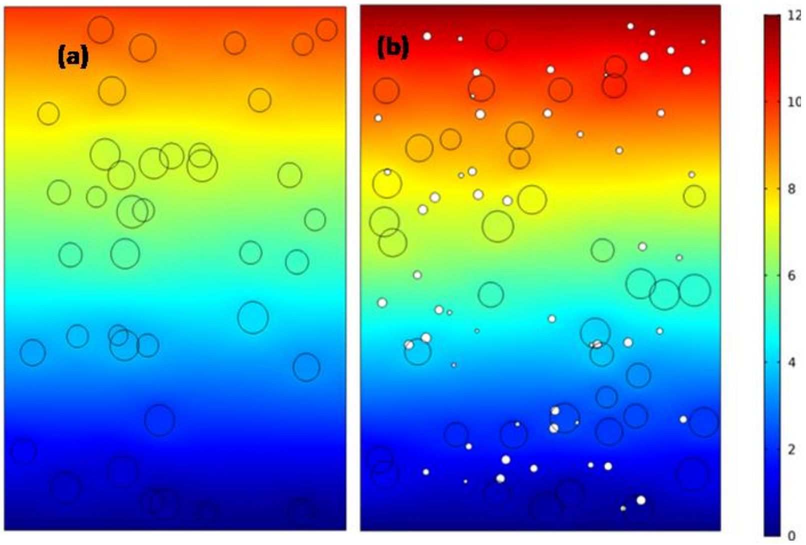

Fig. 3.3.13 *Simulated piezoelectric potential distribution of* ***(a)*** *PVDF-ZnO,* ***(b)*** *PVDF-ZnO-MWCNT composites.*

Fig 3.3.13(a) and Fig. 3.3.13(b) present the corresponding piezoelectric potentials of PZO and PZNT composites, respectively. A close observation of the colour codes for both the simulation (**Fig. 3.3.13(a-b)**) reveal that the piezoelectric potential of PZNT film is significantly higher than that of PZO composite. As CNT has no d_{33} value, this enhancement of piezoelectric potential is plausibly due to the enhanced polarization and improved electroactive β phase of the composite systems after CNT addition. On the other hand, as PZNT films contained conducting MWCNTs, the charge accumulation in the PVDF-filler interface was comparatively high compared to that of PVDF films (confirmed from dielectric studies). This large amount of space charge, upon application of applied stress, may increase the space charge polarization by the effect of piezoelectric potential. This space charge polarization, after being added with piezoelectric polarization, may improve the overall output piezoelectric performance. Therefore, the increased space charge polarization of PZNT film induced by MWCNT may be considered as another possible cause of increase in piezoelectric output voltage [26]. Considering all these facts, the output voltage of different composite system obtained in the present study is justified.

3.3.1.7 Conclusion

Three phase composite films comprising of PVDF matrix, wet chemically synthesized ZnO nanorod fillers and third conductive MWCNT phase were fabricated using drop casting technique. The third phase conductive MWCNT reduced the compatibility issue and supported homogeneous dispersion of ZnO in PVDF matrix which further improved the polarity of resulting composite films by enhancing the interfacial interaction with $–CH_2$ dipoles of PVDF which lead to the enhancement of electroactive phase, dielectric permittivity, ferroelectric polarization, energy storage density and mechanical energy harvesting performance. The observed experimental results of electrical properties were also verified by theoretical simulation. Conductive MWCNT improved the connectivity between ZnO nanorods dispersed in insulating PVDF matrix and between the composite films and electrodes which improved the output mechanical energy harvesting performance. The 15 wt% ZnO and 0.1 wt% MWCNT loaded PVDF film (15PZNT) exhibited maximum 22 V a.c. output voltage and 21.41 μW cm^{-2} power density at 4 MΩ load resistance upon repeated finger tapping on it. After rectification of this a.c. voltage, the obtained d.c. signal was utilized to charge a 10 μF commercial capacitor upto ~ 3 V which was further used to glow 30 commercial LEDs instantly. Therefore, the fabricated piezoelectric nanogenerator device can definitely be explored as a self-powered sensor and applied in powering low power compatible smart electronic devices.

References:

1. J. Nunes-Pereira, P. Sharma, L. C. Fernandes, J. Oliveira, J. A. Moreira, R. K. Sharma and S. Lanceros-Mendez, *Compos. B. Eng.*, 2018, **142**, 1-8.
2. I. Chinya, A Sasmal and Shrabanee Sen, *J. Alloys Compd.*,2020, **815**, 152312.
3. A. Pal, A Sasmal, B. Manoj, D.P. Rao, A.K. Halder and S.Sen, *Mater. Chem. Phys.,* 2020,**244**, 122639.
4. Z.-M. Dang, Y. Shen and C.-W. Nan, *Appl. Phys. Lett.*, 2002, **81**, 4814-4816.
5. Prateek, V.K.Thakur and R. K. Gupta, *Chem. Rev.,* 2016, **116**, 4260-4317.
6. X. J. Zhang, G. S. Wang, Y. Z. Wei, L. GuO and M. S. Cao, *J. Mater. Chem. A.,* 2013, **1**, 12115-12122.
7. K. Silakaewa and P. Thongbai, *RSC Adv*., 2019, **9**, 23498-23507.
8. A Sultana, Md M. Alam, S. Garain, T. K. Sinha, T. R. Middya and D. Mandal, *ACS appl. Mater. Interfaces*., 2015, **7**, 19091-19097.
9. H Sun, H. Tian, Y Yang, D. Xie, Y.-C. Zhang, X.Liu, S.Ma, H.-M.Zhao and T.-L. Ren *Nanoscale.*, 2013, **5**, 6117−6123.
10. S. K. Karan, D. Mandal and B.B.Khatua, *Nanoscale.*, 2015,**7**, 10655-10666.
11. A Sasmal, P Sujatha Devi and S. Sen, *Phys. Chem. Chem. Phys*., 2019, **21**, 5974-5988.
12. M. Pusty, L. Sinha and P. M. Shirage, *New J. Chem.***,** 2019, **43**, 284.
13. W. Wang, H. Fan and Y. Ye, *Polymer*., 2010, 51, 3575–3581.
14. S. Pratihar, S. K. Medda, S. Sen and P. S. Devi, *Polym. Compos*., 2020,**41**,3351–3363.

15. G. Suresh, S. Jatav, M. S. R. Rao and D. K. Satapathy, *Mater. Res. Express.,* 2017, **4,** 075301.
16. D. Mandal, K. J. Kim and J. S. Lee, *Langmuir.*, 2012, **28**, 10310-10317.
17. E. Kabir, M. Khatun, L. Nasrin, M. J. Raihan, M. Rahman, *J. Phys. D: Appl. Phys.*, 2017, **50**, 163002.
18. S. Yu, W. Zheng, W. Yu, Y. Zhang, Q, Jiang and Z. Zhao, *Macromolecules*, 2009, **42**, 8870-8874.
19. B. Adak, I. Chinya and S. Sen, *RSC Adv*., 2016,**6**,105137.
20. I. Chinya, A. Pal and S. Sen, *J. Alloys Compd*., 2017,**722**,829.
21. A. Sasmal, S. K. Medda. P. S. Devi and S. Sen, *Nanoscale.*, 2020, **12**, 20908-20921.
22. H. Luo, D. Zhang, C. Jiang, X. Yuan, C. Chen and K. Zhou, *ACS Appl. Mater. Interfaces.,* 2015, 7, 8061-8069.
23. A.C. Lopes, S.A.C. Carabineiro, M.F.R. Pereira, G. Botelho and S. Lanceros-Mendez, *ChemPhysChem.,* 2013,**14**, 1926-1933.
24. H Sun, H. Tian, Y Yang, D. Xie, Y.-C. Zhang, X.Liu, S.Ma, H.-M.Zhao and T.-L. Ren *Nanoscale.*, 2013, **5**, 6117−6123.
25. I. Chinya, A. Sasmal, A. Pal and S. Sen, *Cryst. Eng. Comm.*, 2019, **21**, 3478.
26. A. Sasmal, A. Patra, P. S. Devi and S. Sen, *Compos. Sci. Technol.*, 2021, **213**, 108916.
27. C. Chen, X. Wang, J. Lin, W. Yang, H. Li, Y. Wen, L. Li, Z. Jiang and Q. Lei, *J. Mater. Chem. C*, 2016, **4**, 8070-8076.
28. P. Yang, L. Li, H. Yuan, F. Wen, P. Zheng, W. Wu, L. Zhang, G. Wang and Z. Xu, *J. Mater. Chem. C.*, 2020, **8**, 14910-14918.
29. P. Martins, A. C. Lopes and S. L. Mendez, *Prog. Polym.Sci.,* 2014,**29**, 683.

30. P. Thakur, A. Kool, N. A. Hoque, B. Bagchi, F. Khatun, P. Biswas, D. Brahma, S. Roy, S. Banerjee and S. Das, *Nano Energy*.,2018, **44**, 456.

31. L. Ruan, X. Yao, Y. Chang, L. Zhou, G. Qin and X. Zhang, *Polymers*., 2018, **10**, 228.

32. S. Satapathy, S. Pawar, P.K. Gupta and K. B. R. Varma, *Bull. Mater, Sci*., 2011,**34**,727.

33. G. H. Kim, S. M. Hong and Y. Seo, *Phys. Chem. Chem. Phys.,* 2009, **11**, 10506–10512.

34. A. Sasmal, A. Patra, P. S. Devi and S. Sen, *Dalton Trans.*, 2021, **50,** 1824-1837.

3.4: Fabrication of co-polymer PVDF-HFP based Al@ZnO nanocomposite: flexible energy harvesting and storing material

3.4.1. Introduction:

Modifications of ceramic fillers such as aspect ratio variation, shape variation, addition of conductive filler etc. have already been investigated to improve the energy storage and harvesting applications of the respective PVDF based composite systems. In this section of work, ZnO filler was further modified by adding dopants. There are several reports regarding doping of different ions in ZnO to increase its electrical property. On the other hand, the doping technique also changes the leakage current of ZnO and modify the surface charge of this nanorods [1-4]. Surface charge of filler plays an important role in determining the strength of interfacial interaction with polymer. Considering all these facts, ZnO was doped with Al^{3+} ion and the effect was studied throughout the present investigation. Herein flexible piezocomposite was developed using Al@ZnO nanorods with PVDF-HFP polymer which is a co-polymer of PVDF. Compared to PVDF and other co-polymer, PVDF-HFP exhibits significantly higher piezoelectric-coefficient (d_{31}) and electromechanical coupling factor. On the other hands, its exhibit good mechanical property with chemical stability compared to other co-polymer [5].

In this work, pure ZnO and Al@ZnO were synthesized by wet chemical synthesis as described in Chapter 2. The simple drop casting method was being utilized to synthesize bare PVDF-HFP and other composite films. 5 wt% and 10 wt% Al@ZnO-PVDF-HFP composite films were named as 5PALZO, 10PALZO, respectively. The effect of Al^{3+} doping in ZnO filler on the dielectric, ferroelectric, energy storage and mechanical energy harvesting performance of its PVDF-HFP based composites is studied throughout the present work.

3.4.1.1. Characterization of filler particles

The structural properties of pure ZnO as well as Al @ZnO nanorods were investigated using X-ray diffractometer (XRD). **Fig. 3.4.1(a)** presents the XRD patterns of ZnO and Al@ZnO nanorods.

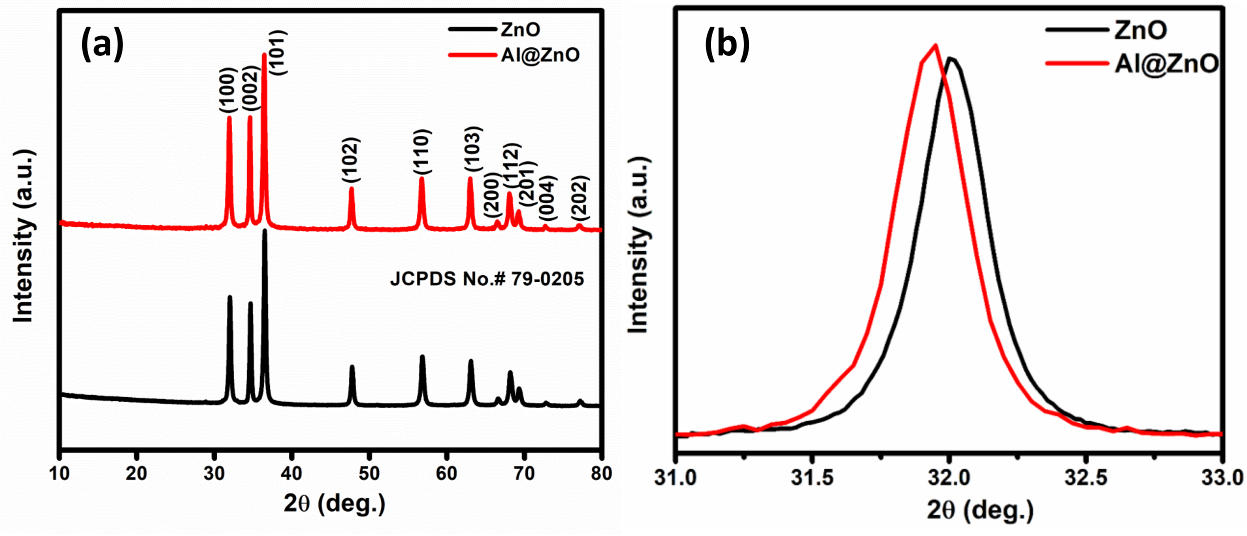

***Fig. 3.4.1 (a)** XRD patterns of pure ZnO and Al@ZnO nanorods, **(b)** magnified view of (100) bragg peak*

The XRD pattern reveals the successful formation of ZnO rods (JCPDS card number #79-0205), with lattice parameter a=b=0.3248 nm and c=0.5205 nm, respectively. The absence of any additional peaks for Al@ZnO nanorods infers that the crystal structure remains invariant after doping. A more careful view of the enlarged image (**Fig. 3.4.1(b)**) reveals a slight shifting of the peak position (100) towards lower diffraction angle for the Al@ZnO nanorods. This shift in the 2θ position can be assigned to the introduction of Al^{3+} ion within host ZnO lattice. To have a further detailed analysis, the crystallite size of ZnO and Al@ZnO nanorods were determined by using Debye Scherrer's formula [6].

The crystallite size for pure ZnO and Al@ ZnO were found to be 32 nm and 24 nm respectively, which implies a decrease in crystallite size after incorporation of aluminium (Al^{3+}) ions in the ZnO host lattice. Reitveld refinement of XRD powder of ZnO and Al@ZnO nanorods was carried out using fullprof software (**Fig. 3.4.2**).

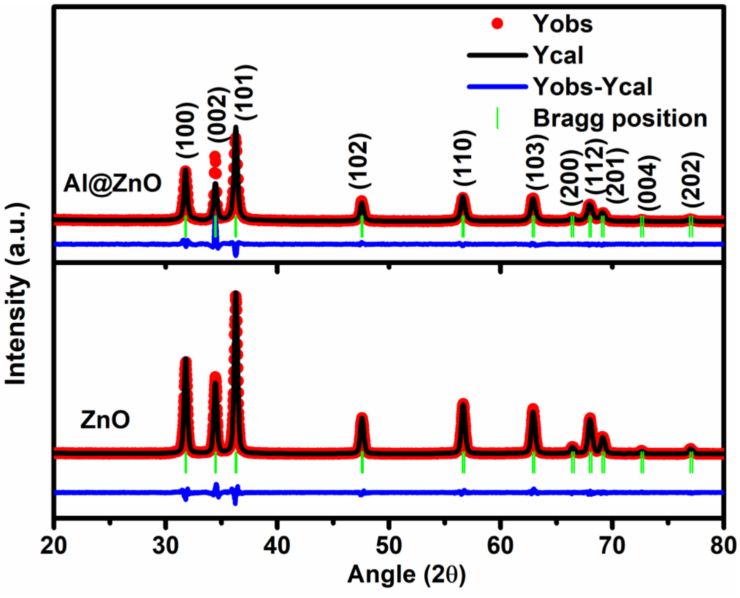

***Fig. 3.4.2** Reitveld refinement XRD patterns of ZnO and Al@ZnO nanorods*

Refined parameters of pure ZnO and Al@ZnO sample were given in **Table 3.4.1**. The value of lattice parameter and volume of unit cell were found to be decreased for Al@ZnO nanorods compared to pure ZnO nanorods. The reduction of lattice parameter as well as cell volumevalue can be attributed due to the smaller ionic radius of Al^{3+} ions than that of Zn^{2+} ions($r_{Al}{}^{3+}$ = 0.63Å, $r_{Zn}{}^{2+}$ = 0.74Å) [7]. This infers successful inclusion of Al^{3+}ion in the ZnO host lattice structure.

Table 3.4.1: Refined parameters from XRD data of pure ZnO and Al@ZnO

Parameters	Pure ZnO	Al@ZnO
Space group	P63mc	P63mc
Lattice parameter, a=b (Å)	3.25070	3.24916
Lattice parameter, c (Å)	5.20620	5.20519
Cell angle α=β (°)	90	90
Cell angle γ (°)	120	120
Cell volume (Å^3)	47.643	47.5893
R_p, R_{wp} & χ^2	8.00, 10.3 & 1.61	15.5, 16.9 & 2.13
S (goodness of fit)= R_{wp}/R_{exp}	1.27	1.45

In order to investigate the effect of Al doping on the vibrational mode of ZnO nanorods, Raman spectroscopy of the sample was carried out. **Fig. 3.4.3(a)** depicted the room temperature raman spectroscopy of pure ZnO and Al@ZnO nanorods. Undoped sample shows a sharp, strong absorption peak at 437 cm^{-1}, assigned to the E_2 (high) active mode which is a characteristics peak of wurtzite ZnO [8]. On the other hand, peak at 580 cm^{-1}, attributed to the E_1 (low) Raman active mode which arises due to impurities or defects. For Al@ZnO sample, there is a shift of peak (E_2 and E_1 active mode) position towards higher wavenumbers which is due to the lattice distortion induced by substitution of Zn^{2+} ions by Al^{3+} ions within the ZnO host lattice that generates compressive stresses [8]. The stresses arise due to the difference of ionic radius of Zn and Al (Ionic radius of Zn, r_{Zn}^{2+} =0.074 nm, r_{Al}^{3+} = 0.051 nm) [7]. **Fig. 3.4.3(b)** depicts the FTIR spectra of ZnO and Al@ZnO nanorods. Both the samples exhibit peak at 3444 cm^{-1} which is attributed to the stretching vibration band of –OH group of ZnO nanorods. The peak at 1631 cm^{-1} is associated with C=O stretching vibration band of –COOH groups, where the peak at 1384 cm^{-1} is ascribed to the bending vibration of hydroxyl group C-OH groups. The peak observed at 519 cm^{-1} and 526 cm^{-1} for undoped ZnO and Al@ZnO respectively, which was due to stretching vibration of

Zn-O bond. The shift of Zn-O bond towards higher wavenumber region for Al@ZnO sample may be due to the local strain acting on the ZnO nanocrystal. On the other hand, intensity of the IR band of Zn-O bond of Al@ZnO sample decreases which may be due to the decrement of Zn-O bond length. This result confirms the substitution of Zn^{2+} ions by Al^{3+} ions in the ZnO host lattice [9].

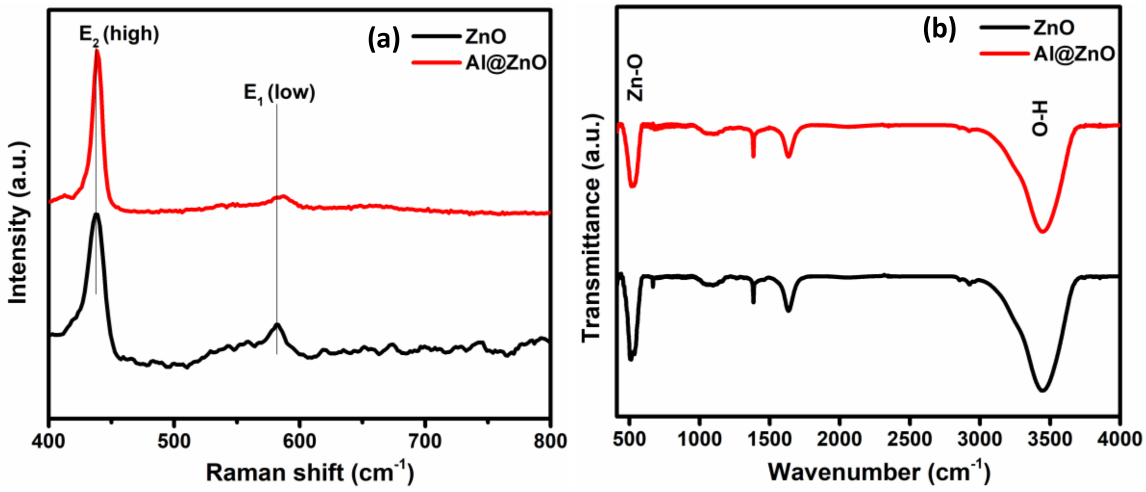

***Fig. 3.4.3 (a)** Raman spectra, **(b)** FTIR spectra of pure ZnO and Al@ZnO nanorods*

Electronic structure of ZnO and Al@ZnO were investigated using UV-VIS spectrophotometer. **Fig. 3.4.4(a)** represents the absorbance spectra of pure ZnO and Al@ZnO nanorods. A strong absorption peak appears at 377 nm for undoped ZnO which is slightly shifted to 381 nm for Al@ZnO nanorods. This shift was mainly due to the shifting of Fermi level towards conduction band which depends on the type of semiconductor. Doping of Al ions (n-type semiconductor) increases conductivity of the intrinsic semiconductor which leads to motion of Fermi level to the conduction band [10]. Optical band gap of ZnO and Al@ZnO were calculated using tauc Equation

$(\alpha h\upsilon)^2 = A(h\upsilon - E_g)$ .... (3.4.1)

Where A is the proportionality constant, hυ is the photon energy, α is the absorption coefficient and $E_g$is the band gap. **Fig. 3.4.4(b)** represents $(\alpha h\upsilon)^2$ vs hυ plot of undoped ZnO and Al@ZnO sample from which band gap of these samples were calculated by extrapolating linear part of the curve to $(\alpha h\upsilon)^2 = 0$. The band gap was found to be decreased from 3.42 eV of pure ZnO to 3.17 eV for Al@ZnO nanorods. This reduction in band gap for Al@ZnO may be due to the higher electronegativity of Zn compared to Al. The difference in electro negativity generates defects within Al@ZnO due to incorporation of Al^{3+} ions in ZnO. Due to these defect sites conduction band shifted downwards and valence band shifted to the upward level resulting in reduction of band gap [10-11].

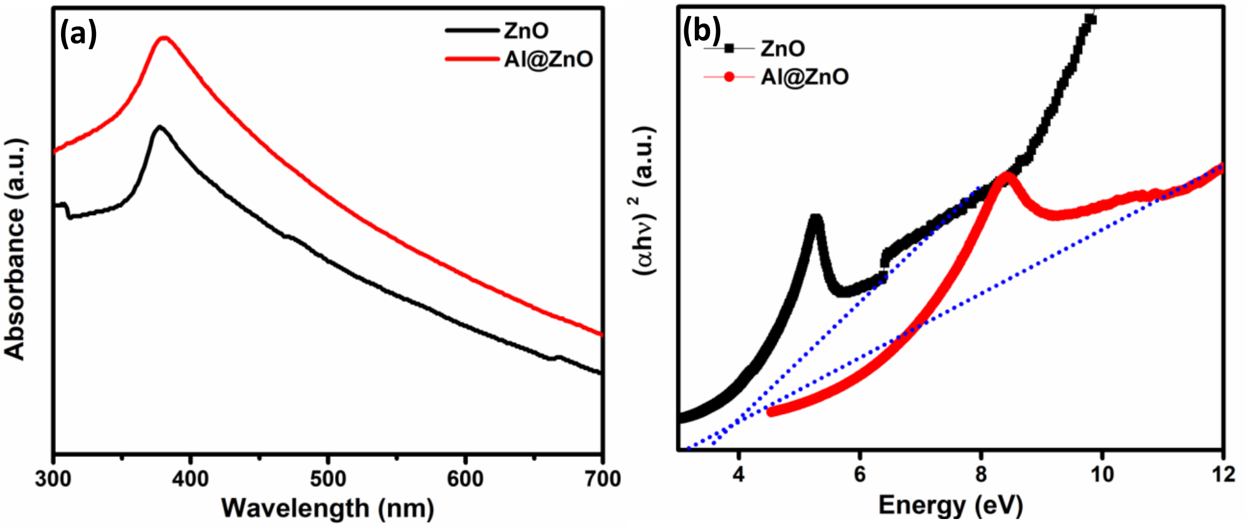

Fig. 3.4.4 *UV spectra of ZnO and Al@ZnO nanorods, (b)$(\alpha h\upsilon)^2$ vs photon energy plots of ZnO and Al doped ZnO samples.*

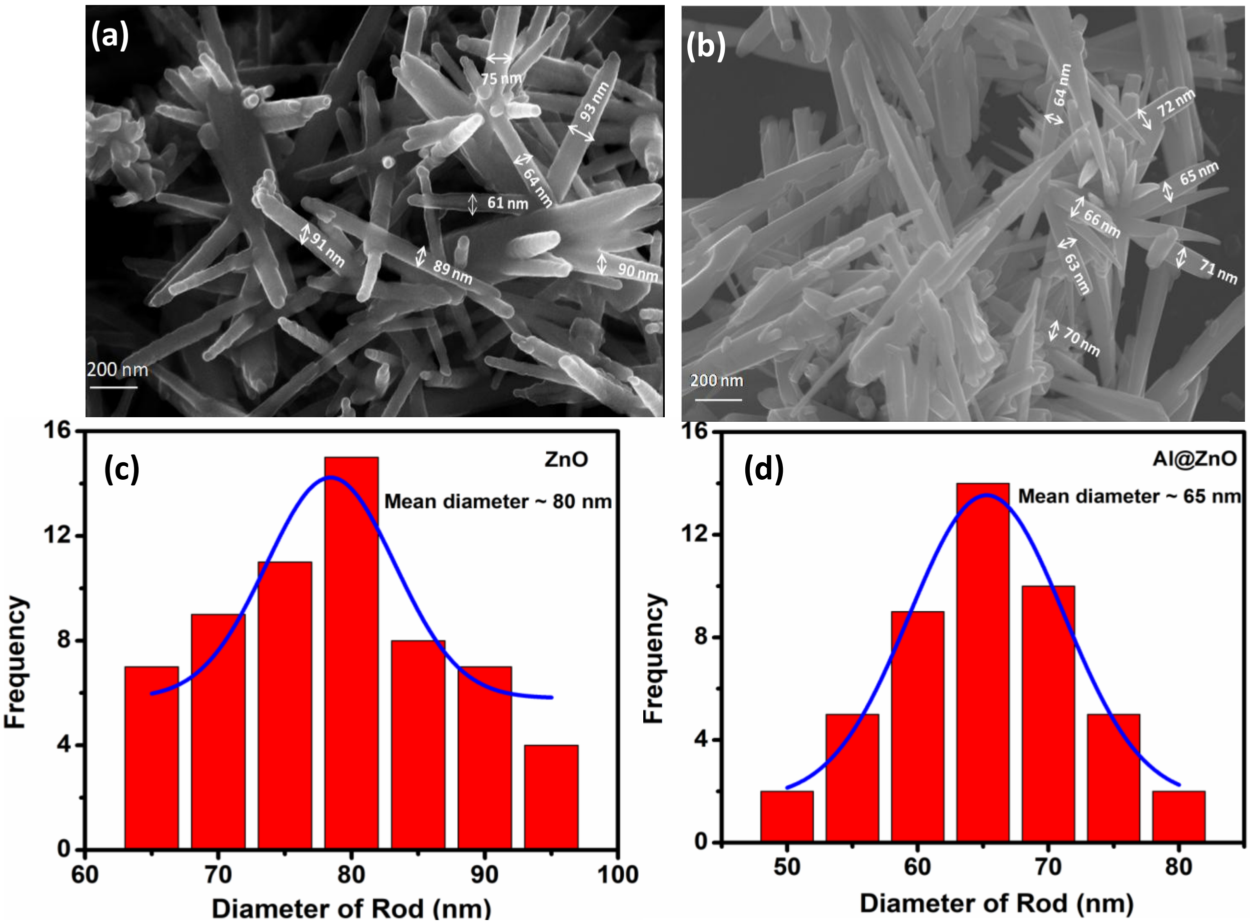

Fig. 3.4.5 *FESEM images of* ***(a)*** *ZnO nanorods,* ***(b)****Al@ZnO nanorods; diameter distribution of* ***(c)*** *ZnO nanorods, showing mean diameter ~80 nm,* ***(d)*** *Al@ZnO nanorods, having mean diameter ~65 nm.*

To have a morphological analysis of the surface of pure ZnO and Al@ZnOnanorods FESEM technique was utilized (**Fig. 3.4.5(a-b)**). The images reveal formation of nanorods with pencil-like tip structure. **Fig. 3.4.5(c)** and **3.4.5(d)** demonstrate the size distribution of ZnO and Al@ZnO nanorods, respectively. Pure ZnO nanorods have an average diameter and length ~80 nm and ~800 nm, respectively whereas Al@ZnO nanorods have an average diameter and length ~65 nm and ~600 nm, respectively.

The typical TEM micrograph of the prepared ZnO as well as Al@ZnO nanorods are depicted in Fig. **3.4.6(a)** and **3.4.6(b)** respectively, which indicated the formation of uniform microstructure of the synthesized nanorods. The crystallinity of both the nanorods was confirmed from the Selected Area Electron Diffraction (SAED) pattern. Further SAED pattern can be indexed to (100), (002), (110) and (102) planes of ZnO and Al@ZnO structures (Fig. **3.4.6(c)** and **3.4.6(d),** respectively). SAED pattern are well matched with the XRD database and confirmed the crystallinity of both the nanorods. High Resolution TEM image (HRTEM) High Resolution TEM image (HRTEM) (**Fig. 3.4.6 (c)** and **3.4.6(d),** respectively) of the nanorods reveals that nanorods grow along the (100) direction.

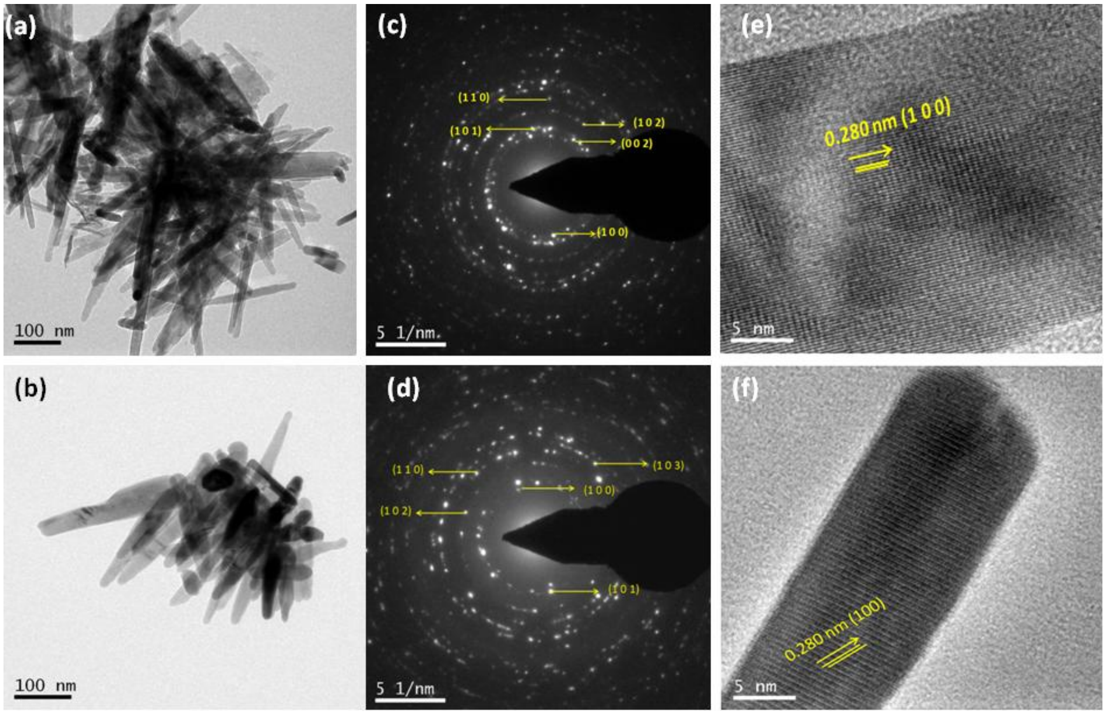

Fig. 3.4.6 *TEM images of **(a)** ZnO nanorods, **(b)** Al@ZnO nanorods, SAED pattern of **(c)** ZnO, **(d)**Al@ZnO nanorods, HRTEM images of **(e)**ZnO nanorods, **(f)**Al@ZnO nanorods*

Fig. 3.4.7 represents Energy-dispersive X-ray spectroscopy (EDS) spectra of Al@ZnO nanorods. The presence of Al with the elements Zn and O were confirmed from the EDS spectra. The use of carbon coated Cu grid during TEM characterization resulted in extra peak Copper (Cu) and C which confirmed the purity of the synthesized samples. The atomic percentage of elements is given in the inset of **Fig. 3.4.7** which almost matched with the doping percentage.

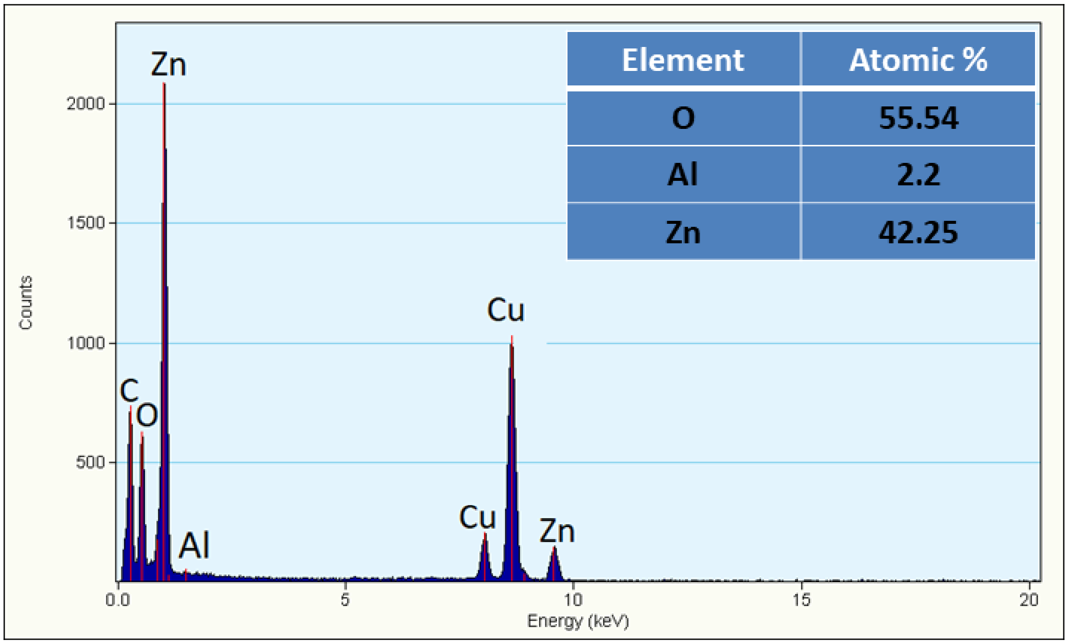

Element	Atomic %
O	55.54
Al	2.2
Zn	42.25

***Fig. 3.4.7** EDS spectra of Al@ZnO nanorods showing the presence of Al, inset shows the atomic percentage of Al*

In order to determine the chemical state of undoped ZnO and Al@ZnO nanorods, XPS measurements were performed. **Fig. 3.4.8 (a)** presents the survey spectra of ZnO and Al@ZnO nanorods which revealed the existence of Zn, O and Al elements in the synthesized samples. The core level of Zn2p state was presented in **Fig. 3.4.8(b)** where the peaks located at binding energy 1021.00 eV and 1044.23 eV attributed to Zn2p$_{3/2}$ and Zn2p$_{1/2}$ state, respectively [12]. For Al@ZnO nanorods, there is a peak shifting towards higher binding energies at 1021.7 eV and 1044.39 eV which corresponds to Zn2p$_{3/2}$ and Zn2p$_{1/2}$ state respectively, which is due to the addition of Al^{3+} into ZnO lattice [13]. The peak observed at ~74.5 eV (shown in **Fig. 3.4.8(c)**) is attributed to Al2p which confirmed the successful incorporation of Al^{3+}dopant in the ZnO host lattice. For better analysis, the core level XPS spectra of Al 2p level were fitted into two Gaussian curves, binding energy atlower value ~74.2 eV is associated with Al-O bonds and binding energy at higher value ~75.2 eV corresponds to Al-OH bonds [13-14], which confirmed that the there is no metallic Al (binding energy ~ 72 eV) in the XPS spectra. No Al phases as observed from XRD and XPS studies conclude the successful addition of Al^{3+} ions into the host ZnO lattice [13]. **Fig. 3.4.8(d)** represents the core level XPS spectra of O1s peaks for both ZnO and Al@ZnO nanorods. O1s spectra were fitted into two Gaussian components where binding energy at~ 530.3 eV is assigned to O^{-2} ions in the ZnO lattice (O$_L$) and the binding energy at ~ 532.2 eV is attributed to O^{-2} ions in the oxygen-deficient regionwithin ZnO structure which is associated with the concentration of oxygen vacancies or point defects (O$_v$) [13]. There is a shifting of those two peaks towards higher binding energy at ~ 530.6 ev and 532.3 eV for Al@ZnO nanorods. The calculated area ratio (O$_v$/O$_L$) decreases for Al@ZnO sample whichreveals that the there is a reduction of oxygen defects. This reduction of oxygen defects helps for the improvement of the electroactive phase within the nanocomposites [15]. Thereby, making the composite suitable for piezoelectric nanogenerator application.

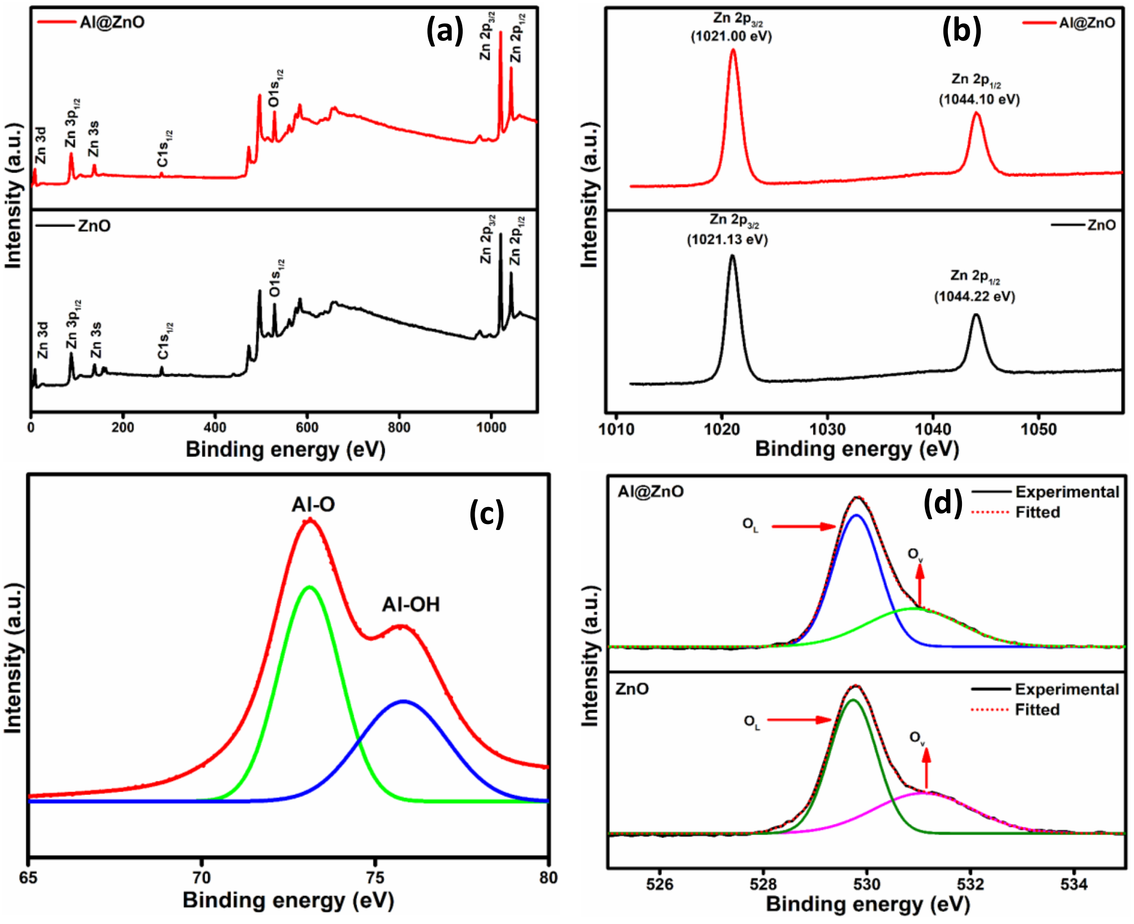

__Fig. 3.4.8 (a)__ XPS spectra, Core level spectra of __(b)__ Zn2p state, __(c)__ deconvoluted Al 2p state and __(d)__ deconvoluted O1s state of ZnO and Al@ZnO nanorods

Surface charge of nanorod is also a key factorto better understand electrostatic interaction between PVDF-HFP chain and ceramic filler. For this purpose, zeta potential measurement of ZnO and Al@ZnO samples were carried out. Surface electrostatic charge of ZnO and Al@ZnO obtained from zeta potential analysis is depicted in **Fig. 3.4.9**. Zeta potential value of ZnO and Al@ZnO were found to be -16.8 mV and -31.4 mV, respectively. Negative zeta potential value for both the sample revealed that ZnO and Al@ZnO have negative surface charge on their surfaces, which interact with $-CH_2$ dipole of PVDF-HFP through ion-dipole electrostatic interaction [16]. This interaction leads to the polar phase formation of PVDF-HFP matrix. Thus the nanofiller's surface acts as a nucleation centre for the formation of polar phase. A closer observation to **Fig. 3.4.9** reveals that the Al@ZnO reveals a higher amount of negative charge in comparison to ZnO nanorods. This higher amount of negative charge makes it a suitable candidate as filler for PVDF-HFP matrix.

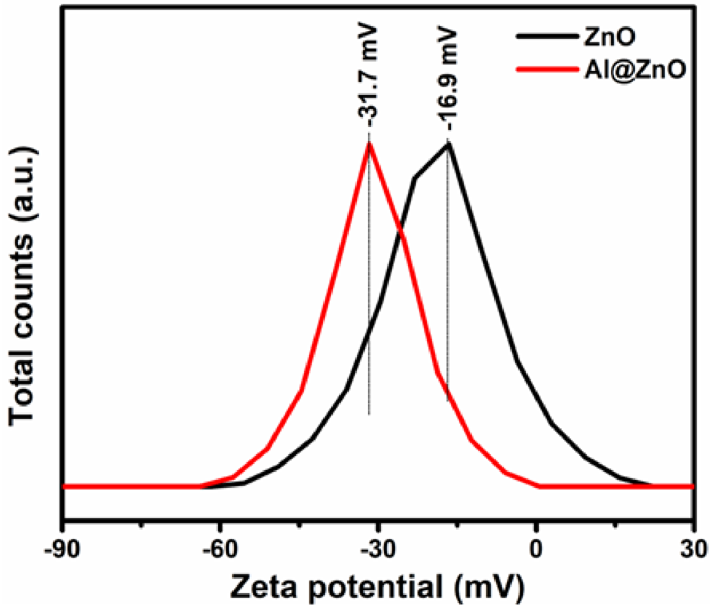

Fig. 3.4.9 (a) *Zeta potential of ZnO and Al@ZnO nanorods*

3.4.1.2 Phase analysis of composite films

The presence of electro-active phase in polymer composites plays an important role for exhibiting good electrical properties of the composites [17, 18]. As a consequence, XRD characterization of the nanocomposites was carried out to investigate the presence of the electroactive phases in the respective samples (**Fig. 3.4.10(a)**).

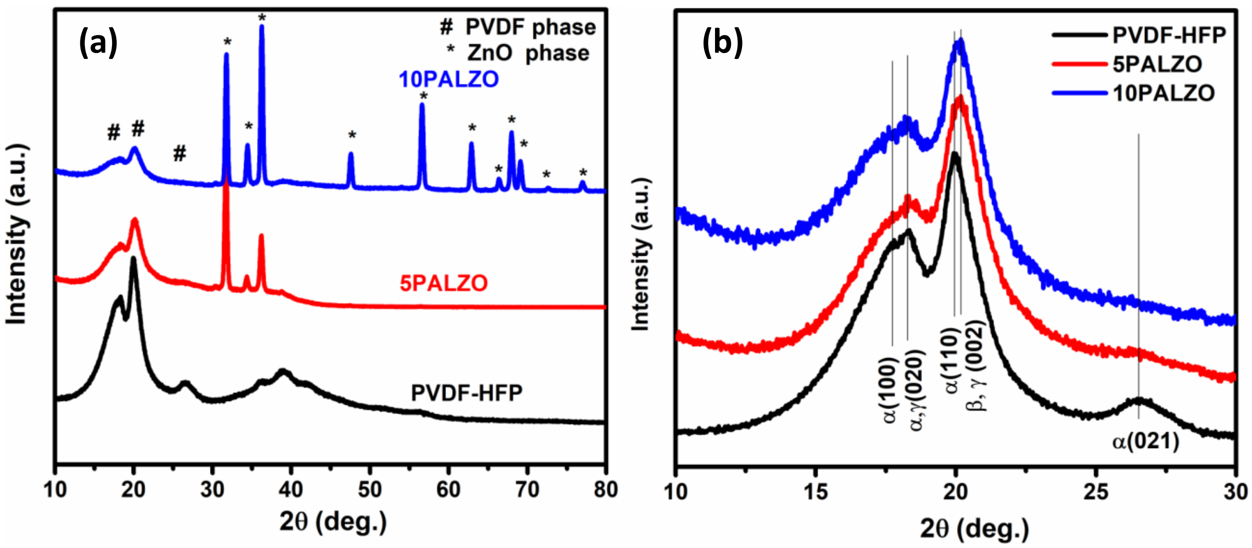

***Fig. 3.4.10 (a)** XRD patterns of pure PVDF-HFP, 10PZO, and 10PALZO composite films, **(b)** XRD pattern in the range of 10º to 30º*

Pure PVDF-HFP exhibits nonpolar α phase due to the TG^+TG^- chain conformation of $-CH_2-/-CF_2-$ dipoles of PVDF-HFP. With the incorporation of ceramic filler in PVDF-HFP matrix, the dipoles reoriented themselves due to interfacial interaction between ceramic fillers and PVDF-HFP. As a result nonpolar phase transformed into polar β & γ phase due to TTTT and T_3G+T_3G- chain conformations. **Fig. 3.4.10(b)** demonstrates the dominance of polar phase fraction in the nanocomposites and 10PALZO is the most enriched one. XRD patterns of pure PVDF-HFP, 5PALZO and 10PALZO composite films indicated that after mixing Al@ZnO nanorods in PVDF-HFP matrix, PVDF-HFP retains their crystallinity. The comparison of XRD patterns of neat PVDF-HFP, 5PALZO and 10PALZO composite film within 2θ range from 10º to 30º are shown in **Fig. 3.4.10(b).** Pure PVDF-HFP exhibits peak at 2θ~17.7º, 18.4º, 19.9º, and 26.6º corresponding to (100), (020), (110) and (021) planes, which is due to the presence nonpolar α phase [19]. For the composite films, the intensity of the peaks at 17.7º, 26.6º decreased gradually with ceramic filler concentration and disappeared completely for 10 PALZO composite films.

Besides, the main characteristics peak at 2θ~19.9º shifted towards higher diffraction angle gradually with filler concentration and maximum shifting was observed for 10PALZO composites film which indicates the phase transformation of PVDF-HFP from non-polar phase to polar phase [18]. For better understanding of this phase transformation from non-polar to polar, total degree of crystallinity and individual amount of beta crystallinity and gamma crystallinity of pure PVDF, 5PALZO and 10PALZO films were calculated using **Equation 3.3.1, 3.3.2, 3.3.3** (as described in section 3.3), respectively, from deconvoluted XRD patterns of these samples (**Fig. 3.4.11(a-c)**) [18].

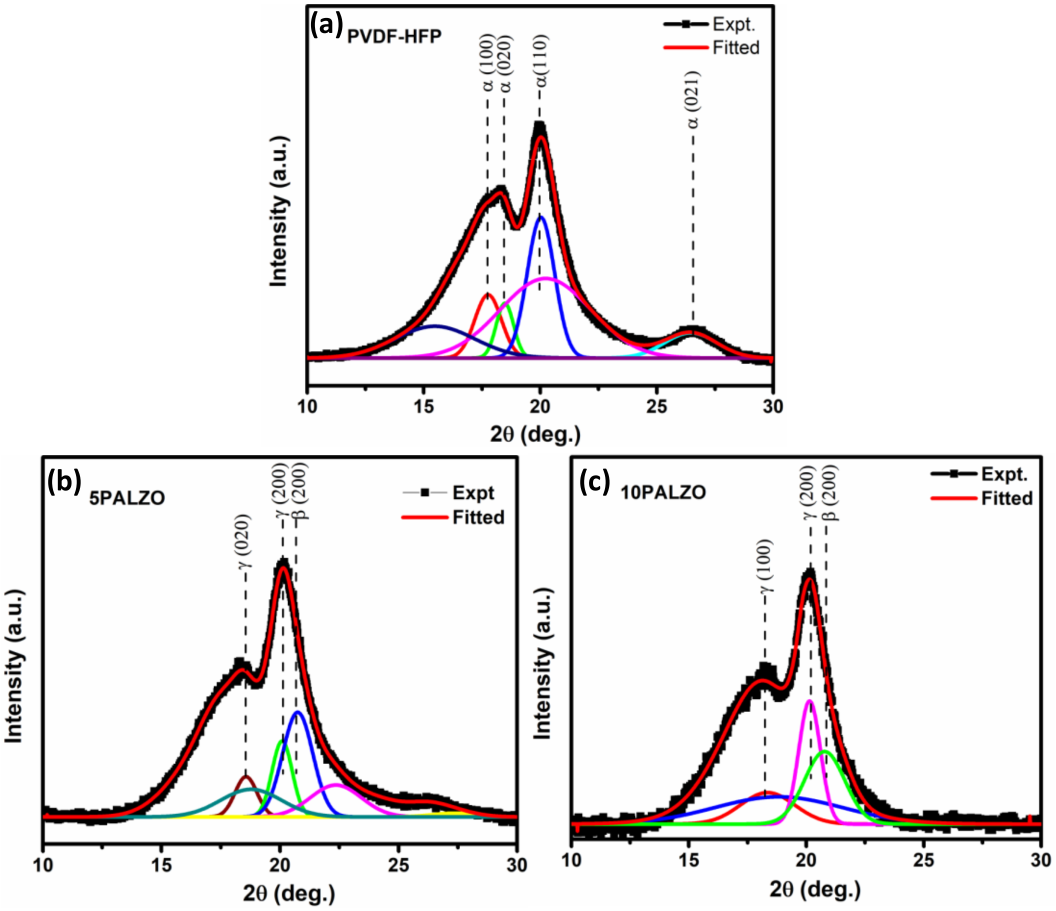

Fig. 3.4.11 *Deconvoluted XRD pattern of* ***(a)*** *PVDF-HFP,* ***(b)*** *5PALZO and* ***(c)*** *10PALZO composites*

The individual quantification of total crystallinity, beta phase crystallinity and gama phase crystallinity of PVDF-HFP, 5PALZO and 10PALZO composite was calculated and represented in **Table 3.4.2**. Total degree of crystallinity increased to ~67% for 10PALZO sample from ~ 52% for PVDF-HFP which was due to the interaction between Al@ZnO filler and PVDF-HFP matrix.

Table 3.4.2 Individual amount of crystallinity calculation for PVDF-HFP, 5PALZO & 10PALZO composite films

Sample Name	Total degree of crystallinity	Beta phase crystallinity	Gama phase crystallinity
PVDF-HFP	51.7	-	-
5PALZO	62.4	37.6	24.7
10PALZO	67.4	27.1	40.2

In order to identify quantitative crystalline phase in terms of local phonon bands of PVDF, FTIR characterization was carried out. FTIR absorption spectra of pure PVDF-HFP, 5PALZO, 10PALZO and 10PALZO-P composite films are presented in **Fig. 3.4.12(a)** [wavenumber region 1000-400 cm^{-1}]. The figure reveals significant enhancement of polar phase within the composite film compared to bare PVDF-HFP. It was observed from FTIR spectra that there is a significant difference between PVDF-HFP and all composite film. FTIR spectra of pure PVDF-HFP shows strong absorption peak at 409 cm^{-1}, 488 cm^{-1} (CF$_2$ wagging), 532 cm^{-1} (CF$_2$ bending), 615 cm^{-1} and 764 cm^{-1} (CF$_2$ bending and skeletal bending), 796 cm^{-1}, 856 cm^{-1} and 976 cm^{-1} (CH$_2$ rocking) which are attributedmainly to nonpolar α phase. FTIR spectra also reveals weak absorption band 431 cm^{-1} (correspond to polar γ phase), 510 cm^{-1} (CF$_2$ stretching associated with polar β phase) and 840 cm^{-1} (CF_2 stretching, CH_2 stretching and skeletal C-C stretching corresponds to polar β and γ phase [18-20]. The relative intensity of the peaks corresponds to nonpolar α phase decreased gradually and some of the peaks disappeared completely with increasing filler concentration.

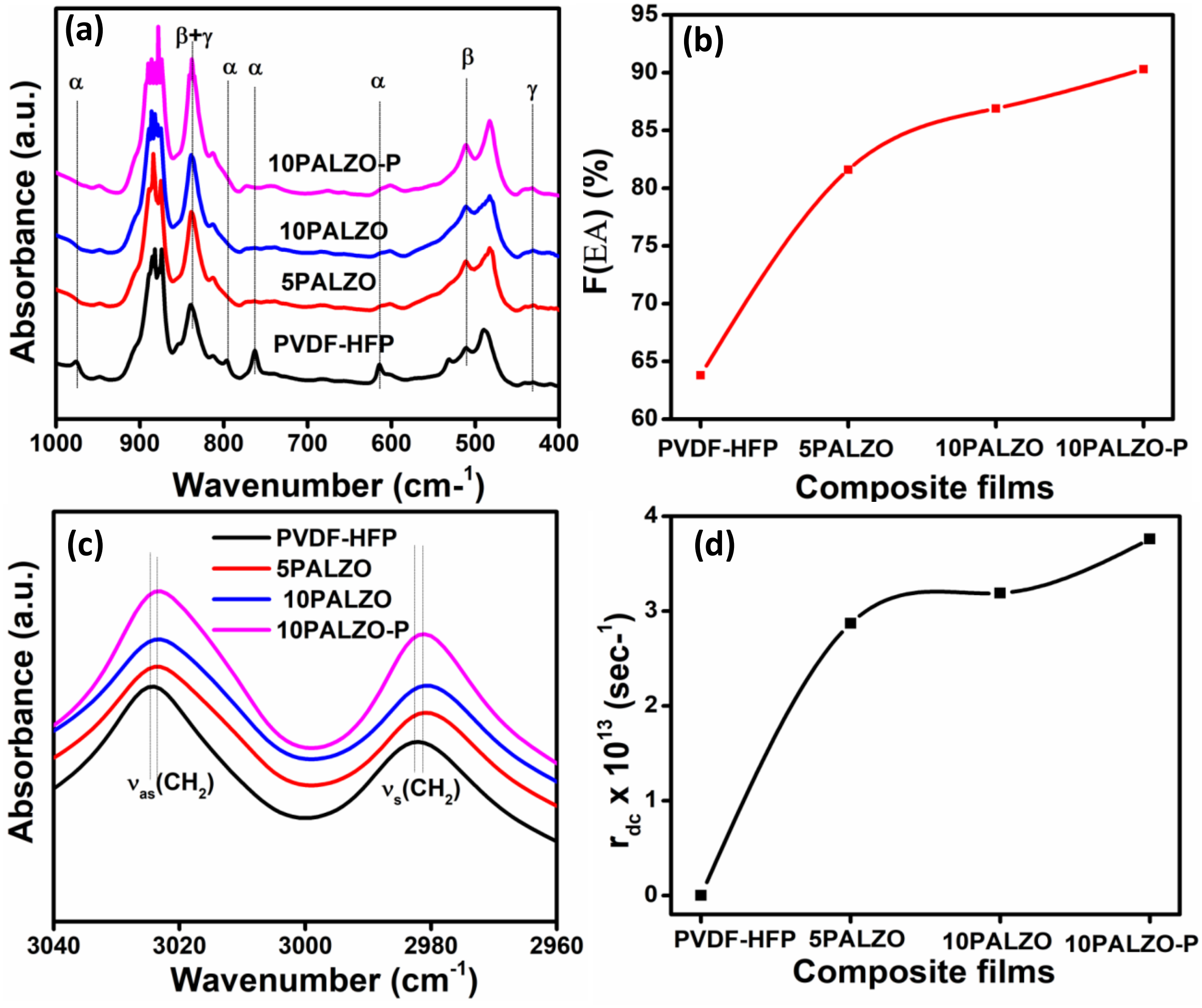

Fig. 3.4.12 (a) *FTIR spectra of pure PVDF-HFP, 5PALZO ,10PALZO and 10PALZO-P composite films,* ***(b)*** *Variation of polar-phase with filler amount* ***(c)*** *Asymmetric and symmetric stretching vibration shift of composite film,* ***(d)*** *damping coefficient evaluated from IR spectra of composite films*

A closure observation to the **Fig. 3.4.12(a)** shows that the relative intensity of the peaks at 510 cm^{-1} and 840 cm^{-1} gradually increased with increasing filler concentration. Therefore polar phase of composite films increased in comparisonwith bare PVDF-HFP which clearly indicates the conversion of PVDF-HFP phase from nonpolar phase to polar phase which also supports the XRD results. The quantitative amount of polar phase for each composite film as well as bare PVDF-HFP was calculated using the **Equation 3.1.1.**

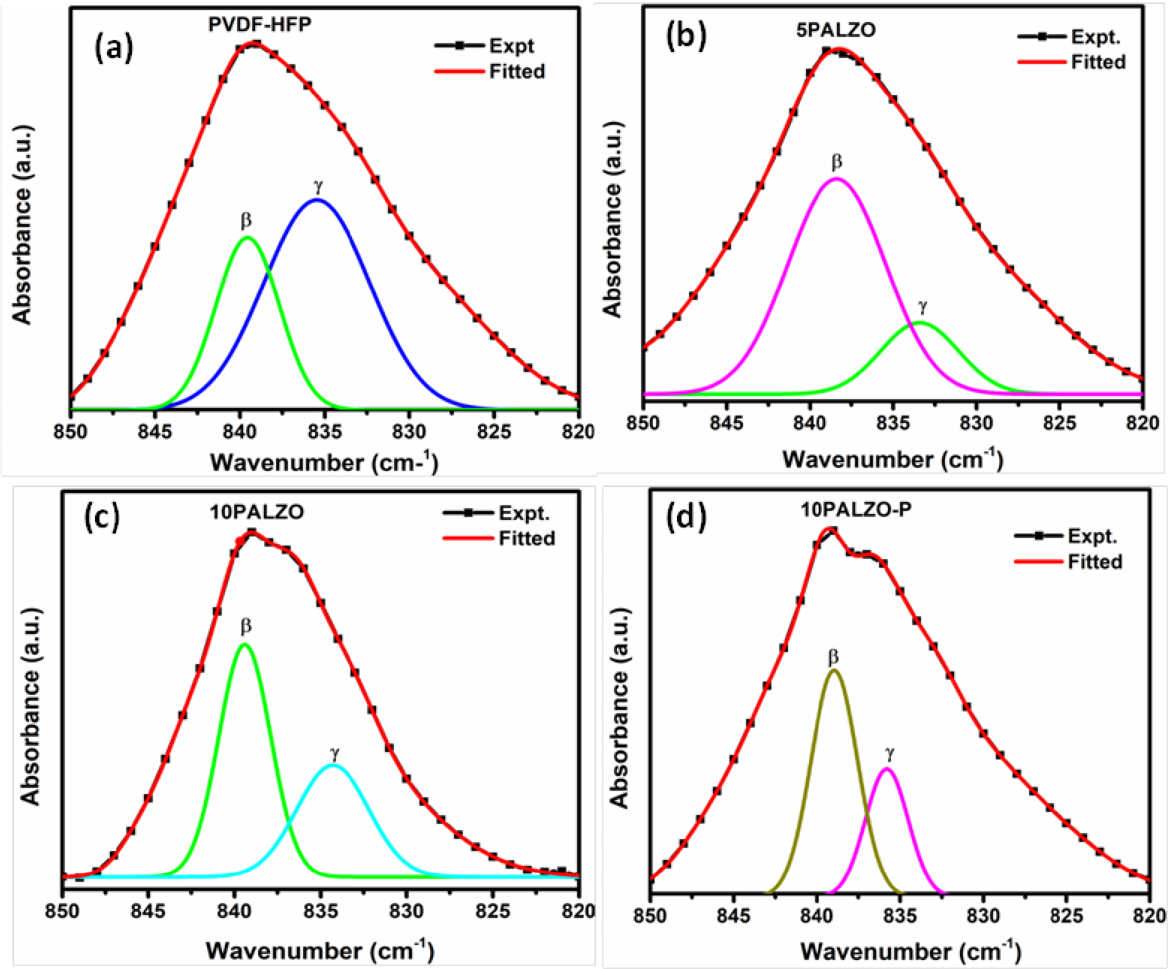

Fig. 3.4.13 (a-d) *The deconvoluted FTIR spectra (range within 850-820 cm^{-1}) of PVDF, 5PALZO, 10PALZO and 10PALZO-P composites, respectively.*

The 840 cm^{-1} absorption bands of neat PVDF-HFP, 5PALZO, 10PALZO and 10PALZO-P films were deconvoluted (**Fig. 3.4.13(a-d)**)) to evaluate the quantitative amounts of individual β and γ phases within them and the results are presented in **Table 3.4.3** [18]. The quantitative amount of F(EA) fraction indicates that (**Fig. 3.4.12(b)**) 10PALZO posses' maximum amount of polar phase (86.9%) (much higher than bare PVDF-HFP ~ 63.8%). The interfacial interaction between nanofillers and $-CH_2$- dipole of PVDF-HFP is responsible for such enhancement. To achieve a further increment in the polar phase fraction the sample with maximum polar phase (10PALZO) was kept under a constant electric field (2.4 MV/cm) for 2 h. As expected the applied electric field results in further alignment of CH_2 dipoles at the filler interface resulting in further increment in the polar phase fraction (**Fig. 3.4.12(b)**). The individual quantification of F(β) and F(γ) from FTIR study for each sample was calculated using **Equation 3.2.1 and 3.2.2**, respectively and shown in **Table 3.4.3**. Relative amount of β phase (w.r.t γ phase) ($F_{\beta\gamma}$) and γ phase (w.r.t to β phase) were also calculated using **Equation 3.2.3 and 3.2.4**, respectively (as described in section 3.2). The accurate percentage of β and γ phase was calculated from FTIR data given in **Table 3.4.3.**

Table 3.4.3: Individual amount of polar phase calculation for PVDF-HFP, 5PALZO and 10PALZO and 10PALZO-P composites

Sample Name	Polar phase Fraction (F_{EA} %)	β phase Fraction (F_β %)	γ phase Fraction (F_γ %)	Relative amount of β phase w.r.t to γ phase ($F_{\beta\gamma}$)	Relative amount of γ phase w.r.t to β phase ($F_{\gamma\beta}$)
PVDF	63.8	15.7	48.1	44.1	55.8
5PALZO	81.6	44.3	37.3	49.7	50.3
10PALZO	86.9	52.1	34.8	50. 9	49.1
10PALZO-P	91.2	63.7	27.5	55.4	44.6

To study the mechanism of interfacial interaction, FTIR spectra of all the samples were investigated within the wavenumber region 3100 cm^{-1} to 2900 cm^{-1} (**Fig. 3.4.12(c)**), as this region mainly assigned for asymmetric (ν_{as}) and symmetric (ν_s) stretching vibration band of –CH_2 dipole only, which are not coupled with any other vibrational modes [21]. A closer observation to the **Fig. 3.4.12(c)** indicates that, both symmetric and asymmetric stretching vibrational band of –CH_2 dipole of the composites shifts towards the lower wavenumber region in comparison with bare PVDF-HFP. The gradual shifting of this vibrational bands towards lower energy can be explained with the help of damped harmonic oscillator model [21]. In light of the model initially it is being assumed that these two vibration bands have no damping for pure PVDF-HFP matrix. With the filler loading, electrostatic interaction occurs between the filler surface and the –CH_2dipole of PVDF-HFP which will generate a source of damping. The interfacial interaction enhanced with increasing filler loading can be clearly seen with the enhanced damping coefficient (**Fig. 3.4.12(d)**). The quantitative amount of electrostatic interaction of the composite films in terms of damping coefficient was calculated from the peak shifting of the asymmetric –CH_2 stretching vibrational band using **Equation 3.1.3. Fig. 3.4.12(d)** also reveals that the damping coefficient was maximum for 10PALZO-P composites confirming the maximum interfacial interaction.

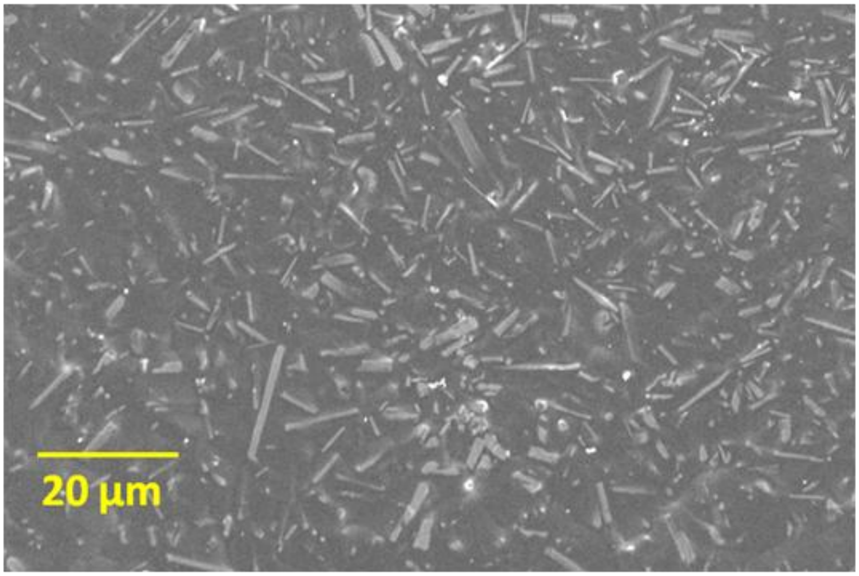

Fig. 3.4.13(a) FESEM image of 10PALZO composite

In order to investigate surface morphology,the image of the10PALZO sample is shown in **Fig. 3.4.13 (a)**. FESEM image infers the nearly uniform dispersion of Al@ZnO nanorods within PVDF-HFP matrix. Al@ZnO nanorods are well embedded in PVDF-HFP matrix which confirmed the successful incorporation of Al@ZnO in PVDF-HFP matrix.

3.4.1.3 Dielectric properties of the composites

Dielectric property is considered as an important parameter for the development of energy storage devices [22]. As a consequence, the dielectric properties for all the composite films at ambient temperature (30ºC) and pressure were carried out and shown in **Fig. 3.4.14 (a)**. **Fig. 3.4.14 (a)** represents an enhancement of the dielectric constant of all the composites than that of pure PVDF-HFP which can be assigned to the Maxwell-Wager-Siller interfacial polarization effect. The dielectric permittivity (at 1 kHz) increased from ~8 for pure PVDF-HFP to ~19 for 10PALZO composite film. The good dispersion of filler particles in the PVDF-HFP matrix is responsible for such enhancement. In the low frequency region dielectric permittivity mainly increased due to the enhancement of space charge polarization with increasing filler loading in PVDF-HFP matrix. Further, increased dielectric permittivity in the high frequency region could be attributed due to the enhanced dipolar polarization. In this context it is pertinent to be mentioned here that the dielectric constant for the composites has been increased with a considering low dielectric loss. In addition to that, the value of dielectric loss is significantly small even less than 0.04 for the poled 10PALZO-P. Thus 10PALZO-P can be considered as the best suitable candidate for energy harvesting as well as storing material. This reduction in the dielectric loss of 10PALZO-P after poling was mainly due to the lower leakage current due to dipole orientation along the field direction. The a.c. conductivity of the composite films were calculated by using **Equation 3.1.4.** Frequency dependent a.c. conductivity of PVDF –HFP and all the composite films were represented in **Fig. 3.4.14 (c)**. a.c. conductivity increased with increasing Al@ZnO concentration in PVDF-HFP which is due to the formation of more conductive network in polymer matrix with increased filler loading.

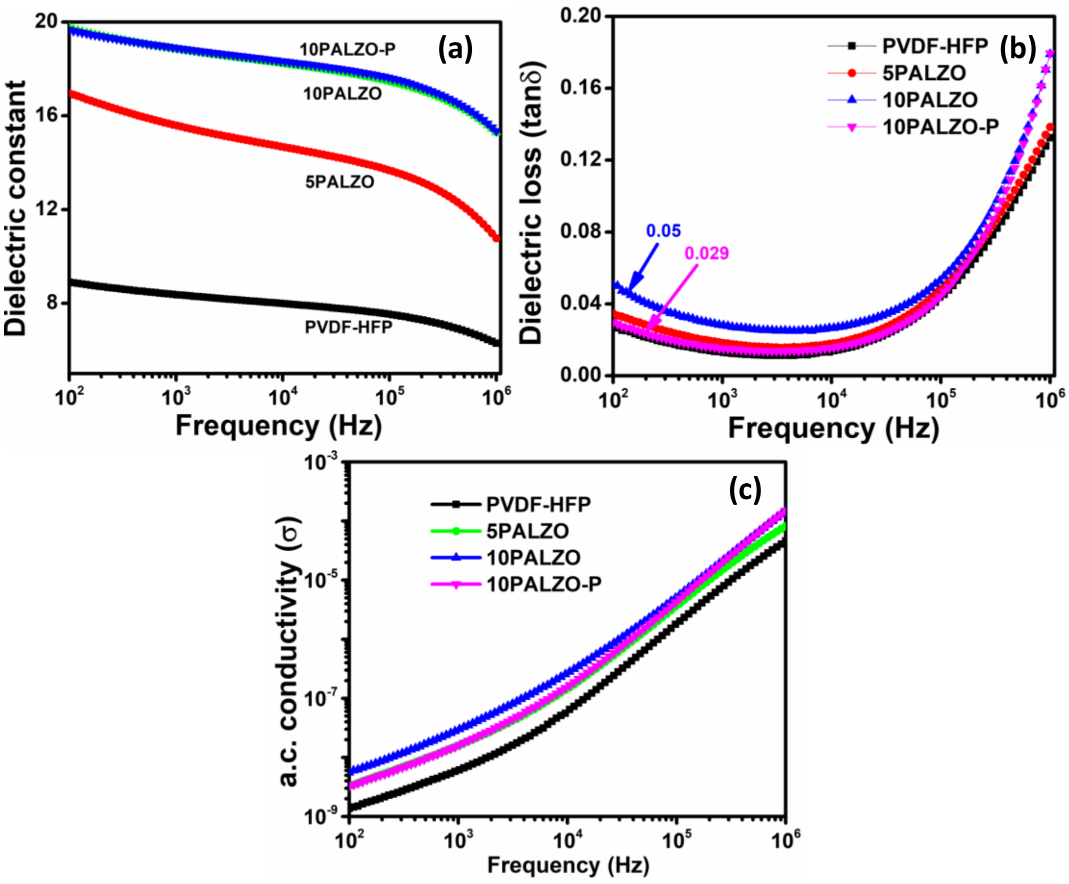

Fig. 3.4.14 *frequency dependent* ***(a)*** *dielectric permittivity,* ***(b)*** *dielectric loss* ***(c)****a.c. conductivity of PVDF-HFP, 5PALZO,10PALZO and 10PALZO-P nanocomposites.*

3.4.1.4 Ferroelectric properties of composite film

An efficient interfacial interaction leads to the enhancement of ferroelectric properties. In light of this, electric field dependent electric displacement or polarization (D-E hysteresis loop or P-E loop) of pure PVDF-HFP as well as composite films were measured to investigate the ferroelectric properties of the composite films (at 1 Hz).

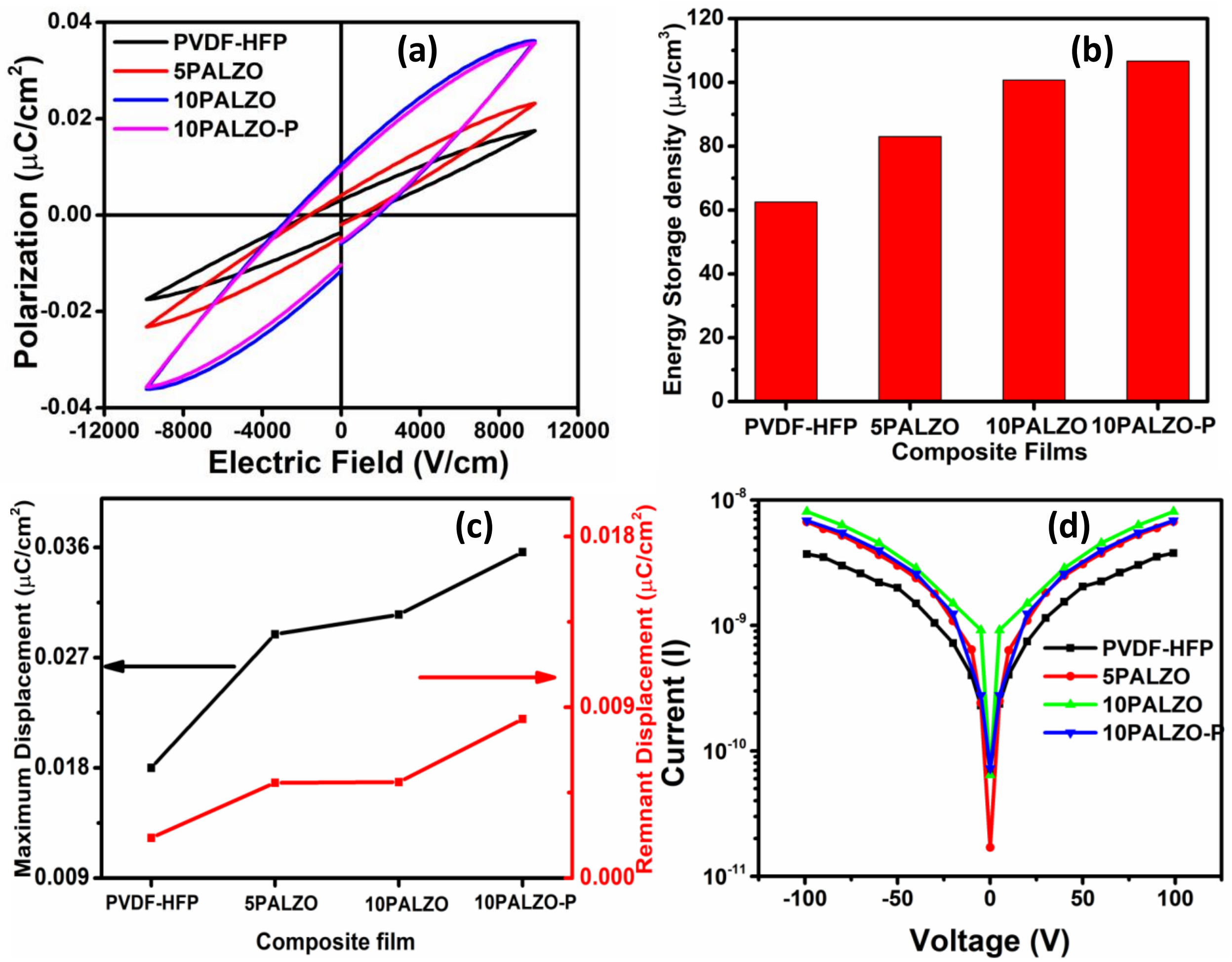

Fig. 3.4.15 *(a)Electric displacement vs applied electric field (D-E) loop, (b)Variation of energy storage density (c)Variation of Maximum displacement and remnant displacement of composite film, (d)leakage current of of PVDF-HFP, 5PALZO, 10PALZO and 10PALZO-P nanocomposites, composite film*

The room temperature D-E hysteresis loops of the pure PVDF-HFP, 5PALZO, 10PALZO and 10PALZO-P films were depicted in **Fig. 3.4.15(a)** which indicates the presence of ferroelectric properties within the sample. Remnant electric displacement (D_r) and maximum electric displacement (D_m) of all the samples (**Fig. 3.4.15(c)**) were enhanced with increasing concentration of Al@ZnO in polymer matrix. This result confirmed the enhancement of ferroelectric properties of the composites with significant small leakage current (**Fig. 3.4.15(d)**). This enhancement of ferroelectric properties was due to the strong interfacial interaction between PVDF-HFP matrix and Al@ZnO filler. The increased interfacial interaction between PVDF matrix and filler leads to an enhancement of polar phase within the composites, which increases the ferroelectric property.

In general, the energy density (U) of a non-linear dielectric material is given by $U=\int EdD$, where E and D denote the electric field and displacement, respectively [15]. Different portions of the D–E loops were integrated to calculate the energy storage and loss density. The energy storage density (U_{stored})of the nanocomposites was calculated using an integral formula given in **Equation 3.1.3.** An increment in the stored energy density for the loaded samples can be seen from **Fig. 3.4.15(b)**. However, it should be mentioned here that the maximum energy density ~ 111.2 μJcm^{-3} is obtained from the poled 10PALZO-P sample, implying the best suitable candidate for energy storage material. Poling process helped to reorient the dipoles along the field direction which increased the polar phase formation [21]. The breakdown voltage of the device was measured through P-E loop with applying different voltages (Shown in Figure S6 of SI). The polarization value of the nanocomposite increased with increasing applied electric field. The breakdown strength of the nanocomposite was 1120 $kVcm^{-1}$.The leakage current of the pure PVDF-HFP, 5PALZO, 10PALZO and poled 10PALZO-P sample are presented in **Fig. 3.4.15(d)** respectively. The reduction of the leakage current value of the 10PALZO-P film **Fig. 3.4.15(d)** after poling was mainly due to the dipole orientation of the composite [21]. This low leakage current also shows the applicability of the poled sample for a good nanogenerator.

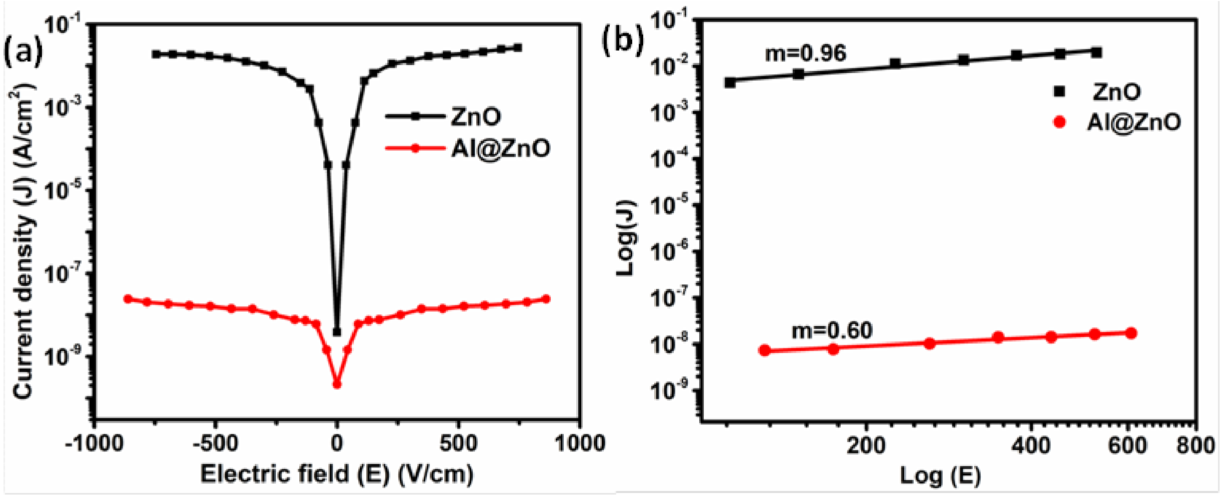

***Fig. 3.4.16** (a) J–E plots, (b) Log (J) versus Log (E) characteristics of pure ZnO and Al-doped ZnO nanorods at room temperature.*

Study of conduction mechanism is important to better understand the ferroelectric characteristics of the material [27-28]. Leakage current density (J) versus applied electric field (E) of both pure ZnO and Al@ZnO nanorods were measured using silver paint on the both side of the ZnO pellets. **Fig. 3.4.16(a)** presents the electric field dependent leakage current density of ZnO and Al@ZnO nanorods measured at room temperature. A closer observation to the figure indicates that leakage current density significantly reduced for Al@ZnO nanorods which was found to be 2.53 x 10^{-8} A/cm^2 from a value 2.9×10^{-2} A/cm^2 for ZnO nanorods . Thus, the leakage current density of Al@ZnO sample is about six times lower (in terms of magnitude) than that of pure ZnO sample. Conduction mechanism of the pellet can be understood from the slope of LogJ vs LogE curve. The slope (m) of the curve may be fitted by the power law given by the following equation

$J \propto E^{m}$ ………………(3.4.2)

Where the slope conveys the nature about conduction mechanism [29].

The values of the slope (m) obtained from linear fitting of exponential data was found to be 0.96 and 0.60 for pure ZnO and Al@ZnO nanorods respectively (shown in **Fig. 3.4.16(b)),** which confirmed ohmic conduction nature of the samples [27-29]. This reduced leakage current density for Al@ZnO nanorods can be attributed due to an increase in Schottky barrier height by Al-doping, which making it suitable for ferroelectric capacitor and nanogenerator [27-29].

3.4.1.5 PFM study of the composites

In order to investigate the local piezoelectric properties and ferroelectric domain switching behavior of the composite film after Al doping within ZnO, piezo force microscopy (PFM) measurement of the unpoled 10PALZO sample was carried out [20, 23]. In this measurement, a Ti/Ir coated conductive tip has been used with an AC voltage in the range of 1-2 V. The sweeping dc bias voltage applied to the samples were in the range of ± 60 V (PVDF-HFP) and ±40 V (10PZO and 10PALZO), respectively.

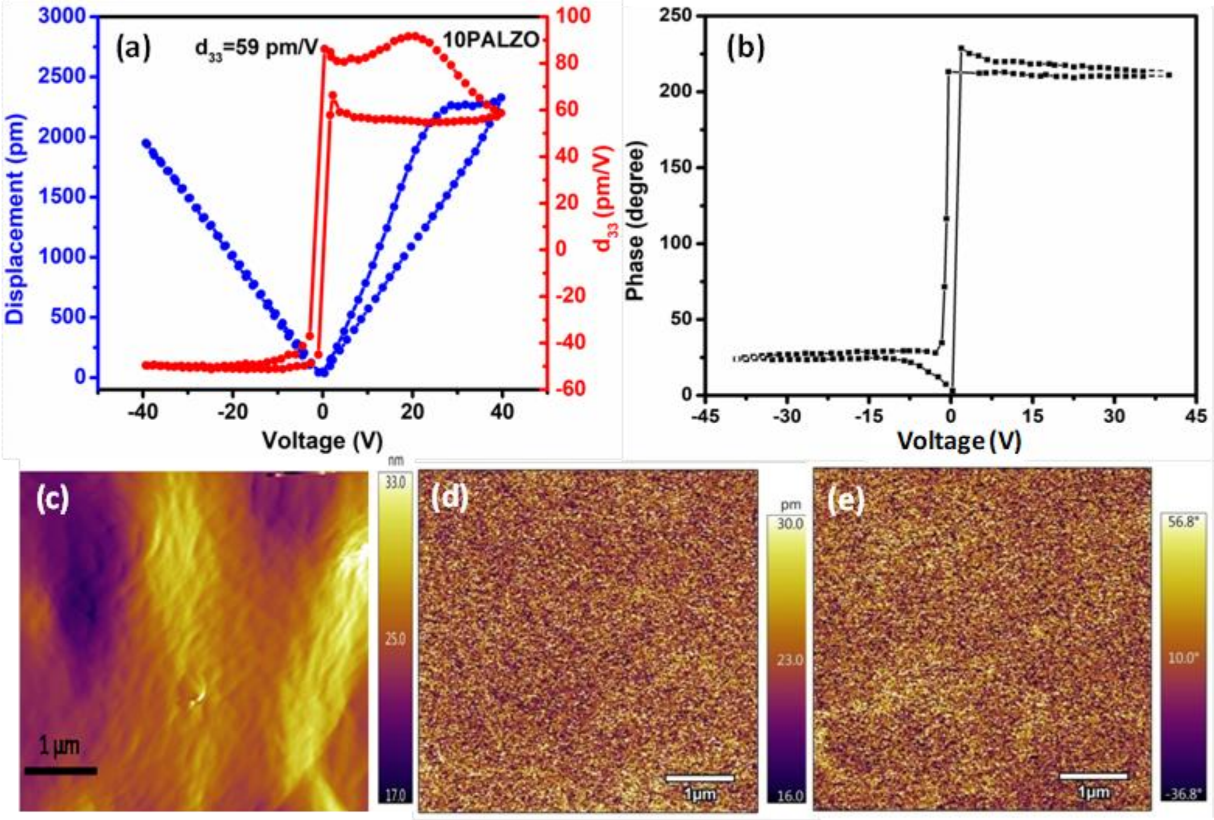

Fig. 3.4.17 (a-c) *Amplitude-voltage butterfly loop and d_{33}-V loop,(b)Phase-voltage hysteresis loop, (c)topography image, (d) Amplitude image and (e)phase image of 10PALZO composite film*

Fig. 3.4.17(a-b) represent the piezoresponse loop and phase hysteresis loop of 10PALZO sample under an applied DC bias voltage ±40V, respectively. Phase-hysteresis loop shows (**Fig. 3.4.17(b)**) the 180° phase difference which proves that the dipoles are easily capable of being switched upward or downward direction under an applied electric field which confirms the existence of ferroelectric domain switching behavior in the composite film [20, 23]. The asymmetric behaviour of the loop arises due to the generated internal bias within composite film [23]. 10PALZO composite contains a significant amount of β phase due to the TTTT trans conformation of –CH_2/-CF_2 dipole of PVDF-HFP. With the application of dc-bias across 10PALZO film, electric dipoles are rotated around the carbon backbone generating ferroelectricity within it which is confirmed from the ferroelectric switching behavior of the phase-voltage hysteresis loop [20]. Since the piezoelectric coefficient (d_{33}) is directly proportional to the electromechanical response of the material, the d_{33}-voltage loops can be indirectly derived from the amplitude-voltage butterfly loop using the modified equation of converse piezoelectric effect d_{33}= D-D_1/V-V_1, where D_1 is the piezoelectric displacement and V_1 is the applied voltage at the intersection [24].

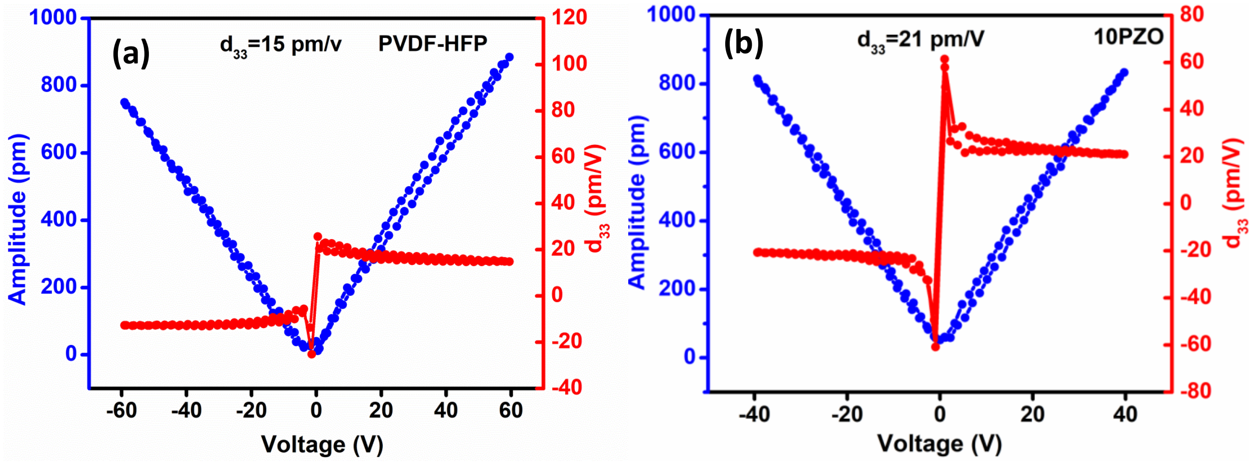

Fig. 3.4.18 *Amplitude-voltage butterfly loop and d_{33}-V loops of* ***(a)*** *PVDF-HFP,* ***(b)*** *PVDF/ZnO (10PZO) composite, respectively*

Figure 3.4.17 (a) represents the d_{33}-V loop of pure 10PALZO composite films. d_{33}-V loops of pure PVDF-HFP and ZnO incorporated PVDF-HFP (10PZO) are shown in **Fig. 3.4.18(a-b),** respectively. The calculated piezoelectric coefficient as obtained from **Fig. 3.4.18 (a)** and **Fig. 3.4.18(a-b),** was ~ 15 pm/V, 21 pm/V and 59 pm/V for pure PVDF-HFP, 10PZO and 10PALZO, respectively. The result infers that incorporation of ZnO nanorods within PVDF-HFP matrix cannot enhance the piezoelectric coefficient significantly. Interestingly, after addition of Al@ZnO filler within matrix, piezoelectric coefficient enhanced drastically to ~59 pm/V which is much higher than that of pure PVDF-HFP. This increment of piezoelectric coefficient with addition of Al@ZnO filler was mainly attributed to the increased polar phase fraction as obtained by FTIR results (**Fig.3.4.12**). **Fig. 3.4.17(c-e)** represents the topography, amplitude and phase images of 10PALZO composite film, respectively. PFM amplitude is associated with the local piezoelectric coefficient due to electromechanical coupling where the orientation of domains or polarization can be reflected by the phase [20, 23]. Domains with opposite polarization can be distinguished by image contrasts (shown in **Fig. 3.4.17(d)).** The dark brown and bright yellow regions are mainly attributed to the polarization of domains with upward and downward direction, respectively. Both amplitude and phase images with different contrasts confirmed the presence of piezoelectric and ferroelectric properties within the composite film [23]. PFM results confirmed that the 10PLZO composite film possesses good ferroelectric and piezoelectric properties, making it suitable for good mechanical energy harvesting [20].

3.4.1.6 Energy harvesting properties of the composites

To investigate the efficiency of the sample as an efficient energy harvesting device (PZEH) the voltage generation capacity of the fabricated composite films, under compressing and releasing process of finger impartingon them were observed (Pressure~4 kPa, Frequency ~5 Hz).

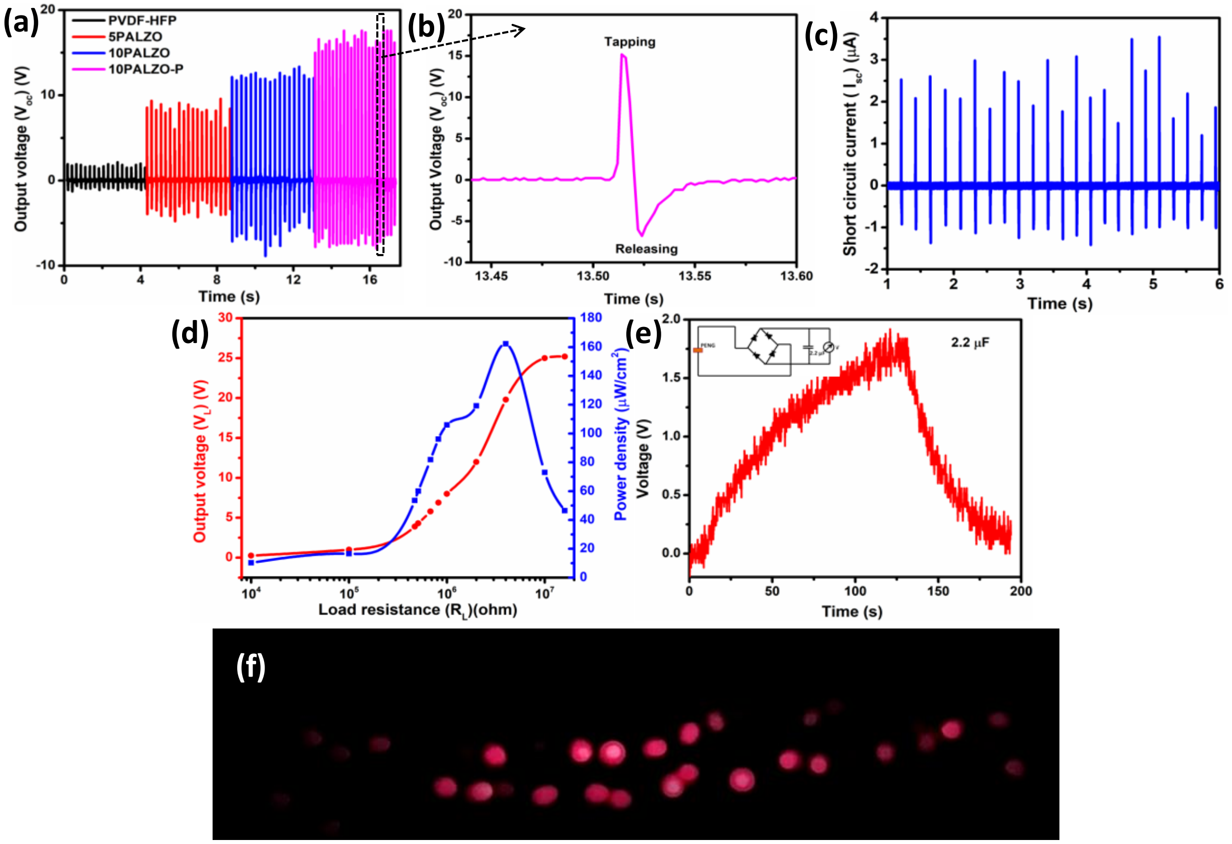

***Fig. 3.4.19 (a)**) Open circuit output voltage of PVDF-HFP, 5PALZO, 10PALZO and 10PALZO-P nanocomposites, **(b)** Magnified image of one cycle of 10PALZO-P film, **(c)**Short circuit output current of 10PALZO-P film, **(d)**The variation of output voltage and power densitywith load resistance, **(e)** capacitor charging and discharging graph, **(f)**LED glowing performance of 10PALZO-P composite film*

The open circuit output voltage as obtained from pure PVDF-HFP and composite films is illustrated in **Fig. 3.4.19 (a).** It can be clearly seen from the figure that with the increasing filler loading, the open circuit output voltage of the nanocomposite films increased gradually and reaches a maximum value of ~ 22 V for 10 wt% of Al@ZnO loading. When mechanical force was applied, the permanent dipoles oscillated and as a result of this oscillation, an electric potential difference generated between top and bottom electrodes. This potential allows free electron to circulate across an external circuit, resulting in the generation of electric signals [21, 25]. Therefore, the increased value of output voltage with filler loading was due to the enhanced polarity of the system. A careful observation to the figure indicates that, output voltage of 10PALZO-P film further increased to ~ 26 V from 22 V which was mainly attributed to the highest polar phase formation within the system generated by reorientation of polymer chains due to poling [21].

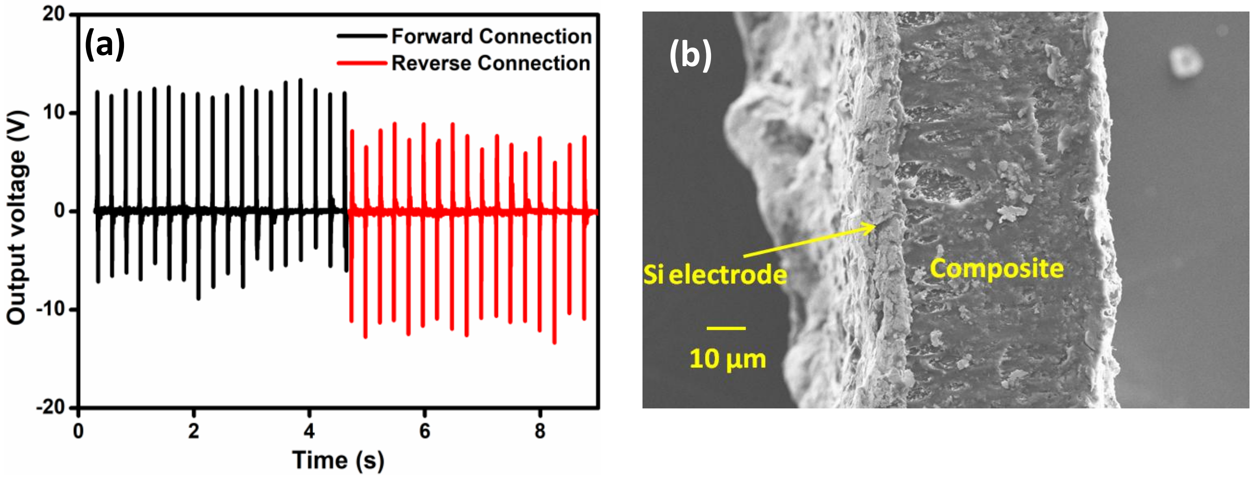

Fig. 3.4.20 (a) Forward and reverse connection of 10PALZO-P sample, (b) Cross sectional FESEM image of 10PALZO-P sample

To confirm piezoelectric voltage of the device, switching polarity test of this composite was done by reversing the electrodes connection. Nearby same voltage was obtained after reversing the electrode connection (shown in **Fig. 3.4.20(a))** which proved that the output voltage arises from the piezoelectric effect [18]. Again, the cross sectional FESEM image of the device as presented in **Fig. 3.4.20(b)** also confirms the piezoelectric nature of the device as no such spacing has been observed between electrode and functional layer [20]. Thus the electric signals are purely piezoelectric. The enlarged image of one output pulse, under compressing and releasing processes of finger tapping was presented in **Fig. 3.4.19 (b). Fig. 3.4.19 (c)** reveals the generated short circuit current (4 μAmp) from the device using 10 wt% Al@ZnO incorporated PVDF-HFP under the action of finger imparting (force 4 kPa, frequency~ 5 Hz).The obtained a.c. output voltage was rectified to d.c. voltage by using a bridge rectifier (DB107) which was capable of charging a 2.2 μF capacitor up to ~ 1.8 V (Shown in **Fig. 3.4.19(e)).** The fabricated PZEH is also capable of illuminating instantly 30 commercial LEDS under repeated finger imparting connected in series (**Fig. 3.4.19(f)**). To examine the real life feasibility of the fabricated device, power density was calculated by using by using the **Equation 3.1.4.** .The obtained output voltage and power density of 10PALZO-P composite film with different load resistance were presented in **Fig. 3.4.19(d).** The output voltage increased gradually with increasing load resistance and reached a maximum value of 26 V across a 8 MΩ load resistance. The maximum output power density of 10PALZO-P composite film was found to be ~160.1 μWcm^{-2} at 8 MΩ load resistance. The maximum power density as well as generated voltage as obtained from PZEH is quite higher than the other previously reported PVDF based nanogenerator. In this context it is pertinent to be mentioned here that the output performance of the fabricated PZEH is quite comparable with other doped ZnO filler loaded matrixes.

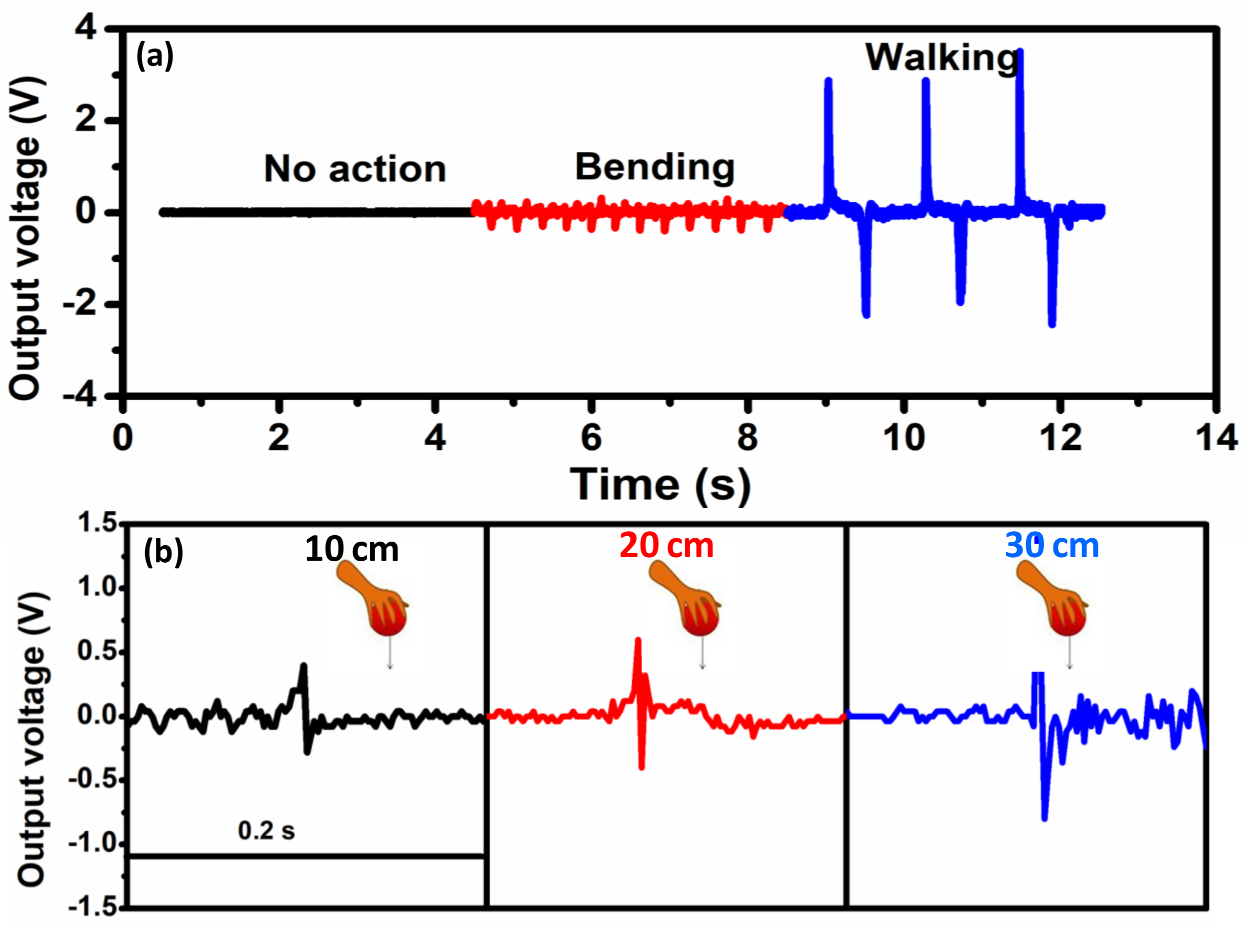

Fig. 3.4.21 ***(a)*** *Variation of output voltage with different human body activities,* ***(b)*** *Output voltage variation for ball dropping from 10 cm, 20 cm and 30 cm heights.*

Further, for real life application, the sensitivity of the 10PALZO-P film was also checked by applying different types of human body motion. As shown in **Fig. 3.4.21(a)**, a output voltage of~2V was generated for bending of the device while for walking the output voltage was ~ 4.5 V. This result indicated that the device showed sensitivity for different type of human body motions.Therefore, this composite can be used as physical activity sensor for detecting body motions or activities. In order to check the pressure sensitivity of the 10PALZO-P sample, a rubber ball of mass 20 g was dropped from 10 cm, 20 cm and 30 cm heights and corresponding output signal were recorded respectively, which was shown in **Fig. 3.4.21(b)**.

Applied pressure by ball dropping was calculated on the basis of kinetic energy and momentum theorem [26]. Actually, there exist two processes during the falling of an object on the film surface (here in this work, ball dropping) ,:1) initially touch the surface of the film, and 2) then completely acting on the film. In the first process, the velocity of the object increases to a maximum value and in second process it decreases to zero. Hence, based on the kinetic energy and momentum theorem, we have the following Equations [26]:

$mgh=\frac{1}{2}mv^2$ .... (3.4.2)

$(F-mg)\Delta t=mv$ .... (3.4.3)

$\zeta= \frac{F}{S}$ .... (3.4.4)

Where, m is the mass of the object, h is the height from where it is fall, v is the maximum falling velocity, ζ is the applied pressure or applied stress, F is the contact force, S is the effective contact area and Δt is the time span during the second process. Here, S= 600 mm^2 is the approximate active area (effective area) of the electrode (area under the external pressure), m= 0.02 Kg is measured using laboratory balance, Δt = 0.01 sec is the estimated average time difference between the two consecutive voltage peak, h is the approximate height (0.1 m, 0.2 m and 0.3 m) and g = 9.80 N/kg. Therefore, these values calculate the input force, F ≈ 2.9, 4.1 and 5.1 N for height 0.1 m, 0.2 m and 0.3m, which gives the approximate contact pressure in the order of $\zeta \approx$ 4.96, 6.88 and 8.33 kPa respectively [26].

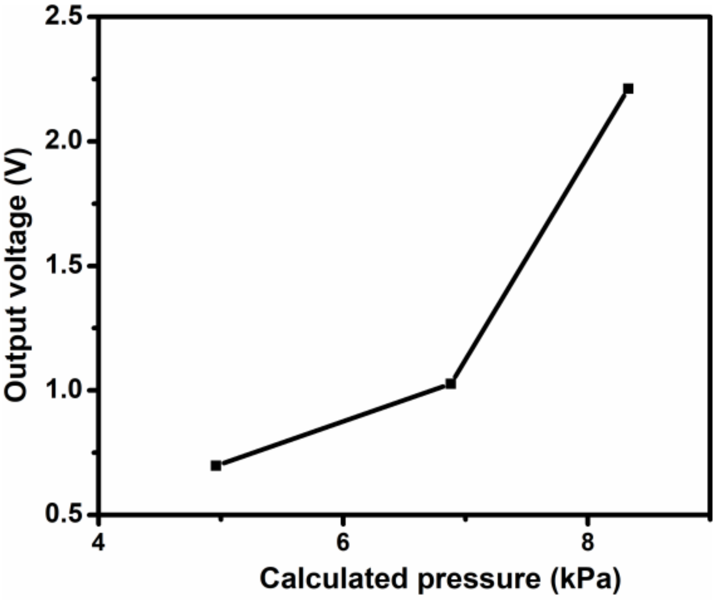

Fig. 3.4.21 *pressure sensitivity as a function of output voltage.*

The impact pressure was calculated from different heights and corresponding ac output voltages are plotted in **Fig. 3.4.22**. This result clearly indicates PZEH can distinguish a very minor change in applied pressure and accordingly this PZEH may be used for application as height monitoring sensors [19]. This result clearly indicates that the fabricated device has high sensitivity and this may be used as a height monitoring sensor too [19].

3.4.1.7 Conclusion:

In summary, it can be concluded that Al@ZnO incorporated PVDF-HFP films were successfully developed using the simple and cost effective solvent casting technique. An increment in electroactive polar phase fraction was found with the increasing loading of Al@ZnO. An effective interfacial intereaction between filler and the polymer matrix results in maximum electroactive phase fraction (F(EA) > 85%) β for 10 wt% Al@ZnO loaded PVDF-HFP composite. Moreover, a more than two times increase in dielectric constant (~19) was achieved in comparison to bare PVDF-HFP (~8). In addition to that, 10PALZO nanocomposite exhibited a good energy storage density of 94.1 μJ/cm^3. The fabricated piezoelectric energy harvesting device using optimized 10PALZO nanocomposits was able to deliver a open circuit output voltage of ~ 22 V under gentle human finger tapping (frequency 4Hz, pressure~ 4 kPa). A further enhancement in electrical performance of 10PALZO nanocomposite was achieved by applying a high electric field (2.4MVcm^{-1}). Applied electric field results in further alignment of polymer chains leading towards a electroactive phase fraction as high as ~91.2 %. Though the dielectric constant has been increased slightly after poling but there is a considerable low dielectric loss (0.03). Owing, to such electrical properties, poled 10PALZO nanocomposite exhibited a good energy storage density of 111.2 μJcm^{-3} (at 1 Hz). A further increment in open circuit output voltage to 26 V was obtained from 10PALZO-P nanocomposite based energy harvester under similar imparting condition. A high instanteneous power density of 159.95 μWcm^{-2} and short circuit current of~ 4 μA, enables the nanogenerater to be used in real life applications such as fast charging of capacitor (2.2 μF upto 1.8 V), energy generation from human body motion, and powering a panel of commercial LEDs. Furthermore, the piezoelectric nanogenerator has been used efficiently as a height-monitoring sensor. Thereby, the fabricated flexible piezoelectric nanogenerator can effectively pave the way towards low cost, flexible as well as wearable piezo-electric energy harvesting devices.

References:

1. T. Minami, H. Nanto, S. Takata. *Japan J. Appl. Phys*., 1984, **23**, 280.
2. H. Wang, S.H. Baek, J.J. Song, J.H. Lee, SW Lim. *Nanotechnology*., 2008, 19, 075607.
3. M.N. Jung, J.E. Koo, S.J. Oh, B.W .Lee, W.J. Lee, S.H. Ha, Y.R.Cho, J.H. Chang. *Appl. Phys. Lett*., 2009, **04**, 041906.

4. P. S. Vijayakumar, K. A. Blaker, R. D. Weiting, B. Wong, A. T. Halani, and C. Park, *U. S. Patent.*, 1988, **4**, 149.
5. H. Parangusan, D.Ponnamma, M. Al. Ali. AlMaadeed, *RSC Adv.*, 2017, **7**, 50156.
6. H. Parangusan, D. Ponnamma, MAA Al-Maadeed. *Scientific Reports.*, 2018, **8**,754.
7. S. Barman, S. Sikdar, A. Biswas, B.K. Mandal, R. Das, *Nano Express.*, 2020, **1**, 020003.
8. A. Shah, M. Ahmad, Rahmanuddin, S. Khan, U. Aziz, Z. Ali, A. Khan, A. Mahmood, *Applied Physics* A., 2019, **125**,713.
9. F. Mouzaiaa , D. Djouadia , A. Chelouchea , L. Hammichea and T.Touamb, *Arab Journal of Basic and Applied Sciences.,* 2020, **27**, 423–430.
10. M. J. Akhtar , H. A. Alhadlaq , A. Alshamsan, M.A. M. Khan & M.Ahamed, *Scientific Reports*, **5**,13876.
11. M. R. Islam, M. Rahman , S.F.U. Farhad , J. Podder, *Surfaces and Interfaces,* 2019, **16**, 120-126 .
12. R. Al-Gaashani, et al., *Ceram. Int.*, 2013, **3**, 2283–2292.
13. B.A. Farsi, T.M. Souier, F.A. Marzouqi, M.A. Maashani, M. Bououdina, H.M. Widatallah , M.A. Abri, *Optical Materials.,* 2021 ,**113**, 110868.
14. E. S. TÜZemen et al. *Turk. J. Phys.*, 2014, **38**,111–117.
15. A. Sasmal, S. Sen, P.S. Devi. *Phys. Chem. Chem. Phys*. 2019, **21**, 5974.
16. H. Parangusan, D. Ponnamma, M. A. A. Al-Maadeed, *ACS Omega.*, 2019,**4**, 4, 6312–6323.
17. S.K. Karan, D. Mandal, B.B. Khatua. *Nanoscale.*, 2015, 7, 10655−10666.
18. S. Pratihar, A. Patra, A. Sasmal, SK Medda, S. Sen, *Soft Matter.*, 2021,**17**, 8483-8495.
19. I. Chinya, A. Pal, S. Sen, *Mater. Research Bulletin.*, 2019, **118**, 110515.

20. E. Kar, N. Bose, B. Dutta, N. Mukherjee, S. Mukherjee. *ACS Appl. Nano Mater*., 2013, **7**, 10424.
21. A. Sasmal, P.S. Devi, S. Sen, *Soft Matter.***,** 2020,**16**, 8492-8505.
22. E. Kar , N. Bose, B. Dutta , S. Banerjee , N. Mukherjee, S. Mukherjee, *Energy Conversion and Management*., 2019,**184**, 600–608.
23. C. Zhang, Y. Fan, H. Li, Y. Li, L. Zhang, S. Cao, S. Kuang, Y. Zhao, A. Chen, G. Zhu, ZL Wang, *ACS Nano*., 2018, **12**, 4803.
24. J Chen, Z. Tang, R. Tian, Y. Bai, S. Zhao, H. Zhang. *RSC Adv*., 2016; **6**: 33834.
25. M.R. Joung, H. Xu, I.T. Seo, DH Kim, J Hur, S. Nahm, C.Y. Kang, S.J. Yoon, H.M. Park , *J. Mater. Chem. A.,* 2014, **2**, 18547-18553.
26. S. K. Karan, D. Mandal , B. B. Khatua, *Nanoscale*., 2015,**7**, 10655-10666.
27. K. Batra, N. Sinha, S. Goel, H. Yadav, A. J. Joseph, B. Kumar, *Journal of Alloys and Compounds*., 2018, **767**, 1003-1011.
28. S. Goel, N.Sinha, H. Yadav, A. J. Joseph, B. Kumar, *Journal of Materials Science: Materials in Electronics.* , 2018, **29**, 13818–13832.
29. A. Sasmal, S. Sen, P. S. Devi, *Materials Chemistry and Physics,*, 2020, **254**, 123362.

CHAPTER-4

SUMMARY AND FUTURE SCOPE

At a glance, the entire research work are reviewed and summarized in this chapter. The major findings that arose from this thesis work with the key outcome of all the experiments have been highlighted. Significant characteristics of all sets of piezo composites, perspective for device development have been summarized in this chapter. Also, consequent future scopes and outlook have also been mentioned in this chapter.

Chapter 4: Summary and future scope

4.1 Summary of the thesis work:

The main objective of this thesis work was the development of lead free flexible polymer ceramic composites for energy storage and energy harvesting application. To achieve this goal, several research works have been carried out including different techniques, characterization and application. Therefore the perspective and implication of mechanical energy harvester along with background, motivation and objectives of the desertion work were described in Chapter 1. Different synthesis procedure and fabrication techniques to develop the PVDF composite film and the methods utilized for characterization have been described in detailed in Chapter 2. The all experimental results and respective analysis have been discussed in Chapter 3. The conclusion of all experimental findings and discussion were described below in brief.

1. In order to investigate the morphological influence of ZnO on the stabilization of β phase of PVDF as well as dielectric, ferroelectric and piezoelectric properties of PVDF based composites, two types of morphologically different ZnO i.e. wet chemically synthesized ZnO particle and hydrothermally synthesized ZnO nanorods were incorporated into PVDF to fabricate their respective composite film. Between the two different shaped of ZnO, filler having rod shape structure was found to be more effective in enhancing the dielectric, ferroelectric, energy storage and energy harvesting performance of their PVDF based composite films compared to particle like structure. This was due to the larger interfacial interaction of ZnO nanorods and PVDF matrix which was attributed not only to the large surface area but also the preferred “in plane” orientation of ZnO nanorods during solvent casting.
2. Taking into consideration, that rod shaped structure exhibited the best performance in improving the electrical properties of the PVDF composite system. Therefore, 1D rod

shaped structure of ZnO was chosen as filler in PVDF for further investigation to improve the output performance of the PVDF composite films.

3. To study the effect of aspect ratio on the electrical properties of PVDF based composite system, ZnO nanorods with different aspect ratio were synthesized by varying growth time 4 h to 20h at a fixed temperature and incorporated into PVDF matrix to fabricate the resulting composite film. High aspect ratio ZnO filler loading in PVDF matrix increased the polar phase fraction in the nanocomposite system which triggered the enhancement of dielectric properties along with ferroelectric and piezoelectric properties. As high aspect ratio fillers have more negative surface charge on its surface, more interfacial interaction occurs between the surface charge of high aspect ratio filler and PVDF matrix which leads to an enhancement of output performance of the composite film.
4. As, the aspect ratio of ZnO nanorods was tuned to achieve the performance enhancement of the resulting PVDF based composites. For further enhancement of output performance, third phase conductive filler was added to improve the electrical performances of the flexible PVDF-ZnO composites. Therefore, three phase composite films comprising of PVDF matrix, ZnO nanorods and MWCNT were fabricated using drop casting technique. The third phase conductive MWCNT reduced the compatibility issue and supported homogeneous dispersion of ZnO in PVDF matrix which further improved the polarity of resulting composite films by enhancing the interfacial interaction with –CH_2 dipoles of PVDF which lead to the enhancement of electroactive phase, dielectric permittivity, ferroelectric polarization, energy storage density and mechanical energy harvesting performance. The observed experimental results of electrical properties were also verified by theoretical simulation. Conductive MWCNT

improved the connectivity between ZnO nanorods dispersed in insulating PVDF matrix and between the composite films and electrodes which improved the output mechanical energy harvesting performance.

5. ZnO filler was further modified by doping Al^{3+} ions into the ZnO host lattice which changed the surface charge of the nanofiller and reduced the oxygen point defects. On the other hand, ZnO doped by Al^{3+} ions enhanced the dielectric constant value with low dielectric loss and reduced the leakage current value . The enhanced surface charge of ZnO filler improved the polar phase, dielectric permittivity, energy storage density and mechanical energy harvesting performance of the resulting PVDF-HFP based composite films. This result was mainly attributed to the modified surface charge of ZnO by Al^{3+} doping which resulted in the improved interfacial interaction of $–CH_2$ dipoles of PVDF –HFP with doped ZnO filler.

For comparison purpose, the output energy harvesting performances of the optimized composite films of are depicted in **Table 4.1** which delivered the maximum electrical output signal compared to other films in the particular series.

Table 4.1 *Comparison of output energy harvesting performance of the optimized composite films*

Si. No.	**Composite film**	**Output voltage (V_{oc}) (V) upon human finger tapping (~4kPa, 5Hz)**	**Output current and power density across the load resistance**		
			Power density P(μW/cm^2)	Current I (μA)	Load resistance (R_L) (MΩ)
1.	PVDF	3	-	-	-
2.	ZR-15	18	4.6	1.7	10
3.	PVDF/ZnO-20	20	9.6	2.5	8
4.	15PZNT	22	21.4	4.2	4
5.	10PALZO-P	26	160.1	5.8	8

The generated open circuit a.c. output voltage (V_{oc}) was further converted to d.c. output voltage by using a bridge rectifier. This rectified d.c. voltage was used to charge some commercially available capacitors. The real life applicability of the piezoelectric devices were demonstrated by lighting up some LEDs under repeated finger imparting connected in series. **Table 4.1** shows that 10PALZO-P composite films exhibited best performance compared to others. Further, for real life application, the sensitivity of the 10PALZO-P film was also checked by applying different types of human body motion. This piezoelectric energy harvester (PZEH) acted very well as a height-monitoring sensor as well as human body motion based energy harvester. Therefore, in this thesis work a series of lead free ZnO based flexible piezoelectric energy harvester were fabricated and their performance have been explored by using different techniques.

4.2 Future scope:

In near future the current work can be extended from multiple viewpoints including material, device structure and application. In future, major research works can be followed by this dissertation followed here.

- Fabrication of flexible piezo-tribo hybrid nanogenerator for highly sensitive device applications.
- Study the effect of p-type and n-type mixed filler loading in polymer matrix.
- Demonstration of different other real life application of the fabricated nanogenerator devices.
- Fabrication of e-skin device with temperature sensing, temperature distribution mapping, humidity sensing and proximity sensing properties.
- Use of other filler materials in polymer matrix to investigate output electrical performance of nanogenerator.
- Development of co-polymers based composites by using PDMS and PVDF-TrFE etc to explore their suitability in energy generation and for different applications.
- Investigation of large scale power from wind energy, ocean wave energy etc by using modified nanogenerator devices.
- Integration of fabricated nanogenerator devices for self-powered gas sensor, humidity sensor, photodetector, photovoltaic cell, solar cell etc.

SYMBOLS

Å	Angstrom
V	Volume
D	Crystallite size
e-	Electron
eV	Electron volt
ϴ	Diffraction Angle
λ	Wavelength of X-ray Radiation
υ	Frequency
W	Watt
V_{oc}	Open circuit voltage
I_{sc}	Short circuit current
P	Power/Power density
U_{stored}	Stored energy density
U_{loss}	Loss energy density
η	Energy discharge efficiency
h	Hour
K	Kelvin
cal	Calorie
J	Joule
K	Kelvin
Ω	Ohm
A	Ampere
k_B	Boltzmann's Constant
KΩ	Kilo Ohm
M	Molar Concentration
mM	milimolar Concentration
R	Resistance
ρ	Density
T	Temperature
c	Velocity of light in vacuum
T_g	Glass transition temperature
ε_0	Free permittivity
ε_r	Relative permittivity
ε	Dielectric constant
tanδ	Dielectric loss tangent
M_w	Molecular weight
A	Effective surface area
d_{33}	Piezoelectric coefficent
Hz	Hertz

ABBREVIATIONS

Abs	Absorbance
AR	Analytical Reagent
DMF	N, N- Dimethylformammide
DMAC	N, N- Dimethylacetamide
PVDF	Polyvinylidene fluoride
HRTEM	High Resolution Transmission Electron Microscopy
EDS	Energy Dispersive X-ray spectroscopy
SAED	Selected Area Electron Diffraction
FESEM	Field Emission Scanning Electron Microscopy
FTIR	Fourier Transform Infrared Spectroscopy
UV-Vis	Ultra Violet- Visible
XPS	X-ray photoelectron spectroscopy
XRD	X-ray Diffraction
FWHM	Full width half maxima
EDX	Energy Dispersive X-ray
FESEM	Field Emission Scanning Electron Microscopy
HRTEM	High Resolution Transmission Electron Microscopy
h	Hour
rpm	Revolution per Minute
SEM	Scanning Electron Microscopy
JCPDS	Joint Committee on Powder Diffraction Standards
% T	Percentage Transmittance
% Abs	Percentage Absorbance
1D	One Dimensional
3D	Three Dimensional
TGTG’	Trans-gauche-trans-gauche
TTTT	Trans-Trans-trans-trans
LED	Light Emitting Diode
NG	Nanogenerator
AC	Alternating Current
DC	Direct Current
µA	microampere
F(EA)	Electroactive polar phase fraction
F(β)	β phase percentage
F(γ)	γ phase percentage
Wt%	Weight percentage
D_r	Remnant electric displacement
D_m	Maximum electric displacement
P_r	Remnant polarization
P_m	Maximum polarization
MEMS	Micro Electro Mechanical Systems

MWCNT	**Multi walled carbon nano tube**
nm	**Nanometer**
NP	**Nanoparticles**
NR	**Nanorods**
R&D	**Research and Development**
R	**Resistance**
RT	**Room Temperature**

LIST OF PUBLICATIONS

1. **S. Pratihar**, S. K. Medda, S. Sen*, P. S. Devi "Tailored piezoelectric performance of self-polarized PVDF-ZnO composites by optimization of aspect ratio of ZnO nanorods " ***Polymer Composites***, 2020,**41**,3351–3363.
2. **S. Pratihar**, A. Patra, A. Sasmal, S. K. Medda, S. Sen*, "Enhanced dielectric, ferroelectric, energy storage and mechanical energy harvesting performance of ZnO-PVDF composites induced by MWCNT as an additive third phase" ***Soft Matter***, 2021,**17**, 8483-8495.
3. **S. Pratihar,** E. kar, S.Sen*, "Aluminium impregnated Zinc Oxide engineered Poly(vinylidene fluoride hexafluoropropylene) based flexible nanocomposite for efficient harvesting of mechanical energy" ***International Journal of Energy Research.*** **(Revision submitted).**
4. K. Kundu, A.Ghosh, **S. Pratihar**, S.Govind Singh, T. K. Kayal, R.Banerjee*,"Boron doped SiC thin film on silicon synthesized from polycarbosilane: A new lead free material for application in piezosensors" *Journal of material science: Material in electronics*, 2021.
5. **S. Pratihar,** E.Kar, S.Sen, "Morphological effect of nanofiller on the stabilization of electroactive phase and electrical performances of their respective ZnO-PVDF based composites" (Communicated)

LIST OF PRESENTATION

1. **S. Pratihar**, S.Sen*, P. S. Devi, Poster presentation entitled, "Controlled hydrothermal synthesis of high aspect ratio ZnO nanorod for energy harvesting application " in the International Conference on Microscope and XXXIX Annual Meeting of Electron Microscope Society of India (EMSI-2018) during 18th-20th July, 2018 at Mayfair Convention Centre, Bhubaneswar (Odisha), India.

2. **S. Pratihar**, S.Sen*, P. S. Devi, Poster presentation entitled "Sol-gel synthesized ZnO nanorods of different aspect ratio for self-powered sensor application" in the International Conference on Complex and Functional Materials (ICCFM-2018) during 13th-16th December, 2018 at Biswa Bangla Convention Centre, Kolkata.

3. **S. Pratihar**, S.Sen, P. S. Devi, E-poster presentation entitled "Effect of ZnO nanofiller on structural and electrical properties of Polyvinylidene Fluoride" in the National Conference on Recent Developments in Nanoscience and Nanotechnology

(NCRDNN 2019 during 29th-31st January, 2019 at Triguna Sen Auditorium, Jadavpur University, Kolkata -700032, West Bengal, India.

4. **S. Pratihar,** S. Sen, P. S. Devi, Poster presentation entitled "MWCNT/ZnO based PVDF composites: structural and electrical properties" in the International Conference on Current Trends in Materials Science and Engineering (CTMSE 2019) during 18th-20th July, 2019, at S. N. Bose National Centre for Basic Sciences, Kolkata.

5. **S. Pratihar**, S. Sen, P. S. Devi, Poster presentation entitled "Structural and electrical properties of Al doped ZnO/PVDF-HFP nanocomposites: dielectric, ferroelectric and piezoelectric properties" International Conference on Advanced Functional Materials (ICAFM-2019) during 9th-10th december 2019, CSIR-NIIST, Kerala, India.

6. **S. Pratihar**, S. Sen, P. S. Devi, Poster presentation entitled "Enhanced flexible piezoelectric energy harvesters based on PVDF/ZnO-CNT composite films" National Conference on Innovations and Technologies for Ceramics (InTec-2019) India during 11th-12th December, 2019, CSIR-NIIST, Kerala,.

7. **S. Pratihar**, S. Sen, P. S. Devi, Poster presentation entitled "Lead-free flexible piezoelectric energy harvester comprised of ZnO nanorods and carbon nano tube " in the 2nd Indian Materials Conclave and 31st AGM at Kolkata, MRSI Kolkata Chapter at CSIR-Central Glass & Ceramic Research Institute, Kolkata during 11th -14th February, 2020.

8. **S. Pratihar**, S. Sen, P. S. Devi, Poster presentation entitled (Online mode) "Enhanced dielectric, ferroelectric, piezoelectric properties of Al doped ZnO/PVDF-HFP nanocomposites" in the International virtual conference on Advances in functional materials (AFM 2020) during 26th-28th august, 2020 at Kalinga Institute of Industrial Technology (KIIT) Deemed to be University, Bhubaneswar, Odisha, India.

9. **S. Pratihar**, S. Sen, P. S. Devi, Poster presentation entitled (Online mode) "Enhanced dielectric, ferroelectric, piezoelectric properties of Ga doped ZnO/PVDF-HFP nanocomposites" at 84th Annual Session of the Indian Ceramic Society and National Seminar on "Propelling Innovations in Glass and Ceramics for Atmanirbhar Bharat" for 11th - 12th of December, 2020, CSIR-CGCRI.

10. **S. Pratihar**, S. Sen, Poster presentation entitled (Online mode) "Enhanced dielectric, ferroelectric and energy harvesting properties of three phase composites based on PVDF/ZnO and modified carbon nano tube " in the International Symposium on Materials of the Millennium: Emerging Trends and Future Prospects (MMETFP-2021) during November 19th-21st, 2021 at Pandit Deendayal Energy University, Gandhinagar, India.

11. **S. Pratihar**, S. Sen, Poster presentation entitled (Online mode) “PVDF-$ZnAl_2O_4$ composite: A new lead free material for energy harvesting application” at International Conference on Advanced Materials and Mechanical Characterization (ICAMMC-2021), during 2nd-4th December, 2021 at SRM university.
12. **S. Pratihar,** S. Sen, Poster presentation entitled (Online mode) “Al@ZnO/PVDF-HFP nanocomposite: a novel flexible piezoelectric energy harvester” in the Advanced Energy Materials & Devices -2022 (AEMD-2022), dated 3rd March, 2022 at CSIR-Central Glass & Ceramic Research Institute, Kolkata.

Received: 1 October 2019 | Revised: 22 April 2020 | Accepted: 24 April 2020
DOI: 10.1002/pc.25624

RESEARCH ARTICLE

Polymer COMPOSITES
WILEY

Tailored piezoelectric performance of self-polarized PVDF-ZnO composites by optimization of aspect ratio of ZnO nanorods

Shewli Pratihar[1] | **Samar Kumar Medda**[2] | **Shrabanee Sen**[1] | **P. Sujatha Devi**[3]

[1]Functional Materials and Devices Division, CSIR-Central Glass and Ceramic Research Institute, Kolkata, West Bengal, India

[2]Speciality Glass Technology, CSIR-Central Glass and Ceramic Research Institute, Kolkata, West Bengal, India

[3]Chemical Science and Technology, CSIR-National Institute for Interdisciplinary Science and Technology, Thiruvananthapuram, Kerala, India

Correspondence
Shrabanee Sen, Functional Materials and Devices Division, CSIR-Central Glass and Ceramic Research Institute, Kolkata 700032, West Bengal, India.
Email: shrabanee@cgcri.res.in

Funding information
Department of Science and Technology, Government of India, Grant/Award Number: DST/INSPIRE Fellowship/2017/IF170048

Abstract

Aspect ratio of filler plays a crucial role to study the electrical properties of polymer based composite system. Here, we investigated the effect of filler aspect ratio on the electrical properties of zinc oxide (ZnO) incorporated poly(vinylidene fluoride) (PVDF) matrix. ZnO nanorods having different aspect ratio were synthesized by the hydrothermal technique with varying reaction time 4 to 20 hours at a fixed temperature and PVDF based nanocomposites of the respective ZnO nanorods with different wt% filler loading were fabricated. Interestingly polar-phase fraction increased with the aspect ratio of ZnO nanorods. The nanocomposites with higher aspect ratio ZnO nanorods showed an increased energy density under same electric field and exhibited maximum open circuit AC output voltage (ie, 20 V) after the application of repeated human finger tapping. This result indicates that high aspect ratio ceramic filler provides an effective approach to enhance the dielectric, ferroelectric, energy storage, and energy harvesting performances of ceramic-polymer nanocomposites.

KEYWORDS

aspect ratio, energy harvesting, energy storage, ferroelectric, nanocomposites

1 | INTRODUCTION

Poly(vinylidene fluoride) (PVDF) and PVDF based flexible nanocomposites are widely studied due to their excellent piezoelectric, ferroelectric, pyroelectric properties, attractive mechanical properties, thermal stability, lightweight, and easy fabrication techniques.[1–8] Therefore, such system has been considered as promising materials for various technological applications such as high performance energy storage and energy harvesting devices, high k-capacitors and gate dielectrics.[9–14] PVDF, a semicrystalline material exists in five different forms, such as α, β, γ, δ, and ε depending on their macromolecular chain conformation of trans (T) and gauche (G) linkages. Among them, α phase (TG^+TG^-) is though thermodynamically most stable phase, but it is an electrically inactive nonpolar phase whereas β and γ phase are electroactive polar phase due to their TTTT and $T_3G^+T_3G^-$chain conformation.[4,5] Therefore, β and γ phases are more suitable for increasing piezoelectric performance. But obtaining electroactive β and γ phases are difficult since PVDF normally exhibits nonpolar α phase, which is kinetically very stable. So it is a great challenge to induce this electroactive phase in PVDF. Therefore, for improving electroactive phases in PVDF, several techniques have been attempted, such as mechanical stretching,[15] electrospinning,[16] applied high pressure,[17] electrical poling,[18] solvent casting,[19] incorporation of nanofiller [20,21] into PVDF matrix, and so on. Among them, the incorporation of ceramic filler in

PVDF matrix is a cost effective approach to enhance electroactive phase. Researchers have established great efforts to induce electroactive phase using different types of piezoelectric materials, such as lead zirconium titanate (PZT), barium titanate ($BaTiO_3$), gallium nitride (GaN), and zinc oxide (ZnO).[22–25] However, among the different polymer-ceramic based composites, ZnO based composite is widely studied due to its superior biocompatibility, piezoelectricity, flexibility, and easy synthesis method.[26–30]

According to previous reports,[31–33] morphology and nanostructures of ZnO filler play an important role in determining the piezoelectric performance of composites. Therefore, it is needed to study the effect of growth condition on the morphology of fabricated nanorods and the corresponding output piezoelectric performances of ZnO. Few reports are available on the piezoelectric performance of controlled growth ZnO nanorods by optimizing morphology and aspect ratio.[31–33] Qiu et al reported that morphology and aspect ratio of ZnO nanorods play a crucial role in determining piezoelectric output performance.[31] Wang et al demonstrated that the piezoelectric output performance can be enhanced by appropriate tuning of aspect ratio.[32] Li et al showed that ZnO nanorods with higher aspect ratio significantly increase the piezoelectric properties of the PVDF/ZnO nanocomposites.[33] Keeping this in view, we planned to investigate the effect of adding ZnO rods with varied aspect ratio in PVDF matrix on the piezoelectric performance of the fabricated composites.

In our study, an attempt was carried out to investigate the effect of ZnO aspect ratio on the electrical performances of PVDF. Here, we have synthesized different aspect ratio ZnO nanorods (7.2, 10.4, and 26.8) by varying hydrothermal reaction time from 4 to 8 to 20 hours, respectively. To investigate the effect of different aspect ratio ZnO filler in PVDF matrix, dielectric, ferroelectric, energy storage, and energy harvesting performances were investigated. The energy storage density was calculated from the P-E loop. The high aspect ratio ceramic filler ZnO in PVDF matrix enhanced the polar-phase formation. Dielectric permittivity of the nanocomposites increased with increasing aspect ratio. This work therefore provides an effective approach to enhance dielectric, ferroelectric, and energy harvesting performances by embedding high aspect ratio ZnO nanorods in PVDF matrix.

2 | EXPERIMENTAL SECTION

2.1 | Raw materials

The analytical-grade zinc nitrate hexahydrate ($Zn(NO_3)_2{\cdot}6H_2O$) (Sigma Aldrich), sodium hydroxide pellets (NaOH) (Merck), ethanol (C_2H_5OH) (Merck), ethylenediamine ($C_2H_4(NH_2)_2$, EDA) (Merck), and distilled water were used as precursor materials to synthesize different aspect ratio ZnO nanorods. PVDF pellets (molecular weight ≈ 275 000 by GPC Sigma-Aldrich) and N,N-dimethylacetamide (DMAc) ($CH_3CON(CH_3)_2$) (Merck) were used to fabricate PVDF/ZnO composite films.

2.2 | Synthesis of different aspect ratio ZnO nanorods

ZnO nanorods were synthesized by hydrothermal technique.[34] In this reaction, zinc nitrate hexahydrate and sodium hydroxide pellets were first dissolved in distilled water separately at a molar ratio (Zn^{2+}:OH^- = 1:20). Then a stock solution was prepared by mixing two solutions. Then 3 mL of the stock solution, 5 mL distilled water, and 25 mL ethanol were mixed and kept under continuous stirring for 1 hour. EDA was then added to the above solution and stirred for 1 hour. The well-mixed solution was sonicated under an ultrasonic water bath for 1 hour. Finally, the mixed solution was transferred to a teflon-line autoclave. To obtain different aspect ratio ZnO nanorods, the hydrothermal reaction time was varied from 4 to 20 hours at a fixed temperature 180°C. After the reaction, white precipitate was collected and washed several times with water and ethanol and then dried in an oven at 70°C. As-synthesized ZnO nanorods are designated as ZnO-4 (for reaction time 4 hours), ZnO-8 (for reaction time 8 hours), and ZnO-20 (for reaction time 20 hours), respectively.

2.3 | Fabrication of PVDF/ZnO nanocomposite films

For fabrication of PVDF/ZnO based composite films, we used simple drop casting technique. At first, 8 wt% PVDF was dissolved in N,N-DMAc ($CH_3CON(CH_3)_2$). Then, to obtain different series (PVDF/ZnO-4, PVDF/ZnO-8, and PVDF/ZnO-20) composite films 5, 10, 15 wt% powder of each sample with respect to PVDF were then added to the DMAc-PVDF solution. A pure PVDF film was also fabricated. The ZnO/PVDF solutions were stirred by magnetic stirrer for 72 hours. The solutions were casted on glass plates and annealed at 90°C for 5 hours. The resulting composite films were then peeled out from the glass substrate. For electrical characterization, two composite films were hot pressed by applying 20 000 lbs pressure for 20 minutes at 150°C. The electroding of the composites was done by applying high quality silver paste on both sides of the hot pressed films.

2.4 | Characterization

X-ray diffraction (XRD) measurements were carried out to understand the phase of ZnO nanorods and PVDF/ZnO composite films using X'pert Pro MPD diffractometer (PAN analytical) with nickel filtered CuK$_\alpha$ radiation (λ = 0.15404 nm). For further determination of phase characteristics vibrational modes of the nanocomposites Fourier transform infrared spectroscopy (FTIR) study (FTIR-Spectrum 2, Perkin Elmer) was also performed. In order to investigate the microstructure and morphology analysis of ZnO rods and composite systems, field emission scanning electron microscope (FESEM) (SEM Supra 35 VP) was utilized. Transmission electron microscopy (TEM) and high resolution TEM (HRTEM) images of ZnO nanorods were also carried out using Tecnai G2, 30ST, (FEI) instrument operating at 300 kV. To obtain the surface charge of synthesized ZnO nanorods zeta potential was measured using HORIBA nanoparticle analyzer (SZ-100). X-ray photoluminescence spectroscopy (XPS) (using a PHI 5000 versa probe II scanning XPS microprobe manufactured by ULVAC-PHI) was used to better understand the interaction between ZnO nanorods and PVDF composites. The room temperature dielectric study of PVDF and PVDF/ZnO nanocomposites was performed with a precision impedance analyzer (6500 B Wayne Kerr). Ferroelectric study and leakage current density measurement were carried out using RADIANT ferroelectric test system (Radiant Technologies) using Vision software (version 3.1.0). All the ferroelectric hysteresis loops were measured at room temperature. The piezoelectric properties of PVDF and PVDF/ZnO composite films were measured by a digital Oscilloscope (YOKOGAWA, DL 1640) by applying different pressure and different applied frequencies. PFM measurement was performed in an Asylum Research AFM (MFP-3D BIO) by applying voltage to investigate the local ferroelectric and piezoresponse properties existing within composite film.

3 | RESULT AND DISCUSSIONS

3.1 | Characterization of ZnO nanorods

XRD study was performed to investigate the phase of synthesized ZnO nanorods grown at different reaction times (4, 8, and 20 hours). XRD patterns of as-synthesized samples are shown in Figure 1. All the diffraction peaks matched well with standard powder diffraction data of ZnO (JCPDS card number #790205). There is no additional peak present in the XRD patterns, which indicates that pure hexagonal structure phase of ZnO is formed. Average crystallite sizes (L) of the sample were calculated using Debye-Scherrer equation.[35] Average crystallize size of samples were 41, 43, and 47 nm for reaction time, respectively, which indicates that crystallite size increases with increasing reaction time.

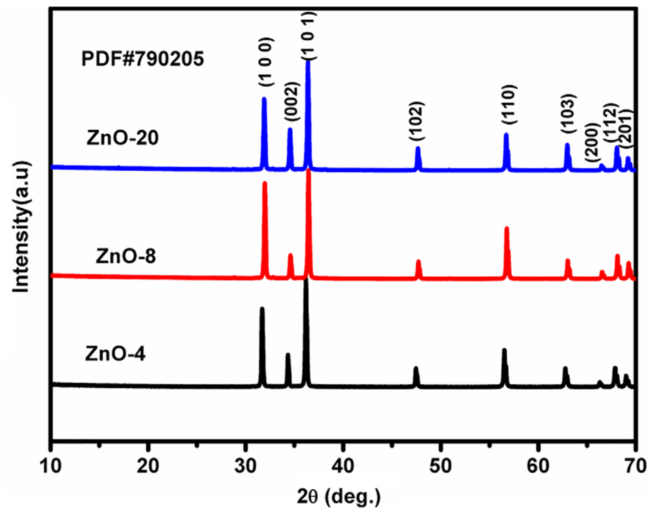

FIGURE 1 XRD patterns of ZnO-4,ZnO-8, and ZnO-20 nanorods. XRD, X-ray diffraction [Color figure can be viewed at wileyonlinelibrary.com]

Qiu et al demonstrates that growth time is an important parameter, which determines both morphology and aspect ratio of ZnO nanorods.[31]Figure 2A-C represents the FESEM images of the synthesized ZnO nanorods. From FESEM images, we observed that the length of synthesized ZnO nanorods increased with increasing hydrothermal reaction time. To calculate average length and diameter of synthesized nanorods we used ImageJ software. The length and diameter distribution of ZnO-4,ZnO-8, and ZnO-20 samples are shown in Figure 3A-F. It is found that the calculated average diameter and length of ZnO-4,ZnO-8, and ZnO-20 nanorods are 275, 220, 175 nm and 2, 2.3, 4.7 μm, respectively. The calculated aspect ratios of ZnO-4,ZnO-8, and ZnO-20 nanorods are found to be 7.2, 10.4, and 26.8, respectively, which indicated a direct correlation between the reaction time and aspect ratio of formed rods. Well-aligned uniform microstructure was observed for high aspect ratio ZnO-20 nanorods.[31]Figure 4A represents bright field TEM image of ZnO-20 nanorods, which further indicated the uniform microstructure of synthesized rods. The selected area electron diffraction (SAED) pattern of ZnO-20 samples is shown in Figure 4B. The planes indexed in SAED pattern matched well with XRD database and confirmed the crystallinity of nanorods. HRTEM study of ZnO-20 (shown in Figure 4C) further confirmed the good crystallinity of the nanorods.

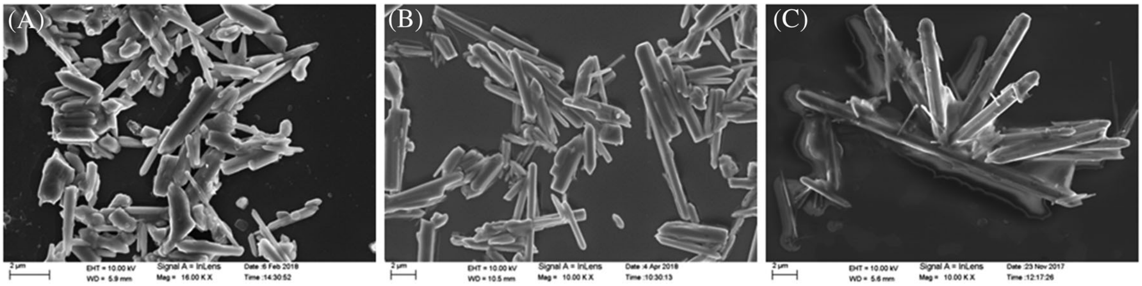

FIGURE 2 FESEM images of A, ZnO-4 nanorods; B, ZnO-8 nanorods; and C, ZnO-20 nanorods. FESEM, Field emission scanning electron microscope; ZnO, zinc oxide

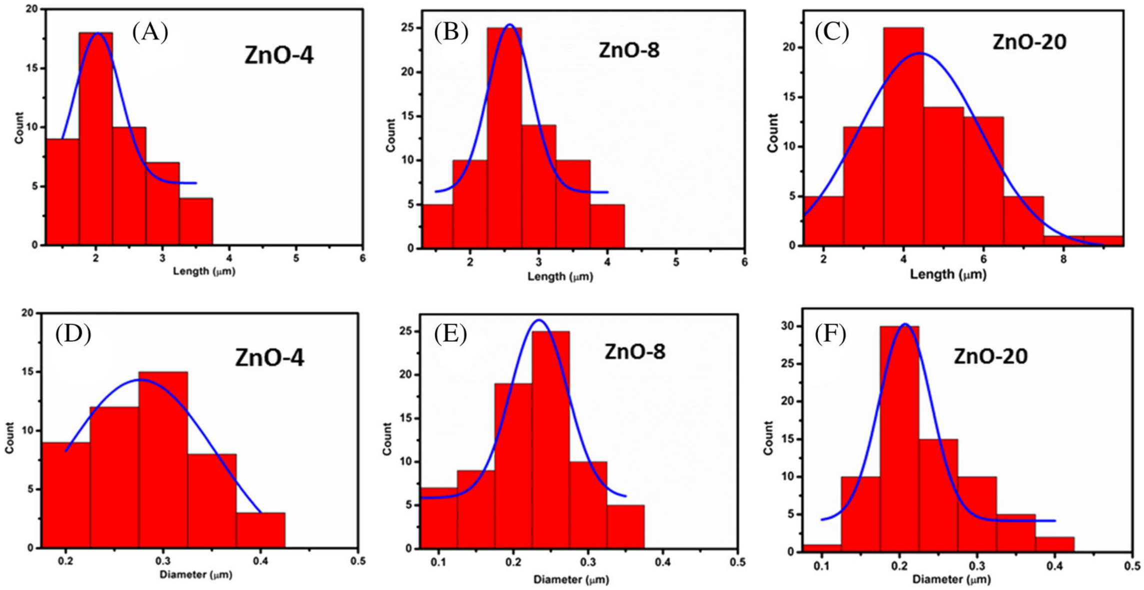

FIGURE 3 ZnO nanorods size distribution: length distribution of A, ZnO-4 nanorods; B, ZnO-8 nanorods; and C, ZnO-20 nanorods. Diameter distribution of D, ZnO-4 nanorods; E, ZnO-8 nanorods; and F, ZnO-20 nanorods. ZnO, zinc oxide [Color figure can be viewed at wileyonlinelibrary.com]

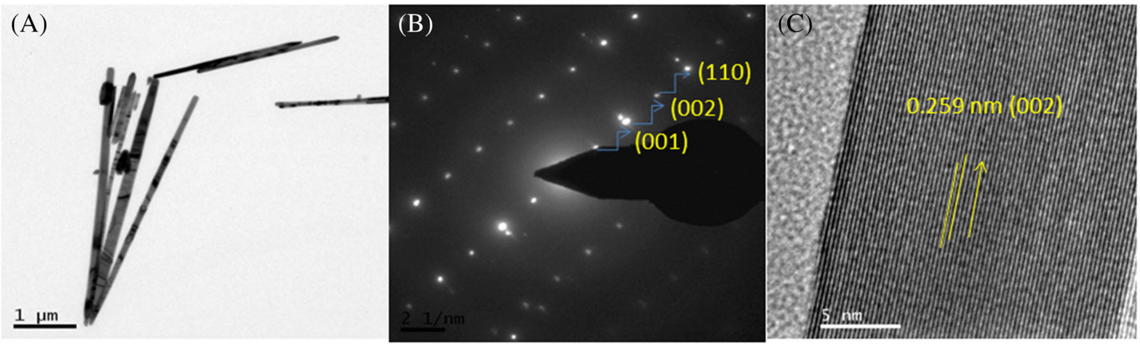

FIGURE 4 TEM images of A, ZnO-20 nanorods; B, SAED pattern of ZnO-20 nanorods; and C, HRTEM images of ZnO-20 nanorods. HRTEM, high resolution transmission electron microscopy; SAED, selected area electron diffraction; TEM, transmission electron microscopy; ZnO, zinc oxide [Color figure can be viewed at wileyonlinelibrary.com]

3.2 | Characterization of composite films

The XRD study is carried out to investigate the polar-phase formation in the PVDF based composite system. Figure 5A represents the XRD pattern of pure PVDF, PVDF/ZnO-4, PVDF/ZnO-8, and PVDF/ZnO-20 composite films. In the pure PVDF XRD pattern peaks observed at 2θ = 17.7°, 18.4°, 19.6°, and 26.6° corresponding to

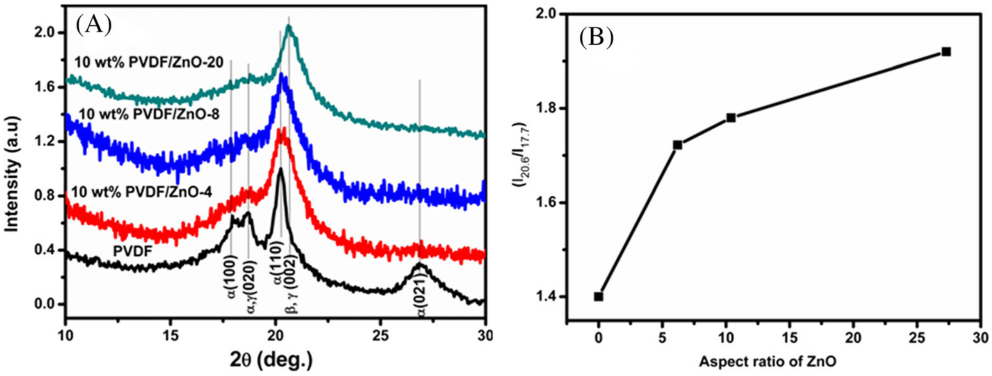

FIGURE 5 A, XRD patterns of pure PVDF, PVDF/ZnO-4, PVDF/ZnO-8, and PVDF/ZnO-20 composite films; B, ratio of $I_{20.6}$ and $I_{17.7}$ of the samples with aspect ratio of ZnO calculated from XRD pattern. PVDF, poly(vinylidene fluoride); XRD, X-ray diffraction; ZnO, zinc oxide [Color figure can be viewed at wileyonlinelibrary.com]

(100), (020), (110), and (021) planes, respectively, which is basically due to the nonpolar α phase.[36,37] But after the incorporation of ZnO nanorods in PVDF matrix the peaks at $2\theta = 17.9^\circ$ and 26.5° both disappear, which indicates that the crystalline ZnO nanorods have changed the PVDF crystallinity. It is found that the peak at $2\theta = 19.9^\circ$ shifted toward higher value angle in the PVDF/ZnO-20 composite system, which indicates that after addition of high aspect ratio ZnO nanorod in PVDF matrix, polar phase of PVDF is enhanced. The maximum polar phase is observed in PVDF/ZnO-20 composite system. The quantitative-phase fraction (α and β) present in the samples are calculated from the intensity ratio of the peaks at 20.6° and 17.7° ($I_{20.6}/I_{17.7}$) and the obtained values are plotted with respect to aspect ratio of ZnO (represented in Figure 5B). The value of $I_{20.6}/I_{17.7}$ is enhanced with increasing aspect ratio of ZnO nanorods and reaches maximum value for PVDF/ZnO-20 composite system. This result indicated that highest polar-phase nucleation occurred in PVDF/ZnO-20 composite system.

The effective nucleation of polar phase in ZnO incorporated composites film is further confirmed from FTIR spectroscopy. Figure 6A represents the FTIR spectra (in the region 400-1500 cm^{-1}) of pure PVDF, PVDF/ZnO-4, PVDF/ZnO-8, and PVDF/ZnO-20 composites system. The IR spectra of pure PVDF exhibits peak at 409, 488 (CF_2 wagging), 532 (CF_2 bonds bending), 614 and 764 (CF_2 bending and skeletal bending), 796, 856, and 976 cm^{-1}(CH_2 rocking) which is due to the nonpolar α phase.[37] Some α characteristics peaks are suppressed after addition of ZnO nanorods in PVDF matrix. Small characteristics peaks are observed at 431 (polar γ phase), 510 (CF_2 stretching corresponding to polar β phase), and 840 (CH_2 rocking, CF_2 stretching, and skeletal C—C stretching), 1233 (ϒ phase), and 1273 cm^{-1} (polar β phase) in the composite films, which represents the polar-phase formation. The amount of electroactive polar phase ($F(\beta)$) present is calculated from Beer-Lambert law equation

$$F(\beta) = \frac{A_\beta}{\left(\frac{K}{K_\alpha}\right)A_\alpha + A_\beta}. \tag{1}$$

Here, $F(\beta)$ is the electroactive-phase fraction, A_α and A_β are the absorbance intensities at 764 and 840 cm^{-1}, $K_\beta = 7.7 \times 10^4\ \text{cm}^2\ \text{mol}^{-1}$ (the absorption coefficient at 840 cm^{-1}) and $K_\alpha = 6.1 \times 10^4\ \text{cm}^2\ \text{mol}^{-1}$ (the absorption coefficient at 764 cm^{-1}).[37] The calculated percentage of electroactive-phase fraction are 63.1%, 73.7%, 80.7%, and 88% for pure PVDF, PVDF/ZnO-4, PVDF/ZnO-8, and PVDF/ZnO-20 composite films, respectively. The amount of phase fraction with respect to aspect ratio of ZnO is represented in Figure 6B. Maximum 88% polar phase was obtained in PVDF/ZnO-20 composite system which was also supported by the XRD study. In order to investigate the individual β and ϒ phases in PVDF composites, the peak of 840 cm^{-1} of FTIR curves were deconvoluted.[38] The deconvoluted figure is shown in Figure 6C-F, where the broadening peak was considered for the ϒ peak and the sharp peak was considered for the β peak. The following equations were used to quantify the β and ϒ phases individually.

$$F(\beta) = F_{\text{EA}} \times \frac{A_\beta}{A_\beta + A_\Upsilon} \times 100\%, \tag{2}$$

$$F(\Upsilon) = F_{\text{EA}} \times \frac{A_\Upsilon}{A_\beta + A_\Upsilon} \times 100\%, \tag{3}$$

peak of the deconvoluted curve, respectively. The individual quantification of $F(\beta)$ and $F(\Upsilon)$ from FTIR study for each sample was calculated and shown in Table 1.

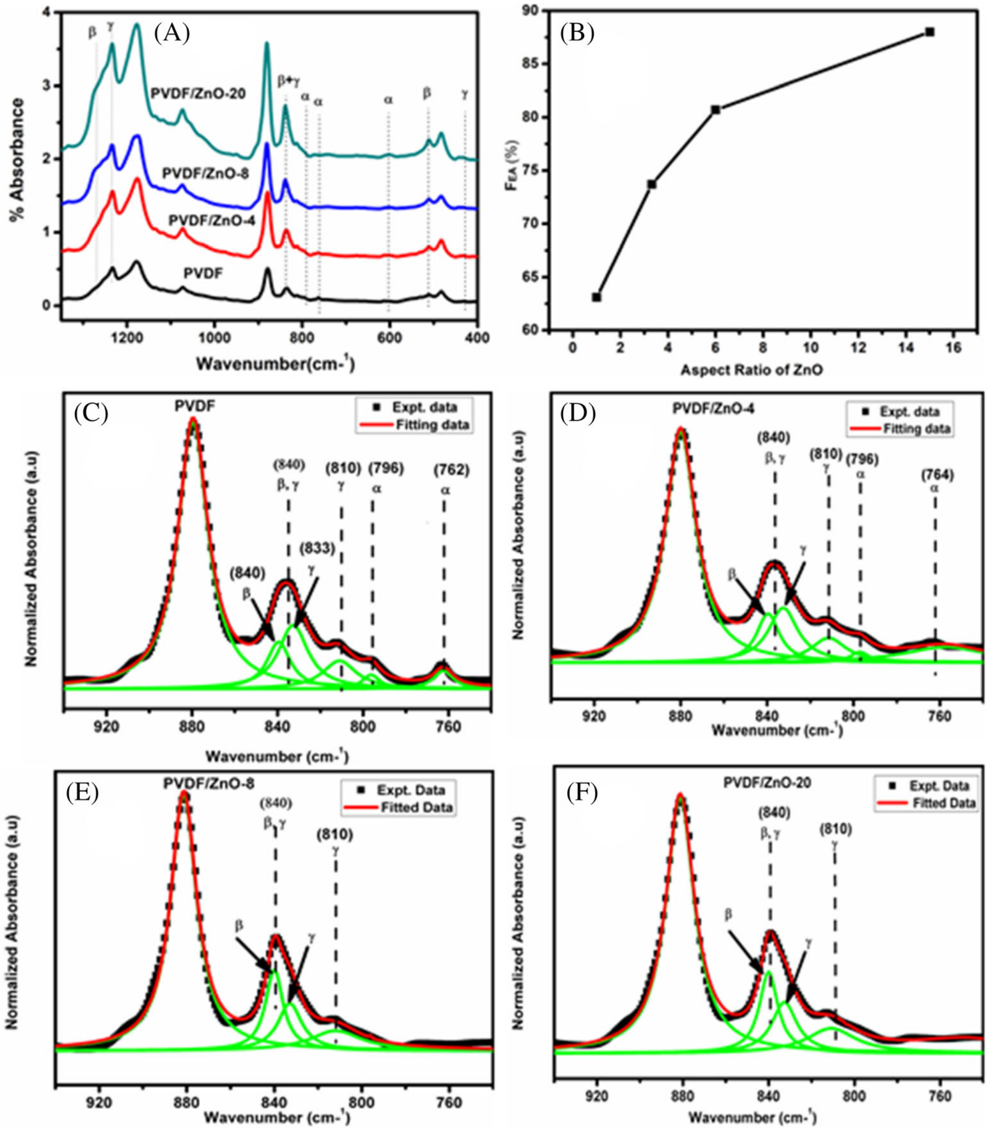

FIGURE 6 A, FTIR spectra of pure PVDF, PVDF/ZnO-4, PVDF/ZnO-8, and PVDF/ZnO-20 composite films; B, variation of polar phase with aspect ratio of ZnO evaluated from IR spectra. The deconvolution curve of FTIR spectra in the region 940 to 740 cm^{-1}: C, pure PVDF film; D, PVDF/ZnO-4; E, PVDF/ZnO-8; F, PVDF/ZnO-20 nanocomposites film. FTIR, Fourier transform infrared spectroscopy; PVDF, poly(vinylidene fluoride); ZnO, zinc oxide [Color figure can be viewed at wileyonlinelibrary.com]

TABLE 1 Detailed comparison of polar phase of PVDF and PVDF composites

Sample name	Polar-phase fraction (F_{EA} %)	B-phase fraction (F_{β} %)	Υ-phase fraction (F_{Υ} %)	Relative amount of β phase wrt to Υ phase ($F_{\beta\Upsilon}$)	Relative amount of Υ phase wrt to β phase ($F_{\Upsilon\beta}$)
PVDF	63.1	27.9	35.18	44.2%	55.71%
PVDF/ZnO-4	73.7	34.5	39.1	46.87%	53.12%
PVDF/ZnO-8	80.7	41.66	39.03	51.61%	48.38%
PVDF/ZnO-20	88	46.59	41.4	52.9%	47.09%

Abbreviations: PVDF, poly(vinylidene fluoride); ZnO, zinc oxide.

Relative amount of β phase (wrt Υ phase) ($F_{\beta\Upsilon}$) and Υ phase (wrt to β phase) were also calculated using following equation:

$$F_{\beta\Upsilon} = \frac{F(\beta)}{F(\beta)+F(\Upsilon)} \times 100\%, \tag{4}$$

$$F_{\Upsilon\beta} = \frac{F(\Upsilon)}{F(\beta)+F(\Upsilon)} \times 100\%. \tag{5}$$

The accurate percentage of β and Υ phase was calculated from FTIR data given in Table 1.

Figure 6D-F clearly indicated that the deconvoluted β peak is more prominent for high aspect ratio ZnO nanorod where the Υ peak gets gradually weakened with increase aspect ratio of ZnO nanorods. From Table 1, it was observed that the relative amount of β phase (with respect to Υ phase) increased gradually with aspect ratio of ZnO nanorods and relative amount of Υ phase (with respect to β) decreases with increase aspect ratio of ZnO nanorods. High aspect ratio PVDF/ZnO-20 nanocomposite exhibited maximum β phase. Thus, the polar-phase fraction is enhanced after high aspect ratio ZnO-20 filler loading in PVDF matrix. This is caused mainly due to the interaction of the interfaces between PVDF matrix and ZnO filler. Above result confirmed that the introduction of high aspect ratio ceramic filler enhanced the formation of polar phase, which indicates that the high aspect ratio ceramic filler may be more effective for increasing electrical properties.[39] ZnO filler has negative surface charge on its surface, which is confirmed from zeta potential study (shown in Supporting Information Figure S1). After inclusion of ZnO filler in PVDF matrix, an interaction occur between positive —CH_2 dipole of PVDF and negative surface charge of ZnO fillers, which leads to TTTT and ($T3G^+T3G^-$) configuration in PVDF. It is also observed that the zeta potential value is increased with increasing aspect ratio of ceramic filler, which suggests that the negative surface charge increases on ZnO-20 filler surface. As a result, more polar electroactive (β and γ) phases are obtained in PVDF/ZnO-20 composite system than the other composite. According to Luo et al, the effective nucleation of polar phase in ferroelectric polymers like PVDF is very helpful to enhance the permittivity and piezoelectric/ferroelectric properties of the composite due to large dipole moment of this phase.[39] Incorporation of ceramic filler into PVDF matrix led to the transformation of nonpolar phase to polar phase of PVDF.[40–43]

The interfacial interaction between ceramic filler ZnO and PVDF matrix was further confirmed by XPS study. The C1s core level XPS spectrum of neat PVDF and PVDF/ZnO composite is shown in Figure 7A. The C1s spectrum of neat PVDF exhibited peaks at 286.5 and 291.4 eV, which indicated the presence of —CH_2 dipole and —CF_2 dipole of PVDF, respectively (shown in Figure 7C). The intensity of the peaks were decreased and shifted toward higher binding energy in the composite system, which may be due to interfacial interaction between PVDF and ZnO nanorods. The peak area of —CH_2 (A_{CH2}) dipole is reduced by 43% for composite system with respect to neat PVDF, which clearly indicates the presence of interfacial interaction between PVDF matrix and ZnO.[36] The F1s spectrum of neat PVDF and PVDF/ZnO composite system is shown in Figure 7B. F1s spectrum shows that the line broadening of peak is asymmetrical and the peak shifted toward lower binding energy which further indicates the existence of interfacial interaction.[44,45] Thus, the XPS study supported the FTIR result.

The SEM micrographs of PVDF/ZnO-4, PVDF/ZnO-8, and PVDF/ZnO-20 nanocomposite films are shown in Figure 8A-C. FESEM images indicated the good dispersion of ZnO nanorods in PVDF matrix. It was observed that high aspect ratio ZnO-20 nanorods exhibited better homogeneous dispersibility in PVDF matrix, which may be due to the strong interaction between —CH_2 dipole of PVDF and more negative surface charge of ZnO-20 filler. Finally, nanocomposites with higher aspect ratio nanorods showed excellent dispersion and compatibility in PVDF matrix.

The frequency dependent dielectric permittivity, dielectric loss and electrical conductivity of the PVDF/ZnO-4, PVDF/ZnO-8, and PVDF/ZnO-20 composite system with different wt% ZnO nanofiller loading are shown in Figure 9A-F. The variation of dielectric permittivity and dielectric loss as a function of ZnO filler loading of PVDF/ZnO-4, PVDF/ZnO-8, and PVDF/ZnO-20 composite systems are represented in Figure 9A-C. It is found that, the dielectric permittivity of the PVDF/ZnO composites increased with ZnO filler loading for both high

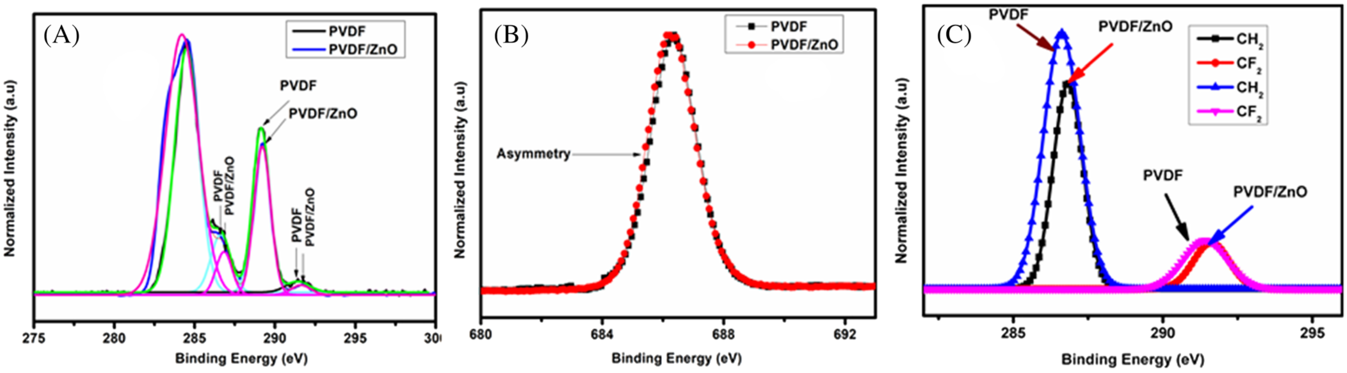

FIGURE 7 Core level XPS spectrum of A, C1s, B, F1s of pure PVDF and 15 wt% PVDF/ZnO-20 nanocomposite system. C, Comparison of —CH2 peak and —CF2 peak of C1s spectra of pure PVDF and 15 wt% PVDF/ZnO-20 composite system. PVDF, poly(vinylidene fluoride); XPS, X-ray photoluminescence spectroscopy; ZnO, zinc oxide [Color figure can be viewed at wileyonlinelibrary.com]

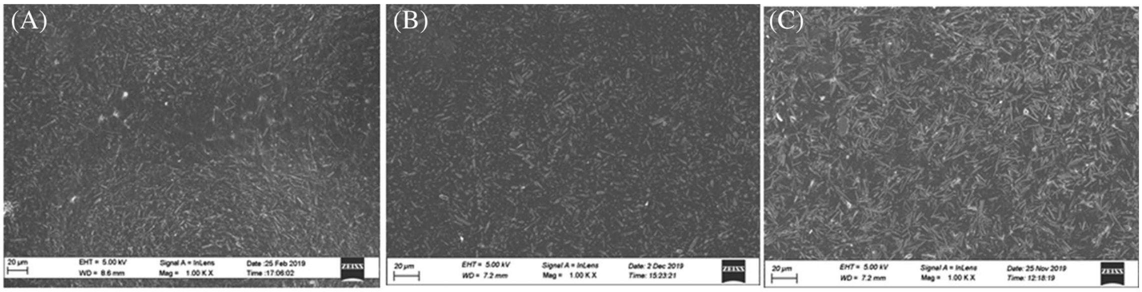

FIGURE 8 SEM micrograph of A, PVDF/ZnO-4; B, PVDF/ZnO-8; and C, PVDF/ZnO-20 nanocomposites. PVDF, poly(vinylidene fluoride); SEM, scanning electron microscope; XPS, X-ray photoluminescence spectroscopy; ZnO, zinc oxide

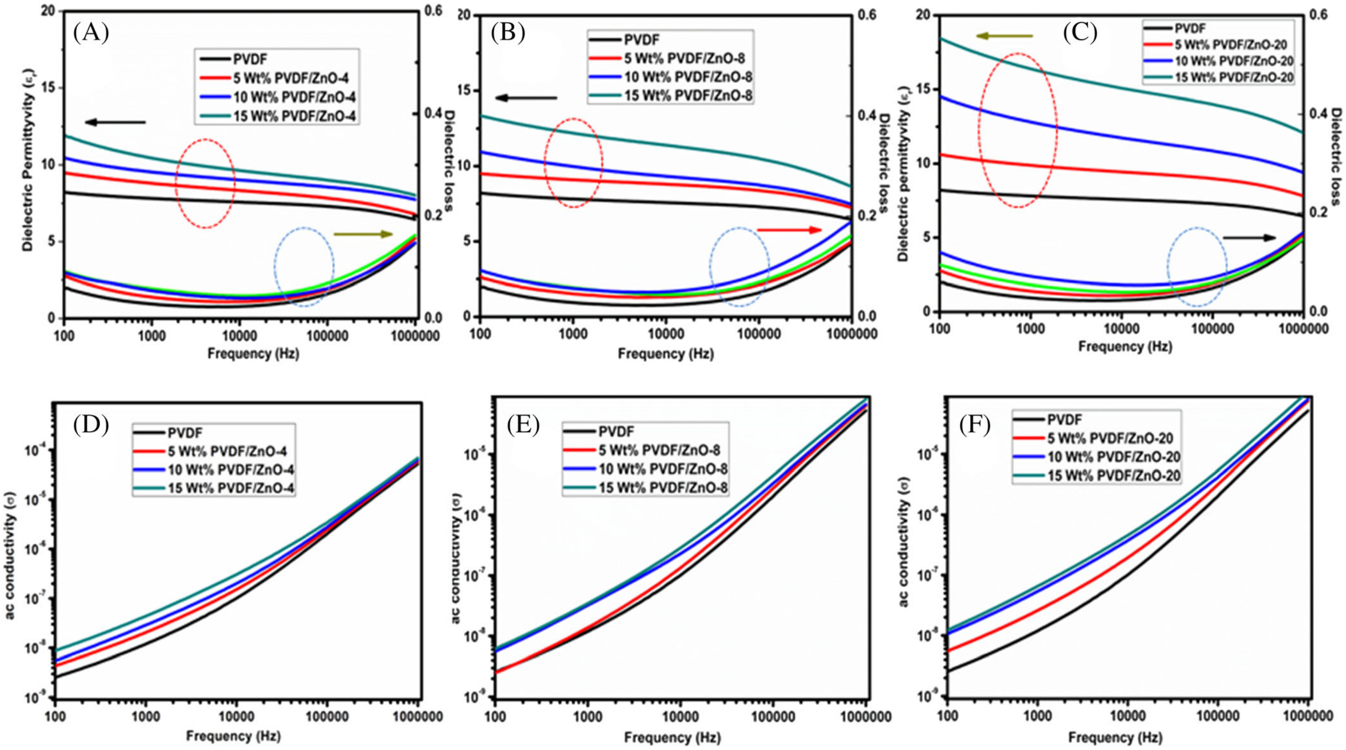

FIGURE 9 Frequency dependent dielectric permittivity and dielectric loss of A, PVDFZnO-4; B, PVDF/ZnO-8; and C, PVDF/ZnO-20 nanocomposites. AC conductivity of D, PVDF/ZnO-4; E, PVDF/ZnO-8; and F, PVDF/ZnO-20 nanocomposites. PVDF, poly(vinylidene fluoride); ZnO, zinc oxide [Color figure can be viewed at wileyonlinelibrary.com]

and low aspect ratio ZnO nanorods. It is also observed that the dielectric permittivity of the nanocomposites improved significantly compared to PVDF after incorporation of ZnO nanorods, which is due to the interaction between —CH_2 dipoles of PVDF and negative surface charge of filler. Besides, Maxwell-Wagner-Sillars (MWS) interfacial polarization exists in the interfaces between PVDF and ZnO nanorods. The enhancement in polar phase leads to an increased dielectric value. The dielectric permittivity of 15 wt% PVDF/ZnO-20 nanocomposite exhibited ∼19 whereas the dielectric constant of 15 wt% PVDF/ZnO-4 nanorods value is ∼12. This indicated that dielectric constant can be improved with increasing aspect ratio of ZnO nanorods.

This dielectric study clearly indicates that the aspect ratio plays an important role for enhancement of dielectric constant of the nanocomposites. Tang et al already demonstrated that there is a relationship between aspect ratio of fillers and dielectric constant of the composites.[3]Many previous reports and theoretical models such as Maxwell garnet model have shown that the dielectric properties of the nanocomposites can be enhanced significantly with increasing filler aspect ratio.[3,46] Moreover, high aspect ratio ceramic filler has many advantages compared to low aspect ratio filler. A high aspect ratio filler reaches the percolation threshold easily, which leads to the formation of a continuous pathway in the system resulting in an improvement of dielectric constant of the composite system that was explained.[3] Besides, the high aspect ratio ceramic filler possesses large dipole moment, which may be very effective to improve dielectric constant of the nanocomposites and high aspect ratio ceramic filler have low surface energy which is favorable for good dispersion, which can enhance the dielectric constant of the nanocomposites.[39] Additionally, high aspect ratio ceramic filler promotes the formation of polar phase, which play a very important role on the increment of dielectric constant of the nanocomposites.[39] PVDF/ZnO-20 nanorods exhibited maximum permittivity value due to the above said reason.

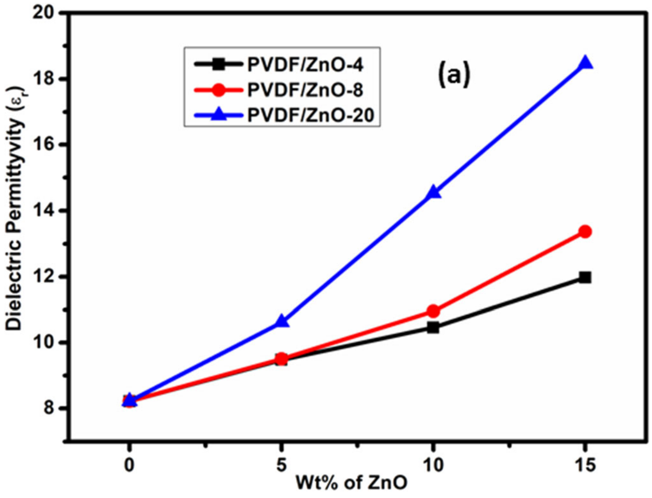

FIGURE 10 Comparison of dielectric permittivity of nanocomposites as a function of different wt% of ZnO (measured at same frequency). ZnO, zinc oxide [Color figure can be viewed at wileyonlinelibrary.com]

The variation of dielectric loss tangent value of the samples PVDF/ZnO-4, PVDF/ZnO-8, and PVDF/ZnO-20 with ZnO filler loading are shown also in Figure 9A-C. It is observed that the dielectric loss increased with increasing ZnO filler concentration. Both dielectric constant and dielectric loss of PVDF nanocomposites increases with ZnO filler concentration due to the interfacial space charge polarization. Higher amount of filler loading creates more interfacial area, which increases conductive network between PVDF and ZnO filler. High aspect ratio ZnO nanorods showed higher dielectric loss than low aspect ratio ZnO rods. As high aspect ratio ZnO nanorods exhibit better dispersion in PVDF matrix, interfacial area between filler and PVDF matrix also increased and as a result polymer chains were separated into smaller domains.[20,36] Thus, more PVDF dipoles get rotated, which enhanced the dielectric loss.

This is further confirmed from AC conductivity plot of the composites where AC conductivity increased with increasing ZnO filler loading for all composite system (Figure 9D-F). AC conductivity of dielectric material can be expressed as

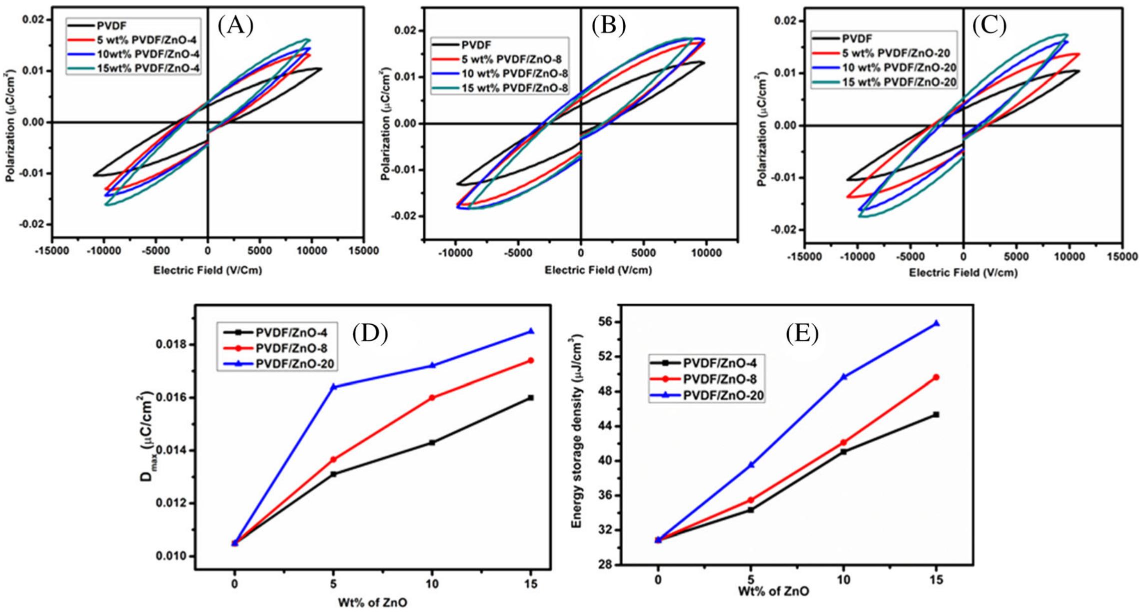

FIGURE 11 Electric displacement vs applied electric field (*D-E*) loop of A, PVDF/ZnO-4; B, PVDF/ZnO-8; C, PVDF/ZnO-20 composites; D, comparison of $D_{\max}$ of the nanocomposites with different wt% of ZnO; E, variation of energy storage density of nanocomposites with different wt% of ZnO. PVDF, poly(vinylidene fluoride); ZnO, zinc oxide [Color figure can be viewed at wileyonlinelibrary.com]

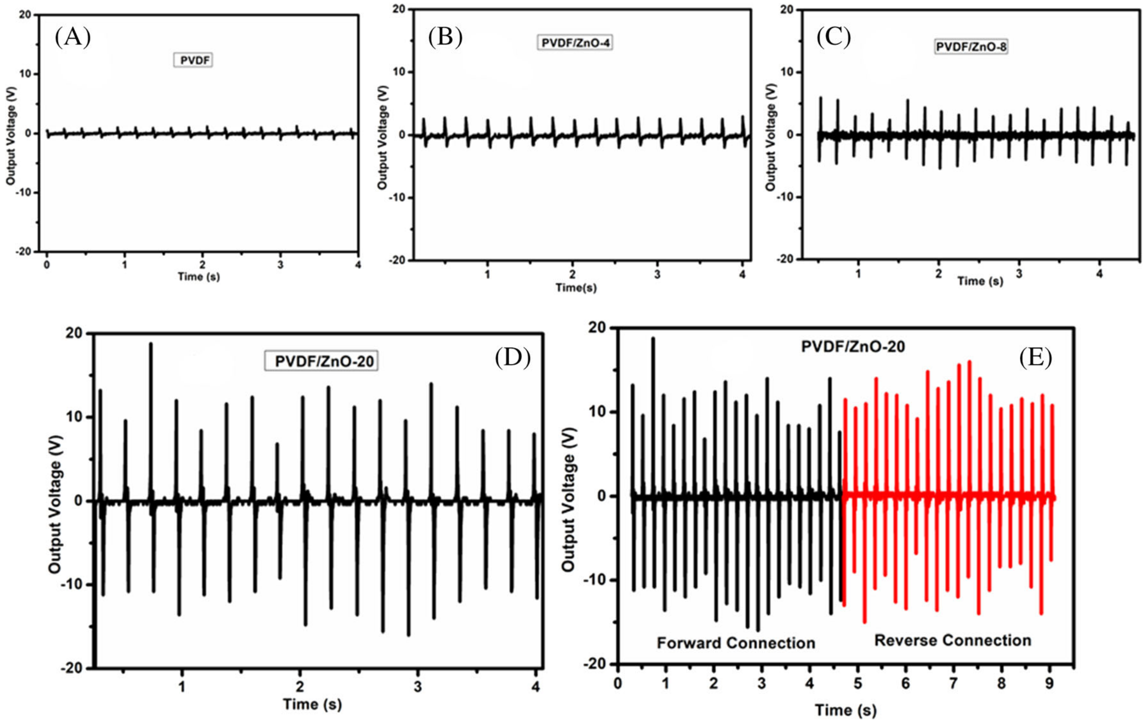

FIGURE 12 Comparison of open circuit output AC voltage of A, PVDF; B, PVDF/ZnO-4; C, PVDF/ZnO-8; D, PVDF/ZnO-20 nanocomposites; and E, switching polarity test of PVDF/ZnO-20 sample. PVDF, poly(vinylidene fluoride); ZnO, zinc oxide [Color figure can be viewed at wileyonlinelibrary.com]

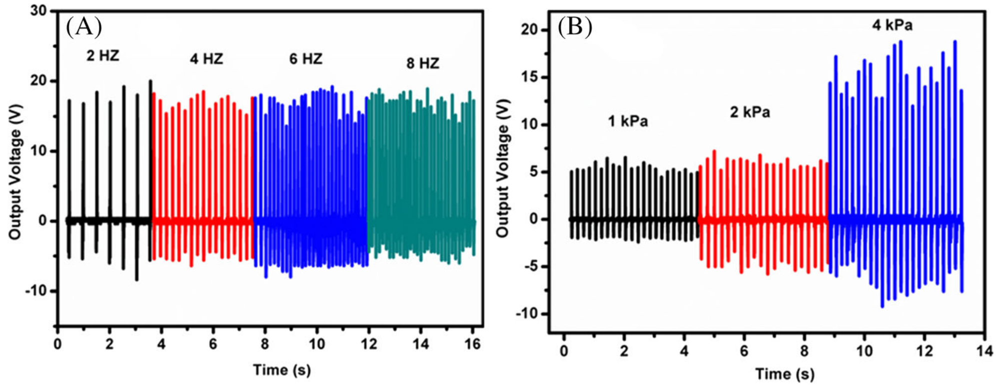

FIGURE 13 A, Comparison of output AC voltage of PVDF/ZnO-20 sample at different frequencies. B, Comparison of output AC voltage of PVDF/ZnO-20 sample at different pressure. PVDF, poly(vinylidene fluoride) [Color figure can be viewed at wileyonlinelibrary.com]

$$\sigma = 2\pi f \cdot \varepsilon_0 \cdot \varepsilon_r''. \tag{6}$$

This result shows that AC conductivity of the composite films is greater than PVDF polymer which is due to the more conducting network causing more leakage current (shown in Supporting Information Figure S2) in the composite system.

Figure 10 represents the variation of dielectric permittivity of PVDF/ZnO-4, PVDF/ZnO-8, and PVDF/ZnO-20 samples with different filler loading (at same frequency). The permittivity value increased with ZnO filler loading for all the samples. It also showed that PVDF/ZnO-20 composite films exhibited higher dielectric permittivity than other composite films for same ZnO filler loading.

Figure 11A-C represents the typical electrical displacement-electric field (*D-E*) loops of the PVDF/ZnO-4, PVDF/ZnO-8, and PVDF/ZnO-20 composite films with different percentage of ZnO filler loading. It was observed from Figure 11A, maximum electric displacement (D_m) and remnant electric displacement (D_r) increased after ZnO addition in PVDF matrix. Figure 10B,C also followed similar trend. It was also observed that D_m can be improved with increasing aspect ratio of ZnO nanorods. 15 wt% PVDF/ZnO-20

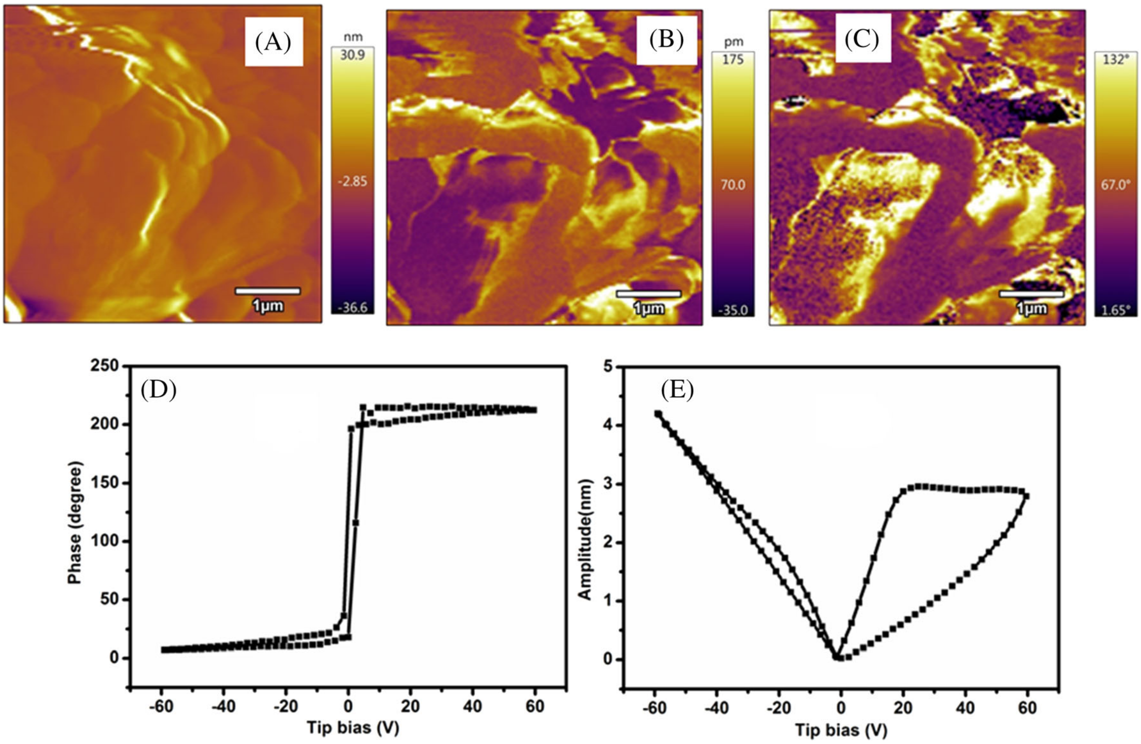

FIGURE 14 A-C, Topography image, PFM amplitude, and phase images of PVDF/ZnO-20 sample; D, PFM amplitude-voltage loop of PVDF/ZnO-20 sample; and E, PFM phase-voltage hysteresis loop for PVDF/ZnO-20 sample. PFM, piezoresponse force microscopy; PVDF, poly(vinylidene fluoride); ZnO, zinc oxide [Color figure can be viewed at wileyonlinelibrary.com]

nanocomposite exhibited maximum polarization value under an same applied electric field 100 V/cm. This result suggested that ferroelectric properties of the composites increased with increasing aspect ratio and filler loading. This may be due to the interaction of ceramic ZnO filler and PVDF matrix. Electric displacement equation can be expressed as $D = \varepsilon_0 \varepsilon_r E$, where ε_0 and ε_r are free space permittivity and relative permittivity of the nanocomposites, respectively.[46] Therefore, $D_{\max}$ of composite system will increase with increasing dielectric value of the composite. The variation of $D_{\max}$ of the nanocomposites with increasing filler loading or aspect ratio of ZnO under the same electric field (E) is shown in Figure 11D. Therefore, it is assumed that ferroelectricity is increased due to the above mentioned factors.

The dielectric and ferroelectric property of the composite film increased with addition of ZnO filler or increasing aspect ratio, and hence it can be assumed that energy storage density will also increase. The value of energy storage capability of the fabricated composites were evaluated from D-E loops using an integral formula given in equation

$$U_{\text{stored}} = \int E dD, \tag{7}$$

where E is the applied electric field and D is the electric displacement.[46] Figure 10E represents the stored electrical energy density of PVDF/ZnO-4, PVDF/ZnO-8, and PVDF/ZnO-20 composite systems as a function of filler loading of the nanocomposites. Energy density of the nanocomposites increases as the polarization increases with the concentration of ZnO filler. Aspect ratio also plays a crucial role in determining the storage energy density of the composites. It is observed that the PVDF/ZnO-20 nanocomposites exhibited a higher energy storage density than the other composites at same applied electric field. Energy storage density increased due to the enhancement of dielectric permittivity and electrical displacement (D_m) of the PVDF/ZnO nanocomposites with increasing both filler concentration and aspect ratio of ZnO nanorods. In addition, high aspect ratio ZnO filler in PVDF matrix creates larger leakage current, which enhances the conductive network in PVDF film.

ZnO is most extensively studied as ceramic filler in PVDF matrix because of its superior piezoelectric performance. Therefore, it is expected that PVDF/ZnO nanocomposite will exhibit good piezoelectric performance. So, the piezoelectric properties of PVDF, PVDF/ZnO-4, PVDF/ZnO-8, and PVDF/ZnO-20 nanocomposite systems were studied by applying repeated human finger tapping using a digital oscilloscope. Figure 12A-D represents the open-circuit AC output voltage of PVDF, PVDF/ZnO-4, PVDF/ZnO-8, and PVDF/ZnO-20 composite films. It is observed that there is an enhancement of open circuit output voltage with increasing aspect ratio of ZnO nanorods. The 15 wt% PVDF/ZnO-20 composite film showed maximum value compared to pure PVDF and same wt% other composite films. The maximum open circuit AC output voltage of this film was 20 V, which was originated due to its maximum polar-phase formation in high aspect ratio composite system. In addition, the enhancement of this output voltage may be due to more interfacial interaction, which leads to an enhancement of conductive network between the composite films.

In order to investigate that the output voltage was gained from pure piezoelectric effect or not, switching polarity test was carried out simply by changing electrode connections in reverse direction. In reverse connection, almost same level of output voltage with opposite polarity was observed for every sample, which confirmed that the output voltage was obtained from the piezoelectric effect not from any other source.[20] The output voltages are almost same in forward and reverse connection with opposite polarity. Thus the electric signals are purely piezoelectric.

Frequency dependent piezoelectric test performance was done in the frequency region 2 to 8 Hz for the sample PVDF/ZnO-20 (shown in Figure 13A). Output voltage was almost same in the frequency region 2 to 8 Hz. Output voltage did not depend on the applied frequency which may be due to the mismatch between the resonating frequency of the film and the applied frequency.[45]

The piezoelectric output voltage of PVDF/ZnO-20 nanocomposite with different tapping pressure is presented in Figure 13B. Open circuit output voltage increased with increasing applying pressure ~1 to 4 KPa at a applied frequency of 5 Hz. This result indicates that PVDF/ZnO nanocomposite can be explored as self-powered sensors.

Piezoresponse force microscopy (PFM) measurement was carried out to check the local ferroelectric and piezoresponse properties existing within PVDF/ZnO-20 composite film. PFM amplitude represents the local piezoelectric displacement of the sample under an applied electric field and PFM phase represents the direction of polarization of sample domains.[47]Figure 14A-C represents the topography image, out of plane amplitude and phase images, respectively. The polarization of domains (Figure 14C) is in opposite direction can be distinguished by image contrasts.[47] Different contrasts were observed in both amplitude and phase images, which indicated the presence of piezoelectricity and ferroelectricity within the composite film.[48] Phase voltage hysteresis loop is shown in Figure 14D. Phase-voltage hysteresis loop shows 180° difference at a tip voltage $V_{\text{dc}} = \pm 60$ V. Under an applied electric field dipoles are easily switched, which indicated that an *in situ* poling process generated in the composite film.[47] Amplitude voltage butterfly loop is shown in Figure 14E. Under an applied electric field, mechanical strain was generated within the composite film, that is, converse piezoelectric phenomena occurs. The asymmetry of the amplitude loop may be due to the internal bias field inside the composite film.[49] The phase-voltage hysteresis loop and butterfly loop confirmed the local ferroelectric and piezoresponse properties existing within the composite film.

4 | CONCLUSION

Different aspect ratio ZnO nanorods were prepared by hydrothermal technique with varying reaction time and PVDF based nanocomposites of the respective ZnO nanorods with different wt% filler loading was fabricated. In this study, we have highlighted the dependence of aspect ratio of ZnO nanorods on the electrical performance of PVDF when they were embedded in its matrix. It has been demonstrated that piezoelectric properties can be improved significantly with using high aspect ratio filler addition in PVDF matrix. A small amount of high aspect ratio ZnO filler loading in PVDF matrix increased the polar-phase fraction in the nanocomposite system, which triggered the enhancement of dielectric properties. Maximum dielectric permittivity was observed in 15 wt% PVDF/ZnO-20 nanocomposite than that of other two composites comprising of comparatively lower aspect ratio ZnO and PVDF (15 wt% PVDF/ZnO-4 and 15 wt% PVDF/ZnO-8). Further 15 wt% PVDF/ZnO-20 composite system exhibited maximum energy density and maximum open circuit AC voltage (20 V). This work provides a new approach for using high aspect ratio ceramic filler to enhance the dielectric, ferroelectric, and piezoelectric properties of the composites of the same filler and polymer PVDF.

ACKNOWLEDGMENTS

Authors would like to thank Director, CSIR-CGCRI for providing the opportunity to carry out this work. Shewli Pratihar gratefully acknowledges Department of Science and Technology, Government of India for financial support (DST-INSPIRE FELLOWSHIP). We acknowledge the BIO-AFM facility of IIT Bombay.

ORCID

Shrabanee Sen https://orcid.org/0000-0002-6375-8893

REFERENCES

[1] L. Xie, X. Huang, Y. Huang, K. Yang, *ACS Appl. Mater. Interfaces* **2013**, *5*, 1747.
[2] P. Kim, S. C. Jones, P. J. Hotchkiss, J. N. Haddock, B. Kippelen, S. R. Marder, J. W. Perry, *Adv. Mater.* **2007**, *19*, 1001.
[3] H. Tang, Z. Zhou, H. A. Sodano, *ACS Appl. Mater. Interfaces* **2014**, *6*, 5450.
[4] P. Martins, A. C. Lopes, S. L. Mendez, *Prog. Polym. Sci.* **2014**, *29*, 683.
[5] J. Zheng, A. He, J. Li, C. C. Han, *Macromol. Rapid Commun.* **2007**, *28*, 2159.
[6] P. Thakur, A. Kool, B. Bagchi, N. A. Hoque, S. Das, P. Nandy, *Phys. Chem. Chem. Phys.* **2015**, *17*, 13082.
[7] M. Khalifa, A. Mahendran, S. Anandhan, *Polym. Compos.* **2019**, *40*, 1663.
[8] E. Fukada, T. Sakurai, *Polym. J.* **1971**, *2*, 656.
[9] X. Zhang, Y. Shen, Q. H. Zhang, L. Gu, Y. H. Hu, J. W. Du, Y. H. Lin, C. W. Nan, *Adv. Mater.* **2015**, *27*, 819.
[10] A. Biswas, S. Garain, K. Maity, K. Henkel, D. Schmeißer, D. Mandal, *Polym. Compos.* **2019**, *40*, E265.
[11] L. Zhang, X. Shan, P. Bass, Y. Tong, T. D. Rolin, C. W. Hill, J. C. Brewer, D. S. Tucker, Z. Y. Cheng, *Sci. Rep.* **2016**, *6*, 33508.
[12] R. Bhunia, R. Dey, S. Das, S. Hussain, R. Bhar, A. K. Pal, *Polym. Compos.* **2018**, *39*, 4205.
[13] H. Tang, H. A. Sodano, *Nano Lett.* **2013**, *13*, 1373.
[14] M. Zirkl, A. Haase, A. Fian, H. Schon, C. Sommer, G. Jakopic, G. Leising, B. Stadlober, I. Graz, N. Gaar, R. Schwodiauer, S. B. Gogonea, S. Bauer, *Adv. Mater.* **2007**, *19*, 2241.
[15] S. P. Bao, G. D. Liang, S. C. Tjong, *Carbon* **2011**, *49*, 1758.
[16] S. W. Choi, J. R. Kim, Y. R. Ahn, S. M. Jo, E. J. Cairns, *Chem. Mater.* **2007**, *19*, 104.
[17] K. Matsushige, *Phase Trans.* **1989**, *18*, 247.
[18] K. S. Ramadam, D. Sameoto, S. Evovy, *Smart Mater. Struct.* **2014**, *23*, 033001.
[19] S. Satapathy, S. Pawar, P. K. Gupta, K. B. R. Varma, *Bull. Mater. Sci.* **2011**, *34*, 727.
[20] B. Adak, I. Chinya, S. Sen, *RSC Adv.* **2016**, *6*, 105137.
[21] P. Martins, C. M. Kosta, G. Botelho, S. L. Mendez, *Mater. Chem. Phys.* **2012**, *131*, 698.
[22] X. Chen, S. Xu, N. Yao, Y. Shi, *Nano Lett.* **2010**, *10*, 2133.
[23] Y. Qi, J. Kim, T. D. Nguyen, B. Lisko, P. K. Purohit, M. C. Mcalpine, *Nano Lett.* **2011**, *11*, 1331.
[24] Z. L. Wang, J. Song, *Science* **2006**, *312*, 242.
[25] W. Guo, C. Tan, K. Shi, J. Li, X. X. Wang, B. Sun, X. Huang, Y. Z. Long, P. Jiang, *Nanoscale* **2018**, *10*, 17751.
[26] P. Thakur, A. Kool, N. A. Hoque, B. Bagchi, F. Khatun, P. Biswas, D. Brahma, S. Roy, S. Banerjee, S. Das, *Nano Energy* **2018**, *44*, 456.
[27] W. Rahaman, S. Garain, A. Sultana, T. R. Middy, D. Mondal, *Mater. Today: Proc.* **2018**, *5*, 9826.
[28] K. Y. Shin, J. S. Lee, J. Jang, *Nano Energy* **2016**, *22*, 95.
[29] S. Lee, W. Ko, J. Hong, *J. Nanosci. Nanotechnol.* **2014**, *14*, 9319.
[30] Y. H. Ko, G. Nagaraju, S. H. Lee, J. S. Yu, *ACS Appl. Mater. Interfaces* **2014**, *6*, 6631.
[31] Y. Qiu, D. Yang, J. Lei, H. Zhang, J. Ji, B. Yin, J. Bian, Y. Zhao, L. Hu, *J. Mater. Sci.: Mater. Electron.* **2014**, *25*, 2649.
[32] Q. Wang, D. Yang, Y. Qiu, X. Zhang, W. Song, L. Hu, *Appl. Phys. Lett.* **2018**, *112*, 063906.
[33] J. Li, S. Chen, W. Liu, R. Fu, S. Tu, Y. Zhao, L. Dong, B. Yan, Y. Gu, *J. Phys. Chem. C* **2019**, *123*, 11378.
[34] B. Liu, H. C. Zeng, *J. Am. Chem. Soc.* **2003**, *125*, 4430.
[35] S. Singhal, J. Kaur, T. Namgyal, R. Sharma, *Physica B* **2012**, *407*, 1223.
[36] I. Chinya, A. Pal, S. Sen, *J. Alloys Compd.* **2017**, *722*, 829.
[37] A. Sasmal, S. Sen, P. S. Devi, *Phys. Chem. Chem. Phys.* **2019**, *21*, 5974.
[38] S. K. Ghosh, M. M. Alam, D. Mandal, *RSC Adv.* **2014**, *4*, 41886.
[39] H. Luo, J. Roscow, X. Zhou, S. Chen, X. Han, K. Zhou, D. Zhang, C. R. Bowen, *J. Mater. Chem. A* **2017**, *5*, 7091.
[40] S. Liu, J. Zhai, J. Wang, S. Xue, W. Zhang, *ACS Appl. Mater. Interfaces* **2014**, *6*, 1533.
[41] Y. Niu, Y. Bai, K. Yu, Y. Wang, F. Xiang, H. Wang, *ACS Appl. Mater. Interfaces* **2015**, *7*, 24168.
[42] L. Xie, X. Huang, C. Wu, P. Jiang, *J. Mater. Chem.* **2011**, *21*, 5897.
[43] X. Lin, P. H. Hu, Z. Y. Jia, S. M. Gao, *J. Mater. Chem. A* **2016**, *4*, 2314.
[44] L. Ying, P. Wang, E. T. Kang, K. G. Neoh, *Macromolecules* **2002**, *35*, 673.
[45] I. Chinya, A. Sasmal, A. Pal, S. Sen, *CrystEngComm* **2019**, *21*, 3478.
[46] D. Zhang, X. Zhou, J. Roscow, K. Zhou, L. Wang, H. Luo, C. R. Bowen, *Sci. Rep.* **2017**, *7*, 45179.
[47] C. Zhang, Y. Fan, H. Li, Y. Li, L. Zhang, S. Cao, S. Kuang, Y. Zhao, A. Chen, G. Zhu, Z. L. Wang, *ACS Nano* **2018**, *12*, 4803.
[48] A. Ferri, S. Barrau, R. Bourez, A. D. Costa, M.-H. Chambrier, A. Marin, J. Defebvin, J. M. Lefebvre, R. Desfeux, *Compos. Sci. Technol.* **2020**, *186*, 107914.
[49] S. K. Ghosh, P. Adhikary, S. Jana, A. Biswas, V. Sencadas, S. D. Gupta, B. Tudu, D. Mandal, *Nano Energy* **2017**, *36*, 166.

SUPPORTING INFORMATION

Additional supporting information may be found online in the Supporting Information section at the end of this article.

How to cite this article: Pratihar S, Medda SK, Sen S, Devi PS. Tailored piezoelectric performance of self-polarized PVDF-ZnO composites by optimization of aspect ratio of ZnO nanorods. *Polymer Composites*. 2020;41:3351–3363. https://doi.org/10.1002/pc.25624

Soft Matter

ROYAL SOCIETY OF CHEMISTRY

PAPER

View Article Online
View Journal | View Issue

Check for updates

Cite this: *Soft Matter*, 2021, **17**, 8483

Enhanced dielectric, ferroelectric, energy storage and mechanical energy harvesting performance of ZnO–PVDF composites induced by MWCNTs as an additive third phase†

Shewli Pratihar,[a] Aniket Patra,[b] Abhishek Sasmal,[a] Samar Kumar Medda[c] and Shrabanee Sen *[a]

Received 8th June 2021,
Accepted 15th August 2021

DOI: 10.1039/d1sm00854d

rsc.li/soft-matter-journal

The present work highlights an attempt of fabricating a nanocomposite by the addition of multi-walled carbon nanotubes (MWCNTs) as a third phase into flexible ZnO–poly(vinylidene fluoride) (ZnO–PVDF) composites. MWCNTs played a very important role in distributing ZnO fillers in the PVDF matrix more homogeneously and increased the connection capability. Enhancement of the piezoelectric phase, dielectric permittivity, ferroelectric polarization, energy storage density and mechanical energy harvesting performance of ZnO–PVDF composites after the addition of MWCNTs was confirmed from the respective characterization studies. The sensing capability was demonstrated by the generation of ~22 V ac output voltage through the application of human finger tapping on 15 wt% ZnO and a 0.1 wt% MWCNT-loaded PVDF (15PZNT) based composite film. The rectified voltage from the fabricated 15PZNT film was used to charge a 10-μF capacitor up to ~3 V which was used for the illumination of 30 commercial LEDs. The maximum power density from the film was found to be 21.41 μW cm^{-2} at 4 MΩ load resistance. The effect of the addition of MWCNTs was also verified by simulation using COMSOL Multiphysics software.

1 Introduction

During extensive research in the field of materials science, functional nanocomposites are often prepared in order to achieve the desired performance enhancement. They are widely used in various areas of real-life applications including nanotechnology, biotechnology and agriculture, textile and clothing, information technology, energy and environment, food and nutrition, electronic sensors, chemical sensors, data storage, optical fibres, field-effect transistors and many others.[1–7] In this regard, researchers all over the world use different processing techniques and study the effects of these techniques on the functional performance of nanocomposites.[8–14] Considering the increasing energy crisis all over the world, energy storage and harvesting applications, among all the above-mentioned real-life applications of functional nanocomposites, have been mainly focused in the present work.

In recent years, great effort has been devoted to developing new energy harvesting technologies for various applications to overcome the world energy crisis in an environmentally friendly manner. In this study, the conversion of easily available ambient waste mechanical vibrations into electricity has attracted much attention as a renewable power source.[15–19] Therefore, piezoelectric materials such as barium titanate ($BaTiO_3$), lead zirconium titanate (PZT), zinc oxide (ZnO), zinc stannate ($ZnSnO_3$), gallium nitride (GaN), bismuth ferrite ($BiFeO_3$) and many others, which can effectively convert mechanical energy into electricity using their unique property of piezoelectricity, are widely used to fabricate piezoelectric energy harvesters.[20–25] In this regard, piezoelectric nanogenerators are the best known technology which can effectively convert ambient mechanical vibrations into electricity in a portable and wearable manner and can meet the power requirement of low power consuming electronic devices.

After its first discovery in 2006 by Wang *et al.*,[26] research studies were mainly focused on the development of piezoelectric nanogenerators by using crystalline and ceramic materials in the very beginning.[27–29] In this work, ZnO nanorod/nanowire arrays were very extensively studied.[28,29] But, ceramic-based piezoelectric energy harvesters have some limitations in real-field applications. They are very brittle and hence cannot be explicitly used in wearable applications, and their low breakdown strength

---

[a] *Functional Materials and Devices Division, CSIR-Central Glass and Ceramic Research Institute, Kolkata-700032, West Bengal, India. E-mail: shrabanee@cgcri.res.in*
[b] *Dipartimento di Fisica, Universita della Calabria, Rende-87036, Italy*
[c] *Speciality Glass Technology Division, CSIR-Central Glass and Ceramic Research Institute, Kolkata-700032, West Bengal, India*

† Electronic supplementary information (ESI) available. See DOI: 10.1039/d1sm00854d

limits their applications in high applied electric fields. Furthermore, the fabrication techniques of ceramic nanogenerators are comparatively complex and difficult and also involve very high cost for fabrication. On the other hand, polymer materials commonly exhibit very high breakdown strength and superior flexibility. Therefore, polymer-based composites are also widely used in flexible dielectrics and energy storage devices. So, there is utmost demand for fabricating piezoelectric polymer-based flexible nanogenerators which can be comfortably used in portable and wearable electronic devices.

Among the several piezoelectric polymers, polyvinylidene fluoride (PVDF) and its co-polymers are widely used as an active matrix due to their superior piezoelectric properties, electric breakdown strength and cost effectiveness compared to others.[30] Therefore, PVDF has been chosen as the piezoelectric polymer matrix in the present work. But, under normal conditions, PVDF exhibits its non-polar α-phase due to the existence of energetically more favourable TG^+TG^- chain conformation, which is not suitable for real-life applications.[31,32] Therefore, the conversion of non-polar α-PVDF into polar β-PVDF and/or γ-PVDF exhibiting TTTT and $T_3G^+T_3G^-$ chain conformations, respectively, is a mandatory requirement in order to improve their output electrical performance.

Several techniques such as electrospinning, mechanical stretching, incorporation of filler particles, melting under specific conditions, solvent casting, *etc.* have been widely attempted by several researchers for the conversion of the non-polar phase into the polar phase of PVDF.[33–37] Among them, the incorporation of small amounts of filler particles in the PVDF matrix is the most extensively studied and cost-effective method.[37] In this work, different metal nanoparticles like Ag, Pt, *etc.*, different ceramic particles like $BaTiO_3$, $Pb(ZrTi)O_3$, SiO_2, ZnO, $ZnSnO_3$, $BiVO_4$, $ZnFe_2O_4$, *etc.* and many other types of fillers have been explicitly used by several researchers all over the world.[37,38] Among all the materials used as fillers in the PVDF matrix, ZnO is the most extensively studied due to its superior biocompatibility, excellent piezoelectric properties and easy synthesis method.[39–42] Parangusan *et al.*[39] investigated the effect of Co–ZnO fillers on the piezoelectric properties of PVDF-HFP and achieved significantly improved performance. They also studied[40] Fe–ZnO-loaded PVDF-based composite films. AlAhzm *et al.*[41] achieved improved piezoelectric performance of PVDF by loading iron oxide and zinc oxide in its matrix. Singha *et al.*[42] studied the effect of ZnO on stainless steel electrodes for piezoelectric applications. Moreover, ZnO exhibits superior optical and photocatalytic activity and can be used as UV sensors.[43–48] Though the present work is focused on the development of a PVDF-based flexible energy storage and harvesting device, the mentioned functional properties can further be combined with the electrical performance of its PVDF-based composites. Considering all these facts, ZnO was chosen as the filler material for the PVDF matrix in the present work. In our previous work, the aspect ratio of ZnO nanorods was tuned to achieve performance enhancement of the resulting PVDF-based composites. Here in the present work, we have tried to improve the electrical performances of flexible PVDF–ZnO composites by using a third phase addition.

The addition of third phase conductive fillers, such as reduced graphene oxide (rGO), carbon black, graphite, single/multi-walled carbon nanotubes, *etc.*, in polymer-based composites has been previously studied by several researchers in order to improve their electrical and energy harvesting performances.[49–52] Pereira *et al.*[49] fabricated metal (Co, Ni, Pd, Pt)–CNT–PVDF composites and studied their structural, optical, thermal and electrical properties. Chinya *et al.*[50] found significant enhancement of the electrical and energy harvesting properties of $ZnFe_2O_4$–PVDF composites by adding a third conducting phase (polyaniline (PANI)) into it. Pal *et al.*[51] also studied the energy harvesting ability of a PZT–MWCNT–PVDF system and achieved improved output performance. Dang *et al.*[52] succeeded in increasing the dielectric permittivity of $BaTiO_3$–PVDF composites by adding nickel (Ni) as the third conducting phase.

The introduction of a third phase conductive filler within the polymer matrix reduces the dissimilarity of the difference of a local electric field between the ceramic filler and the polymer matrix within the nanocomposite. Besides, third phase conductive fillers improve the homogeneity of dispersion of fillers within the polymer matrix and prevent their agglomeration within the nanocomposite.[50] On the other hand, the electronic conductivity of PVDF is very low and hence, the uniformly distributed fillers in PVDF become isolated due to the PVDF insulation layers between them. But, for achieving enriched output piezoelectric performance, a good connection between each piezoelectric ZnO nanorod is a must needed parameter. So, the addition of optimized amounts of third phase conductive fillers in PVDF–ZnO composites creates good electrical connections between each ceramic particle and hence, enhancement of conductivity in nanocomposites is achieved which in turn improves their peizo-response. Owing to its good electronic conductivity, the third phase conductive filler not only creates an electrical bridge between each ZnO nanorod, but also creates good connectivity between the top and bottom electrodes of the composite film which in turn improves the output piezoelectric performance through good charge transmission between the composite film and the electrodes. Furthermore, the improved homogeneous distribution of nanomaterials in the PVDF matrix induced by the third phase conductive fillers reduces the internal resistance of the nanocomposite and as a result, output electrical performances are improved.[53–57] Considering all these facts, different fabrication technologies with optimized structures and device arrangements have been explored in this study.

In this work, initially, an attempt was made to synthesize ZnO nanorods by a wet chemical route. Then, the as-synthesized ZnO nanorods were added to the PVDF matrix for the fabrication of the composite film. Further enhancement in the output performance of the PVDF–ZnO composite film has been atempted by using multi-walled carbon nanotubes (MWCNTs) as an additive third conducting phase filler into it. Among the different conducting materials, MWCNTs were chosen here in order to match the morphology of the third conducting phase filler with the ceramic ZnO filler which may facilitate the filler distribution and alignment. As described above, the MWCNT addition can also improve the piezoelectric output of the PVDF–ZnO composite. The structural, morphological, vibrational, dielectric, ferroelectric, energy storage and energy harvesting performances of PVDF–ZnO composites before and after MWCNT addition have been studied in detail here in the present work. Theoretical simulations for ferroelectric polarization and piezoelectric potential have also been performed.

2 Experimental

2.1 Raw materials

Zinc nitrate hexahydrate [$Zn(NO_3)_2{\cdot}6H_2O$] (99%, Sigma Aldrich), sodium hydroxide pellets [NaOH] (≥97%, Merck), ethanol (C_2H_5OH) (99%, Merck), ethylenediamine ($C_2H_4(NH_2)_2$) (EDA) (Merck) and distilled water were used as precursor materials to synthesize ZnO rods by wet chemical synthesis. For the fabrication of composite films, polyvinylidene fluoride (PVDF) pellets (molecular weight ≈ 275 000 by GPC, Sigma-Aldrich), MWCNTs (SRL Pvt Ltd, 95%), synthesized ZnO rods, and *N*,*N*-dimethyl formamide (DMF) [$HCON(CH_3)_2$] (≥99%, Merck) were used as starting raw materials.

2.2 Synthesis of ZnO nanorods

ZnO nanorods were synthesized by following a wet chemical synthesis route at room temperature, previously reported by Liu *et al.*[58] in their earlier work. Briefly, 20 mL of zinc nitrate hexahydrate aqueous solution and 20 mL of sodium hydroxide aqueous solution were first mixed together inside a 500 mL capped Teflon bottle (the molarity of these two solutions was chosen so that the ratio $Zn^{2+}:OH^-$ becomes equal to 1 : 20). After 1 h of mixing by continuous stirring, 200 mL of absolute ethanol was added to the mixed solution and continued stirring (350 rpm) at room temperature for 3 h. Then, 10 mL of EDA was added to this mixed solution and the whole mixture inside the capped Teflon bottle was stirred for 3 days at room temperature. After the synthesis, a white precipitate was found which was collected and centrifuged several times with water and ethanol. The obtained white product was dried in an oven at 60 °C for 12 h to get the desired powder sample of ZnO nanorods.

2.3 Fabrication of PVDF composites

Pure PVDF and all composite films were fabricated by the drop-casting technique.[37,50] To obtain different series of composite films, 8 wt% PVDF was first dissolved in *N*,*N*-dimethyl formamide (DMF) with continuous stirring at 40 °C inside an air-tight glass bottle. After the formation of a homogeneous solution of PVDF and DMF, different amounts of synthesized ZnO nanorods (5 wt%, 10 wt%, and 15 wt% ZnO powders with respect to PVDF) were added to the DMF–PVDF solution in three different batches. Furthermore, optimized amounts of MWCNTs (0.1 wt%) (see Fig. S1 and Discussion S1 of the ESI†) were added to each PVDF–ZnO mixed solution for the fabrication of the three-phase composite (characterization of MWCNT is depicted in Fig. S2 and Discussion S2 of the ESI†). The mixed solutions were then continuously stirred (inside air-tight glass bottles) for 72 h (during this process, the solutions were sonicated for ∼1 h after each 24 h of stirring). The resultant solutions were then drop cast in the form of thin films on the glass substrates inside a dust-free oven and annealed at 85 °C for 4 h. Finally, the composite films were peeled off from the glass substrates and cooled down to room temperature. In this regard, it is to be mentioned that, filler loading higher than 15 wt% could not produce free-standing composite films under the present experimental conditions; rather, the films became curly after annealing. On the other hand, along with improved output performance, flexibility was also one of our key objectives and the flexibility of PVDF generally decreases with the increasing filler loading. Considering all these facts, filler concentration was not further increased after 15 wt% loading. A neat PVDF film was also fabricated by following the same technique without adding any filler loading in the PVDF–DMF solution. The compositions and nomenclatures of all the composite films studied in the present work are shown in Table 1.

For electrical measurements, both faces of all the fabricated composite films were electroded with high-quality silver paste. The piezoelectric energy harvesting device was fabricated by connecting two copper wires with these two electrodes.

2.4 Characterization

X-ray diffraction (XRD) measurements were carried out to understand the crystal structure of the synthesized ZnO nanorods and phase formation in pure PVDF and composite films using an X'Pert PRO MPD diffractometer (PAN analytical) with nickel filtered CuKα radiation (λ = 0.15404 nm). For further determination of phase characteristics, vibrational modes of the nanocomposites were determined using Fourier transform infrared spectroscopy (FTIR) (FTIR-Spectrum 2, PerkinElmer). For a better understanding of phase formation, the Gaussian curve fitting of XRD patterns and the FTIR spectra of PVDF, 15PZO and 15PZNT films were obtained using Origin software. Field emission scanning electron microscopy (FESEM) (SEM Supra 35 VP) was used to perform the microstructural analysis of the synthesized ZnO rods, MWCNTs and 15PZNT film. Transmission electron microscopy (TEM) images and high-resolution TEM (HRTEM) images

Table 1 Compositions and nomenclatures of the fabricated composite films

wt% of PVDF pellets w.r. t. DMF	wt% of ZnO filler loading w.r. t. PVDF	wt% of third phase MWCNT loading w.r. t. PVDF	Name of the composite films
8	0	0	PVDF
8	5	0	5PZO
8	10	0	10PZO
8	15	0	15PZO
8	5	0.1	5PZNT
8	10	0.1	10PZNT
8	15	0.1	15PZNT

of ZnO nanorods and MWCNTs were also obtained using a Tecnai G2, 30ST, (FEI) instrument operating at 300 kV. The elemental composition of the ZnO sample was studied using an energy-dispersive X-ray (EDX) spectroscopy unit attached with a TEM instrument. The room temperature dielectric study of PVDF and all the nanocomposites was performed with a precision impedance analyser (6500 B Wayne Kerr). The room temperature ferroelectric measurement was carried out with a RADIANT ferroelectric test system (Radiant Technologies Inc.) using Vision software (Version 3.1.0). The study of the piezoelectric properties of PVDF and the composite films was performed using a digital oscilloscope (YOKOGAWA, DL 1640) upon the application of manual human finger tapping on them. The real-life application of the developed piezoelectric nanogenerator device was demonstrated by rectifying the output ac voltage into dc by using a bridge rectifier IC (DB 107). The obtained dc voltage after rectification was used to charge a 10-μF commercial capacitor which was able to light up some LEDs (connected in parallel) during discharging. The experimental results obtained from the ferroelectric and energy harvesting studies were verified by performing theoretical simulations using COMSOL Multiphysics software.

3 Results and discussion

3.1 Structure and morphology of the filler material

The confirmation of phase formation and morphology of the filler material was evaluated by XRD and TEM characterization studies, respectively. The XRD pattern of the synthesized ZnO powder is illustrated in Fig. 1(a). All the diffraction peaks matched well with the standard JCPDS data for ZnO (JCPDS card no.: 79-0208) with lattice constants $a = b = 3.264$ Å and $c = 5.219$ Å. Therefore, the peaks were indexed in the figure on the basis of this JCPDS file which confirmed the hexagonal wurtzite structure (with $P6_3mc$ space group) of the synthesized ZnO filler. The absence of any additional peak confirmed the phase purity of the synthesized ZnO sample. The peak broadening of the XRD pattern was found to be very low suggesting the large crystalline size of the synthesized ZnO sample which is very common for ZnO rods having lengths in the micrometer range. As the XRD characterization suggested the large crystallite size of the synthesized ZnO, its morphological characterization is inevitable. Its morphology and crystalline characteristics were investigated by TEM characterization. Fig. 1(b) presents the bright field TEM image of the synthesized ZnO filler which confirmed its rod-like morphology. The calculated average length and diameter of the synthesized ZnO nanorods were found to be ∼60 nm and ∼300 nm, respectively. The diameter distribution of the nanorods is shown in Fig. S3(a) (ESI†). The HRTEM image of the ZnO nanorods is presented in Fig. S3(b) (ESI†) confirming the presence of the (101) plane which matched with the maximum intense peak of the XRD pattern. Fig. S3(c) (ESI†) presents the EDX spectra of the synthesized nanorod, which confirmed the existence of the desired elements with almost the desired proportion. The absence of signals from any other elements except copper (Cu) (signal from Cu appeared due to the usage of Cu grid during TEM characterization) proved the purity of the synthesized ZnO nanorods.

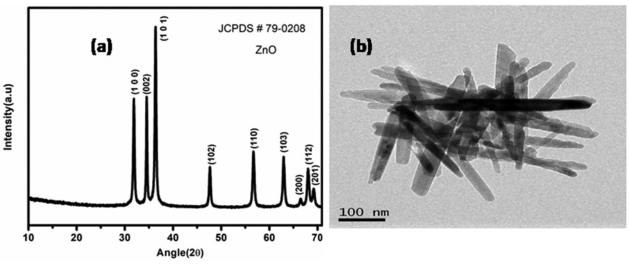

Fig. 1 (a) XRD pattern and (b) TEM image of ZnO nanorods.

3.2 Morphology of the composite films

In order to obtain an idea about the mixing of the constituents of the fabricated composite films, their morphology needs to be studied. The morphology of the 15PZNT film was studied by FESEM characterization and is presented in Fig. 2(a) which confirmed the presence of ZnO nanorods and MWCNTs embedded within the PVDF matrix. Thus, the mixing of all the constituents was visualized from this characterization. In this regard, it is to be mentioned that, during the preparation of PVDF-based composite films, a total of 3 h of ultrasonication was performed; under this condition, there is always a chance of structural damage to the MWCNTs due to extensive ultrasonication. Therefore, to study this fact, ZnO, MWCNT and ZnO–MWCNT mixtures were ultrasonicated in an ethanol medium for 3 h and their morphologies were studied by FESEM, which are presented in Fig. 2(b), (c) and (d), respectively. No structural damage to the fillers was seen from these figures. On the basis of this characterization, proper mixing of the constituents of the composite film without any structural damage was confirmed.

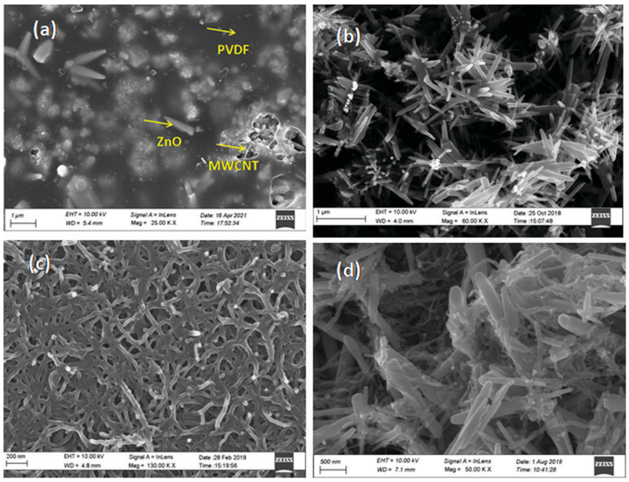

Fig. 2 (a) FESEM image of 15PNZT film and FESEM image of (b) ZnO nanorod, (c) MWCNT and (d) ZnO–MWCNT mixture after extensive sonication.

3.3 Phase formation in the composite films

The presence of a polar phase in the composite film is an important parameter for exhibiting good piezoelectric performance. The piezoelectricity arises due to the preferential orientation of CH_2/CF_2 dipoles which are positioned perpendicular to the polymer backbone.[59] The inclusion of filler particles in the PVDF matrix generally improves the polarity of the resulting composite films.[37,50] Actually, the filler material takes part in different types of interfacial interactions with $-CH_2/-CF_2$ dipoles of the non-polar α-PVDF exhibiting TG^+TG^- chain conformation. As a result of this interfacial interaction, preferential re-orientation of the dipoles of PVDF occurs. Due to this re-orientation of dipoles, the TG^+TG^- structure (α-PVDF) of PVDF changes to TTTT (β-PVDF) and/or $T_3G^+T_3G^-$ (γ-PVDF) chain conformation resulting in non-polar to polar phase transformation. XRD and FTIR are two well-known techniques which are widely used by researchers all over the world to determine this phase transformation.

To investigate the polar phase formation in the composite films, XRD characterization was first performed. Fig. S4 (ESI†) presents the XRD patterns of pure PVDF, 15PZO and 15PZNT composite films. Pure PVDF exhibits characteristic peaks at the diffraction angles 17.7°, 18.3°, 19.9° and 26.6° corresponding to the planes (100), (020), (110) and (021), respectively, which confirmed the predominant presence of α-phase for this film.[60–62] On the other hand, for the 15PZO and 15PZNT films, the peaks at 17.7° and 18.3° disappeared completely and the intensity of the 26.6° peak gradually decreased. A new peak at 18.6° corresponding to γ-PVDF also appeared for these two films. Furthermore, the main characteristic peak at 19.9° for pure PVDF gradually shifted to a higher diffraction angle for the 15PZO and 15PZNT films, respectively. For the 15PZNT composite, the intensities of the γ and β peaks enhanced significantly, which indicates the momentous enhancement of the polar phase for this film. All these observations suggested that the polar phase of PVDF successively increased after the addition of ZnO and ZnO–MWCNT. For a better understanding of this non-polar to polar phase transformation, the total degree of crystallinity and individual amounts of beta crystallinity and gamma crystallinity of pure PVDF, 15PZO and 15PZNT films were calculated from the deconvoluted XRD patterns of these samples (Fig. 3(a–c)). The detailed calculation method and the obtained results are depicted in Discussion S3 and Table S1 (ESI†).

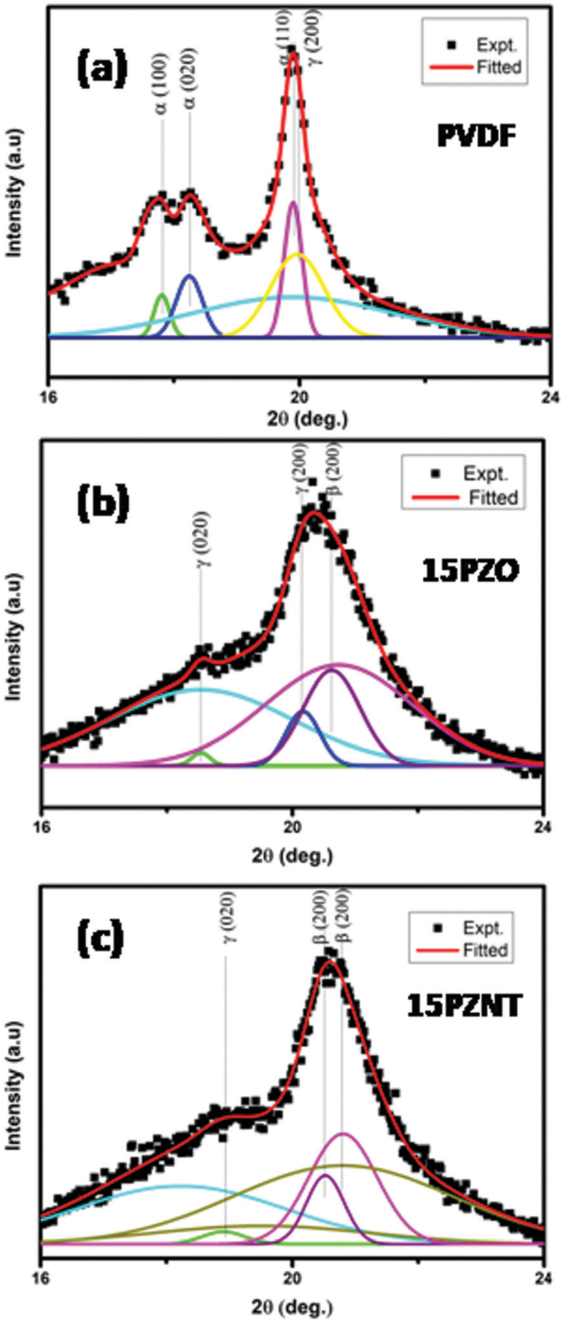

Fig. 3 (a–c) Deconvoluted XRD patterns of pure PVDF, 15PZO and 15PZNT composite films.

The total degree of crystallinity is reduced to 56.1% and 32.4% for the 15PZO and 15PZNT films from a value of 67.2% for pure PVDF. This reduction in crystallinity of PVDF may be explained on the basis of the induced polymorphism after filler addition in its matrix.[63] When no fillers were included in the PVDF matrix, homogeneous growth of its α-crystallites occurred and as a result, the total degree of crystallinity became comparatively high. But when fillers were included in its matrix, they acted as nucleation centres and interacted strongly with the PVDF dipoles. Therefore, the homogeneous growth of the crystallites of PVDF was restrained and heterogeneous nucleation of crystallites occurred. The fillers also prevented the formation of extended chain conformation due to their existence in the region of inter-chain spacing. On the other hand, a large number of fillers, which did not interact with the PVDF dipoles and existed as dormant in the PVDF matrix, also inhibited the growth of crystallites. All these factors together caused the reduction in the total degree of crystallinity of PVDF after filler addition. The cross-linking of polymers induced by fillers may also be another possible cause of the hindrance in crystallinity. The heterogeneous nucleation of crystallites is mainly governed by the interaction of PVDF dipoles with fillers. On the other hand, the interaction of PVDF dipoles with fillers commonly helps in the re-orientation of chain conformation of PVDF which causes the non-polar to polar phase transformation

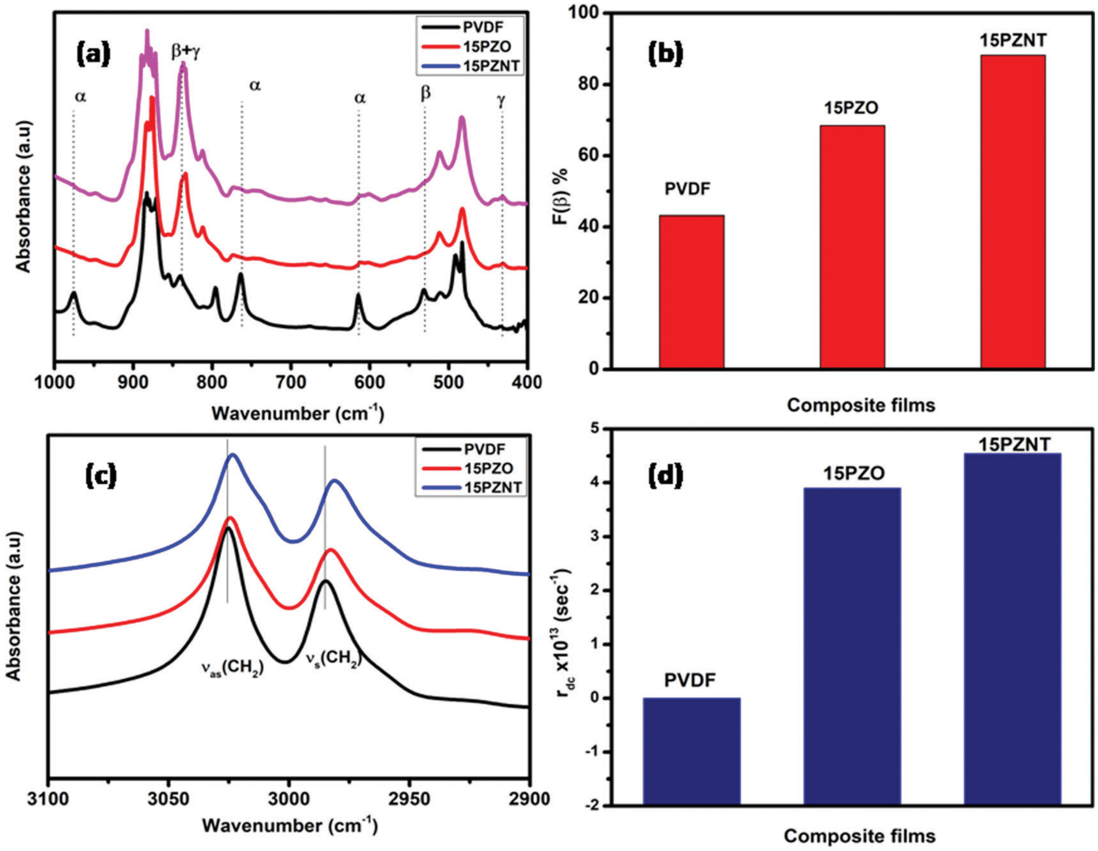

Fig. 4 (a) FTIR spectra, (b) polar phase of composite films calculated from FTIR spectra, (c) FTIR stretching vibration band shift and (d) damping coefficient of pure PVDF, 15PZO and 15PZNT films.

(discussed earlier). Therefore, the induced polymorphism may also be considered as a possible cause of the enhancement of polarity of the composite films after filler addition. Beta crystallinity is significantly enhanced after CNT addition within the ZnO–PVDF composite which indicated that the PVDF–ZnO–CNT composite may exhibit better piezoelectric response.

For a detailed study of polar phase formation in the fabricated composite films, an extensive FTIR study was also performed. Fig. 4(a) presents the FTIR absorption spectra of pure PVDF, 15PZO and 15PZNT composite films within the wavenumber region of 1000–400 cm^{-1}. Pure PVDF exhibited vibrational bands at 612, 764, 796, and 976 cm^{-1} corresponding to the nonpolar α-phase, 510 cm^{-1} to the β-phase and 840 cm^{-1} to both the β and γ phases.[62] But after the incorporation of ZnO rods in the PVDF matrix, the intensity of these α peaks reduced and the bands were almost diminished. The intensity of the peak at 840 cm^{-1} increased gradually for the 15PZO and 15PZNT films, respectively, which inferred the gradual enhancement of their polar phase. The amount of electroactive polar phase (F(EA)) present is calculated from the Beer–Lambert law given by eqn (1).

$$F(\mathrm{EA}) = \frac{A_{\mathrm{EA}}}{\left(\frac{k_{840}}{k_{764}}\right)A_{\mathrm{NEA}} + A_{\mathrm{EA}}} \quad (1)$$

Here, A_{NEA} and A_{EA} are the absorbance intensities of the non-electroactive 764 cm^{-1} and electroactive 840 cm^{-1} bands, k_{840} = 7.7×10^4 cm^2 mol^{-1} (the absorption coefficient at 840 cm^{-1}) and k_{764} = 6.1×10^4 cm^2 mol^{-1} (the absorption coefficient at 764 cm^{-1}).[62] The calculated electroactive phase fraction (F(EA)) for all the composite samples is presented in Fig. 4(b) and was found to be ∼43.2, 68.5 and 88.9% for pure PVDF, 15PZO and 15PZNT composites, respectively. The 840 cm^{-1} absorption bands of pure PVDF, 15PZO and 15PZNT films were deconvoluted (Fig. S5, ESI†) to evaluate the quantitative amounts of individual β and γ phases within them (Discussion S4, ESI†) and the results are presented in Table S2 (ESI†).[62]

The concurrent incorporation of both ZnO nanorods and MWCNTs produced an upsurge in the polar phase, which was one of the main motives of the present work. The cause of the gradual enhancement of the polar phase after the addition of ZnO and ZnO–MWCNT in the PVDF matrix, respectively, may be explained in the following way. At first, when only ZnO was added to the PVDF matrix, the polar phase increased due to the interfacial electrostatic interaction[37] between the positively charged $-CH_2$ dipole of PVDF[64] and the negatively charged ZnO surface (see Fig. S6, ESI†). In the next step, when the three phase composites were fabricated by the addition of both ZnO and MWCNTs in the PVDF matrix, some extra effects arising from the third MWCNT phase played a very important role along with the previously existed electrostatic interaction between the $-CH_2$ dipoles of PVDF and the ZnO surface. First, the third MWCNT phase improved the homogeneity of filler distribution in the PVDF matrix by reducing the compatibility issue between them. Second, the π-electrons of the carbon atom of the MWCNT interacted very strongly with the –CH$_2$ dipoles of PVDF. These results were also previously established by several researchers all over the world through various experimental and theoretical studies.[50,65,66] Thus, the obtained result for the gradual improvement of the polar phase of PVDF after the addition of ZnO and ZnO–MWCNT, respectively, is justified. The maximum polar phase was exhibited by the 15PZNT film. The gradual enhancement of interfacial interactions between the –CH$_2$ dipoles of PVDF and the filler surface for the 15PZO and 15PZNT films was further confirmed by the study of their FTIR absorption spectra within the wavenumber region of 3100 cm^{-1} to 2900 cm^{-1} (shown in Fig. 4(c)) where the stretching vibrations of the –CH$_2$ dipoles are only responsible for the occurrence of the resulting bands. The gradual shift of the –CH$_2$ stretching vibration band towards the lower energy region and the increase in damping coefficient (r_{dc}) (Fig. 4(d)) confirmed the gradual enhancement of interfacial interactions for pure PVDF, 15PZO and 15PZNT films, respectively.[31,32,37,38] The calculation of r_{dc} and the explanation of this result are depicted in Discussion S5 (ESI†).

Thus, the XRD and FTIR characterization studies of the composite films confirmed the enhancement of polarity of PVDF after the addition of ZnO and MWCNTs. Therefore, the electroactive properties, such as dielectric permittivity, ferroelectric polarization and piezoelectric performance, are expected to be enhanced. In this regard, it is to be mentioned that the interfacial interaction between the –CH$_2$ dipoles of PVDF and the fillers helped in reorienting the TG$^+$TG$^-$ chain conformation of the non-polar α-PVDF in a new fashion such that it achieves polar phase chain conformation. As this reorientation of dipoles could not be controlled in a desirable manner, the TG$^+$TG$^-$ chain conformation took both the TTTT and T$_3$G$^+$T$_3$G$^-$ chain conformations corresponding to the polar β-PVDF and γ-PVDF, respectively. Therefore, though the achievement of improved β-phase in the composite films was one of the main targets of the present work, enhancement of both the β and γ phases was also achieved. It is worth mentioning that for both these cases, the total amount of polarity increased which is very beneficial for the desired purpose of the present work.

3.4 Dielectric properties of the composite films

The dielectric properties are very important parameters for exploring the application of these films as energy storage and harvesting devices. The dielectric constant measures the charge holding capacity of the material.[37] The frequency-dependent

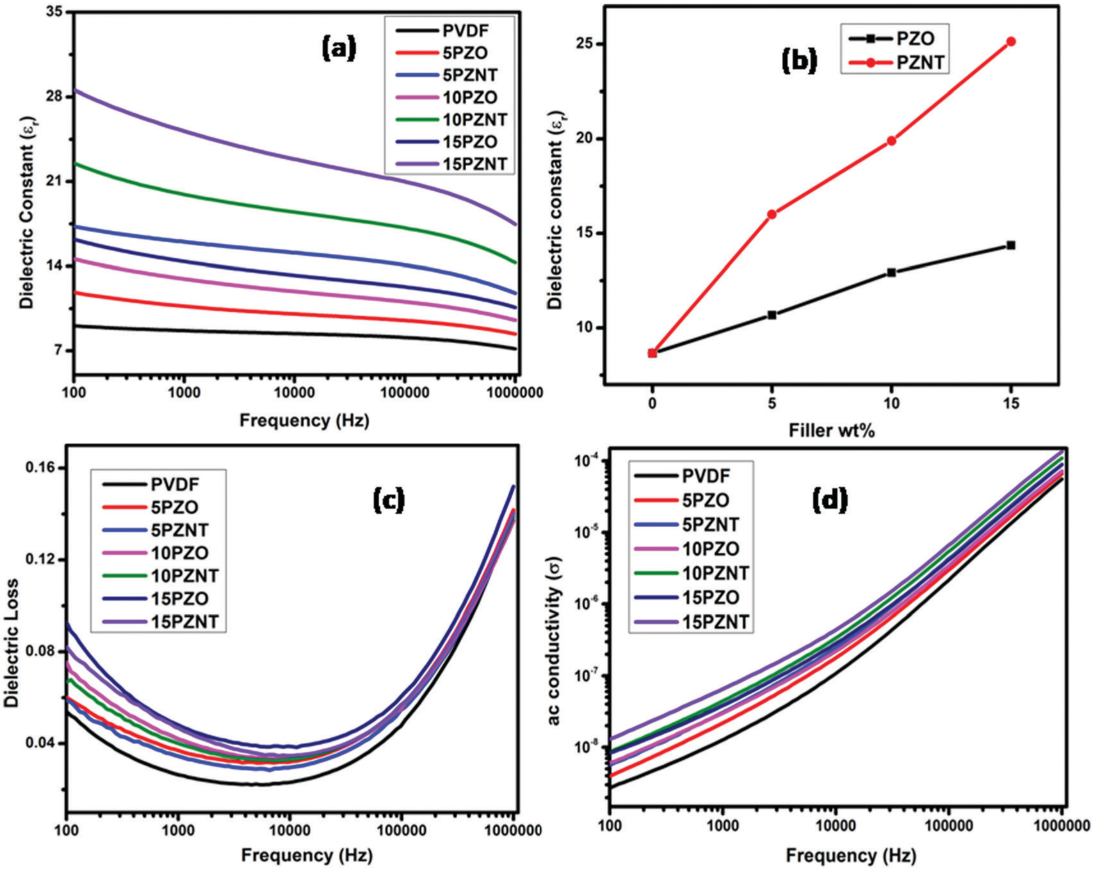

Fig. 5 (a) Frequency dependent and (b) filler concentration dependent dielectric permittivity and frequency dependent (c) dielectric loss, (d) ac conductivity of PVDF and all the composite films.

dielectric permittivity of pure PVDF and all the composite films is shown in Fig. 5(a). The dielectric permittivity decreased with the increasing frequency for all the composites. Generally, the dielectric behaviour of composites comprises four types of polarizations, namely, electronic polarization, ionic polarization, orientation polarization and interfacial polarization. At lower frequencies, the contributions of all these four types of polarizations are present, but at higher frequencies, ionic polarization and interfacial polarization almost disappear.[67–69] Maxwell–Wagner interfacial polarization occurs due to the charge carrier accumulation at the interface between the polymer matrix and the filler particles. The dielectric constant of the PVDF composites increased with the increasing ZnO concentration in the PVDF matrix. After the incorporation of MWCNTs in the ZnO–PVDF composites, the dielectric value increased further (Fig. 5(b)) and the 15PZNT composite system exhibited the maximum dielectric value. When the ZnO filler was added in the PVDF matrix, a capacitor-like arrangement was created in the PVDF matrix. As a result, more charges were stored in the composite system and the dielectric value was enhanced. After the addition of MWCNTs as the third phase conductive filler, the interfacial polarization increased between the fillers and the PVDF matrix leading to further enhancement in the dielectric value of the composite. MWCNTs reduced the internal resistance of the composite system and also created a conduction pathway between the ZnO nanorods and the PVDF matrix. For the MWCNT-based composite system, the interfacial interaction increased due to more compatibility of MWCNTs in the PVDF matrix.[57] On the other hand, the increase in dielectric permittivity may also be associated with the reduction in the total degree of crystallinity as described earlier. The reduced crystallinity of the composite films helped in better movement of dipoles (along the applied field direction) in the amorphous region and as a result, the permittivity increased.[63]

The frequency-dependent dielectric loss of all the composite films was also studied (Fig. 5(c)). The dielectric loss increased successfully after the addition of ZnO rods in the PVDF matrix and the further addition of MWCNTs into it. The increase in dielectric loss was associated with the formation of a conducting network by the addition of ZnO fillers in the PVDF matrix which further increased due to the conductive MWCNT addition into the composite system. The a.c. conductivity of dielectric materials can be calculated by eqn (2).

$$\sigma = 2\pi f \cdot \varepsilon_0 \cdot \varepsilon_r'' \qquad (2)$$

Here, f, ε_r and ε_r'' represent the linear frequency, free space permittivity and the imaginary part of relative permittivity of the composite films, respectively. The frequency-dependent a.c. conductivity for pure PVDF and all the composite films, as shown in Fig. 5(d), increased with the increasing filler loading in PVDF

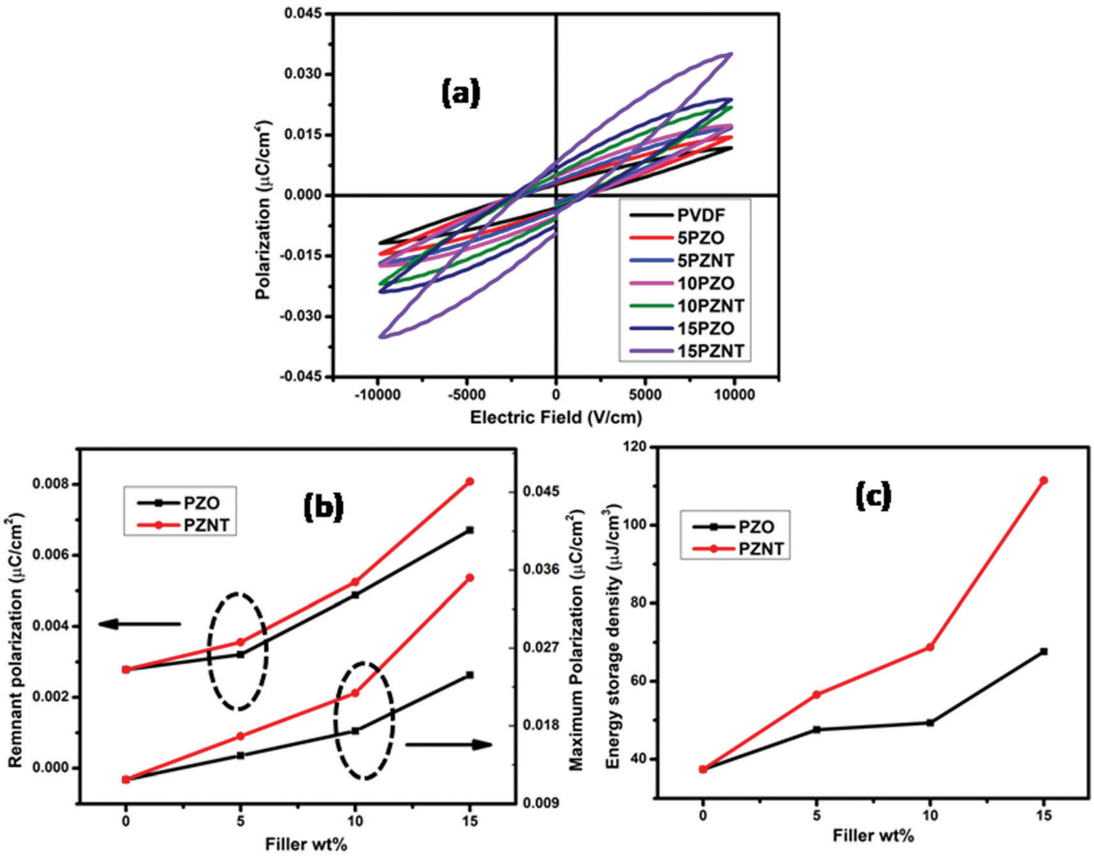

Fig. 6 (a) Electric displacement *vs.* applied electric field (d and e) loop, filler concentration dependent (b) remnant and maximum electric polarization and (c) energy storage density of PVDF and all composite films.

which further increased after the addition of MWCNTs into the system. This result can again be explained on the basis of the formation of the conducting network after filler addition and the further addition of MWCNTs as described earlier.

3.5 Ferroelectric properties and energy storage performance

The ferroelectric attribution of the nanocomposites plays a very important role in determining their application as piezoelectric energy harvesters. Fig. 6(a) depicts the room electric field (E) dependent electric displacement (D) or polarization (P) (P–E hysteresis loop or D–E hysteresis loop) of pure PVDF and all the composite films measured at room temperature. The ferroelectric properties of the PVDF-based composites are dependent on their electroactive phase. The ferroelectric domains consisting of molecular dipoles were randomly oriented in the polymer matrix. With the application of an external electric field, the alignment of the dipoles changed and a preferred orientation of them along the field direction appeared which contributed to the enhancement of net polarization. The variation of remnant polarization and maximum polarization with filler concentration is shown in Fig. 6(b). After the incorporation of ZnO nanorods in the PVDF matrix, both the remnant polarization and maximum polarization values increased compared to PVDF. The addition of MWCNTs as the conducting filler further increased the remnant polarization and maximum polarization values. The 15PZNT composite film exhibited the maximum polarization value of 0.035 μC cm^{-2}. This may be due to the more conducting nature of the added MWCNTs than that of the polymer, which resulted in a change in mobilization within the particles and hence, increased the hetero-polarization of the composite.[51] The ferroelectric properties of the composite films are also strongly dependent on the electroactive phase of PVDF.[51,70] The addition of ZnO–MWCNT into the PVDF matrix played an important role in accelerating the internal change of the nanocomposite, which has changed the polarization within the sample.

The energy storage performance of any ferroelectric material strongly depends on its ferroelectric properties. Therefore, the energy storage density (U_{stored}) of all the composite films was calculated from their D–E loops using the integral formula given below (eqn (3)).

$$U_{\text{stored}} = \int E\,\mathrm{d}D \qquad (3)$$

The electrical energy storage density as a function of filler loading for all the composite films fabricated in the present work is presented in Fig. 6(c). The energy storage density of the nanocomposites increased as the polarization increased with the increase in the concentration of filler loading for both the PVDF–ZnO (PZO) and PVDF–ZnO–MWCNT (PZNT) systems.

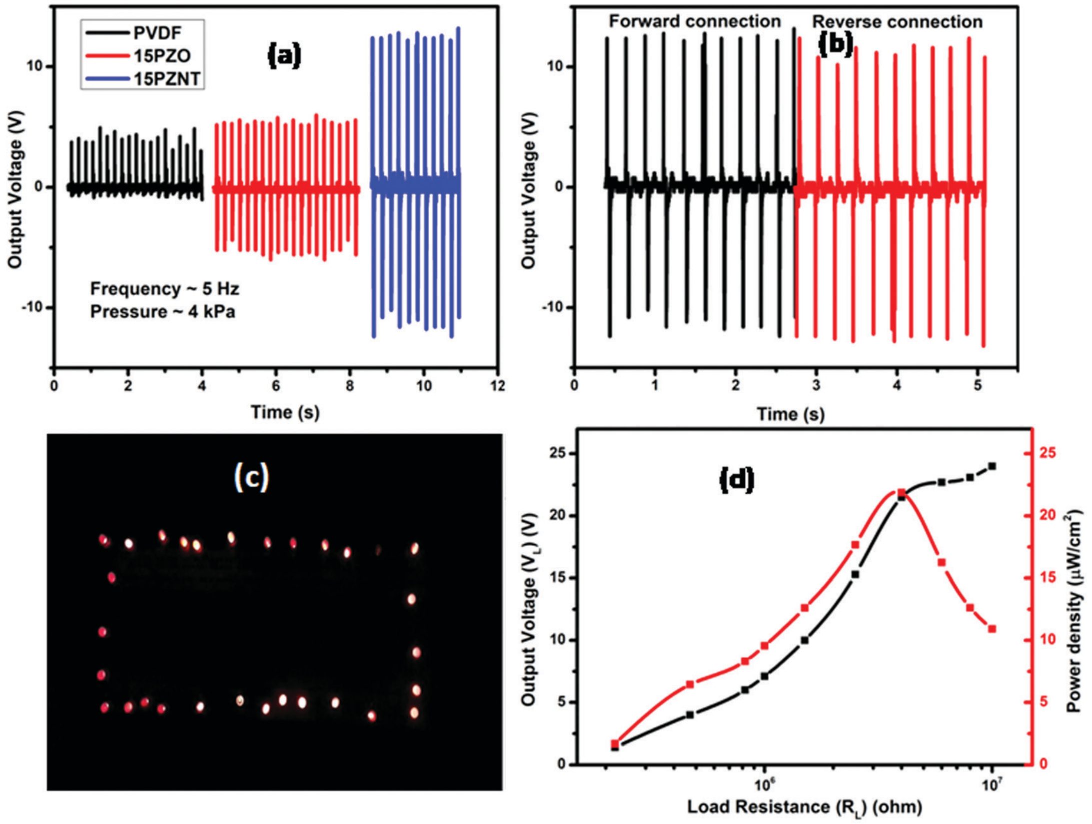

Fig. 7 (a) Comparison of open circuit output ac voltage of PVDF, 15PZO and 15PZNT composite films, (b) switching polarity test of 15PZNT sample, (c) LED glowing performance under the switch-on condition of 15PZNT film and (d) variation of output voltage and power density as a function of load resistance of 15PZNT film.

It is observed that the 15PZNT nanocomposite exhibited the highest energy storage density than the other composites studied here for the same value of the applied electric field. The energy storage density of the PZNT system increased than that of the PZO system due to the enhancement of dielectric permittivity of the MWCNT-added composites.

3.6 Energy harvesting performance

In order to investigate the piezoelectric properties of the composite systems, the output electrical properties of the fabricated composites were studied with a digital oscilloscope using human finger tapping. After applying time-varying forces on the films, dipoles of the PVDF oscillated and an electrical potential was generated across the film. Fig. 7(a) presents the output voltage (open circuit peak to peak a.c. voltage) of pure PVDF, 15PZO and 15PZNT composite films upon the application of repeated human finger tapping and releasing forces (pressure ∼ 4 kPa and frequency ∼ 5 Hz) on them. The maximum output voltage (∼ 22 V) was obtained for the 15PZNT film. This occurred due to the better dispersion of polymer ceramic composites after the addition of MWCNTs.[51,57] Besides, the MWCNTs created a conduction pathway within the polymer composites that reduced the internal resistance of the composite system.[51] The film exhibited the same amplitude of output voltage under the forward and reverse conditions by reversing the electrode connections (Fig. 7(b)) under the application of the same stress. This result confirmed that the output voltage appeared due to the piezoelectric effect only. The generated a.c. output voltage was converted to d.c. output voltage using a bridge rectifier IC (DB 107). This rectified the d.c. voltage that was able to charge a 10-μF capacitor up to ∼3 V which was used to glow some commercial LEDs (Fig. 7(c)). The output voltage *vs.* load resistance graph of the 15PZNT composite film is shown in Fig. 7(d). The output voltage was gradually increased with load resistance and reached a saturation value at 4 MΩ. The power density (P) was calculated from the output voltage (V_L) through different load resistance (R_L) by using eqn (4) given below.

$$P = \frac{1}{A}\frac{{V_L}^2}{R_L} \quad (4)$$

where A is the area of the composite film. The maximum power density of the 15PZNT composite film was found to be 21.41 μW cm^{-2} at 4 MΩ load resistance (shown in Fig. 7(d)).

3.7 Verification of experimental results by theoretical simulation

To verify the experimental results, simulation was performed using COMSOL Multiphysics software. The details of the parameters used for the simulation are presented in Discussion S6 (ESI†). Fig. 8(a and b) presents the simulated electric field distribution of the PZO and PZNT composites, respectively, under an external applied voltage of 100 V. The comparison of electric field enhancement of PZO and PZNT composites as a function of increasing applied voltage is shown in Fig. S7 (ESI†). The PZO and PZNT composites show a similar trend of electric field enhancement. For both composite films, the electric field increased linearly with the increasing applied voltage. Fig. 8(a and b) also suggested that the partial electric field on the MWCNTs (for PZNT composite) is much larger than that on ZnO. This was believed to be due to the increase in local electric field with the increased applied external voltage on the composites by the addition of MWCNTs as conductive fillers within the polymer–ceramic composites. This type of result was previously reported by several researchers.[71–73] Enhancement of electric field is a key factor to improve the polarization of the ferroelectric system.[71] The polarization distribution of the PZO and PZNT composites at an applied voltage (100 V) is shown in Fig. 9(a and b), respectively, depicted by the colour code with the same scale across the composites. The comparison of simulated polarization of the PZO and PZNT composites as a function of applied external voltage is shown in Fig. S8 (ESI†). From this simulation, it was observed that the polarization is much higher in the PZNT composite system compared to that in the PZO composite. As the fabricated PVDF-based films are ferroelectric,[74] the improved polarization may be considered to be the main consequence of electric field enhancement as described earlier. This result clearly indicates that the addition of the MWCNT conductive filler has significantly enhanced the polarization of ZnO rods. Thus, the increase of polarization in the experimental *P–E* loops after CNT addition is also justified.

In order to check the effect of MWCNTs on the piezoelectric output voltage of PVDF composites, the piezoelectric potentials of PZO and PZNT composites are also simulated using the finite element method under the application of similar pressure on each device. During simulation, the main source of piezoelectric potentials of any composite system is the value of the piezoelectric coefficient (d_{33}) of its individual component. Though PVDF and ZnO are well-known piezoelectric materials,[75,76] MWCNTs show no d_{33} value. Therefore, it is natural that the simulation may not show any increase in the piezoelectric potential after MWCNT addition in the PZO composite system. On the other hand, it is reported that, after ZnO addition, the electroactive β phase of PVDF increases significantly[36] and after CNT addition the β phase of PVDF also increases.[77] From previous experiments in the present work, the electroactive β

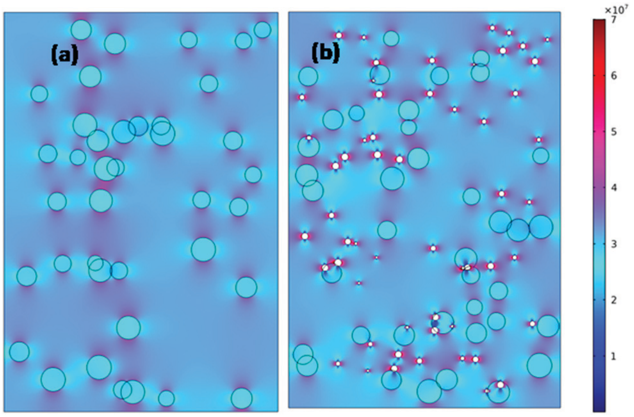

Fig. 8 Simulated electric field distribution under the applied voltage of 100 V for (a) ZnO–PVDF and (b) ZNO–MWCNT–PVDF composites.

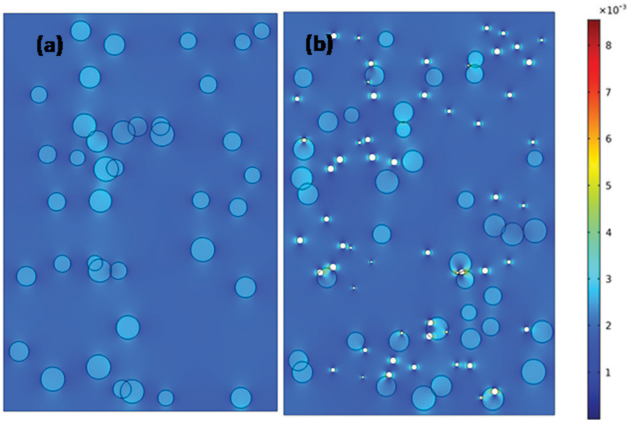

Fig. 9 Simulated polarization distribution under the applied voltage of 100 V for (a) ZnO–PVDF and (b) ZNO–MWCNT–PVDF composites.

phase of PVDF, 15PZO and 15PZNT films was also found to be enhanced gradually. On the other hand, a linear relationship exists between the polar phase of PVDF and its d_{33} value.[76] Therefore, the d_{33} value of PVDF was gradually enhanced during simulation by certain amounts for PZO and PZNT films compared to that of bare PVDF.[71,78] Fig. 10(a and b) presents the corresponding piezoelectric potentials of PZO and PZNT composites, respectively. A close observation of the colour codes for both simulations (Fig. 10(a and b)) reveals that the piezoelectric potential of the PZNT film is significantly higher than that of the PZO composite. As CNT has no d_{33} value, this enhancement of piezoelectric potential is plausibly due to the enhanced polarization and improved electroactive β phase of the composite systems after CNT addition. On the other hand, as PZNT films contained conducting MWCNTs, the charge accumulation in the PVDF–filler interface was high compared to that in the PVDF films (confirmed from dielectric studies). This large amount of space charge, upon the application of applied stress, may increase the space charge polarization by the effect of piezoelectric potentials. This space charge polarization, after being added with piezoelectric polarization, may improve the overall output piezoelectric performance. Therefore, the increased space charge polarization of the PZNT film induced by MWCNTs may be considered as another possible cause of the increase in the piezoelectric output voltage.[71] Considering all these factors, the output voltage of the different composite systems obtained in the present study is justified.

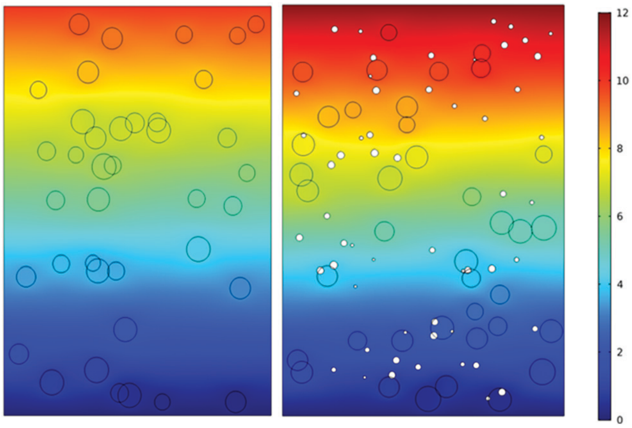

Fig. 10 Simulated piezoelectric potential distribution of (a) PVDF–ZNO and (b) PVDF–ZNO–MWCNT composites.

4 Conclusions

Three phase composite films comprising the PVDF matrix, wet chemically synthesized ZnO nanorod fillers and third conductive MWCNT phase were fabricated using the drop-casting technique. The third phase conductive MWCNT reduced the compatibility issue and supported the homogeneous dispersion of ZnO in the PVDF matrix which further improved the polarity of the resulting composite films by enhancing the interfacial interaction with the $-CH_2$ dipoles of PVDF which leads to the enhancement of the electroactive phase, dielectric permittivity, ferroelectric polarization, energy storage density and mechanical energy harvesting performance. The observed experimental results of the electrical properties were also verified by theoretical simulation. The conductive MWCNT improved the connectivity between the ZnO nanorods dispersed in the insulating PVDF matrix and between the composite films and electrodes which improved the output mechanical energy harvesting performance. The 15 wt% ZnO and 0.1 wt% MWCNT-loaded PVDF film (15PZNT) exhibited the maximum a.c. output voltage (22 V) and power density (21.41 μW cm^{-2}) at 4 MΩ load resistance upon repeated finger tapping on it. After rectification of this a.c. voltage, the obtained d.c. signal was utilized to charge a 10-μF commercial capacitor up to ∼3 V which was further used to glow some commercial LEDs instantly. Therefore, the fabricated piezoelectric nanogenerator device can definitely be explored as a self-powered sensor and applied for powering low power compatible smart electronic devices.

Conflicts of interest

The authors declare no competing financial interest.

Acknowledgements

The authors would like to thank the Director, CSIR-CGCRI, Kolkata, for allowing them to carry out this work and the Department of Science and Technology, Government of India for financial support (Grant No. DST/INSPIRE Fellowship/2017/IF170048).

References

1 T. Hassan, A. Salam, A. Khan, S. U. Khan, H. Khanzada, M. Wasim, M. Q. Khan and I. S. Kim, *J. Polym. Res.*, 2021, **28**, 36.
2 M. R. Begley, D. S. Gianola and T. R. Ray, *Science*, 2019, **364**, 1250.

3 R. Sahay, V. J. Reddy and S. Ramakrishna, *Int. J. Mech. Mater. Eng.*, 2014, **9**, 25.
4 H. C. Camargo, K. G. Satyanarayana and F. Wypych, *Mater. Res.*, 2009, **12**, 1–39.
5 B. B. Bohara and A. K. Batra, *Progr. Nat. Sci.: Mater. Int.*, 2018, **28**, 1–6.
6 S. Chen, A. Skordos and V. K. Thakur, *Mater. Today Chem.*, 2020, **17**, 100304.
7 A. Vorobjova, D. Tishkevich, D. Shimanovich, M. Zdorovets, A. Kozlovskiy, T. Zubar, D. Vinnik, M. Dong, S. Trukhanov, A. Trukhanov and V. Fedosyuk, *Nanomaterials*, 2020, **10**, 173.
8 D. I. Tishkevich, S. S. Grabchikov, S. B. Lastovskii1, S. V. Trukhanov, T. I. Zubar, D. S. Vasin and A. V. Trukhanov, *ACS Appl. Energy Mater.*, 2018, **1**(4), 1695–1702.
9 D. I. Tishkevich, A. I. Vorobjova and D. A. Vinnik, *Mater. Sci. Forum*, 2019, **946**, 235–241.
10 D. I. Tishkevich, A. I. Vorobjova and A. V. Trukhanov, *Solid State Phenom.*, 2020, **299**, 281–286.
11 D. I. Tishkevich, A. I. Vorobjova and D. A. Vinnik, *Solid State Phenom.*, 2020, **299**, 100–106.
12 K. Muller, E. Bugnicourt, M. Latorre, M. Jorda, Y. E. Sanz, J. M. Lagaron, O. Miesbauer, A. Bianchin, S. Hankin, U. Bolz, G. Perez, M. Jesdinszki, M. Lindner, Z. Scheuerer, S. Castello and M. Schmid, *Nanomaterials*, 2017, **7**, 74.
13 H. Porwal and R. Saggar, *Compr. Compos. Mater. II*, 2018, **6**, 138–161.
14 N. Singh, R. Mazumder, P. Gupta and D. Kumar, *Bull. Mater. Sci.*, 2017, **40**(3), 527–535.
15 M. Khalifa, A. Mahendran and S. Anadhan, *Polym. Compos.*, 2019, **40**, 1663–1675.
16 X. Ren, H. Fan, C. Wang, J. W. Ma, S. H. Lei, Y. Zhao, H. Lia and N. H. Zhao, *Nano Energy*, 2017, **35**, 233–241.
17 M. I. Friswell and S. Adhikari, *J. Appl. Phys.*, 2010, **108**, 014901.
18 M. R. Hasan, S.-H. Baek, K. S. Seong, J. H. Kim and I.-K. Park, *ACS Appl. Mater. Interfaces*, 2015, **7**, 5768–5774.
19 H. B. Kang, J. Chang, K. Koh, L. Lin and Y. S. Cho, *ACS Appl. Mater. Interfaces*, 2014, **6**, 10576–10582.
20 Z. H. Lin, Y. Yang, J. M. Wu, Y. Liu, F. Zhang and Z. L. Wang, *J. Phys. Chem. Lett.*, 2012, **3**, 3599–3604.
21 K. I. Park, C. K. Jeong, J. Ryu, G. T. Hwang and K. J. Lee, *Adv. Energy Mater.*, 2013, **3**, 1539–1544.
22 B. Saravanakumar, R. Mohan, K. Thiyagarajan and S. J. Kim, *RSC Adv.*, 2013, **3**, 16646–16656.
23 M. M. Alam, S. K. Ghosh, A. Sultana and D. Mandal, *Nanotechnology*, 2015, **26**, 165403.
24 C. T. Huang, J. Song, W. F. Lee, Y. Ding, Z. Gao, Y. Hao, L. J. Chen and Z. L. Wang, *J. Am. Chem. Soc.*, 2010, **132**, 4766–4771.
25 X. Ren, H. Fan, Y. Zhao and Z. Liu, *ACS Appl. Mater. Interfaces*, 2016, **8**, 26190–26197.
26 Z. L. Wang and J. H. Song, *Science*, 2006, **312**, 242–246.
27 J. Volk, T. Nagata, R. Erdélyi, I. Bársony, A. L. Tóth, I. E. Lukács, Z. S. Czigány, H. Tomimoto, Y. Shingaya and T. Chikyow, *Nanoscale Res. Lett.*, 2009, **4**, 699.
28 A. Khan, M. A. Abbasi, M. Hussain, Z. H. Ibupoto, J. Wissting, O. Nur and M. Willander, *Appl. Phys. Lett.*, 2012, **101**, 193506.
29 M.-P. Lu, J. Song, M.-Y. Lu, M.-T. Chen, Y. Gao, L.-J. Chen and Z. L. Wang, *Nano Lett.*, 2009, **9**(3), 1223–1227.
30 S. N. Cha, S. M. Kim, H. J. Kim, J. Y. Ku, J. I. Sohn, Y. J. Park, B. G. Song, M. H. Jung, E. K. Lee, B. L. Choi, J. J. Park, Z. L. Wang, J. M. Kim and K. Kim, *Nano Lett.*, 2011, **11**, 5142.
31 B. Adak, I. Chinya and S. Sen, *RSC Adv.*, 2016, **6**, 105137.
32 I. Chinya, A. Pal and S. Sen, *J. Alloys Compd.*, 2017, **722**, 829.
33 A. H. Zheng, J. Li and C. C. Han, *Macromol. Rapid Commun.*, 2007, **28**, 2159.
34 V. Sencadas, Jr., R. Gregorio and S. Lanceros-Mendez, *J. Macromol. Sci., Phys.*, 2009, **48**, 514.
35 R. Gregorio and N. C. P. D. S. Nociti, *J. Phys. D: Appl. Phys.*, 1995, **28**, 432.
36 S. Satapathy, S. Pawar, P. K. Gupta and K. B. R. Varma, *Bull. Mater. Sci.*, 2011, **34**, 727.
37 A. Sasmal, P. Sujatha Devi and S. Sen, *Phys. Chem. Chem. Phys.*, 2019, **21**, 5974–5988.
38 A. Sasmal, S. K. Medda, P. S. Devi and S. Sen, *Nanoscale*, 2020, **12**, 20908–20921.
39 H. Parangusan, D. Ponnamma and M. A. A. Al-Maadeed, *Sci. Rep.*, 2018, **8**, 754.
40 H. Parangusan, D. Ponnamma and M. A. A. Al-Maadeed, *Soft Matter*, 2018, **14**, 8803.
41 A. M. AlAhzm, M. O. Alejli, D. Ponnamma, Y. Elgawady and M. A. A. Al-Maadeed, *J. Mater. Sci.: Mater. Electron.*, 2021, **32**, 14610–14622.
42 M. K. Singha and A. patra, *IEEE Sens. Appl. Symp.*, 2019, 1–4, DOI: 10.1109/SAS.2019.8705997.
43 M. K. Singha, A. Patra, V. Rojwal, K. G. Deepa and D. Kumar, *AIP Conf. Proc.*, 2019, **2082**, 030023.
44 M. K. Singha and A. Patra, *Opt. Mater.*, 2020, **107**, 110000.
45 M. K. Singha, A. Patra, V. Rojwal and K. G. Deepa, *J. Mater. Sci.: Mater. Electron.*, 2020, **31**, 13578–13587.
46 D. Thomas, S. Augustine, K. K. Sadasivuni, D. Ponnamma, A. Y. Alhaddad, J.-J. Cabibihan and K. A. Vijayalakshmi, *J. Electron. Mater.*, 2016, **45**, 4847–4853.
47 D. Thomas, K. A. Vijayalakshmi, K. K. Sadasivuni, A. Thomas, D. Ponnamma and J.-J. Cabibihan, *J. Electron. Mater.*, 2017, **46**, 6480–6487.
48 A. Hezam, K. Namratha, Q. A. Drmosh, B. N. Chandrashekar, K. K. Sadasivuni, Z. H. Yamani, C. Cheng and K. Byrappa, *CrystEngComm*, 2017, **19**, 3299–3312.
49 J. Nunes-Pereira, P. Sharma, L. C. Fernandes, J. Oliveira, J. A. Moreira, R. K. Sharma and S. Lanceros-Mendez, *Composites, Part B*, 2018, **142**, 1–8.
50 I. Chinya, A. Sasmal and S. Sen, *J. Alloys Compd.*, 2020, **815**, 152312.
51 A. Pal, A. Sasmal, B. Manoj, D. P. Rao, A. K. Halder and S. Sen, *Mater. Chem. Phys.*, 2020, **244**, 122639.
52 Z.-M. Dang, Y. Shen and C.-W. Nan, *Appl. Phys. Lett.*, 2002, **81**, 4814–4816.
53 Prateek, V. K. Thakur and R. K. Gupta, *Chem. Rev.*, 2016, **116**, 4260–4317.

54 X. J. Zhang, G. S. Wang, Y. Z. Wei, L. GuO and M. S. Cao, *J. Mater. Chem. A*, 2013, **1**, 12115–12122.

55 K. Silakaewa and P. Thongbai, *RSC Adv.*, 2019, **9**, 23498–23507.

56 A. Sultana, M. M. Alam, S. Garain, T. K. Sinha, T. R. Middya and D. Mandal, *ACS Appl. Mater. Interfaces*, 2015, **7**, 19091–19097.

57 H. Sun, H. Tian, Y. Yang, D. Xie, Y.-C. Zhang, X. Liu, S. Ma, H.-M. Zhao and T.-L. Ren, *Nanoscale*, 2013, **5**, 6117–6123.

58 B. Liu and H. C. Zeng, *Langmuir*, 2004, **20**(10), 4196–4204.

59 S. K. Karan, D. Mandal and B. B. Khatua, *Nanoscale*, 2015, **7**, 10655–10666.

60 M. Pusty, L. Sinha and P. M. Shirage, *New J. Chem.*, 2019, **43**, 284.

61 W. Wang, H. Fan and Y. Ye, *Polymer*, 2010, **51**, 3575–3581.

62 S. Pratihar, S. K. Medda, S. Sen and P. S. Devi, *Polym. Compos.*, 2020, **41**, 3351–3363.

63 G. Suresh, S. Jatav, M. S. R. Rao and D. K. Satapathy, *Mater. Res. Express*, 2017, **4**, 075301.

64 D. Mandal, K. J. Kim and J. S. Lee, *Langmuir*, 2012, **28**, 10310–10317.

65 E. Kabir, M. Khatun, L. Nasrin, M. J. Raihan and M. Rahman, *J. Phys. D: Appl. Phys.*, 2017, **50**, 163002.

66 S. Yu, W. Zheng, W. Yu, Y. Zhang, Q. Jiang and Z. Zhao, *Macromolecules*, 2009, **42**, 8870–8874.

67 H. Luo, D. Zhang, C. Jiang, X. Yuan, C. Chen and K. Zhou, *ACS Appl. Mater. Interfaces*, 2015, **7**, 8061–8069.

68 A. C. Lopes, S. A. C. Carabineiro, M. F. R. Pereira, G. Botelho and S. Lanceros-Mendez, *ChemPhysChem*, 2013, **14**, 1926–1933.

69 A. Sasmal, S. Sen and P. S. Devi, *Soft Matter*, 2020, **16**, 8492–8505.

70 I. Chinya, A. Sasmal, A. Pal and S. Sen, *CrystEngCommun*, 2019, **21**, 3478.

71 A. Sasmal, A. Patra, P. S. Devi and S. Sen, *Compos. Sci. Technol.*, 2021, **213**, 108916.

72 C. Chen, X. Wang, J. Lin, W. Yang, H. Li, Y. Wen, L. Li, Z. Jiang and Q. Lei, *J. Mater. Chem. C*, 2016, **4**, 8070–8076.

73 P. Yang, L. Li, H. Yuan, F. Wen, P. Zheng, W. Wu, L. Zhang, G. Wang and Z. Xu, *J. Mater. Chem. C*, 2020, **8**, 14910–14918.

74 P. Martins, A. C. Lopes and S. L. Mendez, *Prog. Polym. Sci.*, 2014, **29**, 683.

75 P. Thakur, A. Kool, N. A. Hoque, B. Bagchi, F. Khatun, P. Biswas, D. Brahma, S. Roy, S. Banerjee and S. Das, *Nano Energy*, 2018, **44**, 456.

76 L. Ruan, X. Yao, Y. Chang, L. Zhou, G. Qin and X. Zhang, *Polymers*, 2018, **10**, 228.

77 G. H. Kim, S. M. Hong and Y. Seo, *Phys. Chem. Chem. Phys.*, 2009, **11**, 10506–10512.

78 A. Sasmal, A. Patra, P. S. Devi and S. Sen, *Dalton Trans.*, 2021, **50**, 1824–1837.